

University of the West of England

**Safe and Effective Physical Human-Robot
Interaction: Approaches to Variable Compliance
via Soft Joints and Soft Grippers**

Maria Elena Giannaccini



University of the
West of England

A thesis submitted in partial fulfilment of the requirements of the University of the
West of England, Bristol for the degree of Doctor of Philosophy
Faculty of Environment and Technology
University of the West of England, Bristol
September 2014

Declaration

I declare that the work in this dissertation was carried out in accordance with the requirements of the University's Regulations and Code of Practice for Research Degree Programmes and that it has not been submitted for any other academic award. Except where indicated by specific reference in the text, the work is the candidate's own work. Work done in collaboration with, or with the assistance of, others, is indicated as such. Any views expressed in the dissertation are those of the author.

Signed

Date

Abstract

The work described in this thesis focusses on designing and building two novel physical devices in a robotic arm structure. The arm is intended for human-robot interaction in the domestic assistive robotics area. The first device aims at helping to ensure the safety of the human user. It acts as a mechanical fuse and disconnects the robotic arm link from its motor in case of collision. The device behaves in a rigid manner in normal operational times and in a compliant manner in case of potentially harmful collisions: it relies on a variable compliance. The second device is the end-effector of the robotic arm. It is a novel grasping device that aims at accommodating varying object shapes. This is achieved by the structure of the grasping device that is a soft structure with a compliant and a rigid phase. Its completely soft structure is able to mould to the object's shape in the compliant phase, while the rigid phase allows holding the object in a stable way.

In this study, variable compliance is defined as a physical structure's change from a compliant to a rigid behaviour and vice versa. Due to its versatility and effectiveness, variable compliance has become the founding block of the design of the two devices in the robot arm physical structure. The novelty of the employment of variable compliance in this thesis resides in its use in both rigid and soft devices in order to help ensure both safety and adaptable grasping in one integrated physical structure, the robot arm.

The safety device has been designed, modelled, produced, tested and physically embedded in the robot arm system. Compared to previous work in this field, the feature described in this thesis' work has a major advantage: its torque threshold can be actively regulated depending on the operational situation. The threshold torque is best described by an exponential curve in the mathematical model while it is best fit by a second order equation in the experimental data. The mismatch is more considerable for high values of threshold torque. However, both curves reflect that threshold torque magnitude increases by increasing the setting of the device. Testing of both the passive decoupling and active threshold torque regulation show that both are successfully obtained. The second novel feature of the robot arm is the soft grasping device inspired by hydrostatic skeletons. Its ability to passively adapts to complex shapes objects, reduces the complexity of the grasping action control. This gripper is low-cost, soft, cable-driven and it features no stiff sections. Its versatility, variable compliance and stable grasp are shown in several experiments. A model of the forward kinematics of the system is derived from observation of its bending behaviour.

Variable compliance has shown to be a very relevant principle for the design and implementation of a robotic arm aimed at safely interacting with human users and that can reduce grasp control complexity by passively adapting to the object's shape.

Acknowledgments

The work described in this thesis would not have been possible without the help of Ian Horsfield and Sam Coupland, two technical support engineers of rare dedication. I will not be able to thank enough the undergraduate and master students who helped and inspired my work: Anthony Meunier, Pasindu Peiris, Yue Zheng, Bastien Bonard, Michelle Freret and Peng Huang. Great encouragement and advice was also provided by the Bristol Robotic Laboratory's team at large: most notably, Dr Chris Harper, Dr Ioannis Georgilas, Dr Tareq Assaf and Dr Daniel Raabe.

This doctoral experience would have lost much of its depth if it had not been shared with the other members of the INTRO project: Sasa Bodiroza, Dr Guido Schillaci, Guillaume Doisy, Dr Aleksandar Jevtic, Prof. Verena Hafner and all the others, your presence has been an inspiration and source of constant learning.

Saving the best for last, I am most grateful for the support and guidance of my supervisory team: Prof. Anthony G. Pipe, Prof. Sanja Dogramadzi and Dr Alexander Lenz. You taught me the multiple, complex and rewarding aspects of Research.

Contents

Contents	1
List of Figures	4
List of Tables	16
1 Introduction	19
1.1 Assistive Robotics	19
1.2 The FP7 INTRO project	20
1.3 Aims, objectives and methodology	21
1.4 Publications	24
1.5 Structure of the thesis	25
2 Variable Compliance and its application in Safety and Grasping	26
2.1 Compliance and Variable Compliance: definitions	26
2.2 Robot Safety	27
2.2.1 Inherent safety	27
2.2.2 Active Variable Compliance	30
2.2.3 Variable Stiffness/Impedance Actuators	33
2.2.4 Passive Variable Compliance	34
2.2.5 Pain Thresholds	36
2.3 Embodied Intelligence	38
2.4 Grasping in Human Environments	39
2.4.1 Physical Structure Based Approach	39
2.4.2 Bioinspiration	45
2.4.3 Hydrostatic Skeletons	46
2.5 Summary	50
2.6 List of Requirements for this Thesis' Work	51
2.7 Variable Compliance and Novel Contribution	52
3 Manipulators' State of the Art and INTRO-BRL Robotic Arm	53
3.1 Background	53
3.2 Non-hyper-redundant Arms	54
3.2.1 Safety Characteristics	56
3.3 Hyper-redundant and soft arms	57

3.3.1	Kinematics of Hyper-redundant and Soft Robots	59
3.4	Reflections on the State of the Art leading to New Design	60
3.5	INTRO-BRL arm	61
3.5.1	Arm Design and Inherent Safety	62
3.5.2	Hardware description	63
3.5.3	Forward Kinematics of the Robotic Arm	64
3.5.4	Balance of Energy of the Robotic Arm	67
3.6	Summary	70
4	Adjustable Variable Compliance Mechanism to Improve Safety	73
4.1	Connection to the State of the Art	73
4.2	Novel Approach	74
4.2.1	Active Torque Threshold Adjuster	75
4.2.2	Passive Variable Compliance Mechanism	77
4.3	Materials, Methods and HDF Versions	79
4.4	Integration of HDF with the INTRO-BRL arm	81
4.5	Mathematical Model of the Mechanism	84
4.5.1	Parts Description	85
4.5.2	Application of Wrenches to the HDF Mechanical Study	95
4.6	Experimental Analysis	104
4.6.1	Design-testing Experiments	104
4.6.2	Characterisation experiments	107
4.7	Comparison between Modelled Variables and Experimental Values	112
4.8	Summary	113
5	Hydrostatic Skeleton Gripper	116
5.1	Comparison with the State of the Art	117
5.2	Initial Work	119
5.2.1	Design	120
5.2.2	Qualitative Performance	121
5.2.3	Results	122
5.3	Gripper Application Domain	123
5.4	Bioinspired Working Mechanism	124
5.5	Hardware Implementation	126
5.5.1	Materials, Control and Design	126
5.5.2	Gripper Variants	133
5.6	Experimental Analysis	134
5.6.1	Planar Behaviour	134
5.6.2	Variable Compliance	138
5.6.3	Continuous versus Discrete Design	142
5.7	Forward Kinematics	143

5.8	Grasping Experiments	144
5.8.1	Variable Cross-section Shape Grasping	144
5.8.2	Experiments in the Application Domain	148
5.9	Discussion	149
5.10	Summary	152
6	Conclusions and Future Work	153
6.1	Conclusions	153
6.2	Future Work	155
6.3	Contribution to the Robotics Field	156
	Bibliography	158
	Appendices	167
A	Appendix of Chapter 3	168
A.1	Matlab Code for the INTRO-BRL arm	168
B	Appendix of Chapter 4	172
B.1	Background work on Hybrid Decoupling Feature	172
B.2	Intermediate Results of HDF Mathematical Model	175
B.3	Calculations on the Wrenches Study of the HDF	182
B.4	Design-testing Experiments Results: Statistical Analysis	184
B.5	Matlab Code for Threshold torque determination	188
B.6	Characterisation Experiments Results: Statistical Analysis	190
C	Appendix of Chapter 5	194
C.1	Variable Compliance Experiments Results: Statistical Analysis	194
C.2	Matlab Code for the HS gripper	195
C.3	Forward Kinematics Analysis	208

List of Figures

1.1	Life expectancy at birth in Europe since 1960, from the figure ‘Male and female life expectancy at birth in the sub-regions of Europe since 1960’ in [Avdeev et al., 2011], used with permission of the journal Population, Ined and the authors. For clarification on the composition of the five European regions see Figure 1.2	20
1.2	The five European regions. From the figure ‘Box: List of countries of Europe by region and their ISO codes’ in [Avdeev et al., 2011], used with permission of the journal Population, Ined and the authors. . . .	21
1.3	Methodology of scientific enquiry. The hypothesis process in this flow chart has been substituted in this thesis by a device design solution . .	22
2.1	Diagram of the distributed actuation system, from [Zinn et al., 2002], used with permission of Dr Zinn.	29
2.2	τ_m, τ_F, τ and τ_{ext} are the motor torque, the friction torque, the joint torque and the external torque. The inputs to the disturbance observer are the joint torque, the link position and the link velocity. It can be shown that the estimated external torque ($\hat{\tau}_{ext}$), which is the output of the disturbance observer, is a filtered version of the real external torque (τ_{ext}). The motor positioning sensor is more accurate than the link side position sensor and, due to the good flexible-joint model of the robot, this is used together with the motor position and velocity ($\theta, \dot{\theta}$) to estimate the link side position and velocity ($\hat{q}, \hat{\dot{q}}$). Figure used with permission of SAGE Publications, Inc. Taken from [Haddadin et al., 2009]	32
2.3	The variable stiffness mechanism is located between the harmonic drive gear box of the main actuator and the link. A stiffer configuration is obtained by preloading the springs via the motion of the stiffness adjusting motor. Figure from [Greibenstein et al., 2011] ©2011 IEEE	34

2.4	The non linear spring system, composed by a double-slider mechanism with a spring, in its initial configuration. \vec{F}_s is the force of the spring, \vec{T}_s is the spring torque that induces the force \vec{F}'_s , d_o is the distance between the pivot point and the point of application of \vec{F}'_s , figure from [Park et al., 2009] ©2009 IEEE	35
2.5	Pressure pain thresholds (PPT) of 10 test subjects; they were averaged over three repeated measurements. The complete surface of the plunger used in this pilot study was 1414 mm. The thick line in the box represents the median of the value. The acronym ‘ndom’ stands for non-dominant side. Most measurements in the study were conducted on the non-dominant (ndom) side, since some research suggests that lower pain thresholds might be attributed to the non-dominant side of the body [Özcan et al., 2004]. Figure from [Melia et al., 2014], used with permission of Springer and Dr Melia	37
2.6	Embodiment interplay: the physical system (e.g. musculoskeletal) is driven by motor commands and acts on the environment. Such action causes sensory feedback, which depends on the physical characteristics and morphology of the sensory system and on the motor commands. From Pfeifer, R., Lungarella, M. and Iida, F. (2007). Self-organization, embodiment, and biologically inspired robotics. science, 318(5853), 1088-1093. Reprinted with permission from AAAS.	38
2.7	The unidirectional compliance gripper (left) is able to adapt to the object shape but lacks the shape-matching provided by the multidirectional type gripper (right) which is able to effectively interlock the object in its own structure	40
2.8	SDM hand. The hand is compliant in the workspace of the three link fingers. However, due to the inherent rigidity of the links and to their mechanical coupling between the finger links, the workspace of the SDM hand is inherently limited. Hence, the hand can adapt to external objects but retains movement constraints due to its mechanical structure. Figure from [Ma et al., 2013] ©2013 IEEE	41
2.9	A: the non-anthropomorphic universal gripper mounted on a rigid robotic arm, in its soft state B: the gripper as it lifts an object, in its rigid state. The universal jamming gripper is able to grasp a wide variety of objects without grasp planning or sensory feedback [Amend et al., 2012]. This device is a perfect example of multidirectional compliance. Due to the lack of fixed shape in its flaccid state, there are no mechanical constraints which hinder its adaptation to an external object. Figure from [Brown et al., 2010], used with permission of PNAS	42

2.10	Festo’s fin effect gripper. Sources: Food Engineering Magazine, June 2012, www.foodengineeringmag.com ; www.festo.com	43
2.11	The Whiteside group starfish-like gripper. Figure used with permission. The version being referenced is the Author’s Accepted Manuscript, available via Harvard University’s DASH repository.	43
2.12	Connections between disciplines	45
2.13	Octopus-like robot arm prototype in water. Figure from [Laschi et al., 2012], used with permission of Taylor & Francis.	45
2.14	Diagram illustrating the structure of the octopus arm: From the top: DCT: dermal connective tissue, V: vein, EP: epidermis, CM: circumferential muscle layer, CT: connective tissue, OME: external oblique muscle layer, IN: intramuscular nerve, LM: longitudinal muscle fibres, TR: trabeculae, OMM: median oblique muscle layer, TM: transverse muscle fibres, AR: artery, AN: axial nerve cord, OMI: internal oblique muscle layer and SU: sucker. The figure is from [Trivedi et al., 2008]. Copyright ©2008 Hindawi Publishing Corporation. This is an open access article distributed under the Creative Commons Attribution License.	47
2.15	Cross-section view of the arrangement of transverse actuators in the SSSA artificial muscular hydrostat, the white arrows point towards the direction of movement of the SMAs: once they are given current, the SMAs coils contract and reduce the diameter of the cross-section. Figure from [Laschi et al., 2012], used with permission of Taylor & Francis.	49
2.16	PAM actuators. Figure from [Daerden and Lefeber, 2002], courtesy of Dr Daerden.	49
3.1	Robot classification based on materials and degrees of freedom. The figure is from [Trivedi et al., 2008]. Copyright ©2008 Hindawi Publishing Corporation. This is an open access article distributed under the Creative Commons Attribution License.	54
3.2	The Jaco arm is commercially available and used by disabled and elderly persons. Figure from [Maheu et al., 2011] ©2011 IEEE. . . .	55
3.3	The BioRob Arm: most of the robot’s mass to be located at the base of the robot arm. Figure from [Lens et al., 2011] ©2011 IEEE. . . .	55
3.4	The LWRIII: its most salient features are the joint-integrated power and signal processing electronics including torque sensors mounted on the gear box output in all joints. Figure from [Bischoff et al., 2010], used with permission of Dr Bischoff.	55

3.5	The BHA manipulator with an adaptive gripper based on the Fin Ray Effect, inspired by the movement of a fish tail fin. The figure was taken from [Festo, 2013a] with permission of ©Festo AG & Co. KG	58
3.6	OctArm V: (a) view of the arm, (b) base (c) view of the first section (two actuators for each control channel), (d) photograph of the complete arm. The figure is from [Trivedi et al., 2008], accessed at http://www.hindawi.com/journals/abb/2008/520417/cta/ . Copyright ©2008 Hindawi Publishing Corporation. This is an open access article distributed under the Creative Commons Attribution License.	58
3.7	the INTRO-BRL arm in the apartment set up of the Robosoft company, France. The HDF can be seen between the blue custom made fixture and the revolute joint.	62
3.8	The INTRO-BRL arm mounted on the RobuLAB10 platform. The robot arm comprises: 1:rail, 2:revolute joint, 3:variable torque safety feature, 4:link 2, 5:soft gripper. At the back of the robot arm it is possible to see the laptop and pan-tilt camera installed on the RobuLAB10 for research on cognitive human robot interaction, carried out by other researchers in the INTRO project	64
3.9	the schematics above illustrates the two degrees of freedom present in the manipulator	65
3.10	The value of kinetic energy in the INTRO-BRL arm	70
3.11	The value of potential energy in the INTRO-BRL arm	71
3.12	The value of kinetic energy in an arm similar to the INTRO-BRL arm but with more powerful motors	72
4.1	HDF, its four main components, the angle γ and an example of the position of the external force (due to a collision) which might cause a torque high enough to exceed the threshold torque. The external force might be applied on either side of the T-shaped element and anywhere along the robot arm link, which is fixed to the long side of the T-shaped element, as shown in Figure 4.7	75
4.2	Double slider mechanism with spring in the general configuration, figure from [Park et al., 2009] ©2009 IEEE.	77
4.3	angle γ is shown in light blue in the drawing of a SJM prototype made in BRL. The four bar mechanism has been modified and the short side of the T-element and the connecting link are the parts that are left of it, as already done in the work of Park et al.	78
4.4	The first version of the HDF, in acrylic (left), and the second version, in steel (right).	79

4.5	Different stages of the assembly process of HDF. The assembling steps are explained in detail in Table 4.1. The assembled HDF is mounted on the purposely designed fixture which fixes it to the INTRO-BRL arm link	81
4.6	Lateral view of the HDF, from which it is possible to notice its multiple layers.	81
4.7	The INTRO-BRL robot arm link in normal operational times, when the HDF is in its initial stage and motor and link are coupled. The flat metal plate and the blue box underneath it are the fixtures which hold together the HDF and the arm link	82
4.8	The INTRO-BRL robot arm link after a collision, when the HDF has been triggered and motor and link are decoupled. The flat metal plate and the blue box underneath it are the fixtures which hold together the HDF and the arm link	82
4.9	Solid Edge [®] drawing of the INTRO-BRL robot arm mounted on the RobuLAB10 platform. In this case, the link has been hit by a force which caused a torque above the torque threshold thus the HDF is triggered and motor and link are decoupled	83
4.10	The main parts of the system are: the T-shaped element, the connecting links, the guiding slots, the adjustment arms. The spring is squeezed between the two bottom ends of the connecting links.	86
4.11	The HDF with its global coordinate system. The highlighted component is the T-shaped element. The HDF is in the configuration with the lowest possible value of γ , which yields the minimum torque	87
4.12	The T-shaped element, the global coordinate system is shown, its z axis is pointing outwards, towards the reader and the local coordinate system, relative to the T-shaped element, x_1 - y_1 is also shown, again its z_1 axis is pointing outward, towards the reader. α_1 is the angle between the global and local coordinate system and in the figure is zero, since the HDF is not triggered	87
4.13	The T-shaped element, in this figure α_1 is not zero, since the HDF has been triggered	88
4.14	The HDF with its global coordinate system. The highlighted component is the guiding slot	89
4.15	The guiding slot, the global coordinate system is shown, the z axis is pointing outwards, towards the reader and two local coordinate systems, relative to the guiding slot, x_{2_1} - y_{2_1} and x_{2_2} - y_{2_2} are also shown; their z_{2_1} and z_{2_2} axes are pointing outward, towards the reader. In the first coordinate system x_{2_1} is along the longer segment of the guiding slot, in the second y_{2_2} is along the shorter segment of the guiding slot	90

4.16	The angle α_2 corresponds to the difference in orientation from the global coordinate system to the first local coordinate system of the guiding slot. Since α_2 goes clockwise, it is positive. The angle α_2 depends on the movement on the HDF	90
4.17	The HDF with its global coordinate system. The highlighted component is the connecting link	91
4.18	The connecting link: the global coordinate system, $x-y$ is shown, the z axis is pointing outwards, towards the reader. The local coordinate system, relative to the connection link, x_3-y_3 is also shown, its z_3 axis points outward, towards the reader	92
4.19	The HDF with its global coordinate system. The highlighted component is the adjustment arm	93
4.20	The adjustment arm: the global coordinate system, $x-y$ is shown, the z axis is pointing outwards, towards the reader. The local coordinate system, relative to the adjustment arm, x_4-y_4 is also shown, its z_4 axis is point outwards, toward the reader.	93
4.21	Global and local coordinate systems in the HDF. α_1 in this case is zero since the T-shaped element is in its initial position. All the other angles go clockwise from the general coordinate axis to the local coordinate axis are clockwise, thus positive	94
4.22	A rigid body, Forces F, Couples C, a line l, from [Kumar, 2015], used with permission of Dr Kumar.	95
4.23	The screw axis, from [Kumar, 2015], used with permission of Dr Kumar.	96
4.24	The forces acting on the T-shaped element. This drawing shows the T-shaped element at the equilibrium, before it is triggered. In this case α_1 equal to zero. The general coordinate system is shown in green in the figure	97
4.25	The forces acting on the connecting link	100
4.26	Angle α_2 plotted against m_x , which is the change in orientation of the guiding slot against the threshold torque adjustment	103
4.27	The curves are the values of the absolute of the threshold torque. The red curve was obtained by substituting in the threshold torque equation the friction coefficients for non-lubricated materials and the blue line was obtained by substituting friction coefficients for lubricated materials. For this example the value of the spring stiffness is chosen as 1.74 N/mm.	103

4.28	Experimental curves which describe the relationship between the displacement along the adjustment arms slots and the threshold torque needed for the HDF decoupling of the right side of the HDF, for spring stiffnesses of 0.78 N/mm, 1.34N/mm and 1.74N/mm. The HDF setting is equal to m`x, a displacement produced by the linear motor actuation. Hence is the measure of how much the adjustment arm has been displaced in the bottom slot	106
4.29	Experimental curve which describes the relationship between the displacement along the adjustment arms slots and the threshold torque needed for the HDF decoupling of the left side of HDF, for spring stiffnesses of 0.78 N/mm, 1.34N/mm and 1.74N/mm. The HDF setting is equal to m`x, a displacement produced by the linear motor actuation. Hence is the measure of how much the adjustment arm has been displaced in the bottom slot	107
4.30	From the left: the cylindrical aluminium link, which is inserted into the 3-D printed blue fixture that is, in turn, fixed to the load cell, identified in the figure with an arrow. The load cell is fixed to the T-shaped element of the HDF (on the right side of the figure) by screws. The red potentiometer, identified by the arrow, is fixed to the pivot point of the T-shaped element of the HDF. At the far right of the figure it is possible to see the cylindrical stand where the HDF is fixed. The stand is then clamped to the table in order to avoid any possible movement of the HDF frame during testing.	109
4.31	The external collision force (blue) is applied to the HDF and the resulting angles of displacement (red) of the HDF are plotted versus the sample number: samples are taken every 10ms. The green line shows the moment in which the external force has exceeded the threshold. Simultaneously, the angle of displacement of the T-shaped element goes from its resting value to a higher value. This entails the T-shaped element has rotated, which happens when the HDF is engaged and the entire structure is in compliant mode	110
4.32	The threshold torque is plotted against the linear displacement in the adjustment arm slot in order to characterise the threshold torque variation for various positions of the torque adjusting mechanism, the blue crosses are for the right side of the HDF, the red diamonds are for the left side of the HDF. The HDF setting is equal to m`x, a displacement produced by the linear motor actuation. Hence is the measure of how much the adjustment arm has been displaced in the bottom slot	110

4.33	The threshold torque is plotted against the linear displacement in the adjustment arm slot. The blue crosses are for the right side of the HDF, the red diamonds are for the left side of the HDF.	111
4.34	Relationship between the threshold torque value and the displacement of the slider mechanism that adjusts the position of the lever arm. The theoretical value of the threshold torque (in blue) in the lubricated scenario is plotted together with the experimental values of the threshold torque values of the right hand side of the HDF (in red) and of the left hand side of the HDF (in green). In the experiments lubricant was added to the structure.	112
4.35	The theoretical value of the threshold torque (in blue) in the non-lubricated scenario is plotted together with the experimental values of the threshold torque values of the right hand side of the HDF (in red) and of the left hand side of the HDF (in green). In these experiments no lubricant was utilised.	113
5.1	Robot octopus arm of the Scuola Superiore Sant'Anna. Figure from [Laschi et al., 2012], used with permission of Taylor & Francis. . . .	117
5.2	One of the possible configurations of the STIFF-FLOP manipulator. Figure from [Maghooa et al., 2015], ©2015 IEEE	118
5.3	BRL reproduction of the University of Chicago universal robotic gripper built to test its functionality. This device is a good example of multidirectional compliance. Due to the lack of fixed shape in its flaccid state, there are no mechanical constraints which hinder its adaptation to an external object [Brown et al., 2010]	119
5.4	Top view of the system comprising the general gripper (made up by the vacuum pump, tubes and the compliant pockets), the object to be grasped and the weight gauge	120
5.5	Top view of the multidirectionally compliant arm gripper and the vacuum system	121
5.6	Sketch of the structure of a biological hydrostatic skeleton. Figure from Purves et al., Life: The Science of Biology, 4th Edition, by Sinauer Associates. Used with permission of Sinauer Associates. . . .	122
5.7	HS gripper in its stiff, bent state, when force is applied to its two cables (both are visible in white on the left of the picture, while one is shown in black along the HS gripper body. The other cable is in the exact same position but on the flip side).	123

- 5.8 From the left: the laptop computer is connected to a dsPIC30F4011 micro- controller, which is also connected to an H-bridge driver circuit, connected to a power source, visible in the back (far right). The H-bridge is connected to a brushed DC motor (centre of the picture). The motor is held in place by a custom 3D printed structure (ivory colour) so that it does not move during the experiments. Two cables are tied to the spindle mounted on the motor shaft. These cables run along the whole length of the gripper and are fixed at the tip of the gripper itself. The base of the gripper is also fixed to the table: the gripper holder (in black in the picture) is screwed on the table. The rest of the gripper, instead, is free to move and in this case is pictured in its non-actuated, compliant state resting on the table. The object on the right of the gripper is within its workspace and can be easily grasped. Figure from [Giannaccini et al., 2014], used with permission of Springer. 126
- 5.9 UGS NX6 software drawing of the outer empty shell with silicone tubes. The two tubes and the cables inside them are on one side of the gripper only. The two arrows point to the location of the cables. Figure from [Giannaccini et al., 2014], used with permission of Springer. 127
- 5.10 Drawing of the two quasi-longitudinal cables (almost-longitudinal, since they do not run parallel to the longitudinal axis, there is a 0.0436 angle between the two), which is running along the length of the gripper, (in blue) and the angle they form with the horizontal (in black). The red outline is the HS gripper’s laid out shape. Figure from [Giannaccini et al., 2014], used with permission of Springer. . . . 128
- 5.11 Trial with a 67.57% of the HS gripper filled with water. Force on the cable for each curve: Blue: 0N, Green: 9.8N, Red: 19.6N and Purple: 29.4N. For high forces the gripper is bent in a semi-circular configuration and thus half of the gripper’s body sits in a position along the x axis further than the gripper’s base position. The prototype is curling around its holder, positioned at $x=280$, $y=260$. An object positioned near the gripper could have been crushed between the HS gripper and the holder, shown in Figure 5.7, which is rigid and provides no compliant grasping. Figure from [Giannaccini et al., 2012], ©2012 IEEE. 129

5.12	Trial with a 81.1% of the HS gripper filled with water. Force on the cable for each curve: Blue: 0N, Green: 9.8N, Red: 19.6N and Purple: 29.4N. It can be appreciated that a greater filling quantity allows the HS gripper's whole body to remain in front of the holder, which in this figure is for x values smaller than 280. The gripper holder is in position $x = 280$ and $y = 260$. Figure from [Giannaccini et al., 2012], ©2012 IEEE.	130
5.13	Trial with a 94.6% of the HS gripper filled with water. Force on the cable for each curve: Blue: 0N, Green: 9.8N, Red: 19.6N and Purple: 29.4N. The gripper holder is in position $x = 280$ and $y = 260$. The trend started in the previous experiment continues: in this case the prototype exhibits trajectories that are closer to the origin of the x -axis. Figure from [Giannaccini et al., 2012], ©2012 IEEE.	130
5.14	The silicone tubes have been glued to the corona treated polyethylene sheet, on which the edges of the cone have been stamped. The heat sealer is used to seal the edges together and then the cone is reversed inside out	131
5.15	The polyethylene cone is ready: the silicone tubes are on the inside and only the cables (wound up in the upper right corner) come out of the cone	132
5.16	Gripper variants: the first gripper has continuous tubing, shown by the solid lines. The dotted line in the schematics of the second gripper indicates that the silicone tubes is discontinuous. Figure from [Giannaccini et al., 2014], used with permission of Springer.	133
5.17	The grippers are divided into sections: Section 1 corresponds to the base of the gripper, Section 2 to the middle and Section 3 to the tip. In the picture it is possible to see also the twisted white wires of the pressure sensors, which are fixed on the object's surface area. The internal side of the gripper is the one with the creases (or concertina) and the external one is the one without creases. Figure from [Giannaccini et al., 2014], used with permission of Springer.	135
5.18	Experimental variation of the radius of curvature in the continuous gripper. Please note that the radius of curvature axis has a logarithmic scale. Figure from [Giannaccini et al., 2014], used with permission of Springer.	135
5.19	Experimental variation of the radius of curvature in the discrete gripper. Please note that the radius of curvature axis has a logarithmic scale. Figure from [Giannaccini et al., 2014], used with permission of Springer.	136

5.20	Experimental trajectory on the horizontal plane: continuous gripper. The straight lines are approximations of the gripper's position between two adjacent markers. Figure from [Giannaccini et al., 2014], used with permission of Springer.	137
5.21	Experimental trajectory on the horizontal plane: discrete gripper. The straight lines are approximations of the gripper's position between two adjacent markers. The gripper holder is in position $x = 280$ and $y = 190$ in all three graphs. Figure from [Giannaccini et al., 2014], used with permission of Springer.	137
5.22	Close up of the discrete gripper trajectory on the horizontal plane. The straight lines are approximations of the gripper's position between two markers. The gripper holder is in position $x = 280$ and $y = 190$ in all three graphs. Figure from [Giannaccini et al., 2014], used with permission of Springer.	138
5.23	Stiffness estimation setup. The gripper (pink) is laying flat on the rig table and the only visible parts are its tip and the gripper holder (round structure in black). The gripper holder is fixed to the rig table so that the gripper's base does not move during the experiment. The two cables embedded in the gripper are shown in the figure coming out of the gripper holder towards the reader. The laser probe above the gripper is used to measure the distance between the laser probe itself and the surface of the gripper. The distance between the surface of the gripper and the laser probe is at its minimum when no weight is put on top of the gripper. As more and more weights are put on top of the gripper, the gripper is flattened by the weights and the distance between the two increases. Hence the distance between the probe and the gripper is indicative of the deformation of the gripper and thus its top surface displacement along the y axis, which is shown in the figure coordinate system. The weights are not put directly on the gripper but on top of a flat and rigid platform shown in the figure. Figure from [Giannaccini et al., 2014], used with permission of Springer.	140
5.24	Variation of the continuous gripper stiffness. Trials are repeated three times each, error bars show the standard deviation in the data. Figure from [Giannaccini et al., 2014], used with permission of Springer. . . .	141
5.25	Variation of the discrete gripper stiffness. Trials are repeated three times each, error bars show the standard deviation in the data. Figure from [Giannaccini et al., 2014], used with permission of Springer. . . .	141

5.26	Tip position in the x and y cartesian coordinates against the HS gripper cable displacement. The mean value and the standard deviation (limit in the legend) among the six tests for each coordinate over the full displacement range is given. Figure from [Giannaccini et al., 2014], used with permission of Springer.	143
5.27	Photo: the continuous gripper as it is grasping the irregular object. Schematics: Position of the sensors on the tested objects, S stands for sensor: S1 represents the first sensor, S2 the second sensor and so on. The orientation of the object in the schematics is the same as the orientation of the object in the picture. From the left: square, round and irregular object. Figure from [Giannaccini et al., 2014], used with permission of Springer.	146
5.28	Force readings of the four sensors on the square, round and irregular object. These graphs show the results of three of the fifteen trials performed in this experiments. The important information is the presence of contact, not the value of contact force the HS gripper exerts on the object. The object is fully grasped during the first 15sec but the data has been recorded further to investigate whether the force on each contact point changed during a prolonged grasp. Figure from [Giannaccini et al., 2014], used with permission of Springer.	147
5.29	Maximum and minimum diameter of a standard plastic cup	148
5.30	A: the compliant plastic cup is grasped B: the gripper is able to keep its position without needing the extra support. Figure from [Giannaccini et al., 2014], used with permission of Springer.	149
5.31	Grasping rasping without resting on table. A: the object is held by the human B: the gripper has successfully grasped the object. Figure from [Giannaccini et al., 2014], used with permission of Springer.	150
B.1	Diagram for the connecting link. The friction forces are in green.	173
B.2	The non linear spring system, composed by a double-slider mechanism with a spring, in its initial configuration [Park et al., 2008]	175
B.3	Sum of vectors	176
B.4	Sum of vectors	176
B.5	Sum of vectors	178
B.6	Vectors and angles	178
B.7	Sum of vectors. In this drawing a small distance is shown between the points M_3 and O_3 , so that the difference between the two can be appreciated, but in reality these two points are assumed as being the same in case the HDF has not been triggered, which means that the T-shaped element has not rotated around O_1 and α_1 is zero	180

B.8 Sum of vectors. In this drawing the vectorial sum is divided in two parts, for clarity 180

List of Tables

3.1	Comparison of Jaco arm [KinovaRobotics, 2013], the BioRob Arm [Lens et al., 2010], the LWRIII arm [Bischoff et al., 2010]	55
3.2	Comparison of the Bionic Handling Assistant, [Festo, 2013a] and the OctArm [McMahan et al., 2006]	58
3.3	Denavit-Hartenberg parameters for the INTRO-BRL arm. Out of these parameters, some are variables and some are known constants. The variables are d_1 and θ_3 . The constants are: a_2 , equal to 125mm, a_3 , the length of link 2 and equal to 500mm and θ_2 which is fixed at $\pi/4$ radians.	65
4.1	Steps in the assembly procedure of the HDF structure, pictured in Figure 4.5	80
5.1	Number of Contacted Sensors for Square Object	146
5.2	Number of Contacted Sensors for Round Object	146
5.3	Number of Contacted Sensors for Irregular Object	147
B.1	HDF Threshold Torque Values Statistical Analysis (Right, 0.78 N/mm spring)	185
B.2	HDF Threshold Torque Values Statistical Analysis (Right, 1.34 N/mm spring)	185
B.3	HDF Threshold Torque Values Statistical Analysis (Right, 1.74 N/mm spring)	186
B.4	HDF Threshold Torque Values Statistical Analysis (Left, 0.78 N/mm spring)	187
B.5	HDF Threshold Torque Values Statistical Analysis (Left, 1.34 N/mm spring)	188
B.6	HDF Threshold Torque Values Statistical Analysis (Left, 1.74 N/mm spring)	189
B.7	HDF Critical Force Values Statistical Analysis, Right side (Load Cell)	191
B.8	HDF Critical Force Values Statistical Analysis, Left side (Load Cell)	192
B.9	HDF Critical Force Values Statistical Analysis, Right side (Load Cell)	193
B.10	HDF Critical Force Values Statistical Analysis, Left side (Load Cell)	193

C.1	Continuous Gripper Stiffness Values Statistical Analysis	194
C.2	Discrete Gripper Stiffness Values Statistical Analysis	194
C.3	Parameters Fitting Statistical Analysis	210

Chapter 1

Introduction

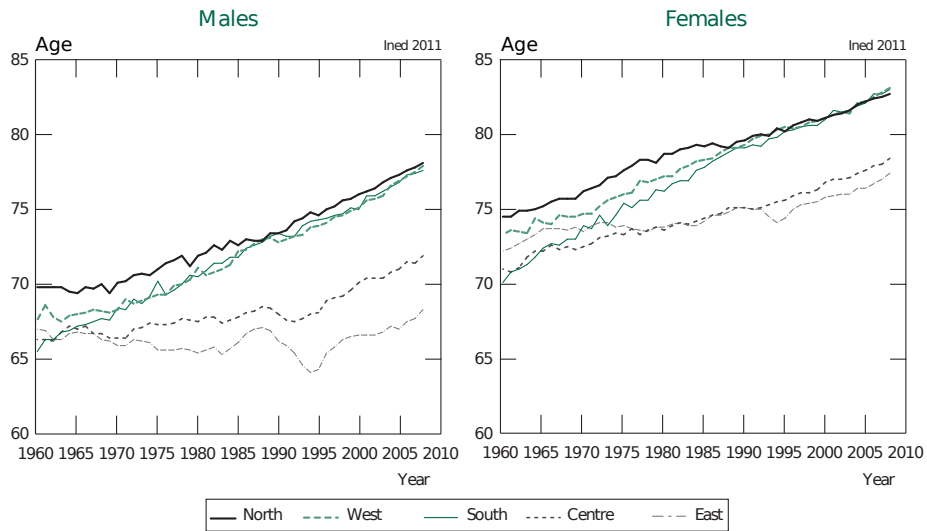
In this chapter, the aims and the novel contributions to the field of interest of this thesis are described together with the methodologies utilised during the development of this thesis' work. First of all, the research field is introduced in order to place this work in the more general context of robotics research and, more specifically, of the European Commission funded project associated with the thesis. Secondly, the aims and objectives are explained in detail, leading to a description of the methodologies and principles utilised to achieve the set goals. Thirdly, the publication record, which is a measure of the relevance and originality of the obtained results, is presented. Finally, an outline of this manuscript is given in order to clarify the structure of this work.

1.1 Assistive Robotics

The focus of this thesis' work is on designing and building structural features of a robotic arm which ensure a safe and effective interaction with a human user. The context of this effort is clearly defined: the interaction between the human and the robot in a domestic environment. For this reason, the wider field of application of this thesis' work is assistive robotics; in this field, robots assist humans in performing activities in everyday environments. Home-assistive robots for the elderly are quickly becoming a field of increasing importance due to the 'greying' of the population. This development is already increasingly apparent in several European Union member states, as shown in Figure 1.1 and Figure 1.2.

People prefer to live in their own homes as long as possible [Broekens et al., 2009], instead of being institutionalised in nursery homes once the problems related to ageing appear [Broekens et al., 2009]. Domestic assistance robots could support the elderly in daily living in their own homes.

In order to better explain and narrow the focus of the work, it is necessary to introduce the project in which it is involved.



Sources: Database of developed countries (INED);
 Division database of the Centre for Population Studies (Moscow).

Figure 1.1: Life expectancy at birth in Europe since 1960, from the figure ‘Male and female life expectancy at birth in the sub-regions of Europe since 1960’ in [Avdeev et al., 2011], used with permission of the journal Population, Ined and the authors. For clarification on the composition of the five European regions see Figure 1.2

1.2 The FP7 INTRO project

This thesis’ work was funded and developed in the context of the FP7 ¹ INTRO project. INTRO’s (www.introbotics.eu) aim was to improve the understanding of issues in human robot interaction and, ultimately, endow robots with cognitive and physical intelligence sufficient to deal with complex situations and safety of typical interactions. The 4 year long, Initial Training Network project, sponsored by the European Commission, has trained 8 young researchers to prepare them for careers in the fast developing area of service robotics. The individual students’ topics have been integrated into two different scenarios developed in cooperation with two European robotic companies - Space Applications (Belgium) and Robosoft (France). The latter developed a Robot-waiter scenario, which is the context of this work. Hence the robot arm built during this thesis’ work needs to be integrated in the robot waiter scenario, which involves grasping a cup of the human customer’s desired drink, bringing it to the customer and releasing it. The robot arm was the contribution of one of the researchers involved in the INTRO project, whose work is described in this thesis. Other researchers, undergraduate and master students contributed to the designing and building of the robot arm and these contributions will be notified where applicable throughout the thesis.

Due to INTRO project integration requirements, specifications for the robot

¹the seventh Framework Programme for Research and Technological Development. It is the European funding program for research. Its money is spent on grants to research actors all over Europe and beyond, in order to co-finance research, technological development and demonstration projects.

North		South		Centre	
Denmark	DK	Albania	AL	Bulgaria	BG
Finland	FI	Bosnia-Herzegovina	BA	Czech Republic	CZ
Iceland	IS	Croatia	HR	Hungary	HU
Norway	NO	Cyprus	CY	Poland	PL
Sweden	SE	Greece	GR	Romania	RO
		Italy	IT	Slovakia	SK
		Macedonia	MK		
		Malta	MT		
		Montenegro	ME		
		Portugal	PT		
		Serbia	RS		
		Slovenia	SI		
		Spain	ES		
West				East	
Austria	AT			Belarus	BY
Belgium	BE			Estonia	EE
France	FR			Latvia	LV
Germany	DE			Lithuania	LT
Ireland	IE			Moldova	MD
Luxembourg	LU			Russia	RU
Netherlands	NL			Ukraine	UA
Switzerland	CH				
United Kingdom	GB				

Source: International Organization for Standardization, www.iso.org/iso/country_codes/iso_3166_code_lists/english_country_names_and_code_elements.htm

Figure 1.2: The five European regions. From the figure ‘Box: List of countries of Europe by region and their ISO codes’ in [Avdeev et al., 2011], used with permission of the journal Population, Ined and the authors.

arm are drawn, especially for the structural interface between the arm and the RobuLAB10 mobile platform, provided by Robosoft, on which the robot arm was to be mounted on. This list of design restrictions includes:

- A maximum arm weight of 15kg
- No bulky compressor could be fitted in the mobile platform, thus excluding a pneumatic system
- The majority of the arm weight needed to be concentrated in its base to help reduce the risk of tipping over of the mobile platform-arm system
- A maximum arm protrusion out of the mobile platform envelope of 1.5m to increase structural stability in dynamical situations
- An arm base of maximum 200mm x 200mm due to space limitations on the mobile platform top
- A maximum power wattage of 12V at 3.3A and 24V at 5A.

The scenario and integration requirements played a big part in the development of the design and characteristic features of the robot arm, together with the aforementioned interest areas of safety in physical human robot Interaction (pHRI) and reliably grasping objects of unknown shape.

1.3 Aims, objectives and methodology

The aim of this research is to exploit the concept of variable compliance in order to design and produce a robot arm with inherently safe features and a gripper which can adaptively mould its shape to objects. As a source of inspiration the principles of embodied intelligence and bioinspiration are considered.

The design methodology utilised for the novel devices started with the definition of the problem, went on to complete the aforementioned literature research, then an initial design solution was proposed, it was tested, the experiment results were analysed and in case they were not satisfactory then a new solution was devised, following an iterative process until a satisfactory solution to the initial problem was found. A graphical representation of the methodology is illustrated in Figure 1.3. The literature review methodology intended to seek both published and unpublished studies identified through electronic database searches. All studies were considered for inclusion that assessed safety in robot arm design, soft robotics and grasping devices.

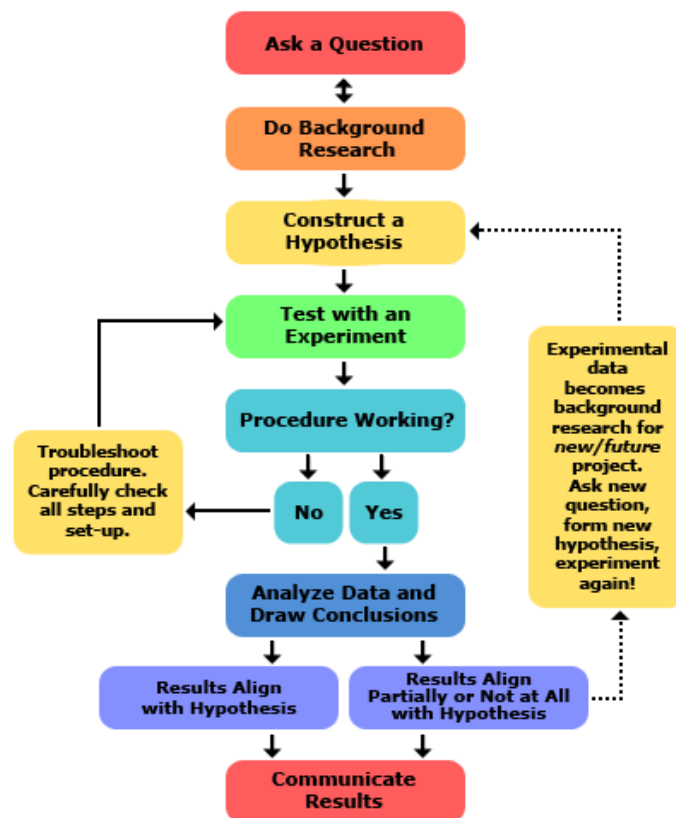


Figure 1.3: Methodology of scientific enquiry. The hypothesis process in this flow chart has been substituted in this thesis by a device design solution

In this thesis, the problem was to integrate a safety device and a soft grasping device into a robot arm that could be mounted on the RobuLAB10 platform. The literature search outlined previous solutions to the two issues but it also pointed out that no integrated solution of the two had been designed, built and tested. The aim was to design novel prototypes that advanced research in both areas. In the case of the safety device, background research suggested that a passive variable compliance solution would be able to react faster to possibly harmful collisions than active variable compliance systems. However, relying only on a passive device would compromise the flexibility of use of the device. Hence a hybrid decoupling device, that reacts passively to collisions but that can be adjusted actively was

devised. A mathematical model of the physical structure of the device was developed to test whether the device had the ability to both increase the arm's compliance in case of collision and to adjust the threshold torque at which the device was triggered. Since the model showed that the device was able to accomplish both tasks, then a first device made of acrylic, shown on the left in Figure 4.4, was built following the new design. The device was tested and it showed both the ability to vary its compliance due to collisions and to change its threshold torque. For this reason it was decided to keep the new design structure. However, acrylic was not suitable for the final device since it does not possess sufficient tensile strength to sustain the weight of the arm links further along the arm, the end effector weight and the payload. For this reason, the final version was made of steel and was increased in size compared to the first one. The final device is illustrated on the right hand side of Figure 4.4. The experiments conducted on the final version of the device, described in Chapter 4, confirmed the device's performance was satisfactory and no more design iterations were needed. The second device built in this thesis' work also underwent an iterative process to reach its final design. The literature review showed that exploiting variable compliance could be useful to achieve an adaptable grasp. Only one of the existing devices was fully exploiting the capabilities given by variable compliance in grasping. The device was able to assume a stiff final configuration to hold objects in a stable manner but only relying on visual feedback. In addition, it could grasp objects only by compressing them against a rigid surface. Hence, new grasping device designs exploiting the same working mechanism of the device in literature but that could grasp objects from their side were designed, built and tested. The devices are illustrated in Figure 5.4 and Figure 5.5. The experiments showed that the working mechanism used was not suited for a side grasp. Hence, a new working mechanism was formulated exploiting bioinspiration. It was hypothesised that the mechanism underlying the stiffening and bending actions of hydrostatic skeletons could be exploited for the novel device. Comparative experiments were conducted to finalise the design; an example is the cable system. In Section 5.5.2 is explained that two variants were built and the experimental results directed the final design choice. This process was also applied to choose the filling quantities and the materials utilised in the grasping device. The final design was tested to measure its effectiveness. The experiments revealed that the working mechanism inspired by hydrostatic skeletons was indeed effective in bending and varying the stiffness of the grasping device. Also, the device showed good grasping abilities, adaptability to unknown shapes and ease of control. For these reasons it was kept as final design. The final manufacturing procedure is explained in Section 5.5.1. A measure of the novelty of the work herein conducted is given by the publications listed in the next paragraph.

1.4 Publications

The work described in this thesis has been presented in workshops and conferences and has been accepted for publication in international journals.

Journal Papers: The work on the gripper is detailed in the paper:

- Giannaccini, M. E., Georgilas, I., Horsfield, I., Peiris, B. H. P. M., Lenz, A., Pipe, A. G., and Dogramadzi, S. (2014). A variable compliance, soft gripper. *Autonomous Robots*, 36(1-2), 93-107.

The study conducted in order to identify the safety requirements is described in the paper:

- Dogramadzi, S., Giannaccini, M. E., Harper, C., Sobhani, M., Woodman, R. and Choung, J. (2014). Environmental Hazard Analysis-a Variant of Preliminary Hazard Analysis for Autonomous Mobile Robots. *Journal of Intelligent and Robotic Systems*, 1-45.

Conferences and Workshops: Different aspects of the study conducted to identify the safety requirements for an autonomous arm in a robot waiter scenario were presented in the 2011 Workshop on Human-Friendly Robotics following and ICRA 2013 in the following papers:

- Harper C., Giannaccini M. E., Woodman R., Dogramadzi S, Pipe T, Winfield A., Challenges for the hazard identification process of autonomous mobile robots, 4th Workshop on Human-Friendly Robotics Enschede, Netherlands, 2011.
- Giannaccini M.E.², Sobhani M., Dogramadzi S., Harper C., Investigating real world issues in Human Robot Interaction: Physical and Cognitive solutions for a safe robotic system, Robotics and Automation (ICRA), 2013 IEEE International Conference on. IEEE, 2013.

The work on early prototypes of the gripper was presented at the 2011 Taros conference and the initial experiments on the current version of the gripper was presented at the 2012 BioRob conference:

- Giannaccini, M.E., Dogramadzi, S., Pipe, T. Solutions for a variable compliance Gripper design, in Proceedings of the 12th Towards Autonomous Robotic Systems (TAROS'2011) Conference, Sheffield, UK, 2011.
- Giannaccini, M.E., Zheng, Y., Dogramadzi, S. and Pipe, T., Towards a variable compliance hydrostatic skeleton inspired gripper, in Proceedings of Biomedical Robotics and Biomechatronics (BioRob) Conference, pp.246 - 251, 2012..

²the first two authors contributed equally and so are considered joint first authors

The initial work on the safety feature and the whole robot arm system were presented at the 2013 Human Friendly Robotics Workshop and the 2013 International Workshop on Soft Robotics and Morphological Computation, respectively:

- Giannaccini, M.E., Meunier, A., Bonard, B., Horsfield I., Coupland S., Lenz A., Pipe A.G. and Dogramadzi S. (2013) Adjustable Torque Limit Variable Compliance Decoupling Joint, Human Friendly Robotics Workshop, Rome, Italy 2013.
- Giannaccini, M.E., Meunier, A., Bonard, B., Lenz, A., Dogramadzi, S. and Pipe, T., Soft Joints and Soft Grippers for Safe and Effective HRI, in 2013 International Workshop on Soft Robotics and Morphological Computation, Monte Verit, Ascona, Switzerland, 2013.

A journal paper describing the whole robotic arm system is currently under development.

1.5 Structure of the thesis

Chapter 2 gives a definition of variable compliance and it outlines its use in the fields of safety in robotics and grasping. The inspiration for a solution to both the safety and grasping issues is searched in the fields of embodied intelligence and bioinspiration, which are described in the same chapter. The literature review shows that variable compliance is a pivotal element to both fields and it can be exploited to obtain mechanical, integrated solutions for both safety and grasping. The robot arm's design is presented in Chapter 3. The novel device aimed at increasing safety in pHRI is described in Chapter 4 and the device developed to obtain both an adaptive and stable grasp of unknown objects is detailed in Chapter 5. The discussion of the thesis' results and future work is presented in Chapter 6.

Chapter 2

Variable Compliance and its application in Safety and Grasping

This chapter introduces the concept of variable compliance, the cornerstone of the whole thesis, given that both novel devices presented in this thesis' work base their working mechanism on variable compliance. The review of the state of the art of the two main research fields involved in this thesis: safety in physical human-robot interaction (pHRI) and grasping, shows that variable compliance is central to both of them. This justifies the choice of variable compliance as main focus and inspiration for the robot arm design. As mentioned in the introduction, the principles of embodied intelligence and bioinspiration are considered as additional sources of inspiration and hence added to the literature review.

2.1 Compliance and Variable Compliance: definitions

Compliance is defined as "the property of a material of undergoing elastic deformation when subjected to an applied force. Compliance is equal to the reciprocal of stiffness" [OxfordDictionary, 2014]. In turn, stiffness is defined as the extent to which an object resists deformation in response to an applied force \vec{F} , [Marghitu, 2001]:

$$k = \frac{\vec{F}}{\delta} \tag{2.1}$$

In this study, variable compliance is defined as a physical structure's change from a compliant to a rigid behaviour and vice versa. Structures built with both rigid or soft materials are considered in this study. That is because rigid structures can behave compliantly, like a panel fixed to a hinge. Both the panel and the hinge are rigid but the panel will give way and rotate around the hinge if impacted by

an external force, thus complying to the environment. Vice versa, a soft structure can be made structurally rigid and act as a rigid agent. For example, an airtight bag partially filled with coffee is a compliant structure but once air is vacuumed out of the bag, the whole structure becomes stiff and behaves rigidly, resisting external forces.

As will be shown by the following literature review, variable compliance is utilised to help achieve both robot safety and object grasping. In the following sections, a review of the most relevant work done in the field of robot arm safety is given, followed by a review of the relevant literature in the field of grasping devices in Section 2.4.

2.2 Robot Safety

Ensuring that domestic robot assistants are safe for pHRI is of primary importance for them to be used outside laboratories and to become a commercial reality.

First of all, in order to facilitate safety in the system, a specification of safety requirements must be drafted; a good starting point is to use the techniques applied in industry. The focus of these techniques is not only to determine the hazards associated with the system, but also to specify and implement features of the design that act to reduce the probability of an accident. Further details of this approach can be found in the paper by Dogramadzi, Giannaccini et al. [Dogramadzi et al., 2014] that describes the assessment of the safety design requirements of a domestic robot assistant in the INTRO robot waiter scenario. The Hazard Analysis methodology has been utilised to this end in order to lay the foundations for the work described in this thesis.

Secondly, the design of the robotic system itself must be tailored to achieve safe interaction with humans and objects. This research area, in this thesis referred to as safety-driven design, forms a vast part of the pHRI efforts and is described in detail in the next section.

2.2.1 Inherent safety

The provision of inherently safe design measures is an important step in the risk reduction process of human robot interaction. In fact, inherent characteristics, by definition, are likely to remain effective throughout the robot operational activity. An inherently safe design system has a low level of danger even if control fails. Conversely, even well designed safety by control and safeguarding can fail. Inherently safe design characteristics reduce dangerous consequences resulting from hazards by providing design features that endeavour to make the exposure of humans to risks unlikely. As suggested by Ikuta et al. [Ikuta et al., 2003], the main mechanical design features which lessen the potential harm in pHRI are: light weight, soft link

covering, joint compliance, rounded shapes and low friction surfaces. The first design specification in this list (weight reduction of the robot's moving parts) is directly derived by the consideration of the force of impact resulting from a collision with a robot. In order to establish the force of impact between the moving robot to the human, two quantities are taken into consideration. The energy of a moving body (for example a robot), or kinetic energy is:

$$\overrightarrow{E}_{kin} = \frac{1}{2}m \cdot \overrightarrow{v}^2 \quad (2.2)$$

where m is the mass of the body and \overrightarrow{v} the velocity of the body relative to the body it is impacting. The work performed by the impact force slowing down the moving body is:

$$\overrightarrow{W} = \int \overrightarrow{F} \cdot d\overrightarrow{s} \quad (2.3)$$

where \overrightarrow{F} is the deceleration force and \overrightarrow{s} the deceleration distance. Considering the case in which \overrightarrow{F} is constant over the integration interval, \overrightarrow{W} can be written as $\overrightarrow{F} \cdot \overrightarrow{s}$. In an impact, the kinetic energy from the moving body is converted into work. The equations can be combined as

$$\overrightarrow{F} \cdot \overrightarrow{s} = \frac{1}{2}m \cdot \overrightarrow{v}^2 \quad (2.4)$$

that gives a deceleration force, which also expresses the force of impact between the two bodies:

$$\overrightarrow{F}_{imp} = \frac{\frac{1}{2}m \cdot \overrightarrow{v}^2}{\overrightarrow{s}} \quad (2.5)$$

The reduction of the kinetic energy in order to reduce the impact force, in Eqn. 2.5, has to be considered to improve the overall safety of robotic systems and thus is one of the main aims of safety-driven design. In order to achieve this, the most efficient method would be to reduce the squared term in Eqn. 2.5, velocity. This can be achieved by setting software limits to velocity or by choosing high gearbox ratios. However, since fast robots are desirable, in many cases the attention is transferred to other variables of Eqn. 2.5, instead. Another way to decrease \overrightarrow{F}_{imp} is to increase \overrightarrow{s} , this can be done by adding padding material on the outside of the robot structure. A further way to reduce \overrightarrow{F}_{imp} is to decrease m , the mass of the robot. This is one of the main requirements of inherent safety: lightweight design. Additionally, the

effective mass can be reduced, by decoupling the part of the robot which is involved in the collision from most of the robot mass.

A successful example of lightweight design is provided by the Deutsches Zentrum für Luft - und Raumfahrt (DLR) III Lightweight Robot [Hirzinger et al., 2001], further described in Section 2.2.2. Light but stiff materials have been used for the links, while harmonic drives supply motor transmission and reduction. Harmonic drives endow the structure with a small degree of compliance, which DLR researchers point out as enough to provide an additional safety feature [Haddadin et al., 2009].

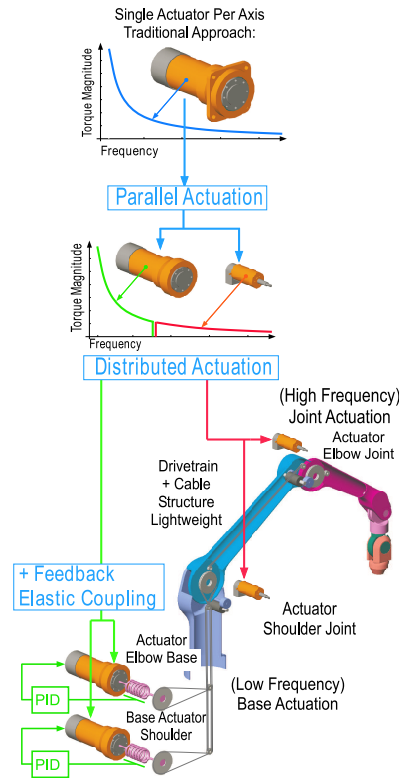


Figure 2.1: Diagram of the distributed actuation system, from [Zinn et al., 2002], used with permission of Dr Zinn.

Utilising compliance as a safety feature is also suggested in Ikuta et al. [Ikuta et al., 2003], where it is proposed that compliance should be largely exploited in the inherent safety design but that it can also be achieved via control techniques. The trade-off between compliance and rigidity is one of the focal points of this thesis' work and in order to better explain the issue, a definition of compliance has been given in the beginning of the chapter. Another structural characteristic that is mentioned quite often in the following sections due to its prominence in safety features for robot manipulators is impedance.

In general, impedance is defined as the ratio between potential and flow. In the case of mechanical impedance (\vec{Z}) the potential is the force vector (\vec{F}) and the flow is the velocity vector (\vec{v}). It is a measure of how much a structure resists motion

if subjected to a given force.

$$\vec{Z} = \frac{\vec{F}(\omega)}{\vec{v}(\omega)} \quad (2.6)$$

Interestingly, the mechanical impedance matrix (\vec{Z} in Eqn. 2.6) is a function of the frequency (ω) of the applied force and thus can vary greatly over frequency [Standford, 2014], [Gatti, 2014].

As suggested in the previous section, inherent safety is facilitated by favouring a mechanical design aimed at reducing manipulator link inertia and weight, complemented by the presence of compliant components in the structure. The provision of compliant elements in the actuation or transmission arrangements allows the actuator's rotor inertia to be dynamically decoupled from the links, in the event of an impact. If the robot link involved in the collision decouples from the motor, it no longer pushes on the colliding object/person, possibly reducing the impact harm. Therefore, the increased robot's compliance is useful as a protection during unexpected collisions in pHRI. Furthermore, collisions often involve the most distal link of the robot arm, so decoupling of this link from the rest of the arm would reduce the inertia involved in the impact, providing smaller potential damage. However, drawbacks of compliant elements in robotics systems must also be considered. Systems with compliant elements present lower accuracy and attenuation/suppression of vibrations excited by disturbances can be difficult to achieve. In addition, torque inputs in an arm with compliant elements are executed more slowly; also, these configurations tend to oscillate around the desired position. Therefore, it may be that the speed of response of an arm with highly compliant elements is reduced.

This analysis shows that compliance is indeed desirable but *not continuously*: during normal operations, the robot compliance should be kept to the minimum, in order to maintain position accuracy, however in case of collision, high compliance can reduce the harm potential [Park et al., 2007]. Hence, what is needed for robot safety is variable compliance and in the literature three main ways to obtain a variably compliant behaviour in a manipulator are reported: active, using variable compliance actuators and passive. These approaches are described in the next three sections.

2.2.2 Active Variable Compliance

Industrial robots are often position controlled, which means that a desired position and orientation of the end-effector in space is achieved via closed loop control. While impacts could be prevented using exteroceptive sensors, interaction forces are not directly controlled, hence the force impacting the object or the human during direct physical contact is usually not measured. This is especially important to recognise,

since the impact force is one of the key factors in potential harm to the human. Hence, force/torque control of manipulators is used in pHRI to reduce the contact forces in case of a collision between human and robot. The next paragraph gives an overview of interaction control strategies.

There are two categories of interaction control strategies: indirect force control and direct force control. The former achieves force control indirectly via a position control loop, without closure of a force feedback loop, while the latter controls the contact force to a desired value, due to the closure of a force feedback loop. Compliance control and mechanical impedance control (usually referred to as impedance control) belong to this first category. Force/torque control belong to the second category [Sciavicco and Siciliano, 2000].

In compliance control [Hogan, 1984] only the static relationship between the end-effector position and orientation deviation from the desired motion and the contact force and moment is considered. This control strategy is designed to achieve a desired static behaviour of the interaction [Villani and De Schutter, 2008]. This is achieved by varying the manipulator stiffness (K_p) so that the manipulator acts either in a stiff or compliant way on the environment. The manipulator stiffness can vary in different directions [Sciavicco and Siciliano, 2000].

A more demanding objective is achieving a desired dynamic behaviour for the end-effector. Specifically, a second-order mechanical system with six degrees of freedom, characterised by a given mass, damping, and stiffness, known as mechanical impedance [Villani and De Schutter, 2008]. This impedance is thus attributed to a mechanical system characterised by a mass matrix M_d , a damping matrix K_d , and a stiffness matrix K_p , which can be used to specify the dynamic behaviour along the operational space directions. The position error is related to the contact force through the mechanical impedance. A mass-spring-damper model is used to describe the robot manipulator [Siciliano and Khatib, 2008].

However, impedance and compliance control systems are not designed to *reactively* control or limit robot impact forces, which are one of the main sources of harm in pHRI. For this reason, force/torque control strategies that can sense external forces/torques and react on them are usually preferred for safety critical systems [Haddadin et al., 2009].

Often a hybrid between position and force control is utilised, as in [Raibert and Craig, 1981], where the position control is used for precise positioning of the end-effector in case there is no physical contact with the environment and the force control is utilised in the opposite case. In general, systems with multiple control strategies proved their efficiency and are often utilised. Another example is the DLR III lightweight robot (LWRIII), which can be controlled in position, impedance and torque [Haddadin et al., 2008].

The torque control strategy in LWRIII is specifically aimed at controlling or

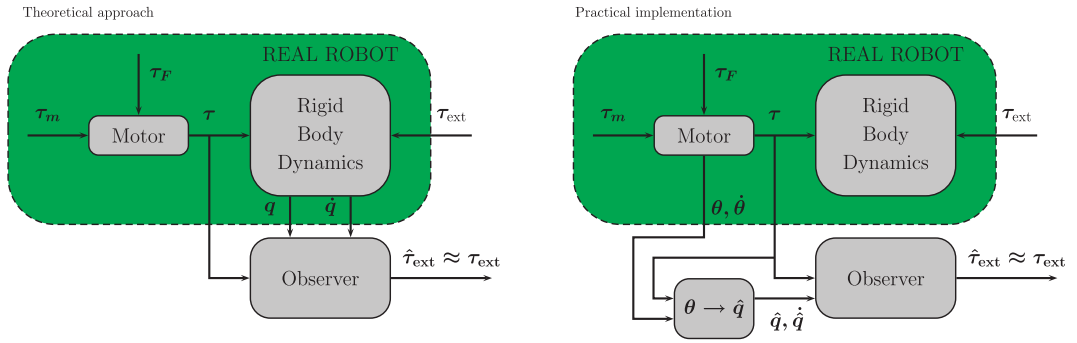


Figure 2.2: τ_m , τ_F , τ and τ_{ext} are the motor torque, the friction torque, the joint torque and the external torque. The inputs to the disturbance observer are the joint torque, the link position and the link velocity. It can be shown that the estimated external torque ($\tau_{ext}^{\hat{}}$), which is the output of the disturbance observer, is a filtered version of the real external torque (τ_{ext}). The motor positioning sensor is more accurate than the link side position sensor and, due to the good flexible-joint model of the robot, this is used together with the motor position and velocity (θ , $\dot{\theta}$) to estimate the link side position and velocity (\hat{q} , $\dot{\hat{q}}$). Figure used with permission of SAGE Publications, Inc. Taken from [Haddadin et al., 2009]

limiting robot collision torques. This control strategy is dependent on the torque created by forces caused by external collisions. A possible way to measure collision forces occurring in any part of a serial robot manipulator is to provide the robot with joint torque sensors. The collision detection used in the LWRIII robot is briefly illustrated in Figure 2.2. The detection is achieved by the disturbance observer, which has an estimated robot arm momentum as an internal state. It takes the joint torque, link position and link velocity as inputs and observes the robot arm momentum $p = M(q)\dot{q}$ of the robot, where $M(q)$ is the inertia matrix of the robot. The momentum, p , of a body is the product of its mass and velocity. $M(q)$ is the inertia matrix and \dot{q} the joint velocity of the robot arm. The signal for collision detection is the estimated first-order filtered version ($\tau_{ext}^{\hat{}}$) of the real external torques (τ_{ext}) [Haddadin et al., 2009].

Using this detection and reaction scheme, multiple experiments of human-dummy collision have been performed by DLR and three main conclusions are drawn by Haddadin et al. Firstly, it is ascertained that there is no physical collision detection and reaction mechanism which is fast enough to usefully reduce the dynamics of fast and rigid impacts for the robot considered in the DLR study. Secondly, for these impacts, a further increase in compliance does not lower impact forces or severity indices because motor and link inertia are already decoupled. Thirdly, padding of the robot arm is an adequate countermeasure to reduce the impact effectively [Haddadin et al., 2009].

The first conclusion is indeed valuable and applicable to all robots, unlike the second conclusion, which is only applicable to the DLR system and similar systems. This is due to the relatively low bandwidth of active collision detection systems like

the DLR one, which does not allow sufficiently fast detection and reaction in response to impacts [Park et al., 2007]. The main impact phase ends before active compliance control can react. This is because the response time of active compliance control is limited by the computational time necessary to process the sensor and actuator signals [Lens et al., 2010]. On the contrary, the performance of passive compliance systems could present less delay issues since it is based on a mechanical decoupling action between motor and link. Following this idea, variable stiffness actuators have been designed. This approach combines the idea that the physical structure of the robot should be directly tailored to provide safety with the principle of active control of compliance. Variable stiffness actuators (also referred to as variable compliance actuators) are described in detail in the next section.

2.2.3 Variable Stiffness/Impedance Actuators

In contrast to active variable compliance, discussed above, in variable stiffness actuators and variable impedance actuators, it is the control of mechanical reconfiguration that is used to vary stiffness and impedance. In variable impedance actuation (VIA), a mechanical/control co-design allows for rapid and continuous change of the parameters of mechanical components (stiffness, damping, and gear-ratio) during task execution. Variable impedance actuation has been applied as a distributed parallel actuation [Zinn et al., 2004], antagonistic actuation [Ham et al., 2009] and other [Bicchi et al., 2008]. The main drawback of such devices is their usually quite complex and heavy structure [Lens et al., 2010], a trait they share with variable compliance actuators. Variable compliance actuators as in [Sardellitti et al., 2012] and [Eiberger et al., 2010] are usually built in order to provide a safety feature for the robotic system. In general, these structures comprise a motor to adjust the link position, one motor for compliance adjustment, springs to ensure variable compliance. The variable stiffness actuator in the DLR Hand Arm System, successor of the aforementioned LWRIII arm, is an example of such structures and presents the aforementioned elements, as shown in Figure 2.3. Sometimes these structures feature also a damper structure. The damping of undesirable vibrations caused by the flexible transmission can be addressed through control techniques [Sardellitti et al., 2012], which have similar drawbacks as active compliance control.

These systems are indeed able to vary their compliance but their claim to safety is uncertain. As stated in [Haddadin et al., 2010], a considerable amount of elastic energy can be stored in the mechanism of a VIA joint once the elastic components in the structure compress due to the impact force. Much of impact energy is stored in the elastic components and released as mechanical movement rather than dissipated at the time via other transduction processes. Thus, once the impacting external object is removed, the energy stored can considerably contribute to increasing the velocity of the link. Since high velocities are one of the main causes of potential

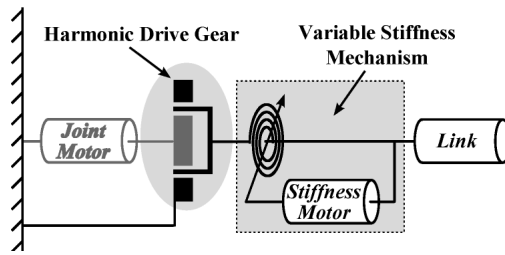


Figure 2.3: The variable stiffness mechanism is located between the harmonic drive gear box of the main actuator and the link. A stiffer configuration is obtained by preloading the springs via the motion of the stiffness adjusting motor. Figure from [Greibenstein et al., 2011] ©2011 IEEE

harm in pHRI, as clear from the force of impact equation, Eqn. 2.5, safety-sensitive applications might not be the most suitable in this case. However, this is highly controversial and many researchers in the field think that VIA are an asset for safety [Vanderborght et al., 2013]. Nevertheless, VIA’s contribution to the robotic structure’s high energy efficiency, fast movements and collision resistance is not disputed.

2.2.4 Passive Variable Compliance

Let us first consider passive compliance systems in general. An alternative to the approaches mentioned so far is to build compliance into the mechanical structure of the joints or links, to provide a more delay-free and compliant behaviour in case of collision, compared to active variable compliance systems [Park et al., 2007]. In addition, passive compliance is lighter to design than variable stiffness/impedance actuators. Most passive compliance-based devices utilise linear springs to obtain compliance. The drawback of using a linear spring is positioning inaccuracy due to the continual operation of the spring, even for small external forces that do not require a switch to a compliant behaviour, and to undesirable oscillations caused by the elastic behaviour of the spring. Another drawback of such systems resides in loss of behaviour flexibility (it is not possible to vary from a compliant to a rigid configuration or vice versa). This is the case for the original Series Elastic Actuator (SEA) [Pratt and Williamson, 1995], which comprises a spring in series with a stiff actuator. In this mechanism, the compliant element cannot change its stiffness and the variable impedance is created by software control.

This loss of accuracy and behaviour flexibility is addressed in the structure described in the work of Park et al. [Park et al., 2007]. In their structure, the Safe Joint Mechanism (SJM), stiffness is assured in normal behaviour but it is possible to switch to low stiffness when a collision force greater than a fixed threshold impacts the arm. The SJM working mechanism exploits a linear spring and a modified four bar mechanism, shown in Figure 2.4. The spring is used to absorb collision

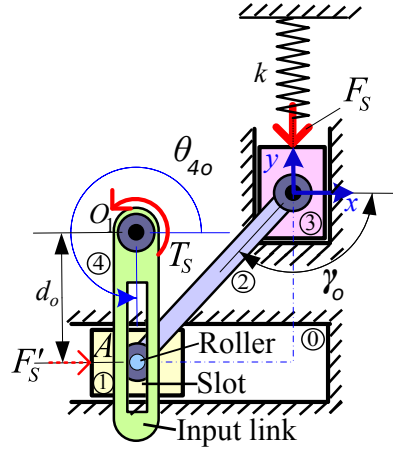


Figure 2.4: The non linear spring system, composed by a double-slider mechanism with a spring, in its initial configuration. \vec{F}_s is the force of the spring, \vec{T}_s is the spring torque that induces the force \vec{F}'_s , d_o is the distance between the pivot point and the point of application of \vec{F}'_s , figure from [Park et al., 2009] ©2009 IEEE

forces for safety, while the modified four bar mechanism permits the SJM to switch between the compliant and rigid state in response to an external force. The switch is obtained due to the mechanical structure and its reaction to the external force, the mechanism is completely passive. The whole mechanism makes up a non linear spring with high stiffness in normal operational times and low stiffness in case of collision.

SJM is activated only when an external torque \vec{T}_{ext} exceeds the threshold torque, \vec{T}_{th} , shown in Eqn. B.11. Once \vec{T}_{th} is exceeded the spring is rapidly compressed causing the mechanism to move until when the spring is completely compressed. Hence the equivalent stiffness of the mechanism quickly decreases, providing the desired compliant behaviour. In general, the arm the feature is mounted on provides a rigid behaviour when the external impact forces are low and a compliant one if \vec{T}_{th} is exceeded. The equation which describes the threshold torque is:

$$\vec{T}_{th} = \frac{d_o k * s_o}{\tan \gamma_o \sin \theta_{4o}} \quad (2.7)$$

where γ_o is the transmission angle and θ_{4o} the angle around point B in Figure 2.4. The subscript 'o' indicates the mathematical expression describes the zero configuration. The spring force \vec{F}_s , shown in the figure, is substituted with the product of s_o , the spring compression, and k , the spring constant. For a full analysis of the forces and moments acting on the SJM mechanism, see Appendix B.

The robot arm with the SJM is clearly aimed for use in the field of pHRI. In robotic systems, there is a trade-off between position accuracy and structural compliance. High position accuracy is required of industrial manipulators. On the contrary, in robot arms designed for pHRI high position accuracy above a certain ap-

plied torque can be sacrificed in order to obtain a safe passive compliance approach, more important in pHRI. The reason for this is that for a robot domestic assistant contact with the human is always possible. Furthermore, the human-robot interaction is unpredictable and it cannot be controlled or pre-planned as is in industrial settings.

A system like this one allows to pre-determine the range of threshold torques at which the arm can maintain its rigid behaviour and the ones for which it will behave compliantly. The selection of the latter depends on the value of impact forces that are categorised as safe. In the research detailed above, especially in the research detailed in [Haddadin et al., 2009], which utilises safety indexes of the automotive industry, an interaction is deemed safe in case the consequence of a collision does not require hospitalisation for the robot user. In this research effort, this concept of safety has been extended to take into account also those physical interactions that can cause pain in the human user. For this reason, the value of an external collision force that is considered unsafe is chosen considering the data of recent pain threshold studies [Melia et al., 2014] detailed in the next section.

2.2.5 Pain Thresholds

This study identifies force values up of 10N as responsible for pain onset only in the chewing muscle, as shown in Figure 2.5. For this reason, this has been chosen as an acceptable value of impact force for human comfort in scenarios which imply close interaction with humans. For example in case the robot arm is operating in close proximity to a disabled person or a child. Thus a force of 10N or below is considered the threshold at which the HDF should be triggered.

It is clear from this review of safety-driven designs that variable compliance, whether active or passive, is instrumental in reducing possible harm. Since the common recommendation from the DLR risk assessment and INTRO hazard analysis is the importance of inherent safety, the overall result of this literature review is that a variable compliance feature inherent to the physical system would be the best way to promote a safe robot behaviour. Hence, a purely active variable compliance approach is rejected, since it would not ensure any inherent safety. A variable stiffness/impedance actuator is also excluded from the possible solutions given the considerable amount of elastic energy can be stored in the mechanism of a VIA joint. The passive variable compliance device seems to be the solution most likely to help ensure inherent safety. However, this solution is not optimal since it is excessively specific for the behaviour being targeted. In other words, if the morphology of the structure is built to tackle a specific scenario this bring about a loss of flexibility. If the targeted behaviour changes, then also the physical structure needs to be altered. This is not practical. For these reasons, a hybrid solution that targets inherent safety but that also allows flexibility of operation in multiple scenarios is targeted for the

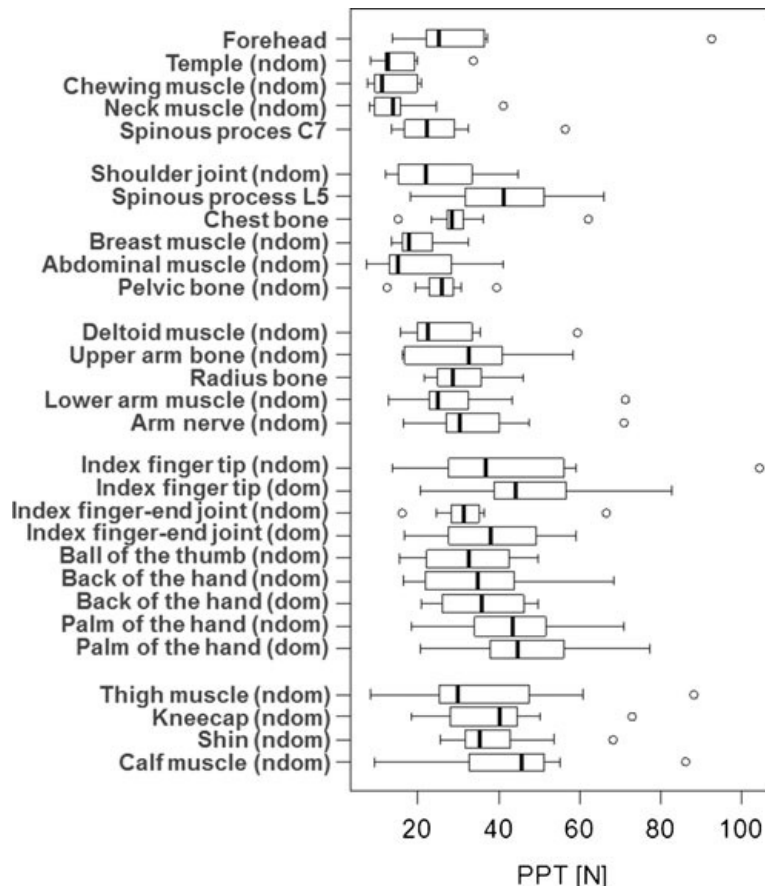


Figure 2.5: Pressure pain thresholds (PPT) of 10 test subjects; they were averaged over three repeated measurements. The complete surface of the plunger used in this pilot study was 1414 mm. The thick line in the box represents the median of the value. The acronym ‘ndom’ stands for non-dominant side. Most measurements in the study were conducted on the non-dominant (ndom) side, since some research suggests that lower pain thresholds might be attributed to the non-dominant side of the body [Özcan et al., 2004]. Figure from [Melia et al., 2014], used with permission of Springer and Dr Melia

novel safety feature described in this thesis’ work. In addition, the insight into pain thresholds provided a numerical figure for the maximum external force that does not cause the onset of pain, setting one more specification for the safety device to be designed. The specifications in terms of maximum velocity of the arm and maximum stored energy in the safety device will be described in Chapters 3 and 4, which describe the novel structures in detail.

the principle of embodied intelligence marks the importance of a smart use of the mechanical structure and materials, which can reduce the amount of active control and necessary sensory information. Thus, the robot safety can partly be transferred from control algorithms to the physical structure: control and processing would be distributed to robot parts. Both these facts are perfectly in line with the importance of inherent safety approach resulting from an exploration of the areas of risk assessment and hazard analysis. These three facts amount to one conclusion:

the safety should be built into the system and should comprise variable compliance features.

The aforementioned relevance of the mechanical structure in influencing the behaviour of a robotic system is also central to a well-known principle in robotics: embodied intelligence, which is described in the next section.

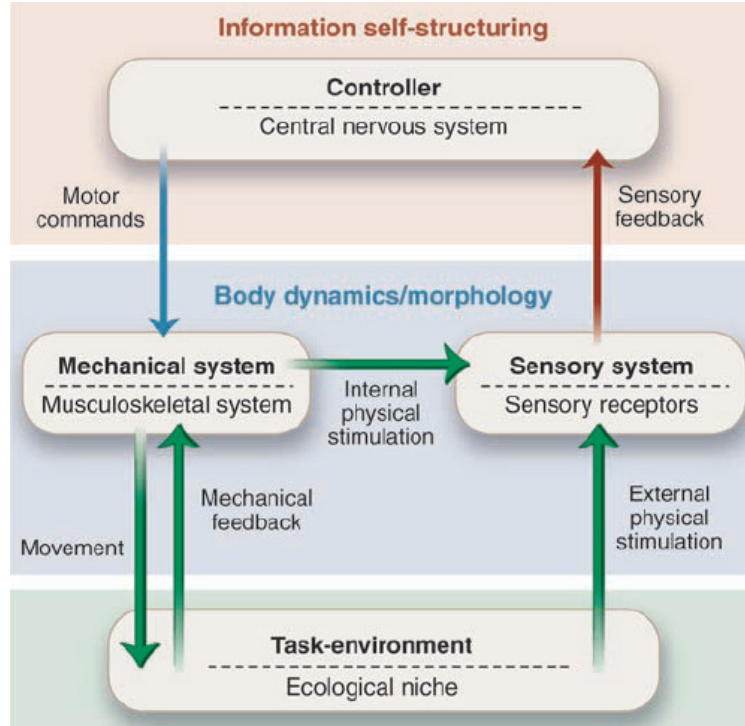


Figure 2.6: Embodiment interplay: the physical system (e.g. musculoskeletal) is driven by motor commands and acts on the environment. Such action causes sensory feedback, which depends on the physical characteristics and morphology of the sensory system and on the motor commands. From Pfeifer, R., Lungarella, M. and Iida, F. (2007). Self-organization, embodiment, and biologically inspired robotics. *science*, 318(5853), 1088-1093. Reprinted with permission from AAAS.

2.3 Embodied Intelligence

It is a tenet of embodied intelligence, namely the reciprocal and dynamical coupling among brain, body and environment, that the shape and materials of the device play a very important role in the ability to control the device itself. In other words, materials and morphology are crucial in order to smartly interact with the environment, and this stresses the importance of the relationship between shape and function of a structure [Pfeifer et al., 2007].

Hence, the design of the controller is inseparable from the design of the morphology, since both affect information processing. However, the problematic aspect of this principle is that robot morphology still largely remains a matter of heuristics. In nature, brain and body co-evolve. It would be desirable to do the same and subject

the robot morphology and control to iterative optimisation. This is much simpler for software but mechanical structures cannot be so easily varied. Tailoring shape and materials for specific interactions with the environment tends to diminish the flexibility of the system. Thus, it would be desirable for a robot to alter its shape depending on the present task. Alternatively, the material properties could vary depending on the circumstances and that would bring about a different interaction with the environment, increasing the system's flexibility and adaptability. Figure 2.6 further explains the embodied intelligence paradigm.

Let us consider just one example to illustrate the points above: grasping a cup with fingers that possess a compliant contact surface, as humans do, is an advantage when compared to metal clamps. This is due to the passive shape adaptation that soft materials provide once pressed against a surface, which ensures a greater contact area between the finger and the object surface. The grasp is effortlessly more stable, due to this shape match. Hence, part of the stability control of the grasping action is achieved exploiting finger compliance. This simple example shows the importance of passive compliance in achieving an adaptable and successful grasp. This has inspired the design of many grasping devices described in the following literature review.

2.4 Grasping in Human Environments

One of the important issues is the ability of the grasping device to accommodate varying object shapes in order to form a stable, multi-point grasp. Particularly in the human environment, where robots are faced with a vast set of objects varying in shape and size, a versatile grasping device is highly desirable. In this environment, it is not always the case that the shape, size, position and orientation of the objects to be grasped are known. For this reason, it is vital to tailor the physical design of the system to respond appropriately to a dynamic environment, in that the position and orientation of objects to be grasped can change at any time. This approach is very relevant to this thesis' work since it deals with the design of the grasping device itself and its literature review is detailed in the next section.

2.4.1 Physical Structure Based Approach

In order to introduce the state of the art of this field, the multiple approaches used to design an effective grasping device are now described and compared.

One approach to achieve effective grasping is to utilise an anthropomorphic end-effector composed of two or more digits with as many as 20 degrees of freedom (DOF) [ShadowRobotCompany, 2013] in total. A good example of this type of end-effector is the highly anthropomorphic DLR hand arm system [Greibenstein et al., 2011] with 19 DOF in the hand and kinematics similar to the human on a functional

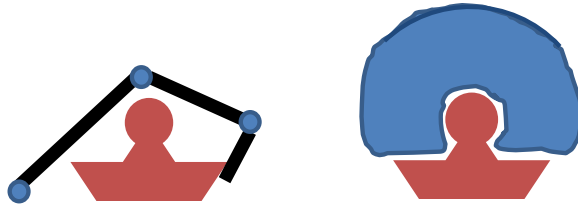


Figure 2.7: The unidirectional compliance gripper (left) is able to adapt to the object shape but lacks the shape-matching provided by the multidirectional type gripper (right) which is able to effectively interlock the object in its own structure

basis. Another example of a state-of-the-art anthropomorphic robot hand is the Shadow Dexterous Hand[®]. This 24-joint-hand is actuated by pneumatic muscles which provide 20 DOF [ShadowRobotCompany, 2013]. Anthropomorphic robotic hands aim to replicate human hands, which is considered beneficial for applications like tele-operation and accurate reproduction of human-like object manipulation. However, the physical structure and control of anthropomorphic robot hands are remarkably complex and demanding. Anthropomorphic end-effectors might need multi-degrees of freedom control and are typically costly to produce. In addition, anthropomorphic hands sometimes feature completely rigid digits, which can be negative for compliance to the object shape. In order to achieve a better grasping autonomy in robotic grippers, some of the control complexity can be substituted with the adaptability provided by structural passive compliance, as suggested by the embodied intelligence paradigm. This is because, in general, a continuum, compliant structure is able to encircle objects more compliantly than any rigid one. A continuum structure has a great number of points of curvature while most anthropomorphic hands can only bend at the joints between rigid parts.

Hence, an alternative to the anthropomorphic approach could be simple, non-anthropomorphic gripper designs based on the principle of intelligence embodied in materials and shape [Pfeifer et al., 2007]. These non-humanoid end-effector designs rely more on material properties and less on control and sensors. Good examples of these devices are the University of Chicago universal gripper and the Festo fin ray effect gripper, which are described in the next paragraphs.

Before starting an overview of non-anthropomorphic gripper designs available in the literature, it is important to select a primary aspect on which to base comparisons between different designs. Since compliance is recognised as a very important component in adapting to the environment, as mentioned in the embodied intelligence section, it has been chosen as the base for comparison. Grasping devices can be divided into structures with either unidirectional or multidirectional compliance. Such distinction characterises a purely physical and morphological issue. The unidi-



Figure 2.8: SDM hand. The hand is compliant in the workspace of the three link fingers. However, due to the inherent rigidity of the links and to their mechanical coupling between the finger links, the workspace of the SDM hand is inherently limited. Hence, the hand can adapt to external objects but retains movement constraints due to its mechanical structure. Figure from [Ma et al., 2013] ©2013 IEEE

rectional compliance is descriptive of a physical structure that will passively comply to an object shape only along a single direction axis. On the contrary, an multidirectional compliant object will passively and compliantly modify its shape when impacted from any direction. This characteristic would ensure that every direction of the passive compliance is exploited to aid the grasping action. Thanks to this, the object would in fact be interlocked with the gripper's structure, facilitating a stable grasp. Further clarification of the concept of unidirectional and multidirectional compliance is provided by Figure 2.7. An example of the first device category is the SDM hand in Figure 2.8 and an example of the second category is the Universal gripper in Figure 2.9. The first device is called 'SDM hand' due to its building technique: shape deposition manufacturing (SDM), a rapid prototyping technology in which mechanisms are simultaneously fabricated and assembled.

Unidirectional compliance can be found, for example, in these three devices: 1) the adaptive gripper implemented by Festo and the Fraunhofer Institute, 2) the SDM hand and 3) Hirose's soft manipulator. The Festo adaptive gripper, shown in Figure 2.10 exploits a parallel linkage to passively obtain a lifting motion of the object while it is being grasped [Festo, 2013b]. Its linkage prevents a compliant behaviour in all directions other than the one intended for grasping. However, its compliance along this direction endows the gripper with the ability to passively adapt to object shapes. As previously argued, compliance and passive adaptability are desirable when dealing with the uncertainty of the human environment. These characteristics are also at the core of the design of 2), the adaptive hand by Dollar et al. [Dollar

and Howe, 2010]. This under-actuated cable driven device, shown in Figure 2.8 is able to successfully grasp objects of various shapes, sizes and masses in multiple orientations. The third unidirectional compliance device, 3) has historically been one of the first adaptive manipulators. This device, called Hirose’s soft manipulator, was the first gripper to adapt itself passively to the grasped object shape [Hirose and Umetani, 1978].

The drawback of these three devices is that their digit structures feature compliance only in one direction, hindering the passive shape-adaptation in non-compliant directions. However, the definition of unidirectionally compliant grippers comprises also the aforementioned anthropomorphic hands, since they can only feature passive compliance in the directions of movements allowed by their degrees of freedom.

Among the grasping devices with multidirectional compliance, the RBO hand [Deimel and Brock, 2013] is vaguely anthropomorphic, while the Whiteside group’s starfish-like gripper, shown in Figure 2.11 is non-anthropomorphic. The latter features fingers that are soft actuators made of elastomer composites with internal air channels. Their lack of rigid structures and the intrinsic flexibility of the elastomer material makes them pliable structures, thus they feature multidirectional compliance [Ilievski et al., 2011]. The same working principle is used in the RBO hand, created in the Robotics and Biology Laboratory, Berlin [Deimel and Brock, 2013]. The compliant nature of these grippers ensures a good shape match with the object

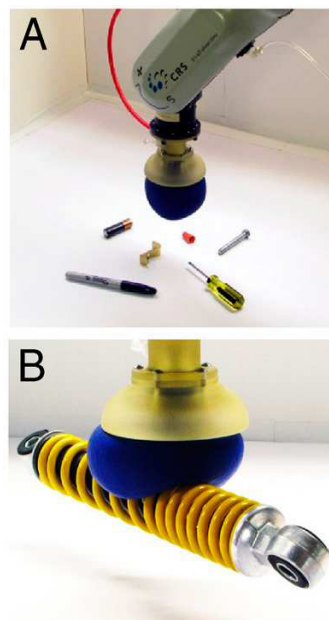


Figure 2.9: A: the non-anthropomorphic universal gripper mounted on a rigid robotic arm, in its soft state B: the gripper as it lifts an object, in its rigid state. The universal jamming gripper is able to grasp a wide variety of objects without grasp planning or sensory feedback [Amend et al., 2012]. This device is a perfect example of multidirectional compliance. Due to the lack of fixed shape in its flaccid state, there are no mechanical constraints which hinder its adaptation to an external object. Figure from [Brown et al., 2010], used with permission of PNAS

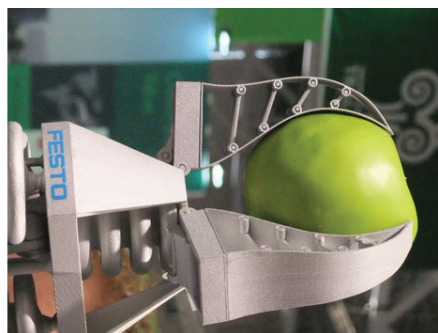


Figure 2.10: Festo’s fin effect gripper. Sources: Food Engineering Magazine, June 2012, www.foodengineeringmag.com; www.festo.com

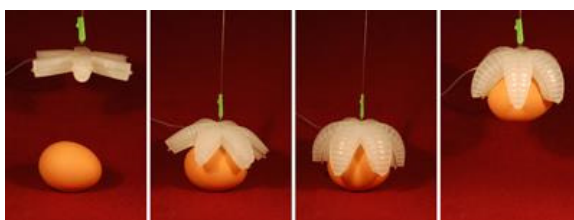


Figure 2.11: The Whiteside group starfish-like gripper. Figure used with permission. The version being referenced is the Author’s Accepted Manuscript, available via Harvard University’s DASH repository <http://nrs.harvard.edu/urn-3:HUL.InstRepos:12967812>.

but makes the fitting of sensors on their surfaces challenging. This is due to the fact that they are made is silicone, a material which stretches, thus possibly deforming the sensor. Furthermore, the physical structure of these designs remains compliant all though the grasping action, which could compromise the stability of the grasp in the final stage of the grasping action. The structural rigidity necessary for a stable grasp is never achieved. In addition, it is not possible to lift heavy objects when operating with this kind of grasping devices since their inherent compliance reduces the amount of force they are able to apply to external objects.

This issue is solved by the University of Chicago universal gripper [Brown et al., 2010], shown in Figure 2.9, by employing the variable compliance principle, the change of the system’s compliance during operation. Such process allows the gripper to initially passively conform to the object shape and then stiffen using material jamming. The same working mechanism has been exploited for a serial manipulator [Cheng et al., 2012] and for a surgical manipulator [Stilli et al., 2014]. Furthermore, the University of Chicago universal gripper is one of the grippers which most successfully utilises multidirectional compliance by interlocking part of the object in the gripper itself, as shown in Figure 2.7. A minor drawback of these and other multidirectional grasping devices is their inability to exert forces on other objects when in their most compliant configuration. For example, in the compliant phase they are not able to push external objects, like a button or switch.

Furthermore, while these devices combines simplicity and low cost, they require

compressors, which are quite bulky, to vary their compliance. In addition, the change from a compliant to a stiff structure needs to be initiated by the high level control and is not passively achieved. In order to grasp an object, an external sensory system needs to detect that the contact between the object and the gripper has taken place (the universal gripper, for example, has no contact sensors). Only at that point the stiffening and thus grasping can happen. The detection of contact by this external vision system could be complex. A system which changes its compliance as it is grasping, without requiring external information could be an improvement. However, it is important to notice how the study of the intrinsic material characteristics of the structure become the focal point of its working mechanism.

Devices like the University of Chicago universal gripper and the Whiteside group's starfish-like gripper both foster the idea that graspers incorporating passive compliance and adaptability in their mechanical structure might be a viable solution to grasping in an environment where object shapes are not defined, as it happens in homes. Due to the complete lack of rigid components, these devices rightly belong to the field of soft robotics.

In general, soft robotics is a fairly new field, the remit of which has just begun to be explored. One of the claims made by researchers involved in this field is that soft and deformable structures are vital in systems that deal with uncertain and dynamic task-environments, e.g. grasping and manipulation of unknown objects [Nurzaman et al., 2013]. Despite the progress already made in the area, soft robotics faces a number of fundamental scientific challenges: sensing, actuation and control in soft bodied robots have not been fully explored. However, successful examples of soft robotic devices have been accomplished: the grippers from the Whiteside group, the caterpillar robots from TUFTS university [Trimmer et al., 2006] and the prototypes from the OCTOPUS project (shown in Figure 2.13) are only a few examples of the results achieved in this discipline.

The field of soft robotics is often tightly associated with bioinspired or biomimetic techniques. In bioinspiration biological studies translate into a physical model which is translated into a physical implementation. In biomimicry the same physical model leads to a robotic platform to be used to either validate or disprove the initial biological study, see the schematics in Figure 2.12.

An example of the latter is the robot octopus arm of the Scuola Superiore Sant'Anna (SSSA) [Calisti et al., 2010], shown in Figure 2.13, which aims at reproducing the structure and behaviour of *Octopus vulgaris* as closely as possible. In this thesis, bioinspiration is applied, not biomimicry. For this reason, bioinspiration is explained in detail in Section 2.4.2.

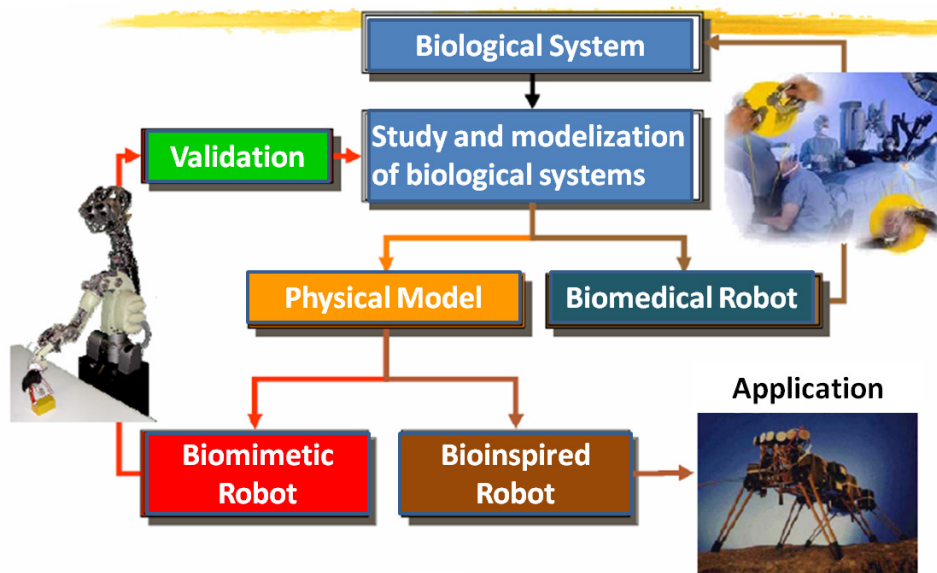


Figure 2.12: Connections between disciplines

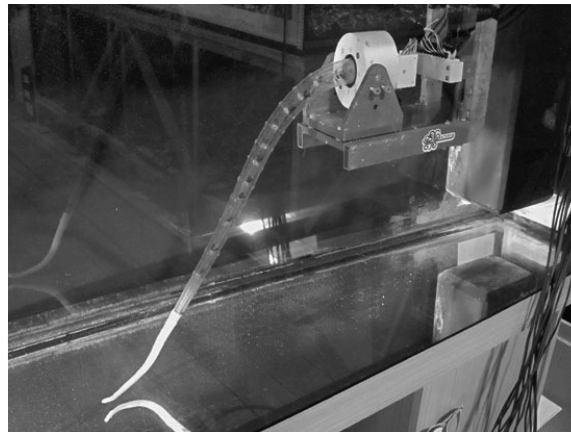


Figure 2.13: Octopus-like robot arm prototype in water. Figure from [Laschi et al., 2012], used with permission of Taylor & Francis.

2.4.2 Bioinspiration

Generally, the principle of bioinspiration, taking inspiration from nature, aims to enable the robotic artefact to deal with the complexities of the real world. In fact, scientists and engineers draw inspiration from biological systems that had to adapt to solve the problems posed by dynamic real world environments. Such solutions are analysed and used as a design reference so that also robots can cope with uncertain situations and react quickly to environmental changes. Because of their diversity, biological systems provide an exceptional source of inspiration. Bioinspired robots include devices inspired by: fish [Hirata et al., 2000], plants [Tonazzini et al., 2012], snakes [Hirose and Umetani, 1978], caterpillars [Trimmer et al., 2006] and many others. In bioinspiration, the scientist needs to identify the system responsible for producing the desired characteristics, extract the key principles underlying their biological function and, finally, translate them to a technological solution.

It is clear from the state of the art review in Section 2.4.1 that variable compliance and a soft structure are both promising characteristics to aid grasping of objects in human environments. In order to find the right physical structure for the grasping device, effort which is at core of this thesis' work, a look into the biological world is utilised to reveal a biological specimen which owns both characteristics and whose physical structure could be a viable inspiration. A number of biological entities have been considered, looking for structures that are soft and can achieve variable compliance. In the end, it has been chosen to focus the attention on hydrostatic skeletons, invertebrates that possess no rigid structures in their body and which can change their compliance with muscle activation. In addition to possessing both characteristics that make a good adaptable gripper, the main working system of hydrostatic skeletons is reproducible in a simple prototype. These are the reasons that caused hydrostatic skeletons to be chosen as the biological specimen for inspiration. A detailed description of these animals is presented in Section 2.4.3.

2.4.3 Hydrostatic Skeletons

Numerous invertebrates possess a hydrostatic skeleton, e.g. snails, caterpillars, earthworms and starfish. Invertebrates have inspired robotics research in the past; walking on land [Trimmer et al., 2006] or in water [Vaidyanathan et al., 2000] and crawling [Menciassi et al., 2006] are among the tasks addressed by devices inspired by hydrostatic skeletons. Animals featuring hydrostatic skeletons have a flexible body with few constraints on their degrees of freedom. Such characteristics are granted by their structure, an incompressible fluid filling an internal cavity surrounded by a flexible container, typically the body wall, comprising passive tissue and muscles [Kier, 2012].

The fluid is usually water, which has a high bulk modulus (very low compressibility) and thus resists significant volume change [Kier, 2012]. In vertebrates, the bones transmit the forces generated by muscle contraction, while in hydrostatic skeletons this is accomplished by the internal pressure. Both the diameter and the length of the hydrostatic skeleton can be actively controlled due to the particular arrangement of the musculature.

There are three different muscle arrangements: (1) longitudinal muscles, which are parallel to the long axis of the structure and can be seen in Figure 2.14, (2) helical muscle fibres, which are wound up around the longitudinal axis like a helix, and (3) the third muscle arrangement is always perpendicular to the longitudinal axis but in different animals it can take three different arrangements: (a) circular musculature, with a layer of fibres wrapping the cylinder circumferentially; (b) radial musculature, with fibres or fibre bundles originating near the central axis of the cylinder and extending towards the surface; and (c) transverse musculature, shown in Figure 2.14. The longitudinal and circular (or radial or transverse) are typically

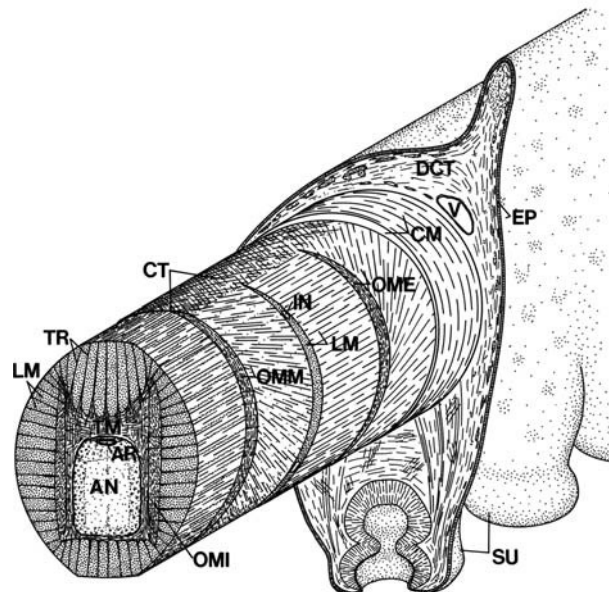


Figure 2.14: Diagram illustrating the structure of the octopus arm: From the top: DCT: dermal connective tissue, V: vein, EP: epidermis, CM: circumferential muscle layer, CT: connective tissue, OME: external oblique muscle layer, IN: intramuscular nerve, LM: longitudinal muscle fibres, TR: trabeculae, OMM: median oblique muscle layer, TM: transverse muscle fibres, AR: artery, AN: axial nerve cord, OMI: internal oblique muscle layer and SU: sucker. The figure is from [Trivedi et al., 2008], accessed at <http://www.hindawi.com/journals/abb/2008/520417/cta/>. Copyright ©2008 Hindawi Publishing Corporation. This is an open access article distributed under the Creative Commons Attribution License.

in two orientations that are perpendicular to each other [Kier, 2012]. Due to the contraction of circular (or radial or transverse) muscle, the diameter of the structure will decrease, thus increasing the internal pressure. Since the volume of the internal water cannot change, due to its effective incompressibility, the decrease in diameter causes an elongation. If at this point the longitudinal muscle fibres are shortened, counteracting the elongation, the diameter of the structure is expanded back to its initial length. The structure dimensions can be controlled actively, with muscles, or passively, with connective tissue, and this results in deformations, movements and changes in stiffness. In order to understand how this is achieved by these invertebrates, it is important to keep in mind that in hydrostatic skeletons the forces of muscle contraction are transmitted through the essentially incompressible fluid, and this results in an increase in the internal hydrostatic pressure and tension in the body wall [Taylor et al., 2007]. This behaviour is also confirmed by Kelly et al. who state that, when the fluid in a hydrostatic skeleton is placed in compression by either the addition of fluid or deformations of the entire structure, its membrane resists fluid movement and is placed in tension [Kelly, 2007]. The described muscle system allows these structures specific behaviours: elongation, shortening, bending, stiffening and torsion.

Elongation is achieved by contracting only the circular, radial or transverse muscle fibres, shortening is obtained by contracting only the longitudinal muscles. The bending behaviour is the result of the contraction of the longitudinal muscle on one side of the body.

Torsion is caused by the shortening of the helically arranged muscle fibres. A further behaviour in the list is stiffening. In a structure of constant volume stiffening occurs when dimensional changes are resisted either by muscles or connective tissue. A structure wrapped with connective tissue that thwarts dimensional change will stiffen in case of muscle contraction [Kier and Smith, 1985]. The stiffening function allows hydrostatic skeletons to change their compliant structure for a more rigid one, hence their bodies can achieve variable compliance. Since hydrostatic skeletons do not possess rigid structures, they possess both the characteristics required by an adaptive grasping device.

Turning Hydrostatic Skeletons into Robots

Muscular hydrostats have loosely inspired quite a number of robotic systems. Despite the great potential of these structures due to their completely soft composition their reproduction presents a great technological challenge. Indeed, muscular hydrostats are very difficult to accurately reproduce since only soft actuators would properly imitate them.

A popular choice for such application are Electro-Active Polymers (or EAPs). Polymers, in fact, are lightweight, pliable, they can be configured in many shapes and their properties can be tailored. Some polymers respond to electrical stimulation with a change in shape and size. EAPs can be divided in two main categories, based on their activation mechanism: electronic and ionic. EAPs can be driven by Coulomb forces and under a DC voltage they hold the induced displacement. These materials can be operated in air but require high activation fields ($>100 V/\mu m$). On the contrary, ionic EAPs involve diffusion or mobility of ions and consist of two electrodes and an electrolyte. The actuation voltage can be as low as 1-2 V but they need to be maintained wet and the induced forces or torques are low [Meijer et al., 2003]. Thus, electronic EAPs are the only ones which can produce the necessary force to be considered. However, the high voltages at which they operate make them potentially hazardous.

The solution used by Scuola Superiore Sant'Anna (SSSA) for their biomimetic robot inspired by the octopus arm has been to exploit shape memory alloys (SMA) in order to reproduce the transverse muscles and to use cables driven by external rigid motors to imitate longitudinal muscles. The SMAs wires are coiled in a spring configuration, shown in Figure 2.15 in order to increase their deformation [Laschi et al., 2012].

It is important to keep in mind, though, that this actuator arrangement is able



Figure 2.15: Cross-section view of the arrangement of transverse actuators in the SSSA artificial muscular hydrostat, the white arrows point towards the direction of movement of the SMAs: once they are given current, the SMAs coils contract and reduce the diameter of the cross-section. Figure from [Laschi et al., 2012], used with permission of Taylor & Francis.

to create enough forces to decrease the robot arm diameter but not enough to move the whole octopus arm structure, even if it is immersed in the aqueous environment, where it does not need to fight the gravitational forces. However, since the aim of the octopus arm robot is to imitate as closely as possible the *Octopus vulgaris* arm, this actuator is appropriate.

Neither EAPs nor SMAs produce high enough forces to be considered for the grasping device describe in this thesis' work. An alternative solution is the use of pneumatic actuators (PAMs), which have a high power to weight ratio and an inherent compliant behaviour. PAMs, shown in Figure 2.16 are frequently used as artificial muscles.

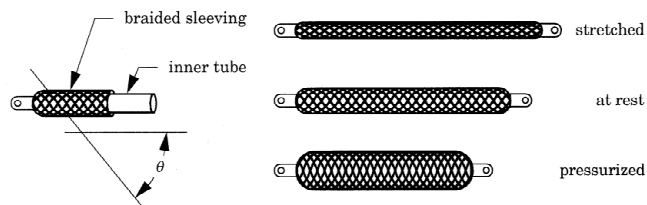


Figure 2.16: PAM actuators. Figure from [Daerden and Lefeber, 2002], courtesy of Dr Daerden.

PAMs are contractile or extensional actuators activated by pressurised air which fills a bladder covered by a woven sleeve. They are one of the most used types because they are easy to assemble, low cost, safe to operate. However, they have some

drawbacks. Firstly, such actuators require the presence of an air compressor which normally has a prohibiting size and weight for mobile applications. Secondly, the control accuracy of PAMs actuators is diminished by long tube connections which can produce unwanted pressure oscillations [Jien et al., 2009]. In the case of the STIFF-FLOP manipulator [Maghooa et al., 2015] pneumatic and cable actuation were used together for a soft, inflatable manipulator inspired by the *Octopus vulgaris*. This approach suggests that a combination of actuation principles can be a way to exploit the advantages of different principles. In summary, hydrostatic skeletons inspired devices show many interesting characteristics but they also provide many technical challenges in their physical implementation, especially when choosing actuators.

2.5 Summary

In the first part of this chapter, it has been explained that the issue of safe human-robot interaction is one of the biggest challenges in modern robotics. In response, much attention has been given to ways to ensure robot safety, as can be gathered from the material proposed above. The importance of building the safety directly into the mechanical structure is one of the main directives of novel safety approaches. It is evident from this chapter’s literature review of safety-driven systems that variable compliance is very relevant in the field. If these two considerations are united, it follows that building the variable compliance directly into the system would bring together both positive aspects. The second part of this chapter and this thesis’ work address another topic of primary importance in manipulators: their ability to grasp objects. Even though it is a different topic to safety, it has been shown that both fields exploit variable compliance or are starting to do so. The grasping devices review starts with a wide review of robotic systems employed in grasping objects of unknown shape, as would be expected in a human environment. A very relevant part of this research field involves designing the grasping device so that the very mechanical structure endows the grasper with the desirable qualities of adaptability and shape-matching. This review is instrumental in finding the areas which need improvement in this field, thus leading to the requirements for the novel grasping device described in this thesis’ work. The outcome of the safety and grasping devices literature review, is the acknowledgement that mechanical compliance is perhaps the simplest method to achieve adaptability in human environments, where physical robot-human interactions and object properties are not known a priori and sensing is prone to error.

2.6 List of Requirements for this Thesis' Work

Given the findings of the literature review it was decided to achieve the design and building of a lightweight arm with two variable compliance devices: one for grasping, placed at the end-effector and one for helping achieve safety, placed near the active joint.

Requirements for the safety device:

- passive variable compliance (for inherent safety)
- maximum acceptable external collision force: 10N (if the force is above this value the device should become compliant)
- maximum weight: 4kg
- maximum dimensions: 200x200x50mm envelope (widthxlengthxheight)
- rigid material (aluminum or steel)
- active along the horizontal plane
- active system to vary the threshold torque (to achieve higher flexibility than the device by Park et al.)

Requirements for the grasping device:

- omnidirectional compliance
- soft material (silicone, fluids, composite material)
- ability to grasp by closing the proximal part of the gripper first and the tip at a later stage
- payload of 0.5kg (so that it is comparable to the Fin Ray effect gripper)
- maximum weight: 0.5kg (to ensure a 1:1 ratio between weight and payload)
- maximum object size: 50mm (diameter of a cup for Robot Waiter scenario)
- variable compliance

The description of the safety device can be found in Chapter 4 and the grasping structure is detailed in Chapter 5.

2.7 Variable Compliance and Novel Contribution

As clearly demonstrated by the literature review detailed above, variable compliance is at the heart of current research efforts in both safe physical human-robot interaction and adaptive grasping. Notwithstanding this, in literature there is no mention of a robot arm structure which has been purposely designed to exploit variable compliance for both issues. In the work described in this thesis, variable compliance is no longer used as a tool to approach safety and grasping issues, as it is done in literature. In this thesis' work variable compliance is redefined as the main inspiration for the physical and control design of the robot arm, its role identified as the guiding inspiration of this research effort. The next chapter will describe the physical structure of the robot arm system, a concept design device, with variable compliance the main characteristic of both its intelligent features. This is where the value of this thesis' effort resides: it theorises and puts into practice the integration of the work on variable compliance both in the safety and grasping fields.

Chapter 3

Manipulators' State of the Art and INTRO-BRL Robotic Arm

In this chapter, a literature review of relevant robotic arm designs is given to provide the necessary background to present the design of the robotic arm described in this thesis' work: the INTRO-BRL robotic arm. First, more traditional rigid robotic arms are presented and examples of the most significant platforms in the area of safe robotic arms are given. Secondly, hyper-redundant and soft manipulators will be examined and compared to other manipulators in the literature. An account of the kinematic descriptions of these structures will also be discussed. The aim of this thesis' work is exploiting variable compliance to design and build a robot arm with structural characteristics that ensure a safe interaction with a human user and grasping of unknown shaped objects. As shown by the analysis in Chapter 2, the physical structure of the arm is very relevant for the safety aspect of the arm structure. This literature review investigates how the inherent safety characteristics drawn from the literature in Chapter 2 have been successfully employed in the literature in order to build robotic manipulators. The sum of the conclusions drawn in this review with the principles described in Chapter 2 drove the design choices established for the INTRO-BRL robotic arm, which is described in the second half of this chapter.

3.1 Background

Robotic arms in industrial and service applications differ greatly in terms of mechanical structure, actuation choices, control algorithms, software implementation and sensors. In this review, robotic arms will be classified based on their mechanical structure and they will be compared mainly on the safety aspect. The first great divide is between robotic arms with a limited number of degrees of freedom (DOF)

and those with a high number of DOFs or hyper-redundant arms ¹.

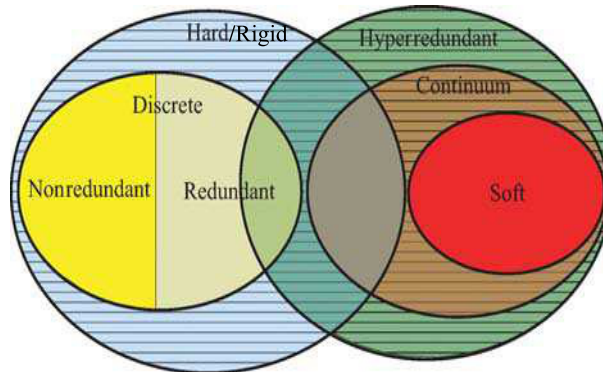


Figure 3.1: Robot classification based on materials and degrees of freedom. The figure is from [Trivedi et al., 2008], accessed at <http://www.hindawi.com/journals/abb/2008/520417/cta/>. Copyright ©2008 Hindawi Publishing Corporation. This is an open access article distributed under the Creative Commons Attribution License.

Figure 3.1 illustrates the different classes of robot arm structures available. Hyper-redundancy allows arms to use many configurations to reach the same end-effector position and orientation. It also endows arms with ability to reach into confined spaces and operate with high dexterity. Soft arms are a subset of hyper-redundant arms and it is claimed that their soft structure is inherently safe [Trivedi et al., 2008]. In this thesis, the definition of [Trivedi et al., 2008] is adopted and manipulator structures are defined as soft on the basis of the compliance of their materials. Hyper-redundant and soft arms will be discussed in detail in Section 3.3. A different arm category includes rigid robotic arms, which are usually kinematically non-hyper-redundant. They are able to perform a prescribed motion with great precision, due to their stiff structure, well defined kinematics and control. The focus of the next section is their state of the art.

3.2 Non-hyper-redundant Arms

Nowadays, a multitude of rigid robotic arms are developed, their shape and physical structure defined by the task they needed to perform. Among these are the manipulators purposely built to be used in the area of domestic assistance. This is a new and not established area of application for robotics. The robotic arms used in

¹A robotic arm with 7 or more DOFs is a redundant arm. If the robotic arm possesses a number of DOF much greater than 7, then it is called a hyper-redundant arm. In literature, there is no universally agreed DOF number which marks the threshold between redundant and hyper-redundant arms. In order to give an example of the number of DOF of a hyper-redundant arm, the Trunk Arm has 32 degrees of freedom. As shown in Figure 3.1, robot arms with an even higher number of DOF are called continuum robots. In this thesis' work no distinction is made between continuum and hyper-redundant robots and both categories are referred to as 'hyper-redundant'. Also in this thesis, arms are classified as 'non-hyper redundant' when they possess 7 or less DOF.

	Jaco Arm	BioRob Arm	LWRIII
Active DOFs	6	4	7
Mass [Kg]	5.7	3.75	14
Material	Carbon-fibre	Aluminium	Carbon Fibre
Max Velocity	0.2 m/s	> 0.25 m/s	2 m/s
Ease of Control	Easy	Medium	Medium
Kinematics	Easy	Easy	Easy
Safety	Inherent	Inherent	Control/Inherent
Autonomy	Tele-operated	Autonomous	Autonomous
Commercial	Yes	No	Yes
Compliant feature	No	Series Elastic Actuation	Harmonic Drive

Table 3.1: Comparison of Jaco arm [KinovaRobotics, 2013], the BioRob Arm [Lens et al., 2010] and the LWRIII arm [Bischoff et al., 2010]

this field are usually rigid, lightweight and not very powerful. Light weight is quite important to ensure inherent safety in the structure, as explained in Chapter 2.



Figure 3.2: The Jaco arm is commercially available and used by disabled and elderly persons. Figure from [Maheu et al., 2011] ©2011 IEEE.

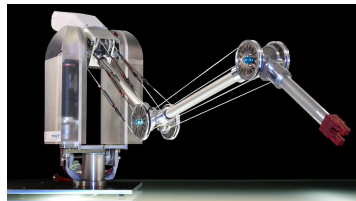


Figure 3.3: The BioRob Arm: most of the robot's mass to be located at the base of the robot arm. Figure from [Lens et al., 2011] ©2011 IEEE.



Figure 3.4: The LWRIII: its most salient features are the joint-integrated power and signal processing electronics including torque sensors mounted on the gear box output in all joints. Figure from [Bischoff et al., 2010], used with permission of Dr Bischoff.

It must be kept in mind, though, that these manipulators are normally tele-operated and not autonomous. With tele-operation the responsibility of any action performed by the robot is left to the human user. This allows the usage of robotic domestic devices. In case domestic robots were autonomous, they would not only need a safe physical structure but also a higher level control system with cognitive abilities advanced enough to judge which actions are safe in which context. A system with such functionality has not yet been achieved, hence, for now, tele-operated systems are used in domestic environments. Both tele-operated and autonomous

domestic device systems have in common the need for a physical structure which increases the safety of the system. This literature review takes a look at devices in the literature which have addressed the issue of a safe human-robot interaction. Three non-hyper-redundant arms that are used in domestic assistance tasks, or have particular claims to safety, stand out in the literature. These arms are the Jaco arm, the Bio-Rob Arm and the LWRIII. Their structure, claims to safety and possible uses in a household environment are reported in Table 3.1.

3.2.1 Safety Characteristics

In reference to the classification of safety methods described in Chapter 2, in the first two robot arms described, safety is sought via inherent characteristics, while the third employs active compliance control. In the first robot arm, the inertia is kept low to reduce its harm potential in case of collision with a human and its maximum velocity is as low as 0.2 m/s. In this arm the safety relies also on the fact that the system is not autonomous but operated by the human. This arm is listed as a medical device and as such it was approved by the United States' Food and Drug Administration (FDA) to be utilised around humans. In order to be used in Europe, it obtained 'Conformit Européenne' (CE) marking and it was certified through the Approval of Electrical Equipment Product Safety Certification Body Scheme (IEECE CB Scheme) for other non-European countries.

With respect to safety, the third robotic arm taken into consideration, the LWRIII, underwent risk assessment based on potential collision with the human [Haddadin et al., 2009]. DLR study outcomes show that the reactive sensory algorithms and compliance control in this arm are sufficient to ensure that the device will generally come to a stop before the collision can be life-threatening [Haddadin et al., 2009]. This arm does not comply with the ISO 10218 standard requirements, however, in view of their thorough risk assessment, DLR experts suggest that the standard limitations do not precisely correspond to the level and risk of human injury. Hence, in their opinion, standards are often too restrictive but sometimes not restrictive enough [Haddadin, 2014] and should be amended.

The case of the BioRob Arm is relatively different from the other two, since this arm is not a commercial product such as the Jaco arm or the KUKA-DLR lightweight robot. For this reason, the BioRob Arm did not strictly need to undergo a formal certification process or a thorough risk assessment. This arm is the prototype resulting from a research effort and not a final product ready for purchase. Its maximum speed is higher than the ISO 10218 recommended limit of 250mm/s but this is not problematic since standard conformity does not affect its research significance. The relevance of the BioRob Arm is in its low mass and inherently compliant structure which suggest the ability to be passively safe even when moving at high speeds, due to the resulting low kinetic energy. While the system mass is

indeed extremely low compared to traditional industrial manipulators, it is also true that kinetic energy is proportional to the mass but proportional to the square of the velocity. Hence, it would be interesting to see what kinetic energy values can be achieved with this arm during collisions. In general, the BioRob Arm seems to have many good claims to safety and it presents an interesting embodied approach to safety for physical human-robot interaction.

In summary, it is clear from the aforementioned examples that a reduced mass is pivotal in ensuring safety, since it is a dominant characteristic of all three arm designs. However, it is equally clear that this characteristic is not sufficient to ensure safety, since complementary measures were taken in all three arms.

So far, this survey has addressed standard rigid manipulators but in recent years research has also been looking at the development of soft arms. Due to their inherent high compliance, they seem quite apt to address the safety-critical issues involved in physical human-robot interaction for a domestic robotic assistant [Trivedi et al., 2008]. For this reason, a review of hyper-redundant and soft arms is given in the next section. Again, representatives of this class of robots are chosen as examples of the devices in the field.

3.3 Hyper-redundant and soft arms

The multiple degrees of freedom in many hyper-redundant and soft robotic arms are inspired by hydrostatic skeletons, described in Chapter 2. Hydrostatic skeletons display a theoretically infinite range of configurations because of their soft bodies. This characteristic endows hyper-redundant and soft robots inspired by them with incredible capabilities for locomotion, manipulation and moving in cluttered environments [Webster and Jones, 2010]. The drawback of hyper-redundant and soft robots is the difficulty in modelling their behaviour, which makes the development of control algorithms challenging. The modelling difficulties are due to the fact that their shape can change in so many ways that it is difficult to accurately determine their precise position and orientation in space. The available sensory information is insufficient to establish the angles of curvature of the structure and, due to its extreme compliance, the structure could bend at almost any point. Due to the aforementioned dexterity in cluttered environments, many practical applications for hyper-redundant and soft robots have been suggested and demonstrated, including undersea manipulation [Lane et al., 1999], nuclear reactor repair [Robotics, 2008], search and rescue [Aoki et al., 2002] and catheters or colonoscopes [Camarillo et al., 2008]. In addition, soft structures are taken into account in this survey due to their intrinsic safety [Trivedi et al., 2008]. The two devices described in the table below are successful examples of a hyper-redundant and a soft robot.

It is important to point out that the figures in the first column of Tables 3.1

	Bionic Handling Assistant	OctArm
Active DOFs	11	9
Mass [Kg]	1.8	6.9 (approx)
Material	Polyamide	pMAs and rigid disks
Max Velocity	0.05 m/s	n/a
Ease of Control	Complex	Very Complex
Kinematics	Complex	Very Complex
Safety	Inherent	Inherent
Autonomy	Tele-operated	Tele-operated
Commercial	Yes	No
Compliant feature	Its overall structure	Its whole structure

Table 3.2: Comparison of the Bionic Handling Assistant, [Festo, 2013a] and the OctArm [McMahan et al., 2006]



Figure 3.5: The BHA manipulator with an adaptive gripper based on the Fin Ray Effect, inspired by the movement of a fish tail fin. The figure was taken from [Festo, 2013a] with permission of ©Festo AG & Co. KG

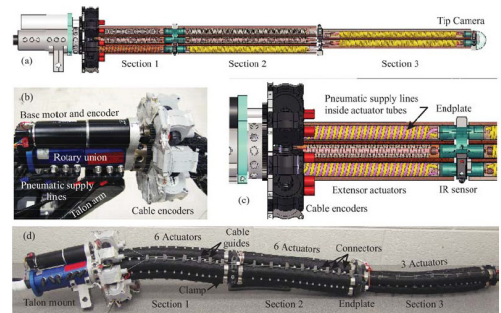


Figure 3.6: OctArm V: (a) view of the arm, (b) base (c) view of the first section (two actuators for each control channel), (d) photograph of the complete arm. The figure is from [Trivedi et al., 2008], accessed at <http://www.hindawi.com/journals/abb/2008/520417/cta/>. Copyright ©2008 Hindawi Publishing Corporation. This is an open access article distributed under the Creative Commons Attribution License.

and 3.2 refer to the number of active degrees of freedom. However, soft robots have, in addition to active degrees of freedom, a quite high number of passive degrees of freedom. Thus, if these structures are hit by an external force, they will be displaced in unpredictable ways and this is one of the reasons for the lack of controllability. The arm mass figures in the non-hyper-redundant and hyper-redundant arms vary considerably but it must be kept in mind that in the Jaco and LWR III motors are embedded in the structure, while in the BioRob Arm, BHA and OctArm motors are remotely located and thus not factored in the total weight. Hence, the lightest arm might need a quite heavy actuation cabinet as is the case for BHA, which requires

a bulky compressor to function. It is interesting to notice the link between safety and autonomy in the arms. For example, the Jaco arm is inherently safe due to its low mass but also due to the fact that the human is always in control of its motion. This arm's simple kinematics would allow it to be autonomous but tele-operation is chosen in order to decrease possibility of harm. It is also important to point out the link between the high complexity of the hyper-redundant and soft arms kinematics and the fact that they are tele-operated. It is their unpredictability of behaviour that makes this choice necessary.

3.3.1 Kinematics of Hyper-redundant and Soft Robots

In traditional rigid-link robots the kinematics and thus the position and orientation of any point on the robot can be fully defined (in closed form) by link lengths and joint angles. On the contrary, the kinematics of the inherently compliant hyper-redundant robots needs to take elasticity into consideration and hence are more complex. In the next subsections, multiple approaches to both direct and inverse kinematics of hyper-redundant and soft robots will be described.

Forward Kinematics

In order to tackle the complex description of soft structures, the work of Chirikjian and Burdick [Chirikjian and Burdick, 1995] uses the basic approach of fitting the physical robot arm to analytically desirable mathematical curves. Another simplifying approach that facilitates closed-form Jacobian formulation is to approximate the robot as a series of mutually tangent constant-curvature arcs. While most hyper-redundant robot arcs are not perfect circles, this is still a good approximation, thus it has been used in multiple research works: Xu and Simaan [Xu and Simaan, 2008], Neppalli and Jones [Neppalli and Jones, 2007], and Webster et al. [Webster et al., 2009]. The usefulness of the piecewise constant-curvature approximation for a wide variety of hyper-redundant robots together with its analytical attractiveness has caused broad application of this modelling approach. However, in case of external forces hitting the robot, its configuration will change, due to its structural compliance, and these models of the robot shape will no longer be valid.

Inverse Kinematics

Inverse kinematics, or finding the joint variables in terms of the end-effector position and orientation, for hyper-redundant and soft robots is quite challenging. In the case of constant-curvature hyper-redundant robots, the first step is computing the inverse mapping between task space and configuration space. This gives the arc parameters of the robot sections, which correspond to the desired tip pose. For a multiple-section hyper-redundant or soft robot, computing all possible solutions to

this problem is quite complex, nonetheless, several approaches for inverse kinematics do exist. In Neppalli et al. [Neppalli et al., 2009], each section is modelled using a spherical joint and a straight rigid link, then an analytical process is applied to solve the inverse kinematics for this model before converting back to arc parameters. This approach can be applied to an n-link robot but does not account for physical actuation limits, e.g. limited actuator lengths, forces, or locations. Each kind of hyper-redundant or soft robot presents a different inverse mapping from arc parameters to actuator parameters. Single-section inverse mapping from arc parameters to actuator parameters is presented in [Xu and Simaan, 2008], [Jones and Walker, 2006a]. Using these mappings, Jones and Walker [Jones and Walker, 2006b] produced an analytical derivation of the robot workspace under actuator length limit constraints.

The above work only takes into consideration constant-curvature kinematics, and hence exclude real world effects, e.g. gravitational loading or friction, which can be important in hyper-redundant robot designs. For example, some hyper-redundant robots undergo noticeable axial compression due to actuator forces. This implies the need of a static analysis of the system in order to compute cable lengths which correspond to desired arc parameters [Camarillo et al., 2009]. In summary, it can be seen that computing the kinematics for a soft or hyper-redundant robot is quite complex and is an issue which would require the full focus of a thesis' work, if it were to be explored in depth.

3.4 Reflections on the State of the Art leading to New Design

In summary, soft robots seem to possess an inherent safety feature in their structural compliance and this makes them quite interesting for this thesis' work. Furthermore, their ability to dextrously adapt to the environment is intrinsic in their soft structure and quite useful to tackle the uncertainty of unstructured environments. However, these robots are quite challenging to control due to the wealth of possible configurations they can take and determining their position and orientation in dynamical conditions, such as under the influence of external forces, is still a challenge.

By looking at the examples provided by these structures, it is clear that inherent safety can be pursued via a low mass structure and compliant features, and that robot autonomy is still problematic for safety in physical human-robot interaction. However, autonomy is particularly challenging for devices like the BHA: its compliant structure makes its control quite challenging, excluding the possibility of making it a completely autonomous system. It is clear that the robot arm required for this thesis' work has to meet different requirements. Namely, the manipulator structure should be such that it can be easily controlled and thus able to operate in-

dependently. On the other hand, soft structures like the OctArm showed very good capabilities in grasping a multitude of objects, confirming the conclusions drawn in Chapter 2. In this respect, the compliance of soft structures is preferable to non-hyperredundant ones. However, non-hyperredundant arms achieved a high level of controllability and very good results in safety for pHRI, due to inherent safety and variable compliance. In summary, this survey shows the positives and negatives of both non-hyperredundant and soft structures but also that these two schools of thought have been primarily kept apart. Thus, there is a lack of a robotic gripper-arm system that takes advantage of both the controllability of non-hyperredundant structures and abilities of soft structures for shape-matching in grasping. In the literature there is a lack of relatively low mass structures with both safety features and which can also passively adapt their grasp to unknown shapes. These reflections were taken into consideration while designing the INTRO-BRL arm structure described in the next paragraph.

3.5 INTRO-BRL arm

Traditional robots with rigid underlying structures can experience limitations in their ability to interact with their environment. These robots can encounter difficulties operating in unstructured and highly congested environments but they can rely on well-established and precise control algorithms. On the other hand, robots with a soft structure and redundant degrees of freedom can be used for delicate tasks in cluttered and/or unstructured environments but suffer from high inaccuracy due to the difficulties their control poses, as explained in the previous section. The aim of the work described in this thesis is to exploit variable compliance to design and produce a robot arm with an inherently safety feature and a gripper. In order to be used together, an arm structure was built around them. This robot arm should be controlled with enough ease to allow a set of real world trials. For this reason, it was decided that the arm main structure would be a non-hyperredundant one, to exploit its controllability and ability to hold heavier payloads than soft structures could. However, it would include the soft gripper, inherent safety characteristics and it would embed a variable compliance safety feature, as suggested by the conclusions reached in Chapter 2. The robot arm design also needed to include the requirements listed in the Introduction and Chapter 2.

The arm-gripper system is described here as ‘mechanically hybrid’ since it combines a soft gripper and a rigid arm in a combined physical structure. The soft gripper has less than perfect position accuracy, because of the aforementioned hard controllability of soft structures. However, the rest of the arm, made of more rigid structures, is able to provide the controllability that the gripper lacks. The choice of placing the compliant part of the arm at the tip of the structure was made necessary

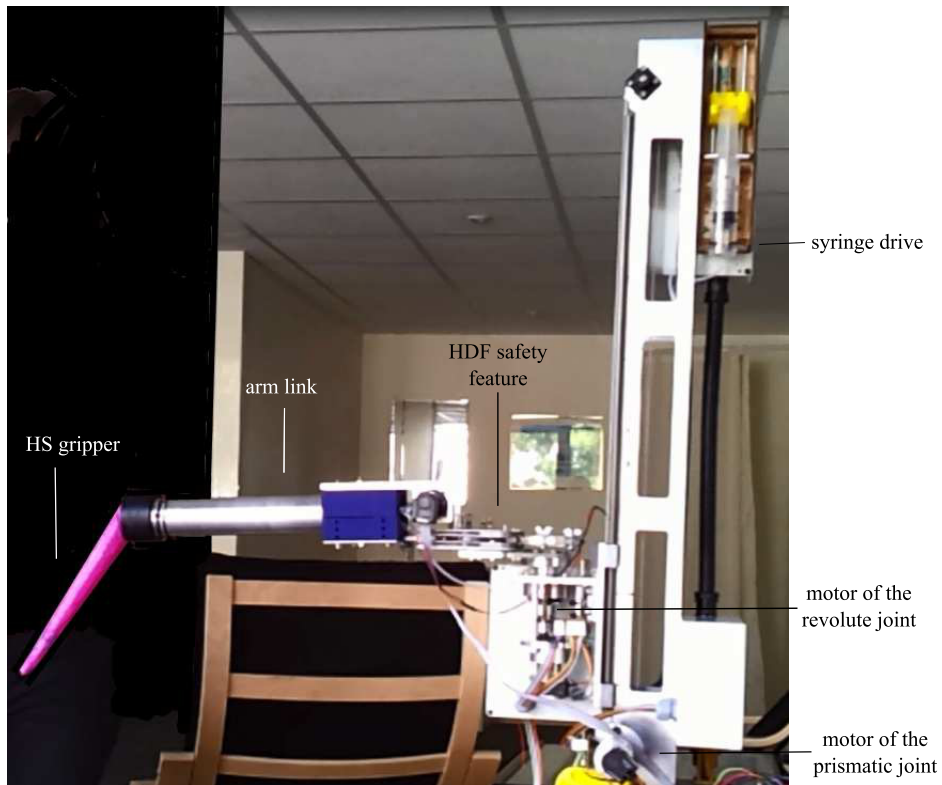


Figure 3.7: the INTRO-BRL arm in the apartment set up of the Robosoft company, France. The HDF can be seen between the blue custom made fixture and the revolute joint.

by multiple considerations. Firstly, the tip is the part that comes into contact with objects and needs to mould itself around them to facilitate their grasping. Secondly, it is necessary for the proximal part (the one closer to the base) of the arm to be the one with greater mechanical resistance and rigidity so that it can withstand dynamical stresses and support the weight of the whole arm. Thirdly, the soft part has the potential to be lighter than the rigid part and in the whole arm structure it is most important that the tip is light so that the torque measured at the base of the arm is kept as low as possible. The INTRO-BRL robot arm design is explained in more detail in the following section.

3.5.1 Arm Design and Inherent Safety

First of all, it is quite important to state that the INTRO-BRL robotic arm novelty resides in the variable compliance safety and grasping features mentioned in Chapter 2 and not in the robot arm structure, which has been kept simple and built around these two features, so that they could be adeptly accommodated. The INTRO-BRL robot arm is arranged in an L-shaped structure and comprises two DOF. The first is obtained by actuating a prismatic joint that is used to control the height of the arm link, which is rotated right and left thanks to an actuated revolute joint. Clearly, an arm with more DOFs may be desirable but the INTRO-BRL arm is able to accommodate both the novel features designed in this thesis' work and thus is a

valid platform to ensure proof of concept. Especially considering the limited time and budget available for this thesis' work. In addition, the low number of degrees of freedom is nonetheless quite adequate to the task at hand. As part of the INTRO project, the robotic arm must be fit to perform in the context of a robot waiter scenario. Due to this, it must be able to grasp cups without spilling their content and deliver them to a customer.

One of the principal inherent safety requirements for a robotic arm is a lightweight structure, as emerged from the rigid arms review in Section 3.2.1 and as specified in the literature reported in Chapter 2. Hence, one of the design aims was to keep the weight as low as possible, without compromising its stability. Thus, the structure has been built in aluminium, a relatively lightweight material. The weight was also lowered by positioning the motors at the base of the arm, which required the gripper to be able to function with remote cable actuation. For this last task, cable actuation was chosen among other solutions for the extreme light weight of its transmission system. Furthermore, the complete softness of the gripper structure could be assured by the delegation of motor activity transmission to wires which do not compromise the compliance of the structure and can be actuated remotely. Regarding the actuators, brushless motors were preferred to brushed ones due to their lower weight. These benefits come at the cost of potentially more complex and more expensive control electronics. This is because brushless motor commutation does not require physical brushes but needs to be implemented in software using a microcontroller.

In order to further increase inherent safety, the structures used for the INTRO-BRL arm are rounded, where possible, to avoid edges that could harm robot users. For example, it has been chosen to use a tube with a round section as a link, and all edges throughout the robotic structure have been rounded.

3.5.2 Hardware description

The INTRO-BRL arm is illustrated in Figure 3.8 integrated with the RobuLAB10 platform from the Robosoft company. This is a concept drawing since the arm was never mounted on the RobuLAB10 platform due to time restrictions. The INTRO-BRL arm comprises three DOFs: two DOFs in the arm and one DOF in the soft gripper, for the opening-closing motion. The DOF present in the whole system structure are described in detail in the following paragraphs.

The arm DOF are the prismatic joint (vertical displacement), which moves along the rail, item 1 in Figure 3.8, and the revolute joint (item 2 in the same figure), which is attached to a plate which moves along the aforementioned rail, and is responsible for the horizontal displacement of the arm. The rail is the arm's base and link 1, link 2 and the safety feature are normally fixed to each other and rotate around the vertical axis. The arm motors are equipped with encoders and controlled in velocity

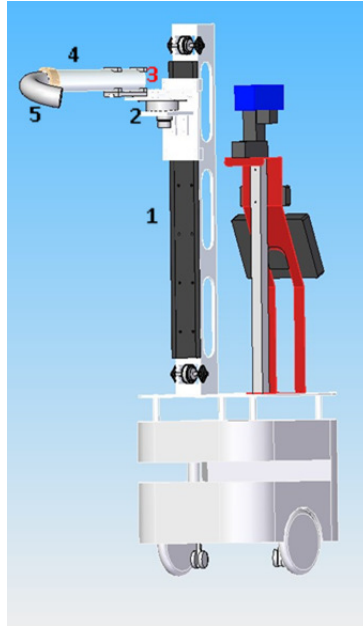


Figure 3.8: The INTRO-BRL arm mounted on the RobuLAB10 platform. The robot arm comprises: 1: rail, 2: revolute joint, 3: variable torque safety feature, 4: link 2, 5: soft gripper. At the back of the robot arm it is possible to see the laptop and pan-tilt camera installed on the RobuLAB10 for research on cognitive human robot interaction, carried out by other researchers in the INTRO project

and position. The soft gripper utilises a winch motor for the closing motion, which can be controlled in velocity or in torque, and a syringe drive for the opening motion. Once this syringe is actuated, the gripper returns to its initial position. The sensors in the syringe drive system are an encoder and two micro switches in the syringe drive box. The arm system starts its motion with a calibration routine, then is switched to normal operation mode. The whole system has been entirely designed and custom built for the project described in this thesis' work in the Bristol Robotics Laboratory²

3.5.3 Forward Kinematics of the Robotic Arm

In order to describe properly the robotic arm structure, its two degrees of freedom were depicted in the schematics below, Figure 3.9. Such graphical illustration is also helpful for the understanding of the kinematics of the robotic arm.

As shown in Figure 3.9, the revolute joint is not along the vertical or z axis of reference frame 1 but it is displaced along the y axis of the same reference frame by a length equal to a_2 . There is a distance b of 100 mm between the platform where the INTRO-BRL arm rests and the bottom end-stop of the prismatic joint. Thus, a distance of 100mm is added to the prismatic joint variable d_1 along the z axis of the global reference frame. The robot arm Denavit-Hartenberg parameters are shown

²in cooperation with the BRL technical team that took care of the manufacturing and consulted in the choosing of components

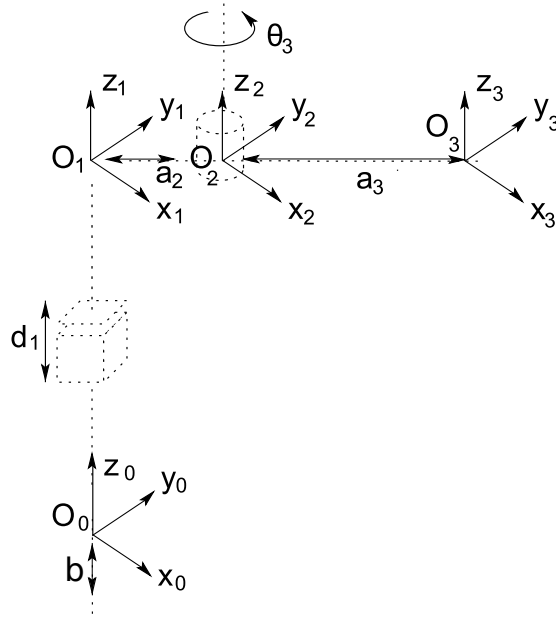


Figure 3.9: the schematics above illustrates the two degrees of freedom present in the manipulator

Link	a_i	α_i	d_i	θ_i
1	0	0	$d_1 + 100$	0
2	a_2	0	0	θ_2
3	a_3	0	0	θ_3

Table 3.3: Denavit-Hartenberg parameters for the INTRO-BRL arm. Out of these parameters, some are variables and some are known constants. The variables are d_1 and θ_3 . The constants are: a_2 , equal to 125mm, a_3 , the length of link 2 and equal to 500mm and θ_2 which is fixed at $\pi/4$ radians.

in Table 3.3.

Two of the Denavit-Hartenberg parameters, d_1 and θ_3 , are the joint variables in, respectively, the prismatic joint and the revolute joint of the arm. In order to translate the position of these joint variables into the position and orientation of the arm end-effector, rotational matrices that transform the global reference frame (0) into the end-effector reference frame (3) are necessary. The rotational matrices of the INTRO-BRL arm are:

$$A_0^1 = \begin{pmatrix} 1 & 0 & 0 & 0 \\ 0 & 1 & 0 & 0 \\ 0 & 0 & 1 & d_1 + 100 \\ 0 & 0 & 0 & 1 \end{pmatrix}$$

$$A_1^2 = \begin{pmatrix} c_2 & -s_2 & 0 & a_2c_2 \\ s_2 & c_2 & 0 & a_2s_2 \\ 0 & 0 & 1 & 0 \\ 0 & 0 & 0 & 1 \end{pmatrix}$$

$$A_2^3 = \begin{pmatrix} c_3 & -s_3 & 0 & a_3c_3 \\ s_3 & c_3 & 0 & a_3s_3 \\ 0 & 0 & 1 & 0 \\ 0 & 0 & 0 & 1 \end{pmatrix}$$

where c_i stands for $\cos(\theta(i))$ and s_i stands for $\sin(\theta(i))$. It is necessary to point out that both the Denavit-Hartenberg parameters a_2 and θ_2 are constants. Specifically, a_2 , is equal to 125mm and θ_2 is equal to $\pi/4$ radians. Hence, the values are:

$$\begin{cases} a_2c_2 = 88.4 \\ a_2s_2 = 88.4 \\ c_2 = 0.7 \\ s_2 = 0.7 \end{cases}$$

Remembering that θ_2 is fixed at $\pi/4$ radians and defining the following variables:

$$\begin{cases} c_{3-\pi/4} = 0.7 \cdot c_3 - 0.7 \cdot s_3 = \cos(\theta_3 + \pi/4) \\ s_{3-\pi/4} = 0.7 \cdot c_3 + 0.7 \cdot s_3 = \sin(\theta_3 + \pi/4) \end{cases}$$

Then the transformation matrix from the frame of reference 0 to the frame of reference 3, becomes:

$$T = A_0^1 \cdot A_1^2 \cdot A_2^3 = \begin{pmatrix} c_{3-\pi/4} & -s_{3-\pi/4} & 0 & 88.4 + a_3c_{3-\pi/4} \\ s_{3-\pi/4} & c_{3-\pi/4} & 0 & 88.4 + a_3s_{3-\pi/4} \\ 0 & 0 & 1 & d_1 + 100 \\ 0 & 0 & 0 & 1 \end{pmatrix}$$

This causes the following relationship between joint variables and Cartesian vari-

ables and the result of forward kinematics:

$$\begin{aligned}
 x &= 88.4 + a_3 \cos(\theta_3 + \pi/4) \\
 y &= 88.4 + a_3 \sin(\theta_3 + \pi/4) \\
 z &= d_1 + 100
 \end{aligned} \tag{3.1}$$

where x , y and z are the position of the end-effector, in mm, in the Cartesian space. Due to the relevance given to safety concerns in this thesis' work, the next section concentrates on the energy balance of the whole INTRO-BLR arm.

3.5.4 Balance of Energy of the Robotic Arm

The balance of energy is vital in order to determine the potential harm which can be caused by a collision with the robot arm. The manipulator's kinetic energy is proportional to the impact energy that the robot arm can transfer to the human user. However, potential energy can also be dangerous, since, in case of a malfunction of the brake or the control system, the arm link could drop, potentially hitting a user, especially if it were a child, short enough to fit and stand underneath the arm's link 2.

The INTRO BRL arm can be seen as a special case of a cylindrical robot arm type. Usually, the cylindrical robot arm type moves in radial, angular and vertical directions [Icosym-nt, 2013]. In the special case of the INTRO-BRL arm, the arm moves only in vertical and angular directions, see Figure 3.9. The first axis provides translational vertical motion (z), the following axis covers the angular region (φ) between the joint limits.

First of all, the kinetic energy of the INTRO-BRL arm is derived. Linear and angular velocities on any link can be expressed in terms of the derivatives of the joint variables and the Jacobian matrix [Spong et al., 2006]. Supposing that the moving mass of link 1 is m_1 , that the mass of link 2 is m_2 , that the mass of link 3 is m_3 and that the mass of the HS gripper, its holder is m_4 and supposing that the inertia matrix of the links, evaluated around a coordinate frame parallel to each frame but whose origin is at the centre of mass, is equal to $I : \frac{m \cdot L^2}{12}$. By substituting these variables in the general equation 3.2, [Spong et al., 2006]:

$$K = \frac{1}{2} \dot{q} \left[\sum_{i=1}^n \{ m_i J_{v_i}(q)^T J_{v_i}(q) + J_{\omega_i}(q)^T R_i(q) I_i R_i(q)^T J_{\omega_i}(q) \} \right] \tag{3.2}$$

where J_{v_i} is the linear velocity Jacobian and the upper half of the entire Jacobian and J_{ω_i} is the angular velocity Jacobian and the lower half of the entire Jacobian.

$$J = \begin{pmatrix} J_{v_i} \\ J_{\omega_i} \end{pmatrix}$$

In the case of the INTRO-BRL arm the Jacobian of link 1 is:

$$J_1 = \begin{pmatrix} 0 & 0 & 0 \\ 0 & 0 & 0 \\ 1 & 0 & 0 \\ 0 & 0 & 0 \\ 0 & 0 & 0 \\ 0 & 0 & 0 \end{pmatrix}$$

the Jacobian of link 2 is:

$$J_2 = \begin{pmatrix} 0 & -62.5 \cdot s_{\pi/4} & 0 \\ 0 & 62.5 \cdot c_{\pi/4} & 0 \\ 1 & 0 & 0 \\ 0 & 0 & 0 \\ 0 & 0 & 0 \\ 0 & 1 & 0 \end{pmatrix}$$

where 62.5mm is the position of the centre of mass of link 2. The Jacobian of link 3 is:

$$J_3 = \begin{pmatrix} 0 & -125 \cdot s_{\pi/4} - l_3 \cdot s_{\pi/4+\theta_3} & -l_3 \cdot s_{\pi/4+\theta_3} \\ 0 & 125 \cdot c_{\pi/4} + l_3 \cdot c_{\pi/4+\theta_3} & l_3 \cdot c_{\pi/4+\theta_3} \\ 1 & 0 & 0 \\ 0 & 0 & 0 \\ 0 & 0 & 0 \\ 0 & 1 & 1 \end{pmatrix}$$

where l_3 is the position of the centre of gravity of link 3. These Jacobians are calculated starting from the forward kinematics in Matlab[®]. The copy of the Matlab[®] file is available in Appendix A. Implementing Eqn. 3.2 in Matlab[®], the kinetic energy for the three links is found. The mathematical expression for the kinetic energy (K) of the moving parts of link 1 is:

$$K_1 = \frac{1}{2} \cdot m_1 \cdot v_1^2 \tag{3.3}$$

where v_1 is the velocity relative to the prismatic joint and m_1 is 0.3kg. As can be seen from Eqn. 3.3, the rotational component is missing, this is because the active revolute joint moves link 3 only. For the same reason, the mathematical expression for the kinetic energy of link 2, which has a mass of 1kg, also has the translational part only:

$$K_2 = \frac{1}{2} \cdot m_2 \cdot v_1^2 \quad (3.4)$$

this is because the angle θ_2 is fixed at the value of $\pi/4$. On the contrary, the kinetic energy of link 3 possesses both the translational and rotational part:

$$K_3 = \frac{1}{2} \cdot m_3 \cdot v_1^2 + \frac{1}{2} \cdot m_3 \cdot l_3^2 \cdot \omega_3^2 + \frac{1}{12} \cdot a_3^2 \cdot m_3 \cdot \omega_3^2 \quad (3.5)$$

where ω_3 is the velocity of the revolute joint and m_3 is 1.87kg. Due to the great variation in shape of gripper in the different grasping phases, no definite shape could be chosen for the end-effector. For this reason, the gripper is regarded as being concentrated in a certain mass location, at the end-effector. This location is reference of the balance of energies. A concentrated mass does not possess an angular velocity nor can a tensor of inertia be defined. Thus the kinetic energy of the gripper is:

$$K_4 = \frac{1}{2} \cdot m_4 \cdot v_1^2 + \frac{1}{2} \cdot m_4 \cdot a_3^2 \cdot \omega_3^2 \quad (3.6)$$

where m_4 is 0.34kg. Summing all the listed kinetic energy components and substituting the known values in the Matlab[®] file, the value of kinetic energy of the INTRO-BRL arm for increasing velocities is found and shown in Figure 3.10.

The total potential energy of the INTRO-BRL arm, P , is equal to the potential energies of all bodies of the open kinematic chain. P is found by utilising the mathematical expression:

$$P = m_1 \cdot m_2 \cdot m_3 \cdot m_4 \cdot g \cdot h \quad (3.7)$$

where g is the acceleration due to gravity, $9.8m/s^2$, and h is the height of link 2. The height h is calculated adding the 0.1m between the base of the robot and the table to the range of motion on the vertical axis. The rail is 0.5m long. The value of the total potential energy for increasing values of the height h is shown in Figure 3.11.

As can be observed comparing the energy values in Figure 3.10 and Figure 3.11,

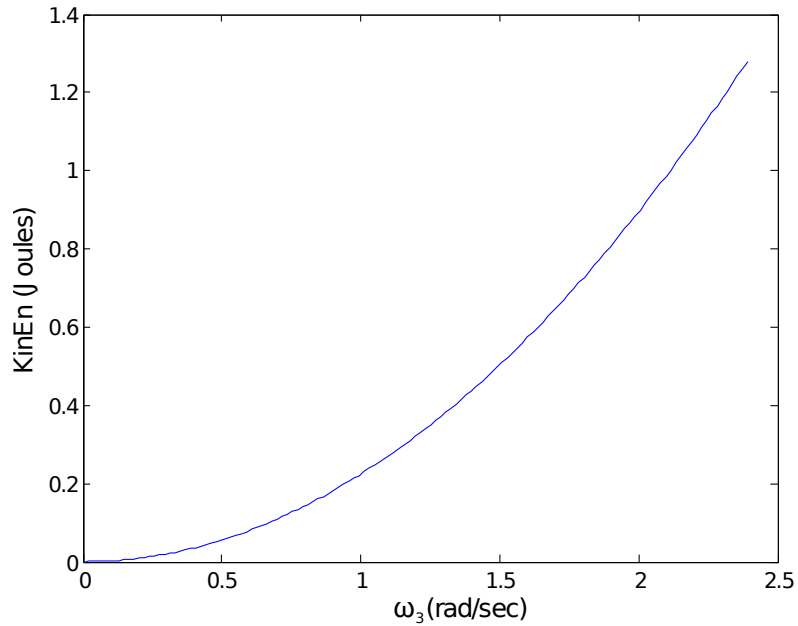


Figure 3.10: The value of kinetic energy in the INTRO-BRL arm

the values of potential energy are considerably higher than the values of kinetic energy. This is due to the very low velocities utilised in the INTRO-BRL arm. This is resulting from the use of low power motors utilised in this project. However, it is worth mentioning that the kinetic energy is proportional to the square of velocity and thus if more powerful motors were used, the velocities values could be much higher and this would result in a substantial increase in the values of kinetic energy. An example of the possible value of kinetic energy when velocities of 1m/s for the prismatic joint and 8rad/s for the revolute joint are plotted in Figure 3.12.

It is important to emphasise that velocities of 1m/s have been recognised as safe in the context of physical human-robot interaction [Haddadin et al., 2009]. Thus the higher velocities in the example of Figure 3.12 could very well be implemented in an arm which is fast enough to be useful in assisting the human users in household tasks.

3.6 Summary

In this chapter, a survey of robotic arms relevant for the field of safe and effective physical interaction with humans is conducted. First it concentrated on hyper-redundant structures and then focussed on soft ones. The positive characteristics and drawbacks of both robot categories are discussed and the subsequent analysis motivates the design choices made for the robotic manipulator described in this thesis. The physical features of the novel robotic structure and the reasons behind the design choices are explained in detail. In addition to a hardware description, the forward kinematics and kinetic/ potential energy of the robotic arm have also been

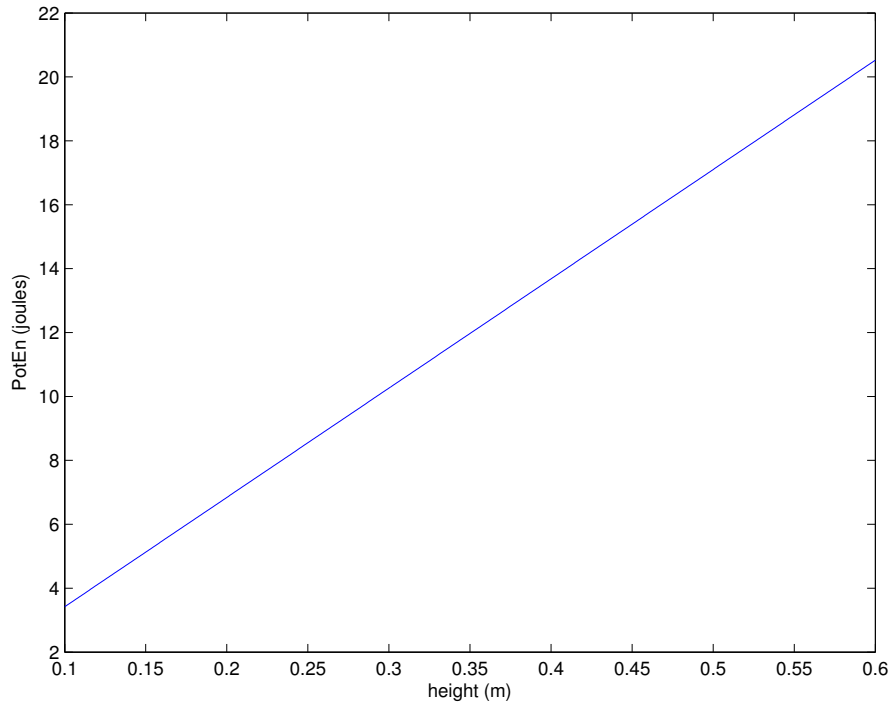


Figure 3.11: The value of potential energy in the INTRO-BRL arm

analysed and reported. The focus of this chapter is on the main structure of the manipulator, however, the novelty of the device resides in the variable compliance safety feature and the variable compliance gripper in the arm, which is not reported here. Both of these physical structures, their working mechanism and the experiments conducted on them are explained in the following chapters. Specifically, the next chapter will focus on the safety feature and Chapter 5 concentrates on the soft gripper.

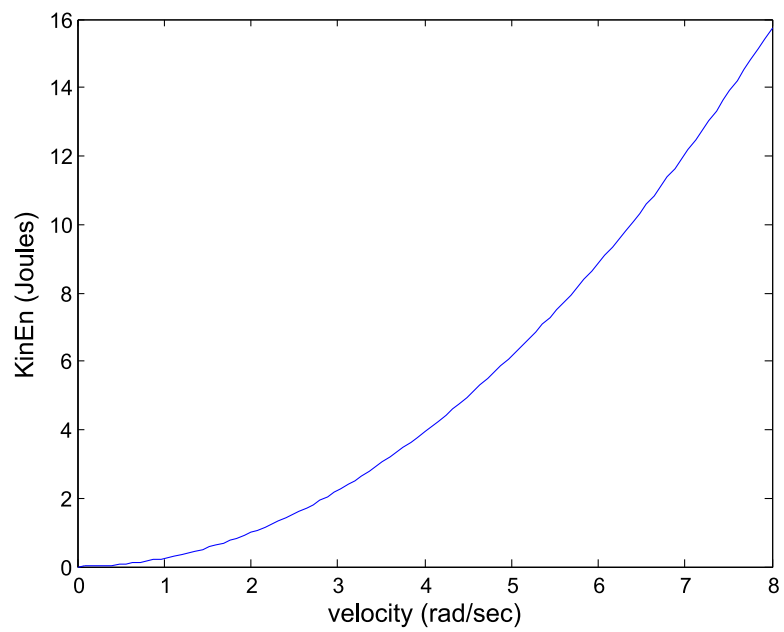


Figure 3.12: The value of kinetic energy in an arm similar to the INTRO-BRL arm but with more powerful motors

Chapter 4

Adjustable Variable Compliance Mechanism to Improve Safety

In recent years the issue of robotic safety has become more and more important because of the desired close interaction and cooperation between human beings and robotic devices. While in traditional industrial robotics such issues are dealt with by separating the human from the robotic appliance with physical barriers and safeguards [De Santis and Siciliano, 2008], such a solution cannot be adopted in the field of assistive robotics, where physical proximity and interaction between humans and robots is inevitable and desired. Hence, physical Human-Robot Interaction (pHRI) is a highly relevant issue to tackle in order to make assistive robotics safe [Zinn et al., 2002]. As mentioned in the robot safety overview in Chapter 2, such issues have been addressed in the literature from multiple points of view. Following from the aims and objectives stated in the Introduction, one the foci of this thesis is to exploit variable compliance to produce a robot arm with inherently safe features. In order to adequately contextualise this work within the literature, the connection between this thesis' work and the state of the art in safety-driven hardware design is described in detail in the next section.

4.1 Connection to the State of the Art

As seen in the literature review in Chapter 2, the safety of variable stiffness/impedance actuators has been effectively questioned and deemed inappropriate for safety purposes, hence this type of mechanism has not been considered. From the literature review, it is also clear that a passive compliance system composed of purely mechanical elements often provides faster and more reliable responses for dynamic collision than an active one involving sensors and actuators [Park et al., 2009]. Also, a passive system has claims to inherent safety, which can ensure that it is behaving in a safe way even if sensors and control fail. This concept is consistent with the inherent safety principles of the ISO 13482 standard [ISO13482, 2014].

The standard states that, whenever possible, safety features need to be embedded directly into the system. One of the negative aspects of passive systems is that building the intelligence in the mechanical structure considerably constrains its behaviour [Sciavicco and Siciliano, 2000]. The system always reacts in the same way and it is not possible to adjust this reaction because that would require changing its physical structure. In other words, deferring control and behaviour to the mechanical and material characteristics excludes flexibility. In contrast, flexibility can be achieved by active variable compliance systems. These considerations have all been taken into account for the design of the new structure presented here. Specifically, the novel design is a hybrid structure: a passive variable compliance mechanism with characteristics that can be changed in an active manner. The new structure combines the best of two worlds, since the intrinsic safety of passive structures is retained but the added flexibility of active ones is also exploited.

The external torque required to trigger the SJM and initiate a compliant behaviour is defined as the threshold torque.

4.2 Novel Approach

This feature works as an adjustable mechanical fuse in the arm, a feature which reacts mechanically to an external impact force and the torque this creates. It keeps the robot arm rigid during normal operational times (when there are no considerable impacts involving the arm) and makes the arm become compliant if the external impact torque is above a set threshold limit. The external torque required to trigger the novel safety feature and initiate a compliant behaviour is defined as the threshold torque. This safety feature comprises the passive variable compliance mechanism and an actuated torque threshold adjuster. Variable compliance is exploited to cause decoupling between the motor and the link of the robot arm in case of collision, hence reducing the inertia actively involved in the collision. The adjustment of the torque is achieved by adding an actuator that changes the positioning of part of the mechanical structure, thus introducing variability in the structure's behaviour. However, this change is made off-line in order to maintain the passive and inherent safety characteristic during operational times. Due to the double nature of this structure, both passive and active, the feature is actually a Hybrid Decoupling Feature and thus is referred to as HDF. The HDF is integrated in the INTRO-BRL arm link, close to the active revolute joint but physically separated from it.

Various design options have been considered in order to achieve a structure as compact as possible which would comprise both the passive variable compliance and variable threshold torque features. The final design is shown in Figure 4.1¹. The top part of the HDF is the one that ensures the passive decoupling once an external

¹structure designed together with Anthony Meunier, who helped with the part adaptation and CAD drawing

torque higher than the threshold torque hits the T-shaped element on top of the figure. The bottom part of the HDF is dedicated to changing the threshold torque; the pin in the centre of the bottom part is attached to the linear motor that actuates the torque change.

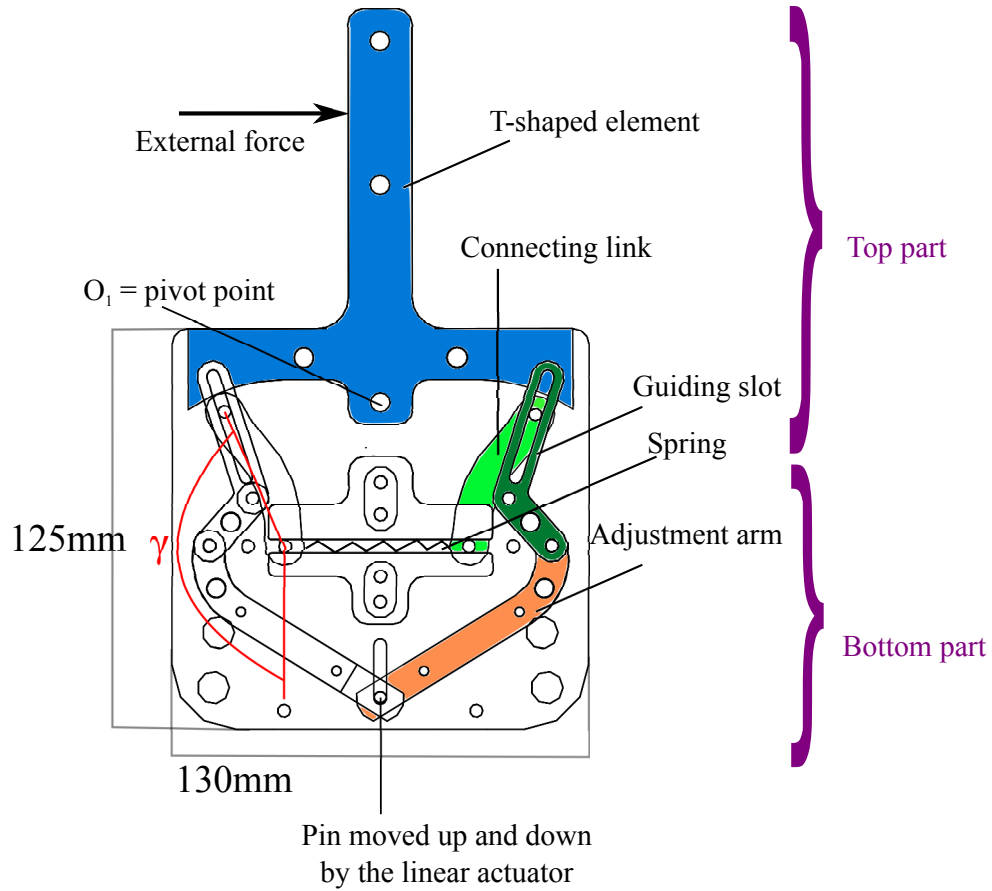


Figure 4.1: HDF, its four main components, the angle γ and an example of the position of the external force (due to a collision) which might cause a torque high enough to exceed the threshold torque. The external force might be applied on either side of the T-shaped element and anywhere along the robot arm link, which is fixed to the long side of the T-shaped element, as shown in Figure 4.7

The explanation of the working mechanism of the actuated torque threshold adjuster is given in Section 4.2.1, the passive variable compliance mechanism is detailed in Section 4.2.2 and the full detail explanation of the physical structure is given in Section 4.3.

4.2.1 Active Torque Threshold Adjuster

The HDF design is inspired by the passive variable compliance system described in the work of Park et al. (described in Chapter 2) but has a major advantage over it: its torque threshold can be actively regulated depending on the operational situation. For example, it would be possible to increase the torque threshold when the arm has to cope with a high load in a given task but the HDF could be made more compliant in the presence of fragile obstacles (objects or humans), thereby reducing

the potential for harm. However, once the torque threshold is adjusted, the HDF resumes its completely passive behaviour, thereby providing inherent safety.

In the Park et al. mechanism, the SJM structure, the threshold torque, \vec{T}_{th} , can only be changed by substituting the spring for one with a different stiffness. This is very impractical, since the SJM needs to be taken apart and then reassembled in order to achieve that. For this reason, in this thesis' work, the mechanism has been substantially modified to allow the adjustment of \vec{T}_{th} without disassembling the mechanical structure. First of all, it was necessary to find a way to modify the structure that would deliver a wide range of \vec{T}_{th} . In case γ , shown in Figure 4.1, is modified, \vec{T}_{th} changes considerably. Hence, varying the angle γ is a very good point to intervene in order to obtain a large range of possible threshold torque values. In order to change γ , the orientation of the connecting link, illustrated in Figure 4.1, needs to be varied. This can be achieved by adding an additional structure and a small motor to actuate the change in orientation. The added structure is the bottom half of the HDF and comprises the guiding slots, the adjustment arms and a linear motor. The adjustment arms are attached to a pin that moves up and down in the bottom slot; this pin is moved by the linear motor. Hence, the position of the pin is proportional to the adjustment arms' position, which in turn changes the orientation of the guiding slot. The latter changes the value of the angle γ , which is proportional to the threshold torque.

The active torque threshold adjuster adjusts the position of the lever arm and, effectively, is the input of the HDF system. The different elements of the HDF are explained in detail in Section 4.5.1 and for a full explanation of the mathematical function that describes the relationship between the pin position (m_x) and the angle of the guiding slot (α_2), see Section B.2. This mathematical function is used at the end of Section 4.5.2 together with the mathematical function that describes the passive mechanism to find the theoretical \vec{T}_{th} for the HDF.

Because of the active adjuster, the HDF's structure also allows online adjustment of the threshold torque and since the adjustment time is short relative to the robot velocity, this would impact minimally on the intrinsic safety of the HDF. In order to determine when to switch from a threshold torque to the other, a set of sensors surrounding the INTRO-BRL arm would be necessary. These sensors would give the whole INTRO-BRL arm-HDF system the awareness to distinguish between situations in which a low threshold torque is required rather than a high threshold torque. For example, a low threshold torque would be required in case the sensory system detects humans or objects in the vicinity of the robot arm. The structure of the HDF is already capable of switching between the two modes in an online manner in its present form.

The upper part of the HDF, the passive triggering mechanism that allows the decoupling between the motor and the INTRO-BRL arm link, is described in detail

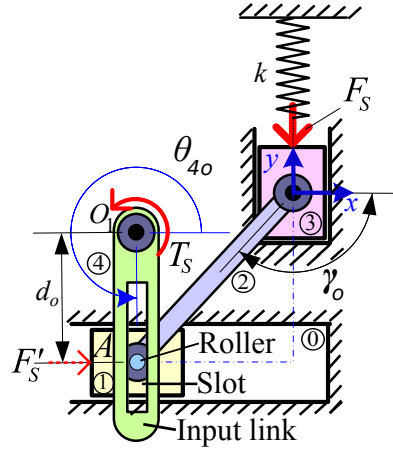


Figure 4.2: Double slider mechanism with spring in the general configuration, figure from [Park et al., 2009] ©2009 IEEE.

in the next section.

4.2.2 Passive Variable Compliance Mechanism

In order to create the passive variable compliance mechanism in the HDF, inspiration is taken from the safe joint mechanism (SJM) by Park et al. [Park et al., 2009]. This mechanism has two modes: a rigid one, which is used in normal operational times and a compliant one. The compliant mode is triggered by external collisions and decouples the arm link from the motor. The switch to one mode to the other is due to the external collision force, hence the passivity of the system. The ability to work in two modes is given to the system by the modified four bar mechanism. Practically, the whole SJM mechanism, illustrated in Figure 4.2, delivers a non linear spring with high stiffness in normal operational times and low stiffness in case of collision.

Initially, the whole system is in equilibrium and torques and forces are balanced by each other. In case an external force impacts the arm link, an extra torque is created. Due to the existence of a spring in the mechanism, the system remains in rigid mode until the external torque \vec{T}_{ext} , exceeds a threshold value. Gravity is not considered in this analysis because the whole system is positioned horizontally, in the plane perpendicular to gravity.

The pre-compressed spring is fit between the output slider and the fixed link, two parts of the modified four bar link mechanism. The force of the spring, \vec{F}_s , shown in Figure 4.2, acts on the output link in the y-axis, thus an appropriate force is required to ensure static equilibrium. The spring torque \vec{T}_s induces the force \vec{F}'_s to the input slider to maintain static equilibrium. The equation that describes \vec{T}_{th}

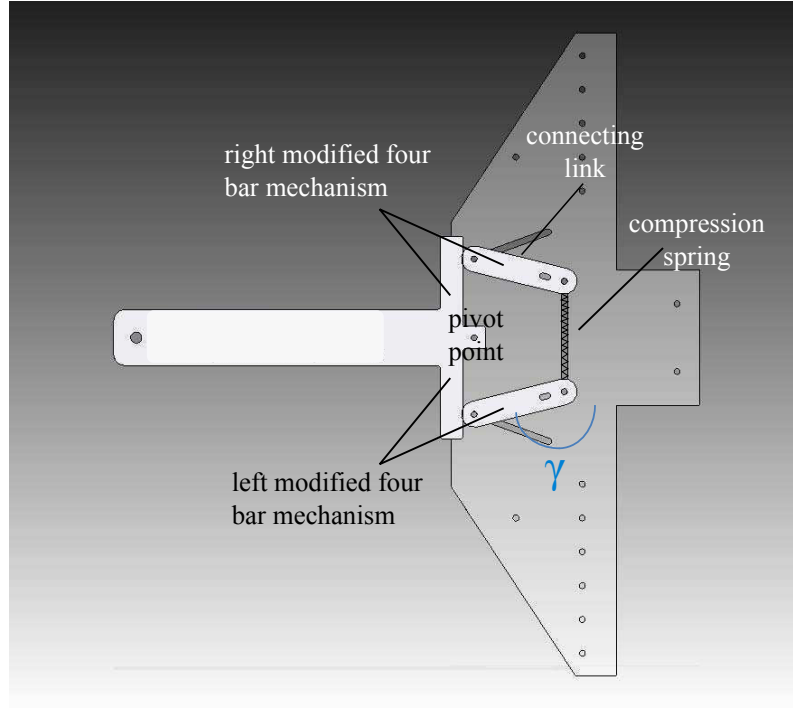


Figure 4.3: angle γ is shown in light blue in the drawing of a SJM prototype made in BRL. The four bar mechanism has been modified and the short side of the T-element and the connecting link are the parts that are left of it, as already done in the work of Park et al.

is shown in Eqn. B.11:

$$T_{th} = \frac{d_0 k * s_0}{\tan \gamma_0 \sin \theta_0} \quad (4.1)$$

In case friction forces are added to the equilibrium, Eqn. B.11 becomes Eqn. B.10 (the complete analysis for this equation can be found in Section B.1):

$$\vec{T}_s = \frac{dks \cdot \cos \gamma}{(-\sin \theta - \mu_s \cos \theta)(\sin \gamma + \mu_s \cos \gamma)} \quad (4.2)$$

In order to understand the mechanism and its advantages and disadvantages, the structure has been built using acrylic. The SolidEdge[®] drawing of the acrylic structure can be seen in Figure 4.3. As can be seen in the figure, the modified four bar mechanism is reproduced on both the right and left side of the structure. Hence, a compliant behaviour in response to collision forces from both the right and the left of the structure is provided.

As mentioned, it is the top part of the HDF that delivers the passive variable compliance. Specifically, looking at Figure 4.1, it is the T-shaped element and the connecting link that are involved in the passive variable compliance mechanism, the mechanical switch that decouples the link from the motor in the overall system. A

detailed description of the both mechanical parts is available in Section 4.5.1. The mathematical model that describes the relationship between the two can be found in Section 4.5.2.

4.3 Materials, Methods and HDF Versions

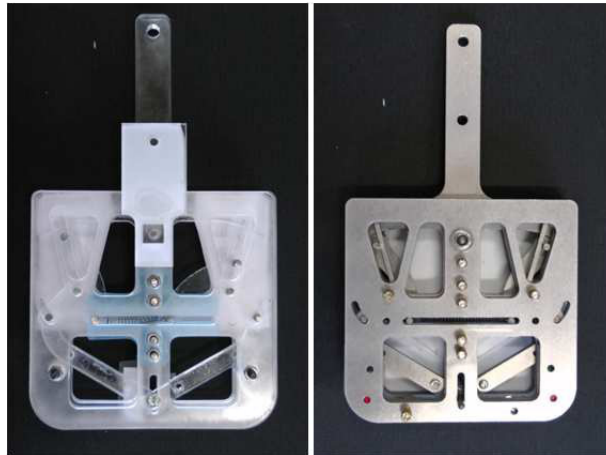


Figure 4.4: The first version of the HDF, in acrylic (left), and the second version, in steel (right).

Before producing the HDF in metal, an acrylic version has been built. A linear motor has been attached to the HDF and controlled with an Arduino board. Since the system has been successfully tested for both the passive variable compliance and the adjustable threshold torque, the HDF has been manufactured in a more durable material. Steel has been chosen over aluminium due to its higher tensile strength. Both versions are shown in Figure 4.4.

The HDF components are flat and assembled together as shown in Figure 4.5. The assembly steps are described in Table 4.1. A detailed description of each component and its interaction with other components is given in Section 4.5.1. As it can be seen in Figure 4.5, the HDF is built in layers.

The dimensioning of the structure is a compromise between the need to keep the structure as compact as possible and the necessity to design a structure which can withstand the arm's weight. The dimensions of the HDF are reported in detail in Section 4.5.1.

Figure 4.6 shows the final arrangement and this view of the structure makes it clear that the HDF works only on the horizontal plane, thus only lateral collisions can activate the HDF. A future development could be a HDF which also absorbs collisions occurring on the vertical plane.

Assembly steps	Detailed step description
step 1	A white acrylic layer is held together with the stainless steel HDF bottom plate by 9 screws. Subsequently, a spacer material (red) is added on top of the plate. This is shown in picture 1 and 2 of Figure 4.5. Holes have been machined in the plate in order to reduce its weight.
step 2	The bottom guiding slots are added to the HDF, as shown in picture 3 of Figure 4.5. There is one on each side of the HDF so that the transmission angle can be varied on both sides of the HDF.
step 3	The top and bottom guide for the spring are added in the centre of the structure, see picture 4 of Figure 4.5. The guides are made of PTFE in order to reduce the friction forces when the connecting link is moving along the guide.
step 4	The connecting links and the adjustment arms are added in picture 5. Four steel pins are inserted at both ends of the connecting link to allow the connecting link to slide along the slot of the guiding slot and along the PTFE guide. Two pins are added on the top of the adjustment arm so it can move along the curved slots in the HDF bottom plates.
step 5	In Figure 6 the connection with the linear actuator is added (bottom of the picture) and attached to the rest of the structure via a pin that holds together the bottom end of the two adjustment arms and that moves along the vertical slot at the bottom of the HDF plates. A clear acrylic part is also added to the HDF. This part acts as a mechanical stop by preventing an excessive displacement of the adjustment arms which would cause the HDF to jam.
step 6	A spring is added between the guides and the middle plate of the HDF. The top set of guiding slots are added on the structure, precisely on top the bottom set of guiding slots, as shown in picture 7.
step 7	Spacer material is added together with the top plate of the HDF, as shown in picture 8 and 9. In picture 9 it is possible to see that bolts are added on the screws: this keeps the HDF in compression and all components in place. Also, a ball bearing and a pin are added to the top of the HDF in order to connect it to the T-shaped element. The HDF structure is now complete.

Table 4.1: Steps in the assembly procedure of the HDF structure, pictured in Figure 4.5

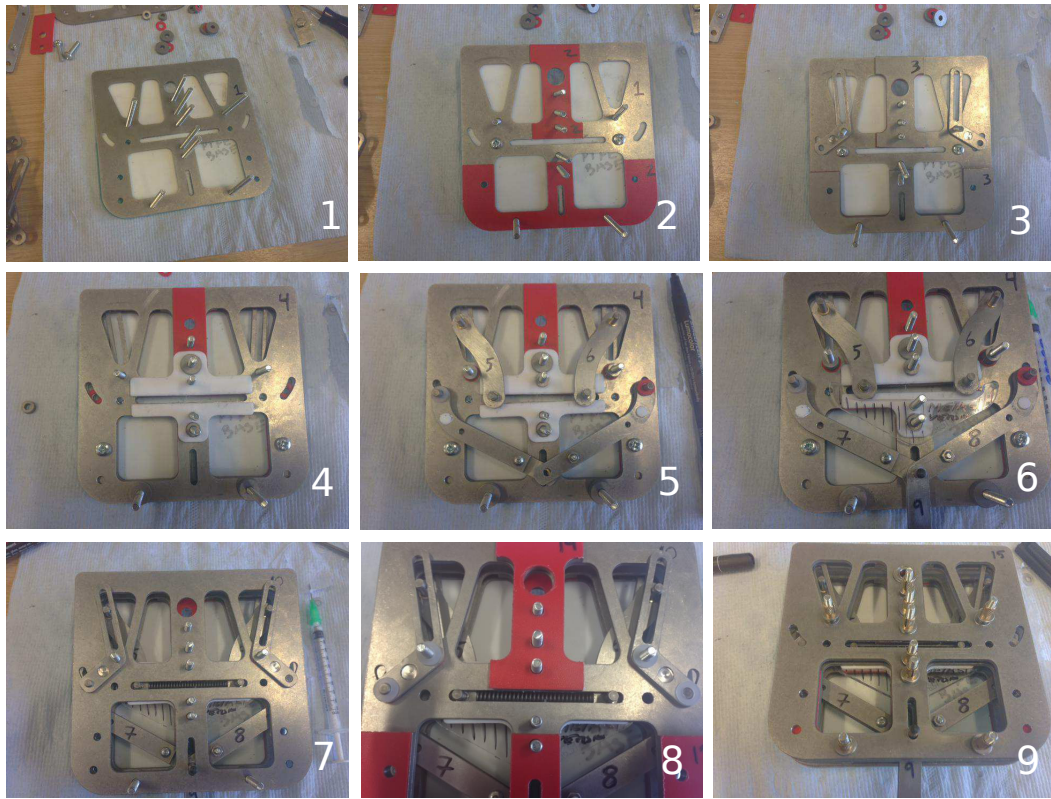


Figure 4.5: Different stages of the assembly process of HDF. The assembling steps are explained in detail in Table 4.1. The assembled HDF is mounted on the purposely designed fixture which fixes it to the INTRO-BRL arm link

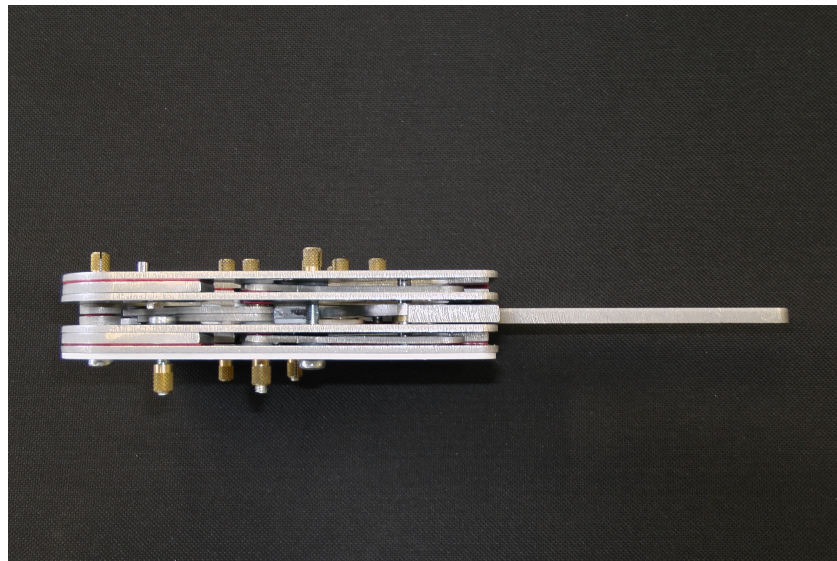


Figure 4.6: Lateral view of the HDF, from which it is possible to notice its multiple layers.

4.4 Integration of HDF with the INTRO-BRL arm

The HDF has been attached to the INTRO-BRL arm link via a metal plate that links it to the active revolute joint, as illustrated in Figure 4.7. This figure shows

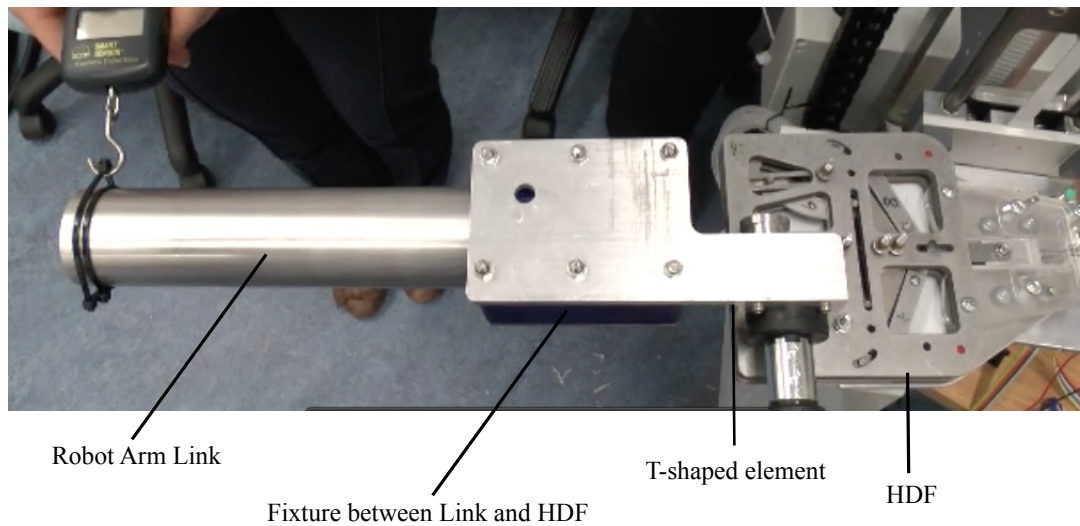


Figure 4.7: The INTRO-BRL robot arm link in normal operational times, when the HDF is in its initial stage and motor and link are coupled. The flat metal plate and the blue box underneath it are the fixtures which hold together the HDF and the arm link



Figure 4.8: The INTRO-BRL robot arm link after a collision, when the HDF has been triggered and motor and link are decoupled. The flat metal plate and the blue box underneath it are the fixtures which hold together the HDF and the arm link

the configuration of the HDF in normal operational time.

This position ensures that the HDF is optimally placed to effectively interrupt the horizontal movement in case of a collision. In fact, in case the collision force exerted by an external object or a person is above the current threshold of the HDF, the T-shaped element of the HDF and the robot arm link, which are fixed together, decouple from the rest of the HDF and the active revolute joint. This is illustrated in Figure 4.8 and Figure 4.9, which show the whole robot-arm and mobile platform system.

In order to design the HDF structure it was necessary to determine the torque thresholds at which the structure should be triggered in order to reduce the potential for harm. The lever arm value is given by the length of the final version of the INTRO-BRL arm link. Here it is assumed that the collisions with the arm will involve the tip of the arm, which is distant 0.5m from O_1 , the point of the HDF

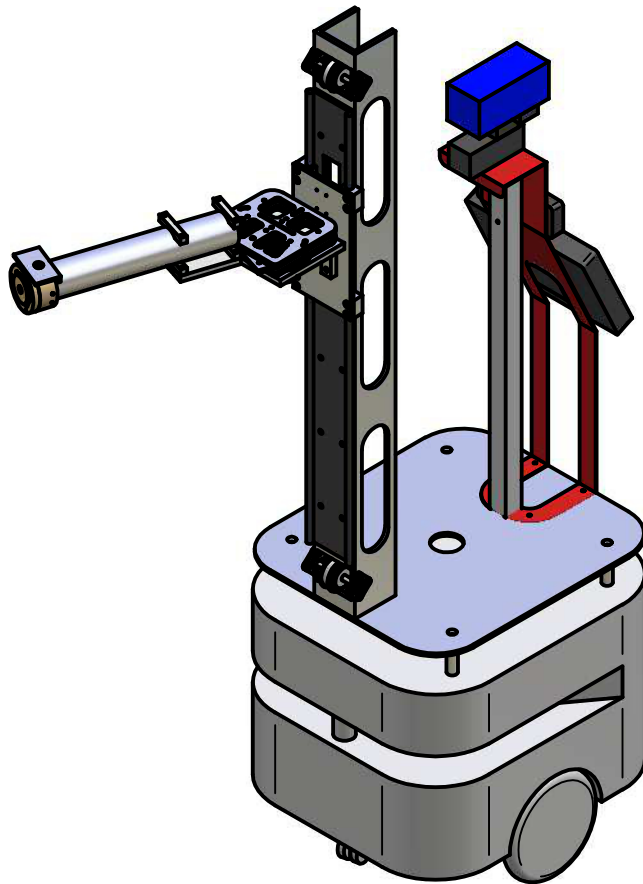


Figure 4.9: Solid Edge[®] drawing of the INTRO-BRL robot arm mounted on the RobuLAB10 platform. In this case, the link has been hit by a force which caused a torque above the torque threshold thus the HDF is triggered and motor and link are decoupled

where the decoupling happens, shown in Figure 4.1. Even though it is possible for the collision to take place anywhere along the arm, it is estimated that most collision would take place in the more distal part of the robot arm. Thus the minimum lever arm distance considered is 0.25m.

As introduced in Chapter 2, in this research effort, instead of focussing on life threatening values, the design of the HDF aims at avoiding collision forces which might induce pain in the user. The maximum external force that does not cause pain is identified as 10N in literature. Applying this to the INTRO-BRL arm geometry, the worst case scenario is that the collision takes place at 0.25m from the tip of the arm. If the HDF needs to get triggered with a 0.25m lever arm at a 10N force this means that the threshold torque at the tip needs to be 2.5Nm. Because of this and similar considerations, the threshold torque at the tip needs to be in the range of 2Nm to 5Nm. The threshold torque would be set to 5Nm in case the robot arm is not working in close proximity of a human user. These specifications, together with the specifications caused by the inspiration to the four bar mechanism shape the design of the HDF. The low threshold torques are compatible with the tasks the INTRO-BRL arm is meant to undertake. An example of these tasks is grasping objects and taking them to the human users, which fits perfectly with the robot waiter scenario envisioned for the INTRO project.

In order to select the desired threshold torque value in the HDF, a better description of the system must be obtained. Specifically, it is necessary to obtain a mathematical description of the relationship between the threshold torque and the displacement of the adjustment arms, which can be controlled directly via the movement of the linear actuator. In order to achieve this, the HDF has been fully modelled, as shown in the next sections.

4.5 Mathematical Model of the Mechanism

The aim of this model is to provide a mathematical relationship between the HDF threshold torque and the orientation of the guiding slot. The orientation of the guiding slot is modified by the movement of the linear actuator. Thus, the orientation of the guiding slot is the connection between the threshold torque and the linear actuator motion. The relationship between the orientation of the guiding slot and the threshold torque and the relationship between the orientation of the guiding slot and the linear actuator movement are not straightforward. They are shaped by the components of the HDF, their orientation and movement. In order to give an accurate description of the mechanical system the model is divided in three parts. Firstly, the HDF components' dimensions and orientation relative to the global coordinate system are described in Section 4.5.1. Secondly, in Section B.2, the interaction of the different components of HDF is given, which further characterises the system and

provides necessary mathematical relationships for the threshold torque. For brevity, this part of the analysis is detailed in Appendix B. Thirdly, further mathematical relationships are derived from the analysis of the forces and torques applied to the mechanical components. These equations are necessary to complete the description of the mathematical relationship between the threshold torque and the linear actuator motion. These equations are described in Section 4.5.2. In this model, only the right side of the system will be taken into account, but since the HDF is symmetrical, the analysis is the same for both sides.

4.5.1 Parts Description

In order to fully describe the behaviour of the system, its main components are described in this section. This part of the model is a representation of the dimensions and orientation of the components in the configuration of HDF at minimum threshold torque. The orientation of the mechanical components is described relatively to the global coordinate system, shown in the HDF drawings. The pivot point (O_1) has been chosen as the origin of the global coordinate system because it is the only point of one of the four main HDF elements that does not move during both the torque adjustment and the triggering motion. Hence this makes it the only point in the structure (apart from the frame) that can at any time be a fixed reference for consistent distance measurements. In addition, the pivot point sits at the centre line of the HDF: this is instrumental for an effective description of the HDF since all the analysis of the right part of the mechanism can also be used for the left side, given the symmetrical nature of the HDF. These are the components already highlighted in Figure 4.1.

In Figure 4.10, multiple points of the HDF are highlighted. The location of these points is useful in order to provide a mathematical descriptions of the HDF. The points shown in Figure 4.10 are listed below.

- O_1 is the centre of rotation of the T-shaped element
- O_2 is the centre of rotation of the guiding slot
- O_3 is the end of the slot which guides the spring
- O_4 is the upper end of the slot which guides the adjustment arms
- A_1 is the right end of the T-shaped element
- A_2 is the upper end of the guiding slot
- B_2 is the right end of the guiding slot
- M_1 is the contact between the T-shaped element and the connecting link

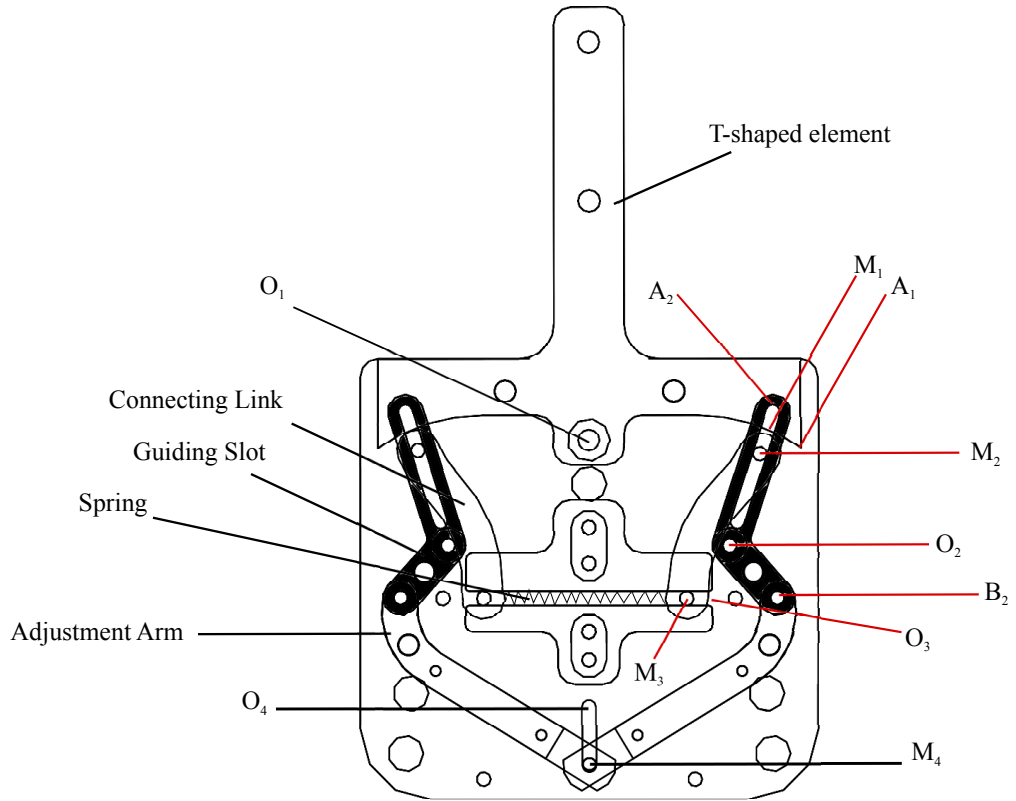


Figure 4.10: The main parts of the system are: the T-shaped element, the connecting links, the guiding slots, the adjustment arms. The spring is squeezed between the two bottom ends of the connecting links.

- M_2 is the position of the upper pin of the connecting link along the guiding slot
- M_3 is the position of the lower pin of the connecting link along the slot which guides the spring
- M_4 is the position of the lower pin of adjustment arm along the vertical slot

The T-shaped element

The T-shaped element, shown in Figure 4.11, is fixed to the INTRO-BRL arm link as shown in Figure 4.7 and Figure 4.9. The T-shaped element's only movement is a rotation around the z -axis; The centre of rotation is the point O_1 .

In Figure 4.11 the x, y axes of the global coordinate system are shown, while the z -axis is pointing outwards, towards the reader. The global coordinate system is fixed and does not move as the HDF moves. On the contrary, the x_1 and y_1 coordinate system is fixed on the T-shaped element and moves with it. $e_{x_1}^{\vec{}}$ is the unit vector along the x_1 axis and $e_{y_1}^{\vec{}}$ is the unit vector along the y_1 axis, see Figure 4.12. α_1 is the angle between the global and the local coordinate system and is different from zero only if the HDF is triggered. In this analysis, angles that go clockwise from the initial side are positive and those that go counterclockwise are

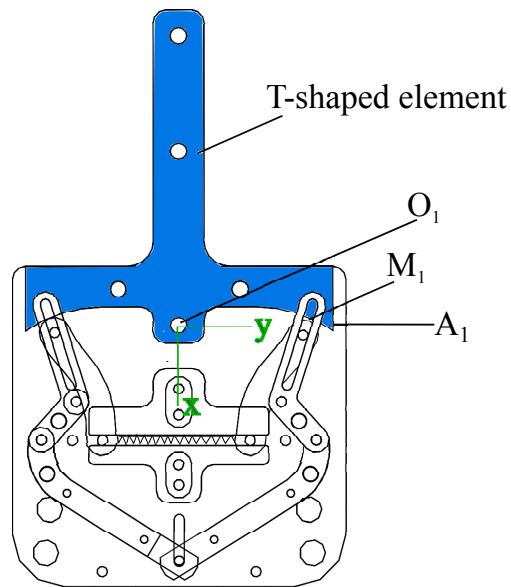


Figure 4.11: The HDF with its global coordinate system. The highlighted component is the T-shaped element. The HDF is in the configuration with the lowest possible value of γ , which yields the minimum torque

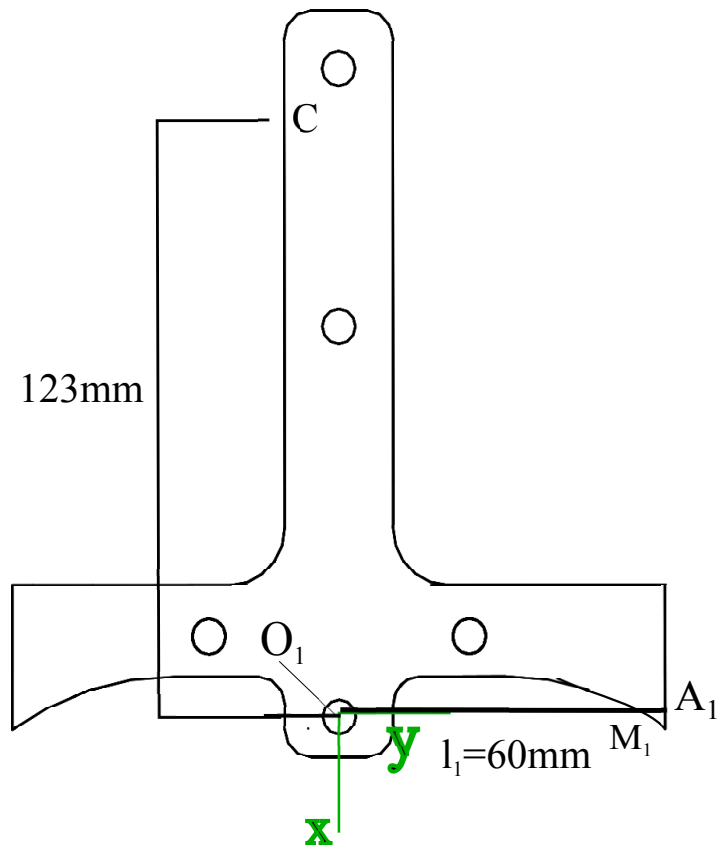


Figure 4.12: The T-shaped element, the global coordinate system is shown, its z axis is pointing outwards, towards the reader and the local coordinate system, relative to the T-shaped element, x_1 - y_1 is also shown, again its z_1 axis is pointing outward, towards the reader. α_1 is the angle between the global and local coordinate system and in the figure is zero, since the HDF is not triggered

negative. The initial side corresponds to the y axis of the global coordinate system.

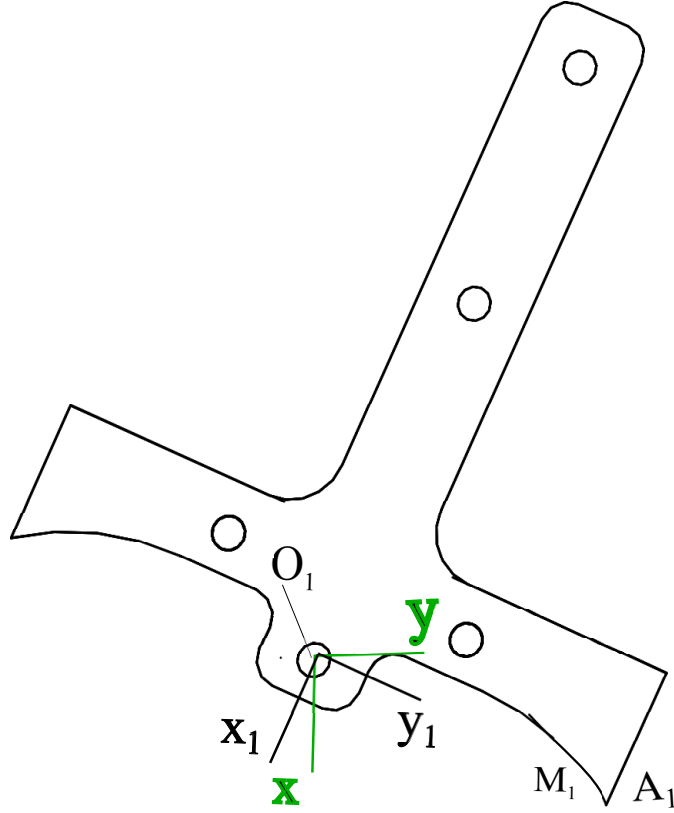


Figure 4.13: The T-shaped element, in this figure α_1 is not zero, since the HDF has been triggered

α_1 could be either positive or negative, since the T-shaped element can rotate both clockwise and counterclockwise around the point O_1 , depending from what side the HDF is hit.

In order to simplify the equations, the curvature of the sides of the T-shaped element is approximated to a straight line. This introduces an error of a few millimeters only. The point A_1 is the end of the T-shaped element, with l_1 being the distance between O_1 (the centre of rotation) and A_1 , as illustrated in Figure 4.12 and Figure 4.13. In Eqn. 4.3 vector $\overrightarrow{O_1A_1}$ is described in the coordinate system of the T-shaped element, x_1 and y_1 .

$$\overrightarrow{O_1A_1} = l_1 \cdot \vec{e}_{y_1} \quad (4.3)$$

In Eqn. 4.4 the vector $\overrightarrow{O_1M_1}$ is described. $\overrightarrow{O_1M_1}$ is adjustable since it describes the engagement point of the T-shaped element with the rest of the mechanism. The parameter p_1 is used to identify a decimal fraction, its value ranges between 0 and 1. This parameter is used to express the magnitude of a vector quantity relatively to another vector magnitude. $\overrightarrow{O_1M_1}$ is a vector with the same direction as $\overrightarrow{O_1A_1}$ but with lower magnitude and p_1 is the ratio of the magnitudes. The vector $\overrightarrow{O_1M_1}$ is described in this way because its magnitude changes as the HDF configuration is changed in order to vary the threshold torque. Thus, it is not

possible to assign a fixed magnitude to $\overrightarrow{O_1M_1}$. For this reason, its magnitude is described with the parameter p_1 , which will later in the model be described as a ratio of HDF dimensions. Eqn. 4.4 first describes $\overrightarrow{O_1M_1}$ in the local coordinate system $x_1 - y_1$ and then in the global coordinate system x, y .

$$\overrightarrow{O_1M_1} = p_1 \cdot \overrightarrow{O_1A_1} = p_1 \cdot l_1 \cdot e_{y_1}^{\vec{}} = p_1 \cdot l_1 \cdot (\sin \alpha_1 \cdot e_x^{\vec{}} + \cos \alpha_1 \cdot e_y^{\vec{}}) = p_1 \cdot l_1 \cdot \begin{pmatrix} \sin \alpha_1 \\ \cos \alpha_1 \end{pmatrix} \quad (4.4)$$

The guiding slot

The guiding slot, shown in Figure 4.14, rotates around the z-axis, the centre of rotation being referred to as O_2 . The point A_2 is the end of the slot in the longer side of the guiding slot, and l_2 is the distance between A_2 and O_2 .

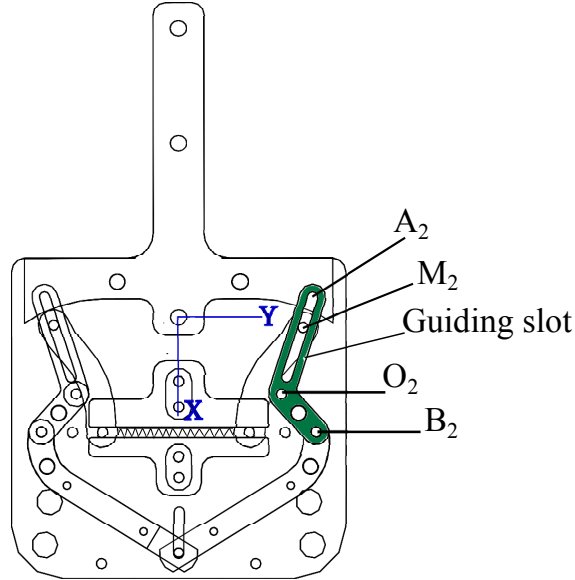


Figure 4.14: The HDF with its global coordinate system. The highlighted component is the guiding slot

B_2 is a link pin, and l_2 is the distance between B_2 and O_2 . Three coordinate systems are present in Figure 4.15: 1) The global coordinate system, $x-y$, 2) the $x_{2_1}-y_{2_1}$ coordinate system, which is in line with the longer side of the guiding slot and 3) the third coordinate system is $x_{2_2} - y_{2_2}$, which is in line with the shorter side of the guiding slot. $e_{x_{2_1}}^{\vec{}}$ is the unit vector along the x_{2_1} axis. $e_{y_{2_1}}^{\vec{}}$ is the unit vector along the y_{2_1} axis. α_2 is the angle between the $x-y$ coordinate system and the $x_{2_1}-y_{2_1}$ coordinate system. The angle between the $x_{2_1}-y_{2_1}$ coordinate system and the $x_{2_2}-y_{2_2}$ coordinate system and is a constant: $\pi/6$ radians. A drawing of the aforementioned angles is shown in Figure 4.16 for clarification. Eqn. 4.5 and Eqn. 4.6 describe the vectorial distances between the rotation centre of the guiding slot, B_2 and its two

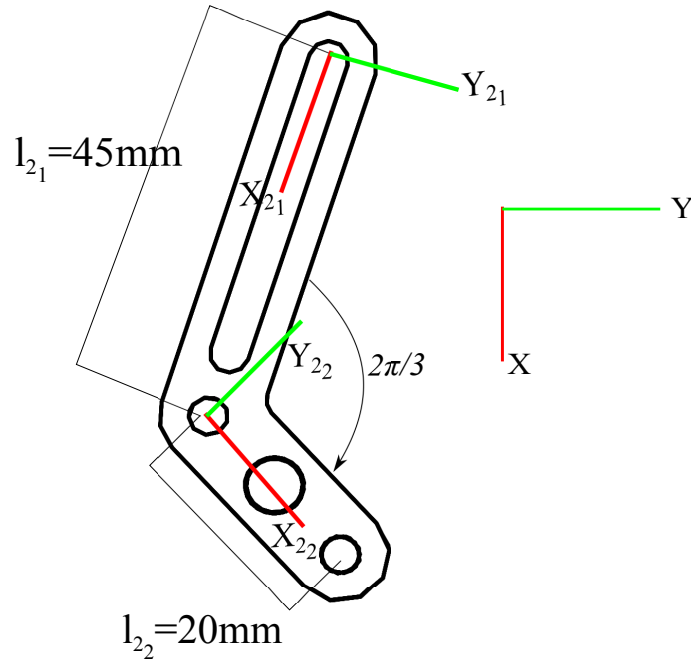


Figure 4.15: The guiding slot, the global coordinate system is shown, the z axis is pointing outwards, towards the reader and two local coordinate systems, relative to the guiding slot, x_{21} - y_{21} and x_{22} - y_{22} are also shown; their z_{21} and z_{22} axes are pointing outward, towards the reader. In the first coordinate system x_{21} is along the longer segment of the guiding slot, in the second y_{22} is along the shorter segment of the guiding slot

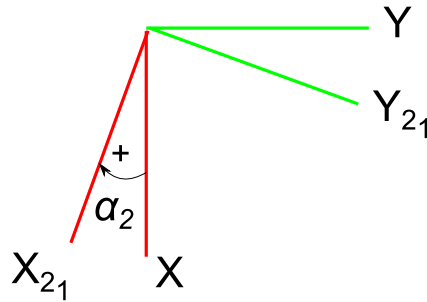


Figure 4.16: The angle α_2 corresponds to the difference in orientation from the global coordinate system to the first local coordinate system of the guiding slot. Since α_2 goes clockwise, it is positive. The angle α_2 depends on the movement on the HDF

extremities.

$$\overrightarrow{O_2A_2} = -l_{21} \cdot e_{x_{21}} \quad (4.5)$$

$$\overrightarrow{O_2B_2} = l_{22} \cdot e_{y_{22}} \quad (4.6)$$

The position of the end point of the connecting link along the guiding slot is

called M_2 . Eqn. 4.7 relates the magnitude and direction of vector $\overrightarrow{O_2M_2}$. The parameter p_2 is used to identify a decimal fraction, its value ranges between 0 and 1. This parameter is used to express the magnitude of a vector relatively to another vector magnitude. $\overrightarrow{O_2M_2}$ is a vector with the same direction as $\overrightarrow{O_2A_2}$ but with lower magnitude and p_2 is the ratio of the magnitudes. The vector $\overrightarrow{O_2M_2}$ is described in this way because its magnitude changes as the HDF configuration is changed to vary the threshold torque. Thus, it is not possible to assign a fixed magnitude to $\overrightarrow{O_2M_2}$. For this reason, its magnitude is described with a parameter, p_2 , which will later in the model described as a ratio of HDF dimensions.

$$\begin{aligned} \overrightarrow{O_2M_1} = \overrightarrow{O_2M_2} &= p_2 \cdot \overrightarrow{O_2A_2} = -p_2 \cdot l_{21} \cdot e_{x_{21}}^{\rightarrow} = -p_2 \cdot l_{21} \cdot (\cos \alpha_2 \cdot e_x^{\rightarrow} - \sin \alpha_2 \cdot e_y^{\rightarrow}) = \\ &= -p_2 \cdot l_{21} \cdot \begin{pmatrix} \cos \alpha_2 \\ -\sin \alpha_2 \end{pmatrix} \end{aligned} \quad (4.7)$$

The connecting link

The connecting link, Figure 4.17, as all the other parts in the HDF, has a planar movement.

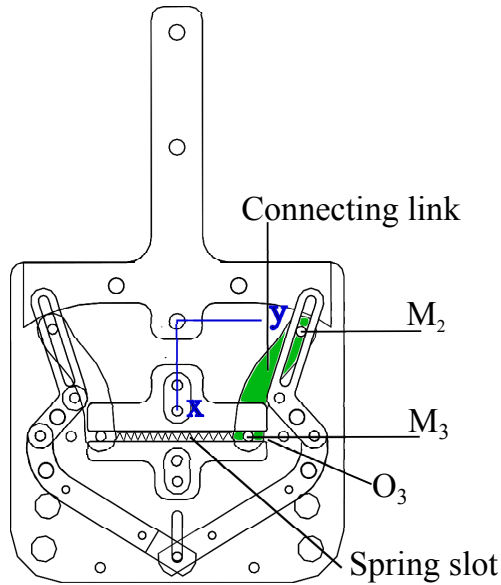


Figure 4.17: The HDF with its global coordinate system. The highlighted component is the connecting link

One end of the connecting link moves along the slot in the guiding slot, the other end moves along the slot which guides the spring. In both cases it is the pin inserted in the connecting link that slides along the slots. The right end of this slot is referred to as O_3 .

In Figure 4.18, the global coordinate system, $x-y$ and the connecting link coordinate system, x_3-y_3 , are shown. α_3 is the angle between the global and the local

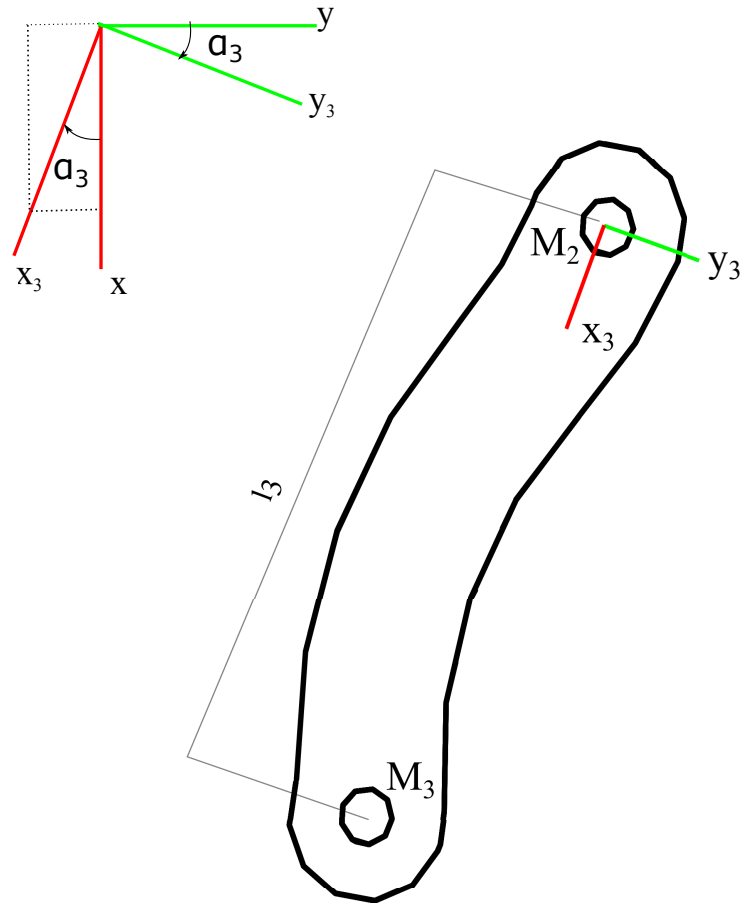


Figure 4.18: The connecting link: the global coordinate system, x - y is shown, the z axis is pointing outwards, towards the reader. The local coordinate system, relative to the connection link, x_3 - y_3 is also shown, its z_3 axis points outward, towards the reader

coordinate system. The position of the point M_3 of the connecting link along the horizontal spring slot is given by $\overrightarrow{O_3M_3}$:

$$\overrightarrow{O_3M_3} = -m_y \cdot \vec{e}_y \quad (4.8)$$

where m_y is the magnitude of the vector. The vector of the distance between the two ends of the connecting link is $\overrightarrow{M_2M_3}$:

$$\overrightarrow{M_2M_3} = l_3 \cdot \vec{e}_{x_3} \quad (4.9)$$

The adjustment arm

The adjustment arm, shown in Figure 4.19, is displaced directly by the linear motor that moves the point M_4 .

The adjustment arm's vertical displacement is transmitted to the guiding slot, which connects to the adjustment arm in B_2 . The guiding slots rotates around

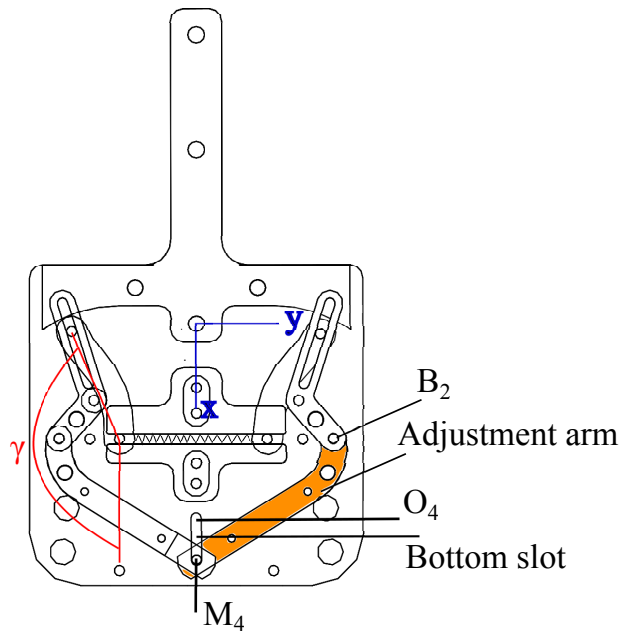


Figure 4.19: The HDF with its global coordinate system. The highlighted component is the adjustment arm

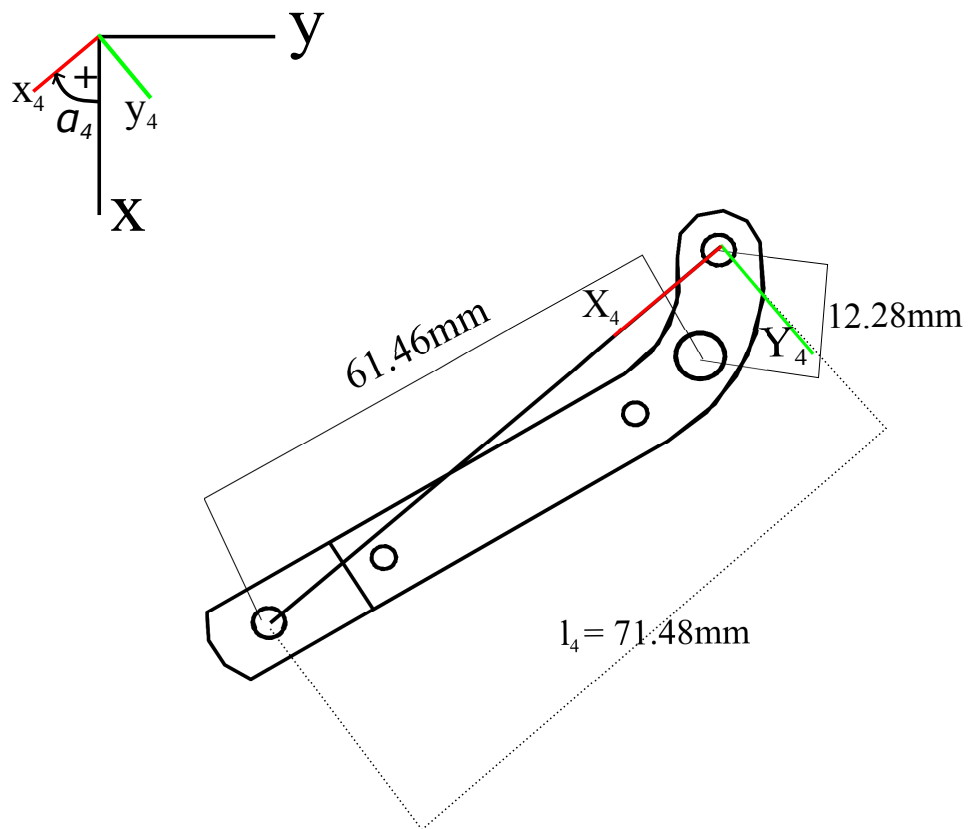


Figure 4.20: The adjustment arm: the global coordinate system, $x-y$ is shown, the z axis is pointing outwards, towards the reader. The local coordinate system, relative to the adjustment arm, x_4-y_4 is also shown, its z_4 axis is point outwards, toward the reader.

the z_{22} axis, see Figure 4.14. This changes its orientation, which, in turn, changes the orientation of the connecting link. This results in a variation of the angle γ , illustrated in Figure 4.19 and thus a threshold torque variation.

In Figure 4.20 the x, y axes of the global coordinate system are shown, while the z -axis is pointing upwards, towards the reader. The global coordinate system is fixed and does not move as the HDF moves. On the contrary, the x_4 and y_4 coordinate system is fixed on the adjustment arm and moves with it. The end points in the adjustment arm are: B_2 which is defined above, and M_4 . The latter moves along a vertical slot which has as an upper limit the point O_4 . α_4 is the angle between the global and the local coordinate system. The position of the adjustment arm along the bottom slot is given by Eqn. 4.10:

$$\overrightarrow{O_4M_4} = m_x \cdot \vec{e}_x \quad (4.10)$$

where m_x is the magnitude of the vector. The vector describing the length of $\overrightarrow{M_4B_2}$ is:

$$\overrightarrow{M_4B_2} = -l_4 \cdot \vec{e}_{x_4} \quad (4.11)$$

An overall view of the coordinate systems present in the HDF is shown in Figure 4.21.

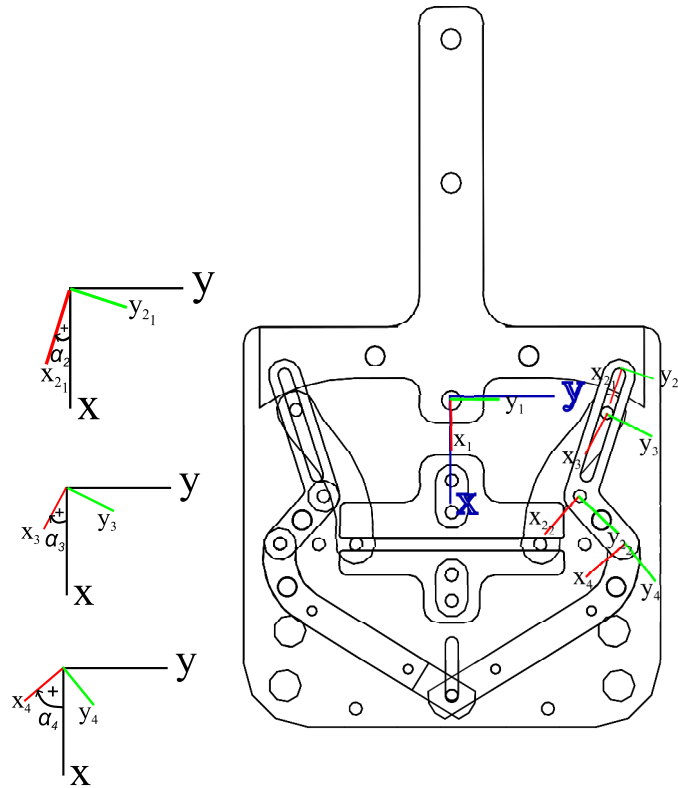


Figure 4.21: Global and local coordinate systems in the HDF. α_1 in this case is zero since the T-shaped element is in its initial position. All the other angles go clockwise from the general coordinate axis to the local coordinate axis are clockwise, thus positive

In the next part of the mathematical model, it is shown how to link the position and orientation of the adjustment arm to the position and orientation of the guiding slot. This makes it possible to determine the linear displacement of the actuator which will yield the right adjustment arm orientation in order to obtain the desired guiding slot orientation, which is directly related to the threshold torque. For brevity, this part of the model, or intermediate results, is placed in the Appendix B, Section B.2.

4.5.2 Application of Wrenches to the HDF Mechanical Study

The aim of the section is to find the expression for the threshold torque in terms of m_x , the displacement of the adjustment arms caused by the linear actuator. To do so, a description of the forces and torques acting on the T-shaped element and the connecting link is necessary. These have been acquired by applying wrenches to the mechanical study of the structure. Applying Newton's laws to a rigid body, the result forces and torques can be grouped into a wrench. In order to describe this approach a definition of wrenches is given.

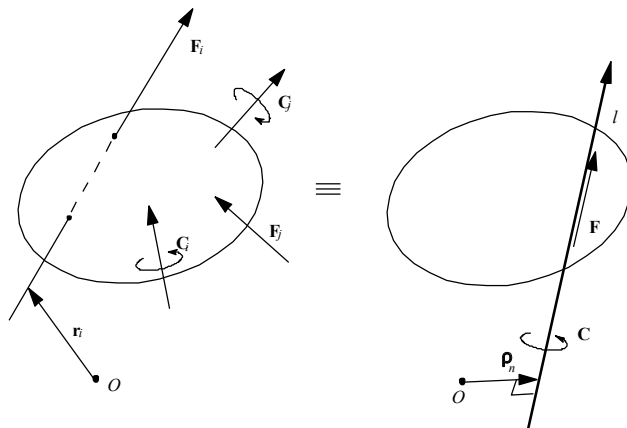


Figure 4.22: A rigid body, Forces F , Couples C , a line l , from [Kumar, 2015], used with permission of Dr Kumar.

A system of forces and couples is equivalent to a pure force along an axis l , and a pure couple parallel to l . This is called a wrench [Kumar, 2015]. The resultant force and couples:

$$\vec{F} = \sum_{i=1}^n \vec{F}_i \quad (4.12)$$

$$\vec{M}_0 = \sum_{i=1}^m \vec{C}_i + \sum_{i=1}^n \vec{r}_i \times \vec{F}_i \quad (4.13)$$

which are equipollent to a Force F along the line l and a couple C parallel to l , as shown in Figure 4.22. The system of forces and torques can be thought of as a wrench about a screw axis, illustrated in Figure 4.23.

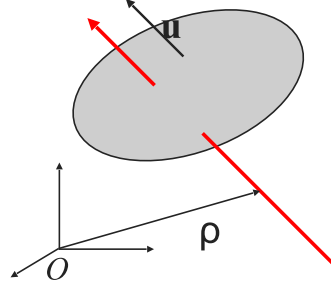


Figure 4.23: The screw axis, from [Kumar, 2015], used with permission of Dr Kumar.

A screw axis is characterised by: u , the orientation axis, ρ , the position vector to a point on the same axis and h , the axis pitch. The sum of forces and couples can be considered a wrench about a screw axis with an intensity S [Kumar, 2015].

In summary, any system of forces and couples can be considered as a wrench vector that can be described as:

$$\vec{w} = \begin{bmatrix} \vec{F} \\ \vec{M}_0 \end{bmatrix} = S \begin{pmatrix} \vec{u} \\ h\vec{u} + \rho \times \vec{u} \end{pmatrix} \quad (4.14)$$

where \vec{w} represents a wrench, \vec{F} a force and \vec{M}_0 a torque. This second term in Eqn. 4.14 is the one used in the analysis of the HDF mechanism in the following paragraphs.

In order to utilise wrenches in the HDF analysis, all the force and couples acting on the HDF mechanical parts must be taken into consideration. The process is done for both the T-shaped element and the connecting link.

The T-shaped Element

The forces acting on the T-shaped element are analysed in static conditions, in other words when the sum of all forces is zero and the HDF elements are not moving relative to each other. Three forces are applied to the T-shaped element: the first is an external force applied to the T-shaped element at a point C which is at a certain distance D from O_1 along the X axis of the global coordinate system, as illustrated in Figure 4.24. The second is the reaction force of the HDF frame on the T-shaped element and it is applied at point O_1 . The HDF frame is fixed to the rest of the INTRO-BRL arm hence it is static and thus it resists any movement of the T-shaped element. The third is the force applied by the connecting link to the T-shaped element at point M_1 , which in this analysis is assumed equal to M_2 . This force's direction is not along any of the axes of the global coordinate system

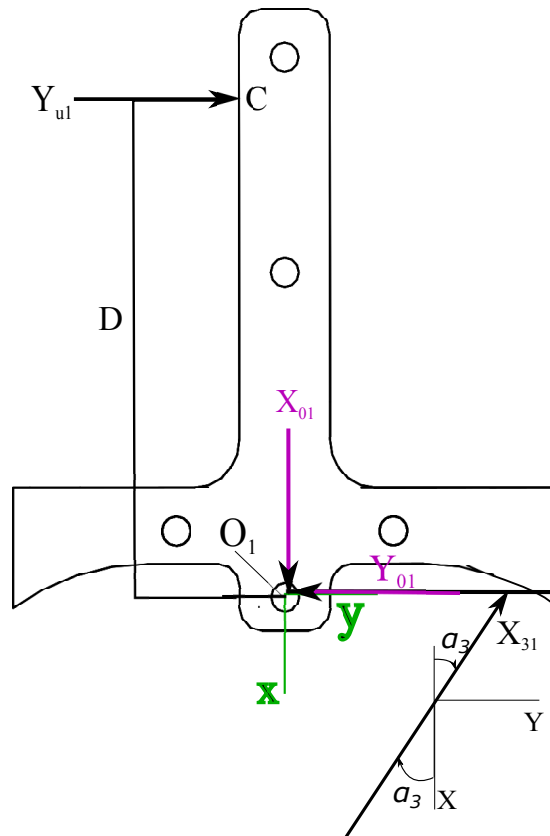


Figure 4.24: The forces acting on the T-shaped element. This drawing shows the T-shaped element at the equilibrium, before it is triggered. In this case α_1 equal to zero. The general coordinate system is shown in green in the figure

but along the X axis of the local coordinate system of the connecting link. In this section, the forces have the name of the axis that corresponds to their direction, the forces' first subscript refers to the component which is exerting the force and the second subscript refers to the component on which the force is exerted upon. These forces and the resulting torques will be expressed as wrenches. The subscript of the wrench identifies the point from which the torque is measured. After the forces and torques are described, the equilibrium of forces along the X and Y axis of the global coordinate system is detailed along with the equilibrium of the torques acting on the T-shaped element.

In addition to the forces mentioned, there is also a friction force caused by the movement of the T-shaped element relative to the connecting link. The contact area between these two elements is quite reduced compared to the area of contact of the friction forces considered in the next section, which lists the forces acting on the connecting link. The T-shaped element relative to the connecting link only make contact in one point, while the rest of the friction forces listed in the next paragraph have four or more points of contact. For this reason, this friction force has been disregarded. Furthermore, there is a friction torque given by the movement of the T-shaped element contacting the pivot of the HDF at O_1 . The arm of this torque is the radius of the pivot pin, which is so small compared to the torque caused by

the external force that it has also been disregarded in this analysis.

- The force $\overrightarrow{Y_{u \rightarrow 1}}$, which is applied to point C of the T-shaped element: $\left\{ \begin{array}{c} \overrightarrow{Y_{u \rightarrow 1}} \cdot \vec{e}_y \\ \vec{0} \end{array} \right\}_C$ This force's direction is along the X axis of the global coordinate system. Since the point from which the torque is measured is the same as the point where the force is applied the torque is zero.
- The reaction force of the HDF frame, 0, applied to O_1 is divided into a component along the X axis of the global coordinate system and a component along the Y axis of the global coordinate system: $\left\{ \begin{array}{c} \overrightarrow{X_{0 \rightarrow 1}} \cdot \vec{e}_x - \overrightarrow{Y_{0 \rightarrow 1}} \cdot \vec{e}_y \\ \vec{0} \end{array} \right\}_{O_1}$ Since the point from which the torque is measured is the same as the point where the force is applied the torque is zero.
- The force transmitted by the connecting link is applied to M_1 and is divided into a component along the X axis of the connecting link local coordinate system and a component along the Y axis of the connecting link local coordinate system: $\left\{ \begin{array}{c} -\overrightarrow{X_{3 \rightarrow 1}} \cdot \vec{e}_{x_3} + \overrightarrow{X_{3 \rightarrow 1}} \cdot \vec{e}_{y_3} \\ \vec{0} \end{array} \right\}_{M_2}$ Since the point from which the torque is measured is the same as the point where the force is applied the torque is zero.

In order to obtain the static equilibrium, the wrenches have to be expressed at the same point; let it be the point O_1 . The forces due to the reaction of the HDF frame are already expressed relatively to the point O_1 , so they do not create any torques. The external force $\overrightarrow{Y_{u \rightarrow 1}}$ instead, does create a torque:

$$\left\{ \begin{array}{c} \overrightarrow{Y_{u \rightarrow 1}} \cdot \vec{e}_y \\ \vec{0} \end{array} \right\}_C \equiv \left\{ \begin{array}{c} \overrightarrow{Y_{u \rightarrow 1}} \cdot \vec{e}_y \\ -\vec{D} \times \overrightarrow{Y_{u \rightarrow 1}} \cdot \vec{e}_z \end{array} \right\}_{O_1}$$

the vector product produces a torque with direction along the negative Z axis of the global coordinate system. The force along the $\overrightarrow{X_3}$ axis produces a torque as well:

$$\left\{ \begin{array}{c} -\overrightarrow{X_{3 \rightarrow 1}} \cdot \vec{e}_x + \overrightarrow{X_{3 \rightarrow 1}} \cdot \vec{e}_y \\ \vec{0} \end{array} \right\}_{M_2} \equiv \left\{ \begin{array}{c} -\overrightarrow{X_{3 \rightarrow 1}} \cdot \cos \alpha_3 \cdot \vec{e}_x + \overrightarrow{X_{3 \rightarrow 1}} \sin \alpha_3 \cdot \vec{e}_y \\ (p_1 \cdot l_1 \cos \alpha_1 \times \overrightarrow{X_{3 \rightarrow 1}} \cdot \cos \alpha_3 + p_1 \cdot l_1 \cdot \sin \alpha_1 \times \overrightarrow{X_{3 \rightarrow 1}} \sin \alpha_3) \vec{e}_z \end{array} \right\}_{O_1}$$

the vector product in this case produces a torque with direction along the positive Z axis of the global coordinate system. The static equilibrium along the X and Y coordinates of the global coordinate system and the static equilibrium of the torques measured at the point O_1 can be written as:

$$\left\{ \begin{array}{l} \overrightarrow{X_{0 \rightarrow 1}} - \overrightarrow{X_{3 \rightarrow 1}} \cdot \cos \alpha_3 = 0 \\ -\overrightarrow{Y_{0 \rightarrow 1}} + \overrightarrow{Y_{u \rightarrow 1}} + \overrightarrow{X_{3 \rightarrow 1}} \cdot \sin \alpha_3 = 0 \\ -\overrightarrow{D} \cdot \overrightarrow{Y_{u \rightarrow 1}} + p_1 \cdot l_1 \cdot \cos \alpha_1 \cdot \overrightarrow{X_{3 \rightarrow 1}} \cdot \cos \alpha_3 + p_1 \cdot l_1 \cdot \sin \alpha_1 \times \overrightarrow{X_{3 \rightarrow 1}} \sin \alpha_3 = 0 \end{array} \right. \quad (4.15)$$

The last equation in the system in 4.15 shows the equilibrium of torques in the T-shaped element:

$$\overrightarrow{D} \cdot \overrightarrow{Y_{u \rightarrow 1}} = \overrightarrow{X_{3 \rightarrow 1}} \cdot p_1 \cdot l_1 \cdot \cos \alpha_1 - \alpha_3 \quad (4.16)$$

this equation points out that the torque created by the external force is counteracted by the torque generated by the connecting link, $X_{3 \rightarrow 1}$, multiplied by the distance between the point of application of this force and the point O_1 . Thus, $\overrightarrow{X_{3 \rightarrow 1}}$ is the force provided by the HDF to resist the external torque. If the initial position of the HDF is considered, when the HDF has not been triggered yet, then $\alpha_1 = 0$. This particular condition is considered since it is the starting configuration of the HDF. In this condition, the HDF resistance torque ($\overrightarrow{T_R}$) to the torque provided by the external force is given by:

$$\overrightarrow{T_R} = p_1 \cdot l_1 \cdot \overrightarrow{X_{3 \rightarrow 1}} \cdot \cos \alpha_3 \quad (4.17)$$

A mathematical expression for the force $\overrightarrow{X_{3 \rightarrow 1}}$ is found in the next paragraph.

The connecting link

Six forces are applied to the connecting link, as illustrated in Figure 4.25.

The first force is applied to the connecting link from the T-shaped element, at point M_2 , which in this analysis is assumed equal to M_1 . The second force is exerted by the guiding slot on the pin at the top of the connecting link and it is applied in M_2 . Since the surface of the guiding slot rubs against the pin, a friction force is created there. The pin cannot move relative to the connecting link along the axis on which these forces are exerted. Hence it is assumed that the pin is fixed the connecting link and that both forces are acting directly on the connecting link. The fourth force is applied to the connecting link by the spring in the HDF, at point M_3 . The fifth force is the reaction force of the HDF frame on the connecting link

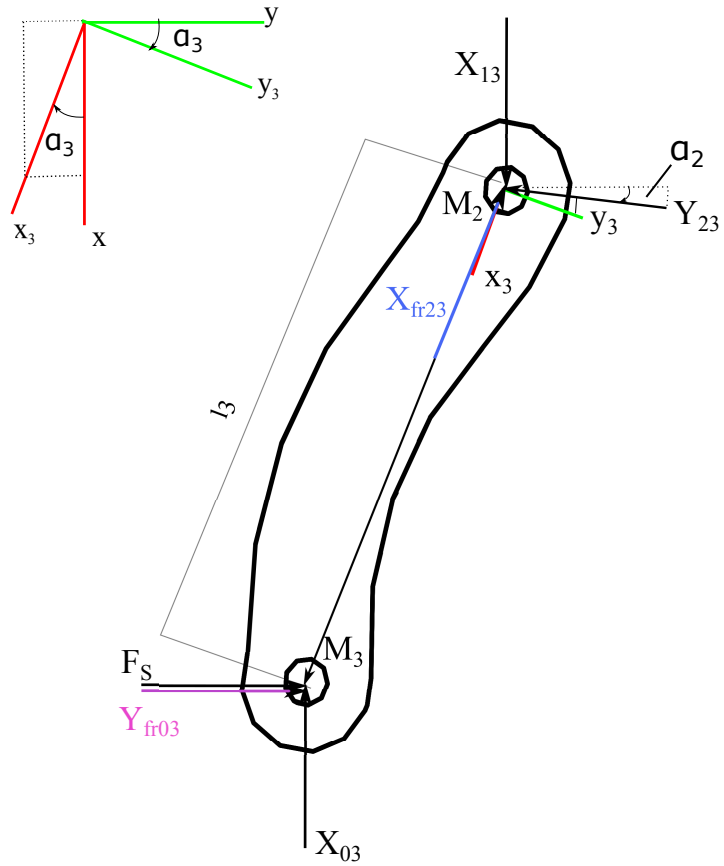


Figure 4.25: The forces acting on the connecting link

at point M_3 . The sixth force is due to the friction caused by the movement against the HDF frame. Both the sixth and the seventh force are acting on the pin and not on the connecting link. However, since the pin cannot move relative to the connecting link along the axis of these forces' direction, also in this instance it is considered that the forces are exerted directly on the connecting link. Forces have the name of the axis that corresponds to their direction, the forces' first subscript refers to the component which is exerting the force and the second subscript refers to the component on which the force is exerted upon. These forces and the resulting torques will be expressed as wrenches. The subscript of the wrench identifies the point from which the torque is measured. After the forces and torques are described, the equilibrium of forces along the X and Y axis of the global coordinate system is detailed along with the equilibrium of the torques acting on the connecting link.

As mentioned in the previous section, there is also a friction force caused by the movement of the T-shaped element relative to the connecting link. Its magnitude is considerably smaller than the aforementioned friction forces since in those the areas of contact are four for each force: each pin is in contact with each slot in two points (right and left) and each pin comes in contact with two slots, at different heights. This is because there are two guiding link elements in each side of the HDF and two spring guides in the HDF, as shown in Figure 4.5.

Six forces are be applied to the connecting link :

- The force applied by the T-shaped element, $\overrightarrow{X_{1 \rightarrow 3}}$ is applied to point M_2 and its direction is along the X axis of the global coordinate system: $\left\{ \begin{array}{c} \overrightarrow{X_{1 \rightarrow 3}} \cdot \vec{e}_x \\ \vec{0} \end{array} \right\}_{M_2}$
- The force exerted by the guiding slot on the connecting link is $\overrightarrow{Y_{2 \rightarrow 3}}$. This force's direction is the same as the Y axis of the guiding slot local coordinate frame and is applied to M_2 : $\left\{ \begin{array}{c} -\overrightarrow{Y_{2 \rightarrow 3}} \cdot \vec{e}_{y_2} \\ \vec{0} \end{array} \right\}_{M_2}$
- The friction force exerted by the guiding slot on the connecting link is $\overrightarrow{X_{fr2 \rightarrow 3}}$. This force's direction is the same as the X axis of the connecting link local coordinate frame and is applied to M_2 : $\left\{ \begin{array}{c} -\overrightarrow{X_{fr2 \rightarrow 3}} \cdot \vec{e}_{x_3} \\ \vec{0} \end{array} \right\}_{M_2}$
- The force due to the spring, $\overrightarrow{F_{s \rightarrow 3}}$, possesses the same direction as the Y axis of the global coordinate system and is applied to M_3 , point at which also the reaction force of the HDF frame, $\overrightarrow{X_{0 \rightarrow 3}}$, is applied. $\overrightarrow{X_{0 \rightarrow 3}}$ has the same direction as the global coordinate system. At M_3 a third force is applied, the friction force $\overrightarrow{Y_{fr0 \rightarrow 3}}$. The three forces are expressed in the same wrench: $\left\{ \begin{array}{c} (\overrightarrow{F_{s \rightarrow 3}} + \overrightarrow{Y_{fr0 \rightarrow 3}}) \cdot \vec{e}_y - \overrightarrow{X_{0 \rightarrow 3}} \cdot \vec{e}_x \\ \vec{0} \end{array} \right\}_{M_3}$

In order to obtain the static equilibrium, the wrenches have to be expressed at the same point; M_2 is chosen as reference point. The wrenches are then expressed relative to the global coordinate system:

$$\left\{ \begin{array}{c} \overrightarrow{Y_{2 \rightarrow 3}} \cdot \vec{e}_{y_2} \\ \vec{0} \end{array} \right\}_{M_2} \equiv \left\{ \begin{array}{c} -\overrightarrow{Y_{2 \rightarrow 3}} \cdot (\sin \alpha_2 \cdot \vec{e}_x + \cos \alpha_2 \cdot \vec{e}_y) \\ \vec{0} \end{array} \right\}_{M_2}$$

$$\left\{ \begin{array}{c} -\overrightarrow{X_{fr2 \rightarrow 3}} \cdot \vec{e}_{x_3} \\ \vec{0} \end{array} \right\}_{M_2} \equiv \left\{ \begin{array}{c} -\overrightarrow{X_{fr2 \rightarrow 3}} \cdot (\cos \alpha_3 \cdot \vec{e}_x + \sin \alpha_3 \cdot \vec{e}_y) \\ \vec{0} \end{array} \right\}_{M_2}$$

The forces $\overrightarrow{X_{1 \rightarrow 3}}$, $\overrightarrow{Y_{fr1 \rightarrow 3}}$, $\overrightarrow{Y_{2 \rightarrow 3}}$ and $\overrightarrow{X_{fr2 \rightarrow 3}}$ are already expressed relatively to the point M_2 , so they do not create any torques. However, force $\overrightarrow{F_{s \rightarrow 3}}$, $\overrightarrow{Y_{fr0 \rightarrow 3}}$ and $\overrightarrow{X_{0 \rightarrow 3}}$ create torques:

$$\left\{ \begin{array}{c} (\overrightarrow{F_{s \rightarrow 3}} + \overrightarrow{Y_{fr0 \rightarrow 3}}) \cdot \vec{e}_y - \overrightarrow{X_{0 \rightarrow 3}} \cdot \vec{e}_x \\ (l_3 \cdot \cos \alpha_3 \times (\overrightarrow{F_{s \rightarrow 3}} + \overrightarrow{Y_{fr0 \rightarrow 3}}) - l_3 \cdot \sin \alpha_3 \times \overrightarrow{X_{0 \rightarrow 3}}) \cdot \vec{e}_z \end{array} \right\}_{M_2}$$

The principle of static equilibrium gives three equations:

$$\begin{cases} \overrightarrow{X_{1 \rightarrow 3}} - \overrightarrow{Y_{2 \rightarrow 3}} \cdot \sin \alpha_2 - \overrightarrow{X_{fr2 \rightarrow 3}} \cdot \cos \alpha_3 - \overrightarrow{X_{0 \rightarrow 3}} = 0 \\ -\overrightarrow{Y_{2 \rightarrow 3}} \cdot \cos \alpha_2 + \overrightarrow{X_{fr2 \rightarrow 3}} \cdot \sin \alpha_3 + \overrightarrow{F_{s \rightarrow 3}} + \overrightarrow{Y_{fr0 \rightarrow 3}} = 0 \\ l_3 \cdot \cos \alpha_3 \cdot (\overrightarrow{F_{s \rightarrow 3}} + \overrightarrow{Y_{fr0 \rightarrow 3}}) - l_3 \cdot \sin \alpha_3 \cdot \overrightarrow{X_{0 \rightarrow 3}} = 0 \end{cases} \quad (4.18)$$

Following Coulomb's law, friction forces can also be expressed as the product of the static friction coefficient and the force normal to the friction force. Utilising Coulomb's Law, the Eqn. 4.18 and the calculations detailed in Section B.3 (they have been located in Appendix B for brevity) the final expression for the threshold torque is found:

$$\begin{aligned} \overrightarrow{T_{th}} = & -(y_2 + x_2 \cdot \tan \alpha_2) \cdot k \cdot s_0 \cdot \\ & \frac{\cos \left(\arcsin \left(\frac{y_2 - y_3 + x_2 \cdot \tan \alpha_2}{l_3} \right) \right) \cdot (\cos \alpha_2 - \mu_{ss} \cdot \sin \alpha_2) + \sin \left(\arcsin \left(\frac{y_2 - y_3 + x_2 \cdot \tan \alpha_2}{l_3} \right) \right) \cdot (\sin \alpha_2 + \mu_{ss} \cdot \cos \alpha_2)}{(\sin \left(\arcsin \left(\frac{y_2 - y_3 + x_2 \cdot \tan \alpha_2}{l_3} \right) \right)) - \mu_{sp} \cdot \cos \left(\arcsin \left(\frac{y_2 - y_3 + x_2 \cdot \tan \alpha_2}{l_3} \right) \right)} (\cos \alpha_2 - \mu_{ss} \cdot \sin \alpha_2) \\ & \cdot \cos \left(\arcsin \left(\frac{y_2 - y_3 + x_2 \cdot \tan \alpha_2}{l_3} \right) \right) \end{aligned} \quad (4.19)$$

From this equation, it is possible to link the values of α_2 , which is the angular displacement of the guiding slot, to the threshold torque. In case a specific threshold torque is required, it is possible to set it by varying the position of the linear actuator. As shown, Eqn. B.45, links the threshold torque to the value of angle α_2 . Since Eqn. B.17 links the value of the angle α_2 to the displacement of the linear actuator, then the link between the latter and the threshold torque is found. Eqn. B.17 is shown again below for clarity.

$$m_x = x_2 - x_4 + l_{2_2} \cdot \sin(\alpha_2 + \pi/6) + l_4 \cdot \sqrt{1 - \left(\frac{y_2 + l_{2_2} \cdot \cos(\alpha_2 + \pi/6)}{l_4} \right)^2} \quad (4.20)$$

The values of the angle α_2 are plotted in Figure 4.26 for increasing linear actuator displacement, m_x . As can be seen, the relationship is linear.

This plot is obtained in Matlab[®] by substituting all known values in Eqn. 4.20 and solving for α_2 . The value of α_2 relates the orientation of the guiding slot and the value of α_3 relates the orientation of the connecting link.

As can be seen in Figure 4.26, the value of the angle α_2 is positive for small displacements of the linear actuator. These values correspond to a low threshold torque in the HDF. For displacement of the linear actuator larger than 9mm the value of the angle α_2 is negative. This is because the orientation of the guiding slot varies the orientation of the connecting link so that the value of α_3 decreases. Small values of the equivalent of α_3 in Eqn. B.45 cause the value of the threshold torque to rise. This is confirmed by feeding the array of the obtained α_2 values in Eqn. B.45 in Matlab[®]. The result is the value of the threshold torque, which

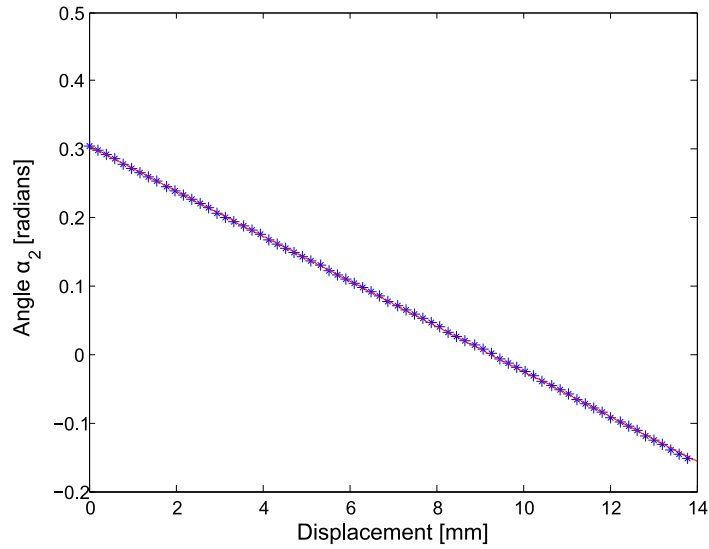


Figure 4.26: Angle α_2 plotted against m_x , which is the change in orientation of the guiding slot against the threshold torque adjustment

is plotted for increasing linear actuator displacement, m_x in Figure 4.27. In this case, the threshold torque is negative, since the external torque has been chosen as positive and the two need to have the same absolute value but opposite directions. In order to ease the comparison with the external torques shown in the experiments, the absolute value of the threshold torque is plotted.

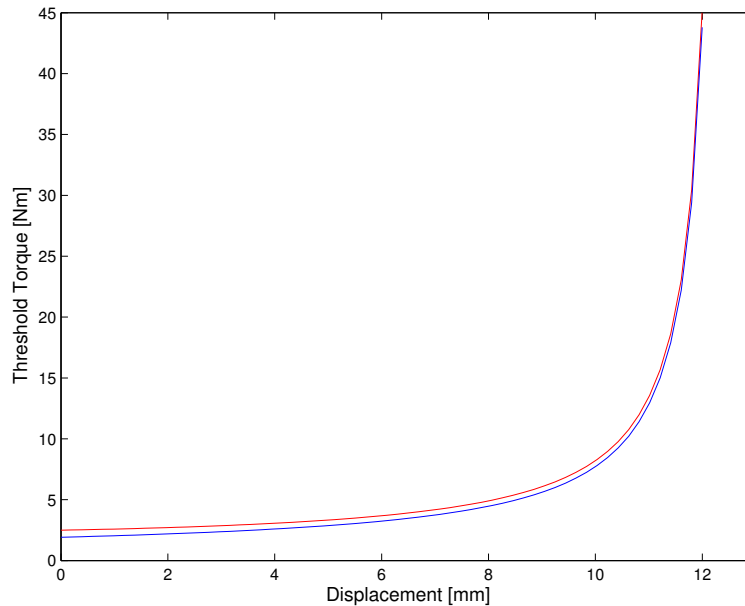


Figure 4.27: The curves are the values of the absolute of the threshold torque. The red curve was obtained by substituting in the threshold torque equation the friction coefficients for non-lubricated materials and the blue line was obtained by substituting friction coefficients for lubricated materials. For this example the value of the spring stiffness is chosen as 1.74 N/mm.

As can be seen in Figure 4.27, the values in the theoretical curve for the non-

lubricated materials (red) are higher than the values for the lubricated materials (blue), as it is expected since in the non-lubricated the friction forces are lower than in the lubricated case. The threshold torque equation increases exponentially with increasing linear actuator displacement. This is one of the two design aims which inspires the HDF. The other is the ability of HDF to achieve a passive variable compliance behaviour in case of an external collision caused by a force above a set threshold. Both the variability of the threshold torque and the passive variable compliance due to the similarity to the non-linear behaviour of the four bar mechanism theoretically discussed in this section are empirically tested in the set of experiments detailed below.

4.6 Experimental Analysis

In order to test the performance of the HDF design, the symmetry of its structure and the effect of springs of different stiffness in the system, a range of experiments has been conducted on the HDF to test its design and working mechanism.

4.6.1 Design-testing Experiments

The performance of both the passive variable compliance feature and the torque adjusting mechanism need to be tested in order to prove their effectiveness. In order to test the first, the decoupling of HDF has been tested with different external forces. In order to test the second, the decoupling action has been tried for increasing displacements of the adjustment arms in their slot. The impact this has on the value of the threshold torque is tested with experiments which also yield the experimental curve that describes the relationship between the adjustment arms displacement in their slot and the threshold torque. These two characteristics, the passive variable compliance feature and the torque adjusting mechanism can be easily tested in the same experiment: for every HDF configuration corresponding to a position of the adjustment arms in their slot, the HDF decoupling is tested with increasing external forces. In addition, another variable has been tested: spring stiffness. Three springs with different stiffness constants have been utilised in the trials to test their direct impact on the threshold torque (see Eqn. B.11). The spring stiffness values are: 0.78 N/mm, 1.34 N/mm and 1.74 N/mm. These values are quite low to avoid the danger of an elevated potential energy stored in the spring. The potential energy of the 1.74 N/mm spring for a compression of 20 mm, which is almost the maximum compression, is 0.348 joules. In order to give a practical example of such value, 0.348 joules is equivalent to the potential energy of 355 grams held 10 cm above the ground.

Experimental setup

The metal plate attached to HDF is detached from the revolute joint and fixed to the ground. In this way no other movement but the decoupling of the HDF is allowed, so that measurement errors can be reduced. On the opposite side, HDF is attached via the custom built fixture to the INTRO-BRL arm link and the external forces act on the end-effector of the link. Due to the physical nature of the structure, only the horizontal component of the external forces can activate the decoupling in the HDF. With reference to the coordinate system in Figure 4.10, the external force components that can actuate HDF lie on the $x-y$ plane. Every experiment has been repeated five times, to improve the statistical relevance of the results. The trials have been repeated for both sides of the HDF in order to accurately characterise the HDF structure. The two sides are symmetrical and should, in theory, behave in the same way but machining errors, less than perfect alignment or other factors may result in differences. Tests involving both sides of HDF can characterise these possible behavioural differences. These experiments are conducted in quasi-static conditions and the collisions are mimicked by pulling the end-effector of the INTRO-BRL arm link manually using a scale to gauge the torque value at which HDF decouples and goes from rigid to compliant (the threshold torque). The sensor used for the experiments is a Smart Sensor[®] electronic digital scale.

Results

All these experiments are conducted under the same conditions and are thus comparable. In order to obtain the threshold torque, the external force at which the HDF decouples is multiplied by 0.345m, the distance between the HDF pivot point and the end-effector of the first prototype of the INTRO-BRL arm link. The results for the right side of HDF for all the aforementioned springs are shown in Figure 4.28 and a statistical analysis has been conducted on the data².

The experimental curves that describe the relationship between the threshold torque necessary to decouple the HDF and the position of the adjustment arms on their slot the fit in Eqn. B.46, in Appendix B, which also contains the statistical analysis of the data. In order to avoid overfitting, a second order polynomial has been chosen as the fit for these data sets. As can be observed in Figure 4.28, this causes the fit to the experimental curve to assume higher values for no linear actuator displacement than for a displacement of 2mm. However, the rest of the experimental curve is fitted well by the second order polynomial, also shown by the fact that the R^2 for the fitting of the experimental curve is 0.966 for the 0.78 N/mm spring, 0.946 for the 1.34N/mm spring and 0.963 for the 1.74N/mm spring.

The fit equations are important to provide a description of the HDF behaviour. They can be used in the control algorithm to determine which threshold torque

²data gathered by Michelle Freret

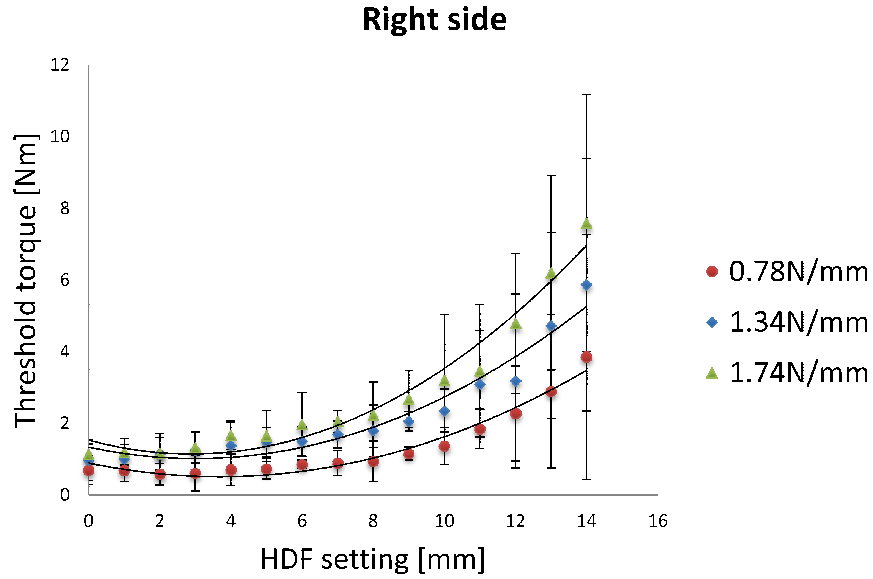


Figure 4.28: Experimental curves which describe the relationship between the displacement along the adjustment arms slots and the threshold torque needed for the HDF decoupling of the right side of the HDF, for spring stiffnesses of 0.78 N/mm, 1.34N/mm and 1.74N/mm. The HDF setting is equal to $m \cdot x$, a displacement produced by the linear motor actuation. Hence is the measure of how much the adjustment arm has been displaced in the bottom slot

corresponds to which linear actuator position and thus to set the HDF for the desired behaviour.

The results for the left side of HDF are shown in Figure 4.29 and a statistical analysis has been conducted on the relative data.

The experimental curve which describes the relationship between the threshold torque necessary to decouple the HDF and the position of the adjustment arms on their slot is described in the second order equation Eqn. B.49, which is in Appendix B together with the statistical data analysis.

As shown in Figures 4.28 and 4.29, the threshold torque does increase with the displacement of the adjustment arms in the slots, which means that the threshold torque is proportional to the angle γ , as predicted by Eqn. B.11. The difference between the two maximum torques with a 0.78N/mm spring is 9.63% and 6.73% with a 1.34N/mm stiffness spring. This shows that the two sides of HDF behave similarly and thus, the symmetry of HDF is acceptable. In the last set of experiments, performed with a 1.74 N/mm spring stiffness, the difference is 16.34%. The number is higher than for previous experiments but it can still be said that the behaviour of HDF is prevalently symmetrical.

Based on these results, the displacement of the adjustment arms in their slots does vary the activation threshold torque. Hence, the effectiveness of both the passive variable compliance feature and torque adjusting mechanism is shown, and it has been proven to be consistent throughout the whole set of experiments. It is evident looking at Figures 4.28 and 4.29 that the relationship between the threshold

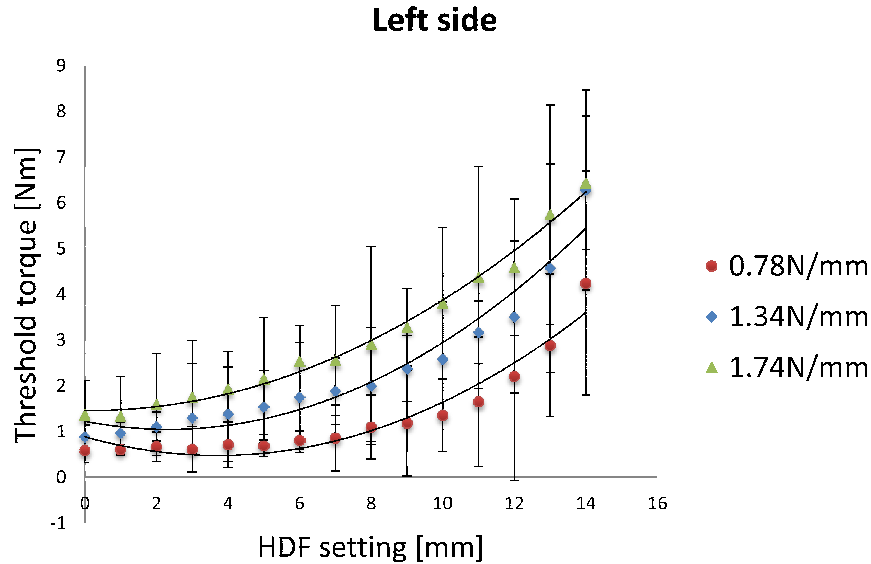


Figure 4.29: Experimental curve which describes the relationship between the displacement along the adjustment arms slots and the threshold torque needed for the HDF decoupling of the left side of HDF, for spring stiffnesses of 0.78 N/mm, 1.34N/mm and 1.74N/mm. The HDF setting is equal to $m \cdot x$, a displacement produced by the linear motor actuation. Hence is the measure of how much the adjustment arm has been displaced in the bottom slot

torque and the displacement in the slots slowly increases for displacements up to 7mm and then rapidly increases for larger displacements. This behaviour is similar for both sides of HDF.

The standard deviation of the threshold torque values generally increases for increasing slot displacements in all experiments, showing that high values of threshold torques are more prone to fluctuation than low values. In general, this might be due to the method used for the experiments: manually using a scale to gauge the torque value. Also, the variability of results could be addressed by lubricating the HDF. For this reason further experiments that use two sensors rather than just the scale, with and without lubrication, have been conducted and are described in Section 4.6.2.

4.6.2 Characterisation experiments

The design-testing experiments described in the previous section showed that the HDF successfully achieves both passive variable compliance in case of impact and the adjusting of its torque. However, in order to obtain more accurate readings of the threshold torque, a load cell is used to accurately measure the impact forces and a potentiometer is utilised to detect that the decoupling has taken place. The potentiometer is attached to the point O_1 of the T-shaped element, shown in Figure 4.10. This point is fixed during normal operation time but it rotates once the HDF has been activated. Thus, when the potentiometer reading changes from its initial

value, it identifies the triggering of the HDF. Since both the potentiometer and load cell signals are acquired simultaneously, by identifying which torque values was being measured when the potentiometer reading changed from its initial value, the threshold torque is found. This helps characterising the structure and describing its behaviour. The force values obtained during the design-testing experiments have helped in choosing an appropriate load cell for the characterisation experiments.

Experimental setup

The setup of this experiment is similar to the design-testing experiment one. The metal plate attached to HDF is detached from the revolute joint and fixed to the ground. On the opposite side, HDF is attached via the custom built fixture to the INTRO-BRL arm link and the external forces act on the end-effector of the arm. Differently from the previous setup, a load cell is positioned between the HDF and the INTRO-BRL arm link and a circular potentiometer is fixed to the HDF pivot point. The potentiometer measures the angular displacement of the T-shaped element, once HDF is activated. The experimental setup is shown in Figure 4.30. Also in this case, the external force components that can actuate HDF lie on the $x-y$ plane in Figure 4.21. These experiments are conducted in quasi-static conditions, with collision velocities lower than 0.6m/s. The collisions are mimicked by pushing the end-effector of the INTRO-BRL arm link. The displacement is given as an angle since once the HDF is activated, its T-shaped element rotates around its pivot point, thus changing its orientation.

For this series of experiments, the 1.34N/mm stiffness spring is used, the potentiometer and the load cell are connected to a board with a PIC18 microcontroller which samples the sensors' output every 10milliseconds. The potentiometer is a 1kOhm rotary device by AB elektronik, Germany. The load cell is a model number 1022, 3kg load cell by Tedeo Huntleigh, Israel. The experiments are conducted for different displacements in the adjustment arms slot, in mm, which cause the torque threshold to vary. The impact force has been exerted by pulling laterally on the end-effector of the INTRO-BRL arm, shown in Figure 4.30. The experiments are repeated ten times for every position of the linear motor, in order to improve the statistical relevance of the results, then the average value between these trials and the standard deviation are plotted in the next section. Both the left and the right side of the HDF are tested to investigate further its symmetry. In addition, the whole experiment has been repeated with the addition of lubricant to the HDF, to test whether friction is an important factor in determining the value of the threshold torque.

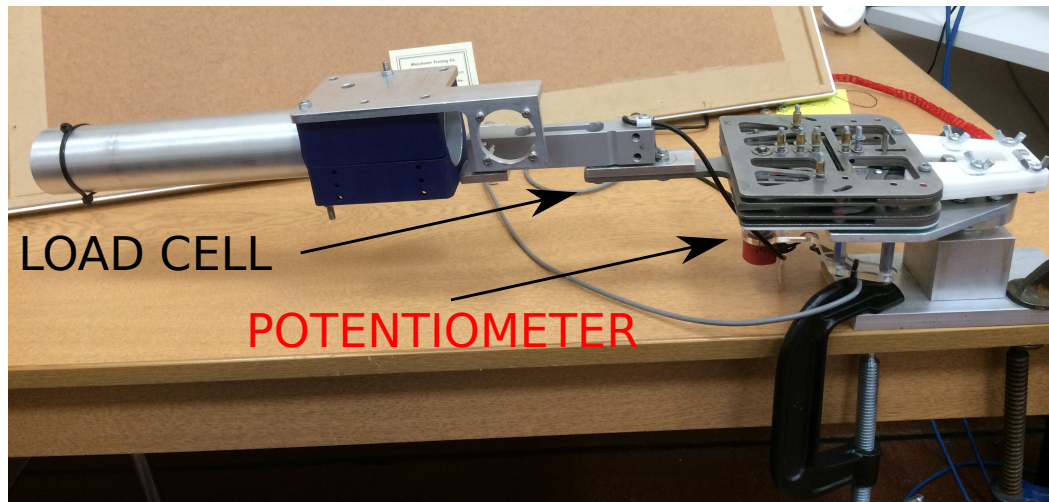


Figure 4.30: From the left: the cylindrical aluminium link, which is inserted into the 3-D printed blue fixture that is, in turn, fixed to the load cell, identified in the figure with an arrow. The load cell is fixed to the T-shaped element of the HDF (on the right side of the figure) by screws. The red potentiometer, identified by the arrow, is fixed to the pivot point of the T-shaped element of the HDF. At the far right of the figure it is possible to see the cylindrical stand where the HDF is fixed. The stand is then clamped to the table in order to avoid any possible movement of the HDF frame during testing.

Results

First, the collision force exerted on the INTRO-BRL arm end-effector as gauged by the load cell is plotted together with the output of the potentiometer. The aim is to show how they vary in case of a collision force high enough to activate the HDF.

As can be seen from Figure 4.31, the angle of the HDF (and thus its orientation) does not change for collision forces below 11N. However, at 11N, the angle does change, meaning that the threshold torque has been reached. Thus, the HDF is engaged and the safety system is in action. In this experiment the collision force is slowly increased and only when it reaches the 11N threshold (it takes 1.2 sec) the triggering action starts. It is also important to point out that once the safety system has been triggered, it does not matter if the collision force is decreased or not: the decoupling between the motor and the link has already taken place. Therefore, the arm link is either rigid or completely compliant, following a collision with impact force high enough to generate a torque equal or higher than the threshold torque. The value of the threshold torque is obtained by multiplying the distance between the HDF pivot point and the collision point (0.525m) by the collision force which activates the HDF.

The following graph shows the values of the threshold torque for the right side of the HDF. In this experiment the HDF is utilised without lubricant.

As can be seen in the Figure 4.32, the values for the right and left side are quite similar, the average percentage difference between the two set of values is 11.5%.

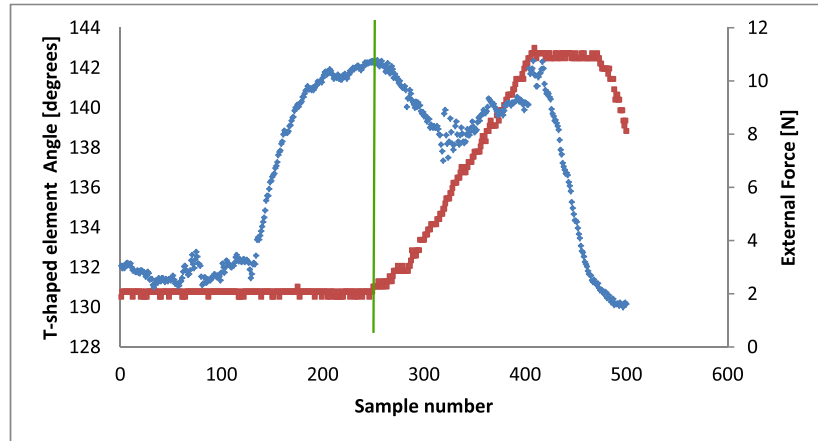


Figure 4.31: The external collision force (blue) is applied to the HDF and the resulting angles of displacement (red) of the HDF are plotted versus the sample number: samples are taken every 10ms. The green line shows the moment in which the external force has exceeded 10ms. Simultaneously, the angle of displacement of the T-shaped element goes from its resting value to a higher value. This entails the T-shaped element has rotated, which happens when the HDF is engaged and the entire structure is in compliant mode

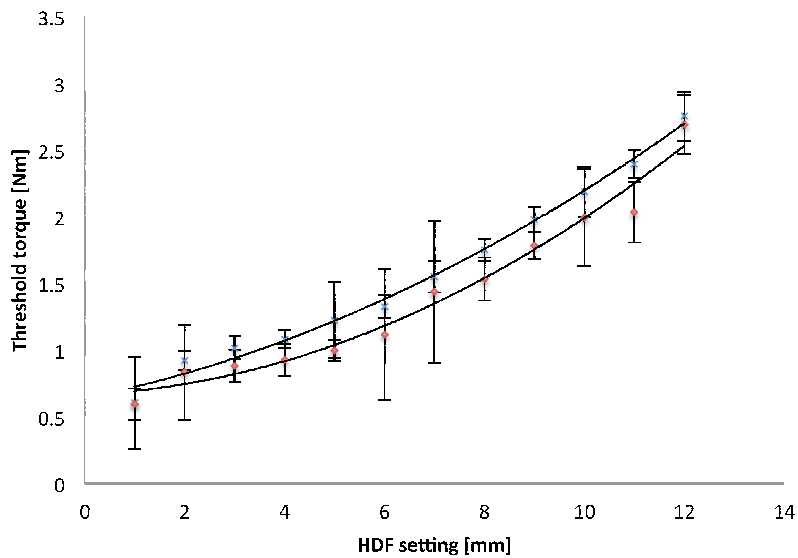


Figure 4.32: The threshold torque is plotted against the linear displacement in the adjustment arm slot in order to characterise the threshold torque variation for various positions of the torque adjusting mechanism, the blue crosses are for the right side of the HDF, the red diamonds are for the left side of the HDF. The HDF setting is equal to $m \cdot x$, a displacement produced by the linear motor actuation. Hence is the measure of how much the adjustment arm has been displaced in the bottom slot

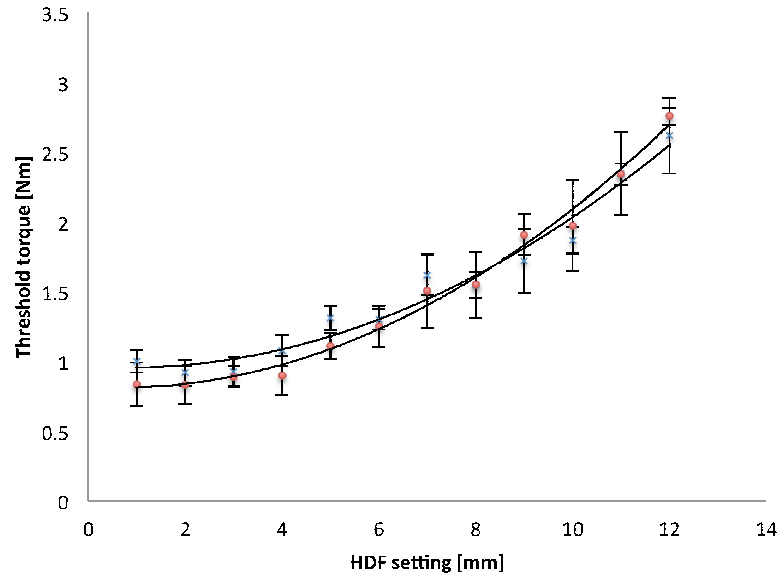


Figure 4.33: The threshold torque is plotted against the linear displacement in the adjustment arm slot. The blue crosses are for the right side of the HDF, the red diamonds are for the left side of the HDF.

The whole experiment explained above has been replicated with the addition of lubricant to the HDF. The following graph shows the values of the threshold torque for the right side of the HDF.

The two set of values shown in Figure 4.33, relative to the threshold torques for the right and left side of HDF, display an average percentage difference of 8.27%. This low value entails that the behaviour of the HDF is quite similar on the two sides. A comparison is also drawn between the threshold torque values on the right side with and without lubricant, the average percentage difference in this case is 10%. The comparison between the threshold torque values on the left side shows an average percentage difference of 7.5%. These figures show that the value of the threshold torque does not vary in a considerable manner based on the presence of the lubricant.

As can be seen in Appendix B, Section B.6, the standard deviation in these experiments is lower than in the experiments in Section B.4 and it does not reach the peaks it reached without lubricant. The average standard deviation for the left side of HDF without the lubricant is 0.25 and with the lubricant is 0.15. Hence, the best way to reduce the standard deviation and thus ensure repeatable results is to lubricate the structure.

The results shown in the figures above all show that the design idea proposed in this thesis was successful: the collision force which is required to trigger the safety system can be varied simply by displacing the adjustment arm positions in their slots.

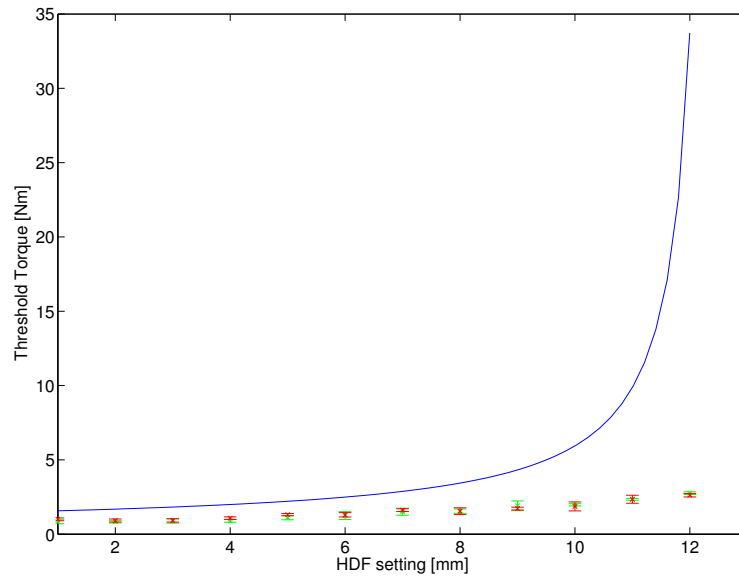


Figure 4.34: Relationship between the threshold torque value and the displacement of the slider mechanism that adjusts the position of the lever arm. The theoretical value of the threshold torque (in blue) in the lubricated scenario is plotted together with the experimental values of the threshold torque values of the right hand side of the HDF (in red) and of the left hand side of the HDF (in green). In the experiments lubricant was added to the structure.

4.7 Comparison between Modelled Variables and Experimental Values

The theoretical relationship between this displacement and the trigger threshold torque is described by an exponential equation, while the one tested in the experiments is better fitted by a second degree polynomial. The latter can be seen in both the data collected in the design-testing and characterisation experiments. The same spring stiffness that has been utilised in the characterisation experiments, 1.34N/mm has been substituted to the Matlab[®] model introduced in Section 4.5.2. This has been done in order to compare the modelled threshold torque curve with the experimental value of the threshold torque given by the characterisation experiments for the right and left sides of the HDF. In Figure 4.34 the model with the lubricated friction coefficients and the characterisation experiments with lubricant are shown, while Figure 4.35 shows the the model with non-lubricated friction coefficients and the experimental values of a non-lubricated HDF.

Comparing the two curves in Figure 4.35 and Figure 4.34, it is clear that the values of the threshold torque in the theoretical model are higher. It is important to remember that a few assumptions have been made in the model for the sake of simplification and those could account for the difference in values. It is also possible that the difference in value is due to an overestimation of the friction forces in the

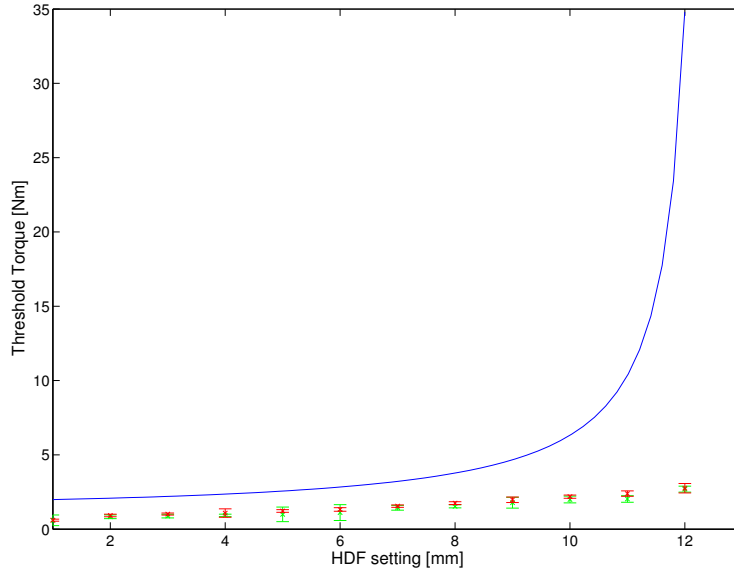


Figure 4.35: The theoretical value of the threshold torque (in blue) in the non-lubricated scenario is plotted together with the experimental values of the threshold torque values of the right hand side of the HDF (in red) and of the left hand side of the HDF (in green). In these experiments no lubricant was utilised.

model. In truth, in the model the friction forces have been considered fully and it has not been taken into account that the areas of contact are quite small. The one considered in the model is the the worst case scenario, the real friction forces are possibly smaller than modelled. In addition, errors in the measuring occurred during the experimental process could influence the accuracy of the experimental values. This might prove to be one of the reasons between the discrepancy between the theoretical and experimental curve in Figures 4.35 and 4.34. Another reason for the difference between the two curves might be the fact that only one HDF has been machined and produced. Hence, machining errors or inaccuracy in the one HDF produced would be quite relevant for the comparison between theoretical and experimental values. In case more than one HDF were produced and tested, the error might decrease.

4.8 Summary

In the introductory section of this chapter, a summary of the positive and negative aspects of the safety-driven designs described in Chapter 2 is given. These considerations play a major role in defining the structure of the novel safety feature introduced in this thesis' work. This device is called HDF: a hybrid variable compliance solution. The HDF's origins and novel features are explained in detail together with its working mechanism. The assembling of the HDF is then described in order to better explain its components and their interaction. Important mechanical parts

of the HDF are then described in detail and a model of the forces and moments present in the HDF is presented. This analysis is useful to both characterise and fully understand the system. In Section B.4, experiments have been conducted to test both the passive variable compliance feature and the threshold torque adjustment mechanism. The trials confirmed that both features work; furthermore, three different stiffness springs have been used in the experiments and it is confirmed that the threshold torque is proportional to the spring stiffness. Additional experiments have characterised the HDF behaviour with and without lubricant. The results show that lubricant can be influential in reducing the threshold torque variability. In both the HDF mathematical model and in the experimental results the threshold torque increases as the displacement of the linear actuator increases.

Thus, the experiments have successfully demonstrated that the threshold torque can be increased actively while preserving the passive variable compliance feature. This allows for better flexibility of usage of the HDF, which can be employed in scenarios where humans are in close proximity. An example of the first case is when the robot is handing an object to a user, who could be a disabled or elderly person. An example of the second scenario is a robot which picks up a drink from a staffed counter.

Notwithstanding the importance of flexibility, inherent safety has been given the priority in the design of the HDF. The characterisation tests on the HDF show that its maximum threshold torques are around 3Nm. In considering this figure, it must be kept in mind that these torques are measured in experiments where the arm is pushed at the end-effector. In this position the effect of the collision force is maximised by the full length of the arm link. In case the same collision force were to impact the arm closer to its joint, a smaller torque would be produced. Thus, the HDF would not be triggered, providing no robot arm compliance. In order to avoid possible risks of harm resulting from collisions along the whole arm link length, the HDF threshold torque range has been kept purposely low. In addition, the experiments conducted on the HDF showed that this system behaves rigidly until a force which can produce an external torque above the threshold torque is exerted on the INTRO-BRL arm link. This fact ensures that inherent variable compliance is maintained while flexibility has been added to the structure.

Furthermore, the fact that the system behaves rigidly until a high force impact is received, allows the use of springs of low stiffness in the HDF. In case the system did not have non-linearity provided by the adapted four bar mechanism, springs would be engaged in any part of the robot arm behaviour. This would call for springs with a high enough stiffness to provide an acceptable accuracy in the arm. This high stiffness of these springs might prove problematic for human-robot interaction. This is because stiff springs can store higher quantities of potential energy and thus are more prone to be a potential risk.

Variable compliance is used in the HDF structure to provide a passive safety feature for the INTRO-BRL arm. In addition, variable compliance is also the starting point of the research for a grasping device which is able to adapt to an unknown object shape. The process of building multiple prototypes and trying them out in order to find the best design for the grasping device is described in the next chapter.

Chapter 5

Hydrostatic Skeleton Gripper

Autonomous grasping is an important and challenging task and has therefore been intensively addressed by the robotics community, as discussed at length in Chapter 2. One of the most important issues in this field is the ability of the grasping device to accommodate varying object shapes in order to form a stable, multi-point grasp. Particularly in the human environment, where robots are faced with a vast set of objects varying in shape and size, a versatile grasping device is highly desirable. Solutions to this problem have often involved discrete structures that typically comprise compliant sections interconnected with mechanically rigid parts.

As stated in the Introduction, one of the aims of this work is to exploit variable compliance to produce a robot arm with a gripper that can adaptively mould its shape to objects. Hence, autonomous grasping of objects with diverse cross-sections would be achieved without previous knowledge of their shape or their exact position. In this case, completely soft and highly redundant structures possess an advantage over rigid structures with a limited number of degrees of freedom. Soft structures in particular can adapt to unknown shapes quite easily due to the adaptability of their compliant structure. Compliance permits the gripper to conform its surfaces to those of the object without needing explicit control and sensing, a process called 'shape match' in research [Deimel and Brock, 2013], [Eppner et al., 2012]. Hence, a novel soft gripper design is chosen to achieve autonomous grasping for pick and place tasks. In particular, the device is a soft, cable-driven gripper, featuring no stiff sections, made of low-cost materials. The gripper is inspired by invertebrates with hydrostatic skeletons, fluid filled cavities surrounded by muscle that, by contracting, can vary the structure's stiffness [Taylor and Kier, 2003]. The inspiration by hydrostatic skeletons gives the name to the gripper: HS gripper. The gripper's soft structure provides adaptability and versatility, which are demonstrated in several experiments in this chapter.

Similarly to other soft grasping structures described in Chapter 2, this gripper's compliance ensures an autonomous but also stable grasp. Compliance is important not only to facilitate autonomy but also to achieve a stable grasp. Specifically, a

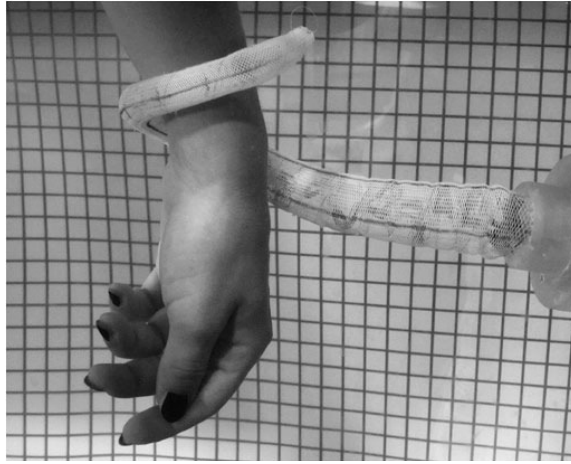


Figure 5.1: Robot octopus arm of the Scuola Superiore Sant'Anna. Figure from [Laschi et al., 2012], used with permission of Taylor & Francis.

compliant grasp permits a robotic end-effector to adaptively conform to the shape of the object, increasing the number of contact points, which is a necessary requirement for stability [Bicchi and Kumar, 2000]. For this reason, initial end-effector compliance when forming the grasp is desirable. However, once the stable grasp is established, an end-effector must be stiff enough to apply sufficient force on the object surface to make holding and lifting the object possible. Hence, the very low initial stiffness of the HS gripper must be increased to a level which allows force transmission to other objects. Thus, in the final phase of grasping, the gripper needs to be stiffer than it is in its completely compliant initial stage. Differently from other continuum variable compliance grasping devices, in the HS gripper the grasping action and the change in compliance are achieved simultaneously and using one motor. This is achieved exploiting the design and materials, choice inspired by the embodied intelligence principle described in Chapter 2. In order to contextualise and further describe the novelty of the grasping device described in this thesis, a comparison with the devices in literature, fully described in Chapter 2, is given in the next section.

5.1 Comparison with the State of the Art

The result of the literature review on grasping devices carried out in Chapter 2 has shown that a soft structure and variable compliance are both promising characteristics to aid grasping of objects of unknown shape, as it happens in unstructured environments.

Regarding the soft structure, a very good example of a soft robot is the robot octopus arm of the Scuola Superiore Sant'Anna (SSSA) [Calisti et al., 2010], shown in Figure 5.1. Some elements of the SSSA arm, for example its cable structure, are important for the implementation of the gripper described in this thesis. However,



Figure 5.2: One of the possible configurations of the STIFF-FLOP manipulator. Figure from [Maghooa et al., 2015], ©2015 IEEE

the intended application of the SSSA arm is different to the the application of the HS gripper. The SSSA's robotic arm is part of a biomimetic effort to reproduce the structure and function of an *Octopus vulgaris* arm in an aqueous environment. On the contrary, the HS this gripper's purpose is to aptively grasp everyday objects in the context of a human-robot interaction. Such difference in aims is reflected in the structure of the two devices. In the HS gripper's design only the hydrostatic skeletons' characteristics which are conducive to an adapting grasp are reproduced. Drawing inspiration by *Octopus vulgaris* for an application other than biomimetic is successfully achieved by the STIFF-FLOP manipulator, shown in Figure 5.2, which can change simultaneously its length and stiffness. Bioinspiration makes possible the manipulator's antagonistic actuation system that is able to achieve variable compliance [Maghooa et al., 2015].

Regarding variable compliance, its importance for grasping is one of the main conclusions of Chapter 2 and it is further explained in the beginning of this chapter. Looking at the state of the art, grasping devices can be divided in two main groups. In the first, anthropomorphic structures, [ShadowRobotCompany, 2013], [Grebstein et al., 2011], [Dollar and Howe, 2010], possess either rigid or semi-rigid 'phalanges', hence they have the necessary rigidity to hold objects in a stable manner. However, this very structure hinders full shape matching to the object. In the second category, [Ilievski et al., 2011], [Deimel and Brock, 2013], omni-directional compliance is exploited to mould to shapes but these devices lack the necessary rigidity to hold the object in a stable manner. This is solved by introducing variable compliance, as it is done, for example, in the universal gripper at University of Chicago [Brown et al., 2010]. However, this gripper needs to push the objects onto

the surface they lay on in order to grasp them. This makes it impossible for the universal gripper to grasp very compliant objects, which would be flattened instead of grasped. Furthermore, the universal gripper needs an external signal to vary its compliance, for the final stage of the grasping action. The variable compliance is achieved actively and thus requires dedicated control. These and other considerations, which come from preliminary experiments conducted on grasping devices inspired by the universal gripper working mechanism, shaped the requirements for the HS gripper. Before choosing this structure, many designs have been considered and two have been built in order to provide experimental proof of concept. Both designs, one of which is the HS gripper first prototype, are detailed in the next section.

5.2 Initial Work

Before the HS gripper was designed, two prototypes of adaptable gripper were designed, built and tested by the thesis' author. The hypothesis that was being tested with these grippers is whether a gripper that uses the same working principle as the universal gripper but a different design can effectively grasp objects from the side, which the universal gripper cannot do. In both cases, the complete system comprises i) the artefact itself, ii) the Minivac[®] vacuum pump with gauge, which delivers a low volume vacuum and, iii) silicone tubes that connect the pump to the filter of the artefact. During the initial soft interaction, the compliant part of the gripper deforms to accommodate the object. Once the object is fully encircled by the gripper, a vacuum is applied to create a hard surface that firmly grips the object. The rigidity of the interaction is highly desirable because it ensures both a firm grip and sufficient forces to hold the object. This behaviour is clearly inspired by the



Figure 5.3: BRL reproduction of the University of Chicago universal robotic gripper built to test its functionality. This device is a good example of multidirectional compliance. Due to the lack of fixed shape in its flaccid state, there are no mechanical constraints which hinder its adaptation to an external object [Brown et al., 2010]

working mechanism of material jamming present in University of Chicago universal gripper. A reproduction of the University of Chicago gripper, shown in Figure 5.3, has been built in the Bristol Robotics Laboratory (BRL) to test its functioning.

5.2.1 Design

The first artefact takes inspiration from the fact that, notwithstanding the ingenious use of variable compliance, the University of Chicago gripper is not able to grasp certain very pliable objects, for example a napkin on a table. This is because the very weight of the gripper that is being pushed against the soft objects is enough to cause them to flatten onto the surface they lay on, rendering them impossible to grasp by the device. For this reason, two granular material filled pockets (ground coffee in both devices) are inserted in the internal part of the two hard rubber jaws of a traditional gripper. This allows gripping of a larger range of objects. The hard rubber jaws enable a rigid interaction between the object and the gripper so that even very pliable objects can be picked up and the pockets full of granular material ensure that the gripper deforms around the object in a malleable configuration. As soon as the object is grasped, suction is applied and the gripping of the object becomes reliable. The gripping of the object is secured in the position since the compliant part moulds around the object and, consequently, is fixed in that shape using suction. The gripper, shown in Figure 5.4, is made of two 220mm long shafts, at one extremity they are united together in a pivot point and at the other extremity two hard rubber jaws 90mm long are present. The Minivac[®] vacuum pump is also connected to the system and two silicone tubes attach the compliant pockets to the pump. Filters are necessary so that the ground coffee does not get sucked out of the pocket once the pump is activated. Each compliant pocket is produced by filling a 60mm x 40mm x 28mm rubber latex pocket with ground coffee.

The second artefact consists of a roughly conic balloon filled with ground coffee.

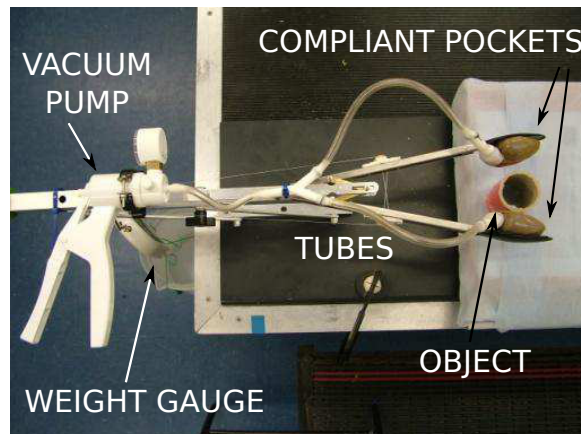


Figure 5.4: Top view of the system comprising the general gripper (made up by the vacuum pump, tubes and the compliant pockets), the object to be grasped and the weight gauge

The device grips the object by wrapping around it, as shown in Figure 5.5. This action is obtained by pulling the cable fixed on the external side of the artefact. Since the artefact is made of soft material, the gripped object does not get damaged during the interaction. Once the object is surrounded by the gripper, the pump is activated and the gripper changes its state from compliant to rigid. The tip of the cone is 17mm in diameter, the diameter of the proximal part is 40mm and the length of the whole artefact is 160mm. The balloon is custom made. A 0.3mm diameter Dyneema cable inside a platinum silicone tubing with a 0.5mm internal diameter (Silex, U.K.) is placed on the external surface of the balloon, on its ventral side. The ventral side is the side to come into contact with the object and which is shortened when the cable is pulled. Silicone paste is used to secure the silicone tubing on the ventral side of the balloon along its long axis. The silicone tubing is used so that silicone paste does not contact the cable directly impeding its sliding motion and also allows the coffee grains filled balloon to return into its initial extended position once the cables are released.

5.2.2 Qualitative Performance

Two simple experiments are performed, one with each prototype, to assert their functionality and the advantage of the variable compliance padding opposed to merely passive compliant padding.

The aim of the experiment is to prove the grasping capabilities of the novel artefact. The experiment is designed to show the greater firmness of grasp achievable with the application of suction in the compliant pockets. The two jaws move to grasp the object which makes contact with the compliant pockets. The vacuum pump is then activated and the pressure maintained at -33.86kPa, since at this pressure the compliant structure has become rigid. A 0.17kg weight is used in order to prove that the firmness of the grip is dependent on the vacuum that is imposed on the compliant pockets. The weight is attached to the object when the suction is still

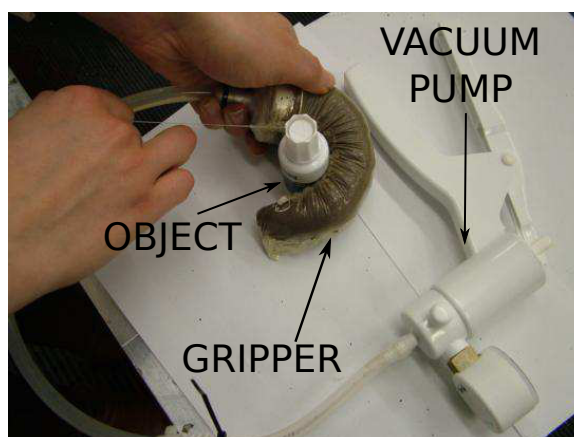


Figure 5.5: Top view of the multidirectionally compliant arm gripper and the vacuum system

activated but this additional weight does not cause the gripper to lose grip on the object; after one minute both the object and the weight are still firmly held by the gripper. As soon as the suction is released, though, the object and the weight drop instantly. This simple experiment proves that the suction caused by the vacuum pump is necessary to maintain a firm grip on the object.

A short experiment is also carried out with the second artefact. The experiment comprises two trials. In both the gripper is placed close to a 0.086kg roll of tape and, once the cable on the ventral side of the balloon are pulled, the gripper grasps the object. In the first trial the object is lifted immediately, in the second trial, instead, the vacuum system is activated first and the object is lifted afterwards. In the first trial the grasp of the object is not very stable. In the second trial, instead, the material inside the gripper is jammed and the grip on the object becomes firm and the artefact and the object are held in place quite stably. As soon as the vacuum is released, though, the object drops to the floor. This proves that it is the stiffness provided by the vacuum system that allows the gripper to sustain the object weight firmly. Conversely, a 0.029kg bottle is successfully grasped and held in place quite stably, probably because of its lower weight.

5.2.3 Results

Between the two prototypes, the second artefact is the most likely to adapt itself to an external object size, because of its multidirectional compliance. However, the total absence of consistently rigid parts makes this device technically challenging to produce reproducibly and control. These drawbacks are, though, more than counter balanced by its ability to adaptively mould to object shapes and by its novelty, which makes it worth pursuing for research purposes. For these reasons, it has been chosen to proceed to research a multidirectionally compliance device.

It is observed in all experiments that stiffening produces a shrinking effect in the radial direction, detrimental to the grasping stability of both devices. Objects are

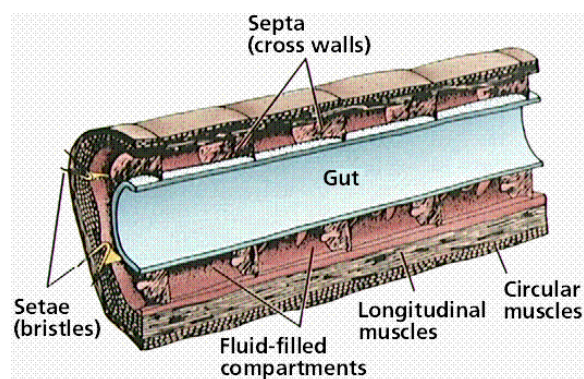


Figure 5.6: Sketch of the structure of a biological hydrostatic skeleton. Figure from Purves et al., *Life: The Science of Biology*, 4th Edition, by Sinauer Associates. Used with permission of Sinauer Associates.

still grasped in a stable manner but the contact with the gripper is loosened by the shrinking, showing that this working mechanism is not ideal for lateral grasping. Since the ability to grasp from the side is desirable in order to grasp a large set of objects, it is decided to change the working principle of the gripper. Material jamming is discarded in favour of a novel working mechanism. However, the multi-directional compliance is retained, in order to achieve multiple contact points and stable grasp. The new structure, the HS gripper, is a simplified version of a biological hydrostatic skeleton, shown in Figure 5.6, where muscles are substituted by motor-actuated cables and the structure is a thin flexible shell partially filled with water. The next sections explain in full detail the application domain, inspiration for the new working mechanism and the physical structure of the device.

5.3 Gripper Application Domain

The research goal of this thesis is to develop a device that can grasp and hold in a stable manner objects without tilting them, while mounted on the INTRO-BRL arm, described in Chapter 3. In general, in a dynamic environment errors could be made in the accurate localisation of objects in space. These errors could be caused by the unreliability of the sensor system or lack of multiple sensory information. For this reason, a greater gripper workspace could be useful to compensate for the positioning inaccuracy of the robot arm.

The HS gripper, shown in Figure 5.7, only addresses the grasping of certain forms (a height of at least 50mm is necessary) but these forms can display a great variability in their shape. However, in its present design, it cannot grasp a flat object like a plate. In order to achieve this, it would be necessary to replicate the design of this device and assemble them in a gripper with multiple ‘digits’. This new structure would be able to trap objects between digits and thus grasping a wider



Figure 5.7: HS gripper in its stiff, bent state, when force is applied to its two cables (both are visible in white on the left of the picture, while one is shown in black along the HS gripper body. The other cable is in the exact same position but on the flip side).

selection of objects compared to the current version of the HS gripper. This could be a future development for the HS gripper, but first it is necessary to test its ability to vary its compliance and to adaptively grasp different cross-section objects due to its passive characteristics. Once these features, that make the HS gripper unique, are confirmed by experimental testing, it would be possible to replicate its structure in a multiple-digit one able to grasp a wider range of object shapes. The variable compliance tests are reported in Section 5.6.2 and its adaptive grasp in Section 5.8.1. First of all, though, a description of the mechanical structure of the novel device and its bioinspiration are given in order to properly introduce the novel device. The inspiration for the gripper is detailed in the next Section, 5.4 and its design and mechanical structure in Section 5.5.

5.4 Bioinspired Working Mechanism

In this section, the engineering implementation of hydrostatic skeletons is analysed focussing on the working mechanism. In general, it is very important to stress that the aim of this work is to design a *bioinspired* device, which takes inspiration from hydrostatic skeletons to tackle a practical grasping issue, and does not have as a first objective to validate or disprove biological study hypothesis, as is the case in *biomimetic* robotics.

The HS gripper's quasi-longitudinal cables on one side provide the bending movement in a similar manner to the longitudinal muscles in hydrostatic skeletons. This device is inspired by the principle of the bending and stiffening movements of hydrostatic skeletons. The flexible material of the gripper's outer shell operates as the connective tissue, which passively controls the various dimensions of the hydrostatic skeleton [Kier, 2012].

Hydrostatic skeletons are filled with liquid, usually water, which has a high bulk modulus and hence resists significant volume changes. Contraction of muscle can decrease their relative dimensions; hence if either circular, radial or transverse muscles are contracted, the diameter will decrease, if longitudinal muscles are contracted, the length will decrease. This dimensional change causes an increase of the internal pressure, and since no significant change in volume of the structure can occur, the decrease in length in one direction must result in an increase in diameter, and vice versa [Kier, 2012]. The act of stiffening in constant volume structures like muscular hydrostats or more generally hydrostatic skeletons, occurs "if dimensional changes are resisted by either muscle activity or connective tissue" [Kier and Smith, 1985]. Kier and Smith propose that "a structure wrapped with connective tissue which prevents dimensional change will stiffen in response to muscle contraction". Hence, after muscle contraction causes shortening in one dimension, the connective tissue resists the dimensional increase in the perpendicular direction and stiffening

occurs. A similar resistance to dimensional change is observed in the HS gripper except that, instead of connective tissue, the gripper shell is made of a relatively high tensile strength material.

The working mechanism for stiffening in the HS gripper is the following: (i) pulling of the longitudinal cables decreases the gripper length. (ii) The shell material, initially loose because it is not fully filled with water, is put into tension, since no significant change in volume can occur and no dimensional increase in circumferential direction is possible. (iii) Hence the fluid pressure in the gripper rises, causing its stiffening. Experiments have been conducted on the gripper in order to test its change in compliance and are reported in Section 5.6.2.

Bending of the biological hydrostatic skeletons, which possess constant volume, can be produced by contraction of longitudinal muscles on one side of their body. Unilateral contraction will cause bending only if a constant diameter is maintained by applying a radial centripetal force, resisting the longitudinal compressional force, which tends to shorten the body. Without this resistance, there would be no bending but only shortening [Kier and Smith, 1985]. Similarly, in the gripper, the bending is initiated by the unilateral contraction of the longitudinal cables. However, in this case both bending and an element of shortening occur. The contraction of the gripper's longitudinal cables folds the shell's material and initially causes shortening of the gripper on one side while shifting the water to the opposite side. This increases the pressure of water on the internal walls of the gripper and the cross-section of the gripper goes from initially elliptical to circular. Any looseness of the wall disappears. Its high tensile strength opposes change of the gripper circumference and results in the bending of the gripper. This aspect of the HS gripper's behaviour has been empirically tested and analysed, the procedure is explained in Section 5.6.1.

It is important to observe that both the processes explained above, the stiffening and bending behaviours, are obtained simultaneously by simply pulling the quasi-longitudinal cables. In contrast to the University of Chicago universal gripper, which requires a dedicated actuation system to stiffen its body, in the case of the HS gripper, the stiffening is the result of the same motor actuation that provides its bending and encompassing of the object. Hence, one motor command is enough to perform two actions: bending and stiffening. Due to this behaviour, it is claimed that one of the two actions is achieved actively (bending) and the other (stiffening) is a consequence of the HS gripper materials and structure and thus is called a passive characteristic. The ability to obtain both bending and stiffening with one motor command simplifies control since no additional motor command needs to be issued to stiffen the structure. This is a unique characteristic of the HS gripper, which marks its novelty in comparison to other grippers in the literature. As mentioned, this unique behaviour is possible due to the specific material and structural characteristics of the device. After the bending and stiffening action, the syringe drive

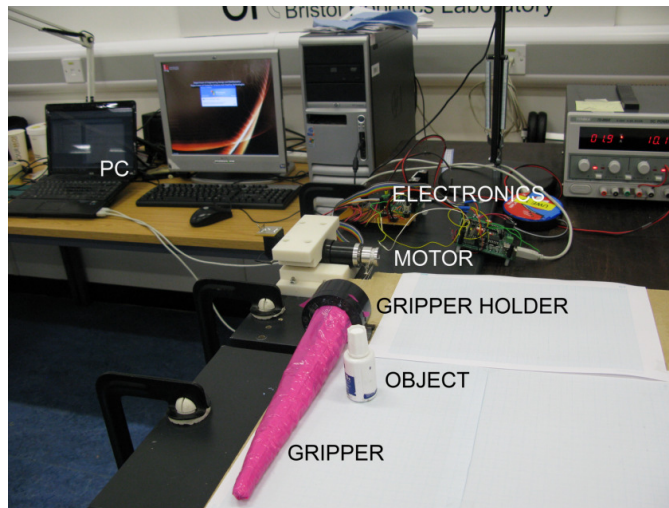


Figure 5.8: From the left: the laptop computer is connected to a dsPIC30F4011 micro- controller, which is also connected to an H-bridge driver circuit, connected to a power source, visible in the back (far right). The H-bridge is connected to a brushed DC motor (centre of the picture). The motor is held in place by a custom 3D printed structure (ivory colour) so that it does not move during the experiments. Two cables are tied to the spindle mounted on the motor shaft. These cables run along the whole length of the gripper and are fixed at the tip of the gripper itself. The base of the gripper is also fixed to the table: the gripper holder (in black in the picture) is screwed on the table. The rest of the gripper, instead, is free to move and in this case is pictured in its non-actuated, compliant state resting on the table. The object on the right of the gripper is within its workspace and can be easily grasped. Figure from [Giannaccini et al., 2014], used with permission of Springer.

shown in Figure 3.7 pushes the HS gripper back to its initial position. Material choices and their characteristics will be discussed in depth in the following section, which describes the hardware structure.

5.5 Hardware Implementation

As explained in Chapter 2, the implementation of hydrostatic skeletons has always posed a challenge for robotics. The solution proposed in this thesis' work is illustrated in this section, with the description of the hardware, shown in Figure 5.8. In Section 5.5.1 the design of the system and the materials used are explained and the experiments aimed at finding the optimum filling quantities are detailed. At the end of the same section, the practical mounting process of the HS gripper is discussed.

5.5.1 Materials, Control and Design

The gripper's design consists of a flexible outer shell, shown in Fig. 5.9, partially filled with incompressible liquid and actuated by a pair of cables. The next section covers the process of choosing the best materials for the gripper, then it describes the experiments needed to determine the optimal percentage of liquid required for

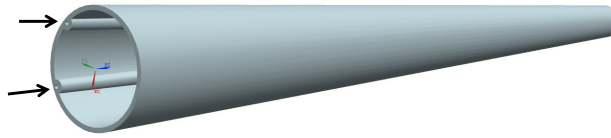


Figure 5.9: UGS NX6 software drawing of the outer empty shell with silicone tubes. The two tubes and the cables inside them are on one side of the gripper only. The two arrows point to the location of the cables. Figure from [Giannaccini et al., 2014], used with permission of Springer.

the filling and finally, it details the production process to build an HS gripper.

Materials

The outer shell, shown in Fig. 5.9, is of conical shape and made of a polyethylene foil, a flexible structure. This material has been chosen since it possesses both relatively high tensile strength and flexibility. The tensile strength ensures that the shell does not expand due the water pressure and flexibility is instrumental in allowing the creasing of the material once the longitudinal cables are pulled, shown in Figure 5.7. Furthermore, polyethylene is an inexpensive and commercially available material. On the other hand, its resistance to wear is not ideal and alternatives, like Dyneema cloth, have been considered but their flexibility is not sufficient to guarantee concertina-like creases to form. Further alternatives which have been tried are composite materials, one of which a nylon cloth embedded in silicone but the higher resistance to wear is not enough to justify the higher production complexity and longer time for a prototype stage. Polyethylene is a good compromise between cost, availability and performance. A corona treated ¹ polyethylene sheet is used to improve adhesion with silicone.

The system also consists of two 0.3mm diameter Dyneema[®] cables (Fireline, Berkley), located at a 0.0436rad angle from the longitudinal axis, as shown in Figure 5.10. Dyneema cable is chosen for its strength, light weight and low stretch.

Each cable is lodged inside a 1.5mm in diameter flexible silicone tube (Silex), chosen for its flexibility, which allows the forming of creases. PTFE tubing has also been tried to take advantage of its low friction surface but its reduced flexibility did not permit the desired creases to form. The silicone tube is attached to the shell with silicone paste (Soudal), which proves to be a very stable fixture due to the corona treatment on the polyethylene. Two configurations of the gripper's cable system

¹The name of this treatment comes from the corona discharge, an electrical discharge brought on by the ionisation of a fluid surrounding a conductor that is electrically energised. Once a high frequency electric discharge is directed toward a surface this causes the long chains of the polymeric surface to rupture. This produces shorter chains and more adhesion points. Hence, the surface energy of the polyethylene is increased improving adhesion to other materials [idspackaging.com, 2014].

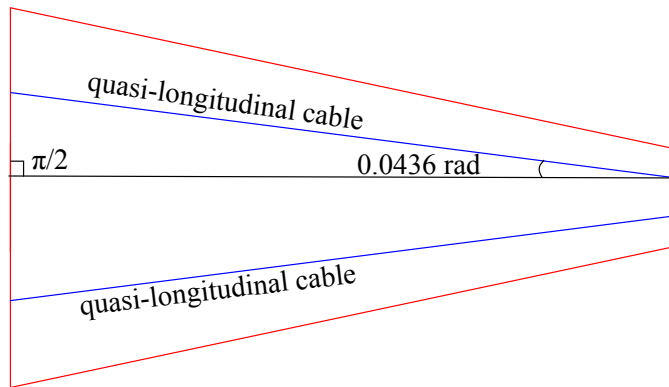


Figure 5.10: Drawing of the two quasi-longitudinal cables (almost-longitudinal, since they do not run parallel to the longitudinal axis, there is a 0.0436 angle between the two), which is running along the length of the gripper, (in blue) and the angle they form with the horizontal (in black). The red outline is the HS gripper's laid out shape. Figure from [Giannaccini et al., 2014], used with permission of Springer.

have been designed, exhibiting different grasping behaviours, which are analysed in detail in Section 5.5.2.

The gripper is 250mm long; with a maximum diameter (at the base) of 40mm and minimum diameter (at the tip) of 15mm. 88% of the internal volume of the gripper is filled with fluid, the process to determine this optimal filling percentage is described in Section 5.5.1. The compliant gripper needs to rapidly acquire stiffness to ensure grasp stability and lifting of the object. Hence a fast transition from a compliant to a rigid structure is needed. This is achieved by choosing an incompressible material for the filling. The lack of compressibility of the fluid ensures a fast tensioning of the gripper's shell due to the increase in the pressure the water exerts against the shell. In case the shell were filled with compressible material, for example with air, this material would decrease in volume before exerting resistance on the shell. Thus, the increase in stiffness would not be as fast as it is for an incompressible material. For this reason, the bulk modulus, a measure of resistance to compressibility, of fluids is considered.

At room temperature, glycerin has a quite high bulk modulus for a liquid: $4.35 \cdot 10^9 \text{Pa}$ and water's bulk modulus is $2.15 \cdot 10^9 \text{Pa}$. Sulfuric acid is highly corrosive, thus not usable for the gripper. Glycerin is safe to use around humans but its 12.4kN/m^3 specific weight is higher than water's specific weight of 9.81kN/m^3 and since excessive weight is an issue, especially since the gripper is the arm's end-effector, water is preferred over glycerin [Engineeringtoolbox, 2013].

Aeration has a significant effect on bulk modulus because air is much more compressible than water [Totten, 1999]. For this reason, water is degassed by boiling before being inserted in the gripper. In order to make experiments more reproducible, only deionised water is used for the HS gripper filling.

As far as the actuation and control system is concerned, the gripper is actuated by a brushed DC motor (Maxon-118797) driven by an H-bridge driver circuit (L298N)

controlled via a dsPIC30F4011 microcontroller (Microchip), the system is shown in Fig. 5.8. For the experiments reported here open-loop control is sufficient, thus no feedback on the position or orientation of the HS gripper is fed back to the control system in order to drive the motor.

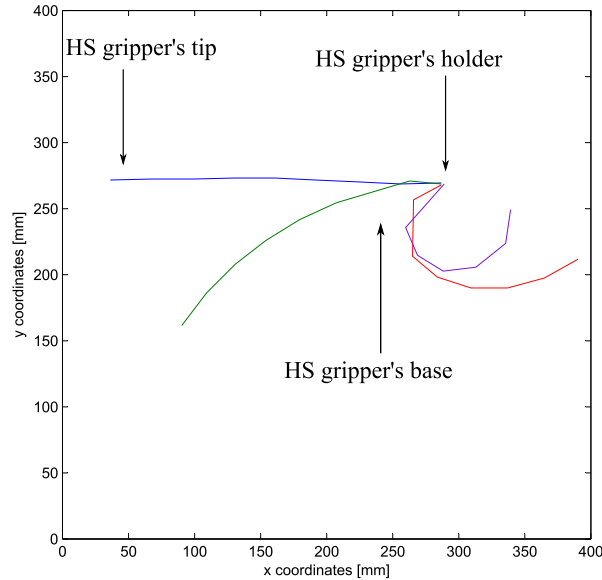


Figure 5.11: Trial with a 67.57% of the HS gripper filled with water. Force on the cable for each curve: Blue: 0N, Green: 9.8N, Red: 19.6N and Purple: 29.4N. For high forces the gripper is bent in a semi-circular configuration and thus half of the gripper's body sits in a position along the x axis further than the gripper's base position. The prototype is curling around its holder, positioned at $x=280$, $y=260$. An object positioned near the gripper could have been crushed between the HS gripper and the holder, shown in Figure 5.7, which is rigid and provides no compliant grasping. Figure from [Giannaccini et al., 2012], ©2012 IEEE.

Filling Quantity Experiments

This experimental session is carried out in order to test the HS gripper's bending behaviour with different filling percentages. These tests also aim at finding the optimal percentage of HS gripper filling for grasping tasks.

At the beginning of every experiment, the gripper is laid on the test rig surface. Subsequently, a sequence of a 9.8N, 19.6N and 29.4N forces is applied to both cables. Before applying a greater force, the full motion achieved under the previous force is completed. For example, the 19.6N force is applied only when the HS gripper has stopped moving due to the application of the 9.8N force. A series of 9 markers 30mm apart are drawn on the HS gripper's upper surface. This is done in order to trace the marked points of the gripper during its movements. The procedure described is repeated for a number of trials with different filling quantities. Here three of those trials are reported. A 50ml graduated syringe is used to introduce a

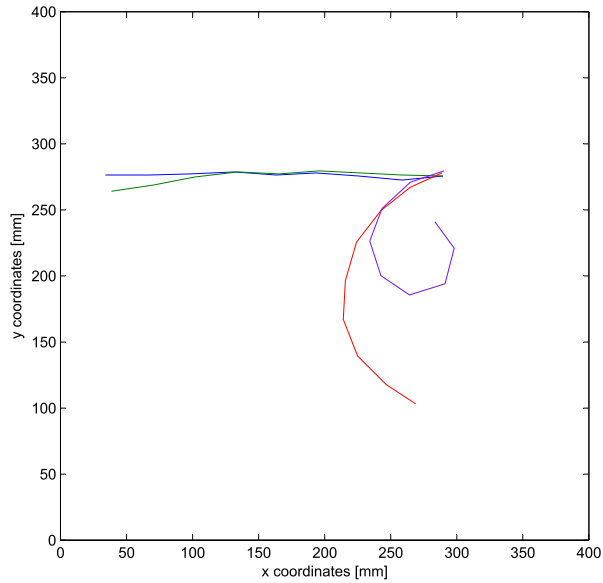


Figure 5.12: Trial with a 81.1% of the HS gripper filled with water. Force on the cable for each curve: Blue: 0N, Green: 9.8N, Red: 19.6N and Purple: 29.4N. It can be appreciated that a greater filling quantity allows the HS gripper's whole body to remain in front of the holder, which in this figure is for x values smaller than 280. The gripper holder is in position $x = 280$ and $y = 260$. Figure from [Giannaccini et al., 2012], ©2012 IEEE.

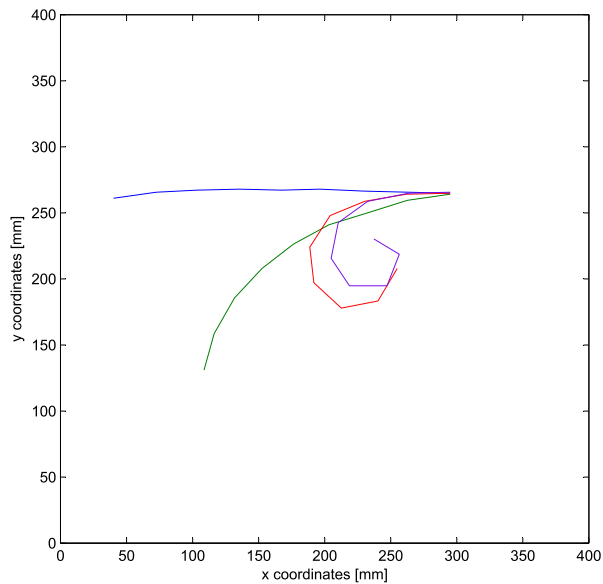


Figure 5.13: Trial with a 94.6% of the HS gripper filled with water. Force on the cable for each curve: Blue: 0N, Green: 9.8N, Red: 19.6N and Purple: 29.4N. The gripper holder is in position $x = 280$ and $y = 260$. The trend started in the previous experiment continues: in this case the prototype exhibits trajectories that are closer to the origin of the x -axis. Figure from [Giannaccini et al., 2012], ©2012 IEEE.

precise quantity of liquid in the HS gripper. The quantities of liquid introduced are: 100ml, 120ml and 140ml (68%, 81% and 95% of the full volume, respectively). The

markers on the gripper are tracked using a video camera and the footage is post-processed experimentally using tracking software (Robo-Realm[®]). This allowed us to produce the x and y positions of the markers in the horizontal plane. These data are further processed with Matlab[®] to permit their comparison and analysis. On the test rig surface, a 30mm square has previously been drawn in order to provide a reference for the transformation of the image pixels into mm. The results obtained are shown in the following figures.

An observation made during these trials is that, for high filling percentages, the gripper no longer lies flat on the rig surface, but lifts itself from the rig surface. This, taken together with the straightening of its proximal part, is a clear indication of the increased rigidity of the structure.

An 88% filling has been chosen for the grasping trials since this amount of filling guarantees that the gripper is not too empty as it is in the case of Figure 5.11. Furthermore, this amount of filling does not hinder the intended compliant interaction between the object and the prototype since the gripper is not filled with too much material. More detailed trials to the ones described in this section have been carried out with a 88% filling and are described in Section 5.6.1.

Production and Mounting Process

Once all materials and quantities to be used have been chosen following the process described in the previous sections, a trial and error process has lead to the current production and mounting process, which is described in this section. The polyethylene sheet is stamped with an impression of the gripper's laid out shape. Subsequently, the polyethylene is cut to match this shape. The Dyneema[®] cables are knotted at the end, inserted in the silicone tubing and secured to the polyethylene sheet with silicone paste, as shown in Figure 5.14. When the cables are pulled, the knot prevents them to slide away from the tube.



Figure 5.14: The silicone tubes have been glued to the corona treated polyethylene sheet, on which the edges of the cone have been stamped. The heat sealer is used to seal the edges together and then the cone is reversed inside out

Once the silicone paste has cured, the extremities of the gripper need to be fused together in order to create a 3D structure out of the sheet. Initially, the two external edges are sealed together with an ultrasonic welding machine but this method does

not provide enough heat to seal the edges of the HS gripper together and provide the necessary water tightness. A more reliable sealing method is provided by heat sealing. To increase durability, every edge is double sealed. The structure is now a 3D cone open at the larger diameter end. However, the cables are on the outside so the structure needs to be folded inside out to present a smooth contact surface, as shown in Figure 5.15.

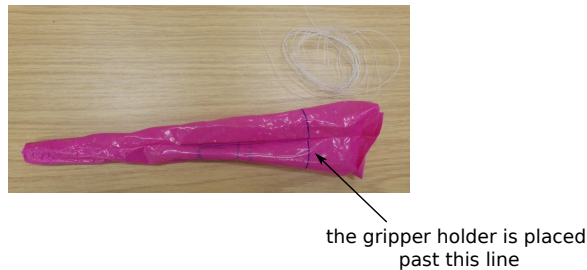


Figure 5.15: The polyethylene cone is ready: the silicone tubes are on the inside and only the cables (wound up in the upper right corner) come out of the cone

The cone base is inserted in the purposely designed holder, shown in black in Figure 5.7. The holder comprises of three parts, a crown that surrounds the base of the shell and a disk that is inserted inside the shell. These two parts lock the polyethylene shell between them and are secured to the third part of the holder, which is fixed on the test rig surface for the experiments and to the end of the INTRO-BRL arm link for the final structure. The disk has an opening that allows the insertion of the fluid. Once the fluid has been inserted with a syringe, the opening is sealed with a screw. Both the disk and the crown have two small indentations where the silicone tubes are fitted so that the cables can be pulled from the outside. The tubes end outside the gripper fluid filled cavity in order to avoid direct contact with the water.

Due to the possible uncertainty in the internal volume of the shell, this is measured for the three prototypes used in this work. This is done by filling the gripper completely with a graduated syringe, taking note of the maximum volume and calculating the quantity of water corresponding to the 88% of the maximum volume. The gripper is then emptied and the newly calculated amount of water is inserted with the graduated syringe. Since the gripper is not completely filled with water, some air enters the structure and it is removed by squeezing the gripper until the water level reaches the brim of the disk opening. At this point, the custom screw is inserted. This process ensures no compressible material (air) enters the gripper. Finally, the gripper's cables are wound around and secured to the motor's spindle.

The process hereby described is the same for both gripper variants, apart from the placement of the silicone tubes on the polyethylene sheet. The process described above is relative to the continuous gripper but it is different for the discrete gripper. In the discrete gripper, pieces of silicone tubing are secured to the sheet rather than one long piece of tubing. The details of the differences in placement of silicone tubes

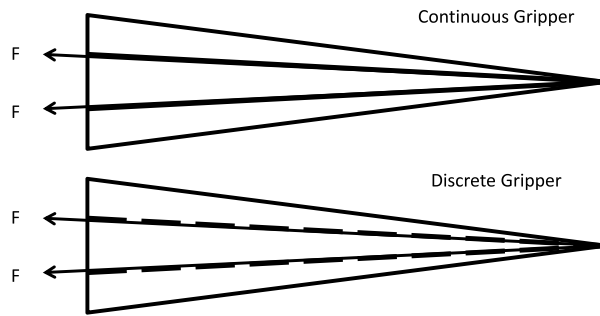


Figure 5.16: Gripper variants: the first gripper has continuous tubing, shown by the solid lines. The dotted line in the schematics of the second gripper indicates that the silicone tubes is discontinuous. Figure from [Giannaccini et al., 2014], used with permission of Springer.

in the two HS gripper variants are described in the following section.

5.5.2 Gripper Variants

Throughout the rest of the chapter the two variants of the gripper, shown in Figure 5.16, similar in every aspect but the silicone tube configuration, are referred to as continuous gripper and discrete gripper. In the continuous gripper the cable aiding the gripping motion is placed inside a single piece of continuous tube. In the discrete gripper a single cable is fed through separate sections of silicone tube. The silicone tube sections are equal lengths of tube (10mm long) attached equidistantly to each other (the distance between the tubing pieces is 24mm).

The performances of both grippers are compared in order to select the best one for stable grasping tasks. The HS gripper is able to perform a power grasp and its case three points of contact are considered a stable grasp. An evaluation is carried out comparing the ability of the two grippers to achieve variable compliance and a large grasping workspace, which is directly related to the range of object size which can be grasped. A completely different curling behaviour is recorded for the second gripper. Thus, conducting these experiments is necessary to fully characterise the grippers under real world conditions. These experiments are fully described in Section 5.6.1 and 5.6.2.

In Section 5.6.1, the workspace of the two grippers is tested. This is an important measurement, which determines the grasping capabilities required for motion planning when employing the gripper as part of the complete robotic manipulator. Secondly, in Section 5.6.2, the two variants of the gripper are tested in order to assess the compliance variability within the applied force range. This is essential since, in the grasping task, the initial compliance allows conforming to the object shape, while in a later phase, a stable and more rigid configuration is more desirable. Once these issues are addressed, the ability of the best performing gripper to conform to object shape and provide multiple points of contact is tested. This experiment

is conducted to demonstrate that the initial compliance is indeed well suited to increasing the contact area with the object, which reduces the local pressure the gripper exerts on it. The full description of these trials is provided in Section 5.8. In the last part of this last section, two experiments evaluating the performance within the specific application domain are conducted: one evaluates whether the object is held in a stable manner after the grasp and the second if the HS gripper is able to grasp without resting on a table.

The main aim of the experiments carried out on the HS gripper is to test its ability to vary its stiffness as the force on the cables increases, its capability to ensure ample workspace, its ability to adaptively mould to the object shape (Variable object cross-section shape grasping) and its ability to grasp and hold an object in free space. Priority has been given to these aspects since the HS gripper design is novel and testing its working mechanism is necessary to decide whether or not it is able of effective grasping and lifting of objects. Hence, emphasis has been given to these aspects rather than systematic grasping trials with all major shapes and sizes to empirically find out which ones are better grasped. While not denying the importance of a systematic characterisation of the grasping ability of an ample sample of objects with different shape and size, such trials are only necessary if the novel design has been proved successful in its grasping capabilities relative to a initial set of objects. Once variable object cross-section shape grasping, effective variable compliance, a large workspace and its ability to grasp and hold an object in free space have been sufficiently proved, a wider characterisation could be undergone in future work.

5.6 Experimental Analysis

The experimental analysis will be described in detail in this section starting with the planar behaviour, which characterises the workspace amplitude of both HS gripper variants. In Section 5.6.2, the capability of the HS gripper to vary its compliance is tested.

5.6.1 Planar Behaviour

In this section the planar behaviour of the gripper is taken into consideration. Its movement can be compared to the bending movement in hydrostatic skeletons. In order to characterise the two gripper variants' planar behaviour, i.e. the motion in the horizontal plane, their curvature profile and planar trajectory are analysed. The curvature profile is analysed utilising the radii of curvature. The experiments are conducted under increasing actuation forces on the cables. In addition, an assessment is carried out of the ability of the HS gripper variants to fit the requirement for a large workspace, under the minimum actuation forces \vec{F}_p .

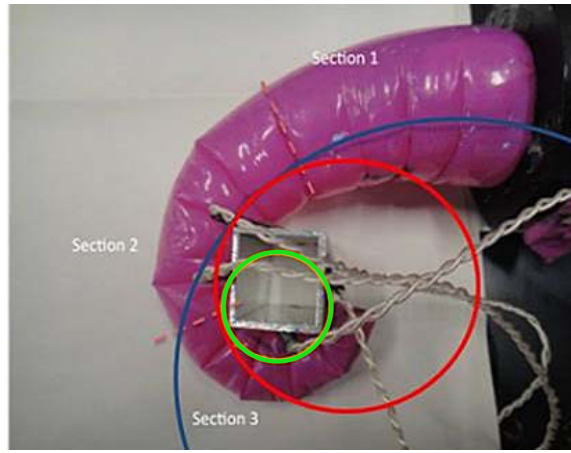


Figure 5.17: The grippers are divided into sections: Section 1 corresponds to the base of the gripper, Section 2 to the middle and Section 3 to the tip. In the picture it is possible to see also the twisted white wires of the pressure sensors, which are fixed on the object's surface area. The internal side of the gripper is the one with the creases (or concertina) and the external one is the one without creases. Figure from [Giannaccini et al., 2014], used with permission of Springer.

Experimental setup

This experiment setup is the same as the one used in Section 5.5.1. Nine equidistant markers are used to identify the different regions of the gripper. The markers are black dots drawn on the outer shell along its centre line. For the actuation, a force range, detailed in Fig. 5.22, is applied to the cables.

Results

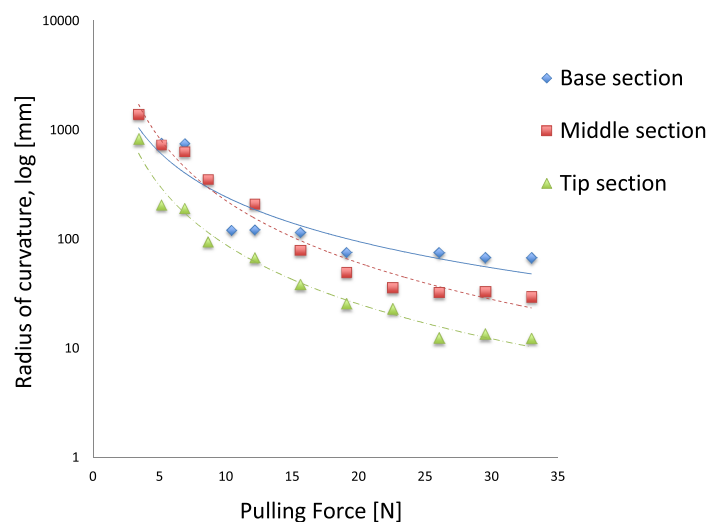


Figure 5.18: Experimental variation of the radius of curvature in the continuous gripper. Please note that the radius of curvature axis has a logarithmic scale. Figure from [Giannaccini et al., 2014], used with permission of Springer.

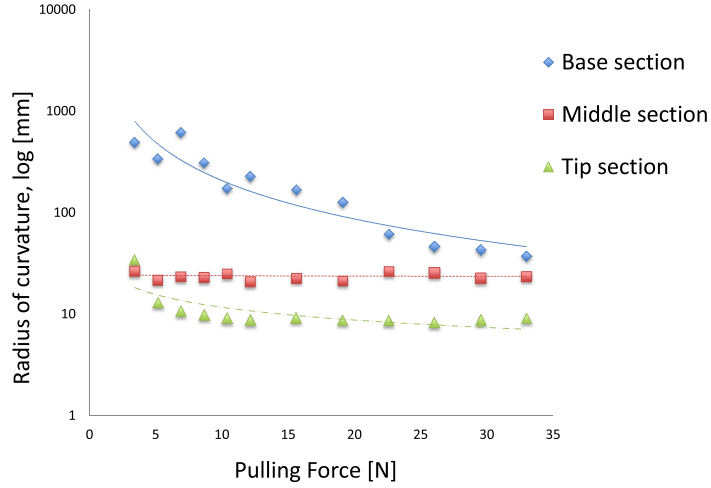


Figure 5.19: Experimental variation of the radius of curvature in the discrete gripper. Please note that the radius of curvature axis has a logarithmic scale. Figure from [Giannaccini et al., 2014], used with permission of Springer.

Curvature profiles Due to the nature of the gripper when ‘curled up’, fitting a single circle through all marker points is not possible. Hence, the decision to divide the gripper into 3 sections, with a respective circle each, shown in Fig. 5.17, is made during the post-processing phase. The circles fitted through the marker points of each sector, have an equation of the form

$$(x - p)^2 + (y - q)^2 = r^2 \quad (5.1)$$

where p and q are the x and y coordinates of the centre of the circle and r is the radius. The radius that better fitted the data was chosen for each section. Fig. 5.18 and Fig. 5.19 show the values of the radii of curvature obtained for the continuous and discrete gripper respectively. In the initial position, when the \vec{F}_p is zero, all the markers are residing along the same line, thus, a circle cannot be defined. Hence, the initial position is not present in the data in Fig. 5.18 and Fig. 5.19.

The graphs exhibit important characteristics of the bending behaviour of both gripper variants. All sections of the continuous gripper show a similar bending trend. Thus, the sections all bend at the same time progressively as the pulling force on the cables increase. Their final radius of curvature is higher in the base section and lowest in the tip section. The discrete gripper shows different characteristics. The movement of the base section is quite similar to the continuous gripper and requires higher pulling forces on the cables to exhaust its movement. On the contrary, the middle and tip sections, see Fig. 5.17, display most of their movement for small cable pulling forces and do not show much movement above a 5N pulling force.

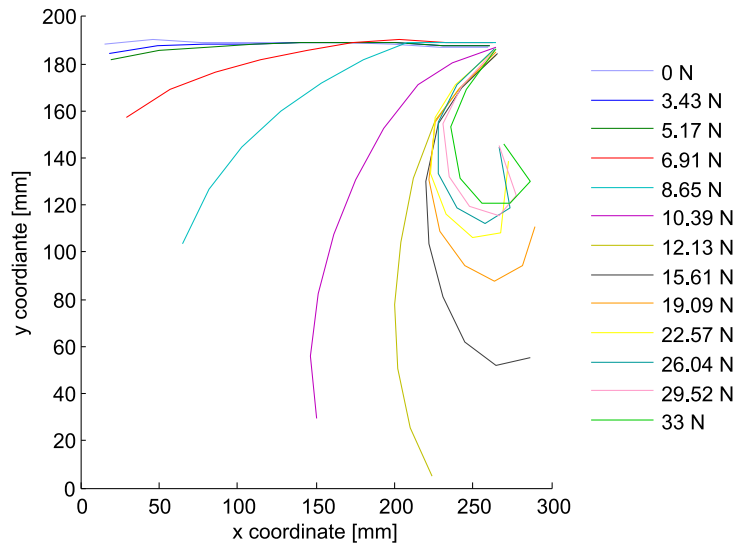


Figure 5.20: Experimental trajectory on the horizontal plane: continuous gripper. The straight lines are approximations of the gripper’s position between two adjacent markers. Figure from [Giannaccini et al., 2014], used with permission of Springer.

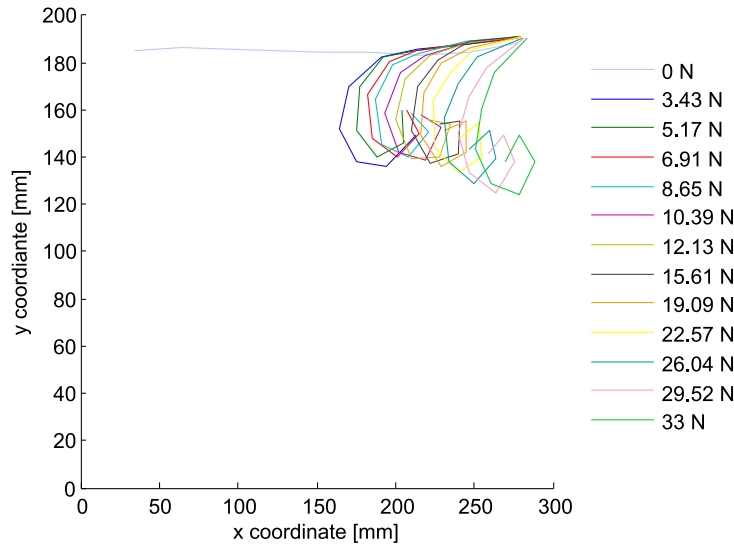


Figure 5.21: Experimental trajectory on the horizontal plane: discrete gripper. The straight lines are approximations of the gripper’s position between two adjacent markers. The gripper holder is in position $x = 280$ and $y = 190$ in all three graphs. Figure from [Giannaccini et al., 2014], used with permission of Springer.

Planar trajectories The planar trajectory results are shown in Figure 5.20 and Figure 5.21.

The behaviour of the two grippers is clearly different, even under the same values of cable pulling forces. The initial force (3.43N) barely makes the continuous gripper (Figure 5.20) move, while the discrete gripper (Figure 5.21) already starts curling. Figure 5.22 is a close up of Figure 5.21, which makes the discrete behaviour more clear by enlarging the area of interest. In the continuous gripper, the base section remains quite straight up to 12.13N. This is interesting for the grasping task since it allows the object to be grasped when distanced from the rigid holder. A further

difference between the two gripper behaviours is that the tip of the discrete gripper bends even for small force values, while the continuous gripper curls simultaneously in all its sections. For this reason, the continuous gripper has a greater workspace, which means that can grasp larger objects than the discrete one. This makes the continuous gripper preferable to the discrete one. In Figure 5.20, relative to the continuous gripper, the maximum reach along the y axis is 160mm, while in Figure 5.21, relative to the discrete gripper, the maximum reach along the y axis is 60mm.

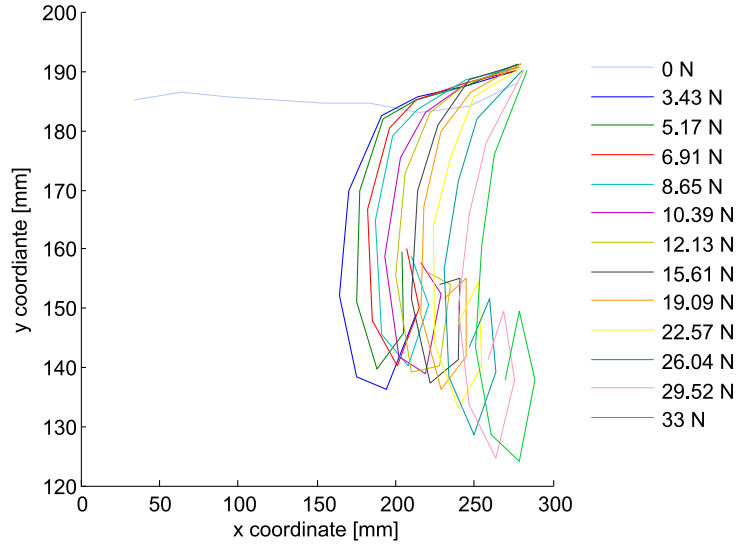


Figure 5.22: Close up of the discrete gripper trajectory on the horizontal plane. The straight lines are approximations of the gripper's position between two markers. The gripper holder is in position $x = 280$ and $y = 190$ in all three graphs. Figure from [Giannaccini et al., 2014], used with permission of Springer.

5.6.2 Variable Compliance

The inspiration for the mechanism's variable compliance is provided by the stiffening movement in hydrostatic skeletons as described in Section 5.4. Compliance is the inverse of stiffness of a structure. Stiffness is the extent to which an object resists deformation once a force is applied to it, see Eqn. 5.2.

$$\vec{k} = \frac{\vec{F}}{\vec{\delta}} \quad (5.2)$$

where \vec{k} is the stiffness, \vec{F} is the force applied on the body and $\vec{\delta}$ is the displacement produced by the force along its direction of action. A smaller $\vec{\delta}$ means a higher \vec{k} .

The change in compliance in the HS gripper is measured as the change in stiffness. In order to explain how the variable stiffness is achieved it is necessary to further explain the gripper's working system. The potential volume, V_{pot} , of the shell is

defined, in this case, as the maximum amount of water which the shell, shown in Figure 5.9 can hold: 170ml. The potential volume depends on the folding of the structure. Thus, if the structure is partially folded, the potential volume is reduced. For example, if the tip of the structure were to be folded on itself and the gripper were filled with water, only part of the 170ml would fit in it. Hence, 170ml is V_{potMax} and all other potential volumes are smaller than that; furthermore, the more the shell is folded, the smaller V_{pot} becomes.

The shell is only filled with 88 % of V_{potMax} and all the air is removed from the system. So, in this geometrical configuration, the current volume of the gripper (i.e. of the water), V_{curr} , is 88 % (148 ml) of V_{potMax} of the unfolded gripper. This deflated structure is soft and compliant since the water can shift around in the shell. This is state A. To increase the stiffness of the structure, the cables, shown on the side of the gripper in Fig. 5.16, are pulled. By pulling the cables with a certain \vec{F}_p , the material will first buckle then form folds along the side of the gripper where the cables are. This effect will cause a progressive shortening of the side of the gripper and a change in its geometry. In this new, partially folded, shape configuration the potential volume is reduced. The reduction of V_{pot} of the shell continues until the potential volume matches V_{curr} , which is also the volume of the water. At this point, since water cannot be compressed, for all practical purposes, further pulling of the cables causes an increase of the pressure on the shell's walls, this is state B. The higher pressure causes the increase in the stiffness of the gripper.

The mechanism of the stiffening is acting through the hoop stresses (σ_τ) the material is exhibiting due to the increase in the shell-water system pressure. Given that the thickness of the shell (t) is 0.06mm, thus much smaller than the 1/10th of the radius (r) of the gripper (25mm), the simple form of Young-Laplace equation can be used to calculate hoop stresses:

$$\sigma_\tau = \frac{P \cdot r}{t} \quad (5.3)$$

Given that r and t are effectively constant, there is an increase of σ_τ , measured in Pa, proportional to the pressure P . Since P increases as V_{pot} tends to V_{curr} , as explained above, then σ_τ increases, too. Increased σ_τ of a surface results in decreased ability to deform this surface by applying a force on it. Stiffness is defined as the amount of force applied over the deformation it creates, see equation 5.2. Hence, via the process of increasing pressure, which leads to higher hoop stresses, stiffness of the gripper is achieved.

The experiment described below has been conducted in order to demonstrate this stiffening effect. It is theorised that compliance decreases with the increase of force on the cables (\vec{F}_p), as the gripper bends.

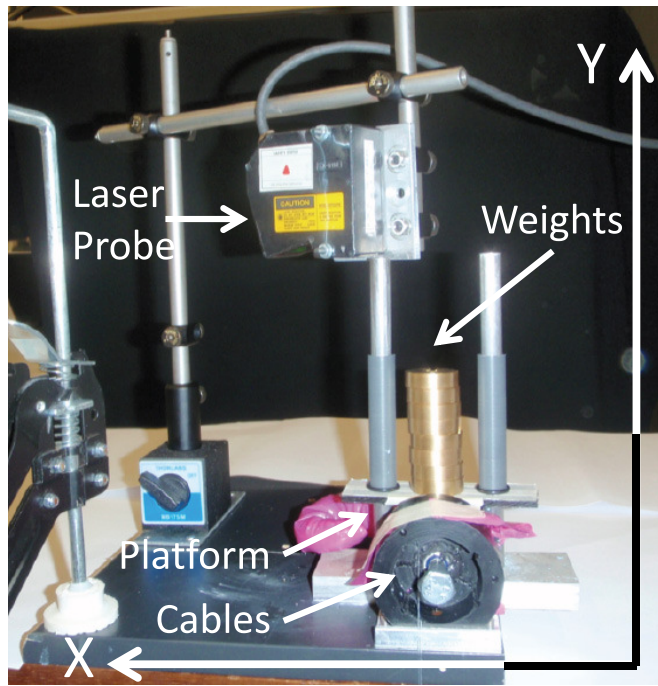


Figure 5.23: Stiffness estimation setup. The gripper (pink) is laying flat on the rig table and the only visible parts are its tip and the gripper holder (round structure in black). The gripper holder is fixed to the rig table so that the gripper's base does not move during the experiment. The two cables embedded in the gripper are shown in the figure coming out of the gripper holder towards the reader. The laser probe above the gripper is used to measure the distance between the laser probe itself and the surface of the gripper. The distance between the surface of the gripper and the laser probe is at its minimum when no weight is put on top of the gripper. As more and more weights are put on top of the gripper, the gripper is flattened by the weights and the distance between the two increases. Hence the distance between the probe and the gripper is indicative of the deformation of the gripper and thus its top surface displacement along the y axis, which is shown in the figure coordinate system. The weights are not put directly on the gripper but on top of a flat and rigid platform shown in the figure. Figure from [Giannaccini et al., 2014], used with permission of Springer.

Experimental setup

The apparatus used to estimate the structure's stiffness is shown in Fig. 5.23. The horizontal platform is resting on the gripper's base in order to provide the compliance measurement in that portion of the structure. During the experiment, an external force \vec{F}_w is applied on the gripper by adding weights (cylinders of 25mm in diameter) on the platform. In order to measure displacement ($\vec{\delta}$), a laser probe (LK-G152 and LK- GD500, Keyence) is used and ($\vec{\delta}$) is measured as a change in length (L) in the vertical direction (y axis) (see Fig. 5.23); horizontal displacement is not measured in this experiment. However, due to the fact that this is a close system and degassed water is incompressible, the horizontal displacement is a function of \vec{F}_w and structural stiffness.

Results

The experimental results can be seen in Figure 5.24 and Figure 5.25, showing the variation of the stiffness of the grippers at four different bending positions². The data plotted in each figure are the mean values averaged over the three trials; error bars show the standard deviation.

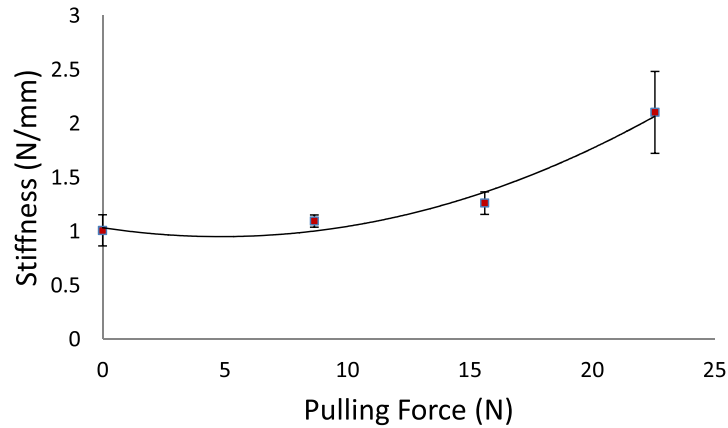


Figure 5.24: Variation of the continuous gripper stiffness. Trials are repeated three times each, error bars show the standard deviation in the data. Figure from [Gian-naccini et al., 2014], used with permission of Springer.

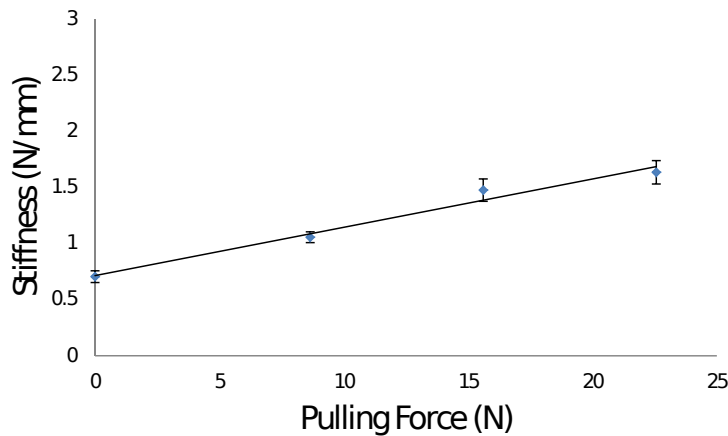


Figure 5.25: Variation of the discrete gripper stiffness. Trials are repeated three times each, error bars show the standard deviation in the data. Figure from [Gian-naccini et al., 2014], used with permission of Springer.

For ease of comparison, the same pulling forces (\vec{F}_p) are used for both the continuous and discrete gripper. These four values in the figures correspond to the initial configuration (no force on the cables) and three pulling force values (\vec{F}_p) for the

²data gathered by Pasindu Peiris

cables (8.6N, 15.6N and 22.5N). Given space restrictions imposed by the measuring rig, the full range of pulling forces (which corresponds to 0N to 33N, as seen in the experiments carried out in Section 5.6.1) could not be tested but the force range used is sufficient to characterise the behaviour of stiffness as forces pulling the cables rise.

The results of the experiments show a change in the compliance relationship demonstrating the variable compliance of the grippers. The results of these two sets of data (one for each gripper variant) show that the continuous gripper's compliance variation follows a different behaviour compared to the discrete gripper's compliance variation at the same cable-pulling force values.

Once the values are obtained, a polynomial fit is used for the data. This is done so that the fitted curves can be used in a model of the HS gripper. These functions could be used to extrapolate the stress-strain relationship values for both gripper variants and can be found in Section C.1 together with the statistical data analysis.

5.6.3 Continuous versus Discrete Design

The continuous gripper is chosen over the discrete gripper and all further experiments in this work are conducted with the continuous gripper. The continuous gripper is chosen because of its greater workspace and ability to grasp a larger range of object sizes than the discrete gripper. Even if the discrete gripper requires lower pulling forces to be actuated, hence reducing the wasted energy in the system, it also presents numerous disadvantages.

First, the discrete gripper has a reduced workspace, meaning the area it 'sweeps' during the closing motion is smaller than in the continuous gripper. A gripper with a reduced workspace needs to be more accurately positioned in order to successfully grasp an object. Provided that the workspace is large, the positioning of the gripper is less of an issue even when using such a compliant gripper with inherent positioning inaccuracy. Furthermore, the discrete gripper behaviour reduces the possible contact area with the object and this causes poor grasping capabilities. This is due to the fact that its tip curls up completely in the beginning of the grasp, as shown in Figure 5.21 and Figure 5.22, which leaves only the base of the gripper available for grasping. Thus, the range of object sizes that can be picked up with the discrete gripper is smaller. The ability to grasp a large range of objects and the possibility to make up for the position inaccuracy inherent to both designs with a larger workspace are so important that it is decided to discard the use of the discrete gripper. For these reasons, the continuous gripper is used in the practical experiments in the following section.

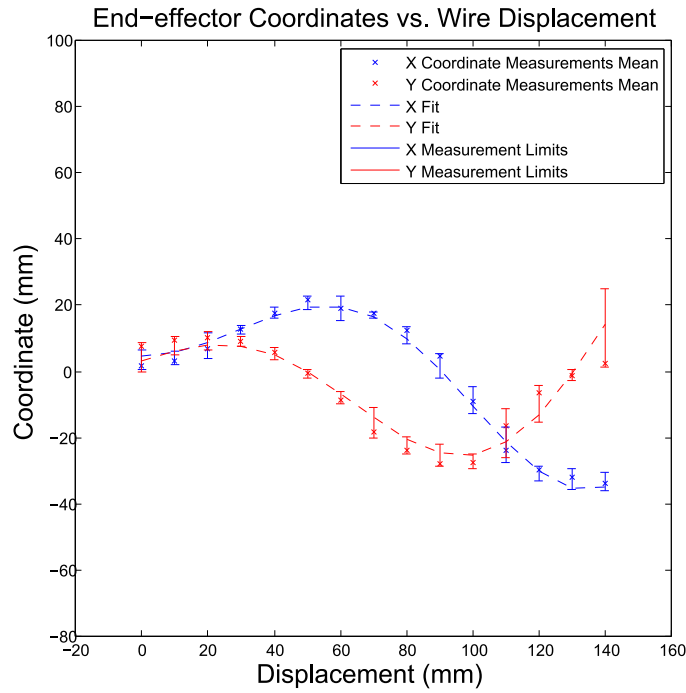


Figure 5.26: Tip position in the x and y cartesian coordinates against the HS gripper cable displacement. The mean value and the standard deviation (limit in the legend) among the six tests for each coordinate over the full displacement range is given. Figure from [Giannaccini et al., 2014], used with permission of Springer.

5.7 Forward Kinematics

As discussed in Chapter 3, describing kinematics of hyper-redundant and soft structures is not straight-forward since they cannot be accurately described using a chain of rigid links normally described by Denavit-Hartenberg parameters [Spong et al., 2006]. For this reason, it is necessary to design an empirical model for the HS gripper. In order to establish a kinematic model it is observed that its tip follows a spiral trajectory. Based on this, a number of experiments are conducted in order to evaluate this assumption and establish a connection between the displacement of the actuating string and the location of the tip, and hence find the forward kinematics of the gripper³. For brevity, only the final results are reported here and the details of the analysis can be found in Appendix C, Section C.3.

The final relation between the polar coordinate angle of the spiral θ and displacement of the HS gripper cables d , in mm, results to be:

$$\theta = \frac{1.5 \cdot \pi}{140} \cdot (140 - d) \Rightarrow \theta = 0.034 \cdot (140 - d) \quad (5.4)$$

The results of the fitting process for the gripper's tip can be seen in Figure 5.26. The statistical details regarding the definition of the parameters can be seen in Section C.3. The R^2 for the fitting of coordinate x to Eq. (C.6a) is 0.985, and

³work made in cooperation with Dr Ioannis Georgilas, who developed the Matlab[®] code

for coordinate y to Eq. (C.6b) is 0.886. Both values indicate that the respective fitting process gave a good result. Finally, the forward kinematics equations for the tip are reported in C.8a and C.8b. These equations provide the mapping between the displacement of the cables d and the tip's position on the horizontal plane.

$$x = a_x \cdot 0.034 \cdot d \cdot \sin(b_x \cdot 0.034 \cdot d + \pi/2) + c_x \quad (5.5a)$$

$$y = a_y \cdot 0.034 \cdot d \cdot \sin(b_y \cdot 0.034 \cdot d) + c_y \quad (5.5b)$$

where a_x is 12.775mm, b_x is 1.075mm, c_x is 6.49mm, a_y is 13.07mm, b_y is 1.045mm, c_y is 4.514mm. These coefficients have been found by fitting a curve on the data set. Therefore, this section and Section 5.6.2 together provide a characterisation of the HS gripper's tip position and stiffness for increasing pulling forces on the cables. The next set of experiments test if the initial compliance, measured in Section 5.6.2 is actually helpful in reducing control complexity for variable cross-section shape grasping and if the final stiffness is enough to hold an object in mid-air.

5.8 Grasping Experiments

In this section, multiple grasping experiments are described. In Section 5.8.1, the HS gripper's ability to adaptively mould to variable object cross-sections is tested. In Section 5.8.2, the realisation of a stable grasp on a cup, an application specific object, is tested. When referring to a stable grasp, the reference is the definition by Feix et al. "A grasp is every static hand posture with which an object can be held securely with one hand". In the experiment, the gripper wrapped around the cup is able to securely suspend it in mid-air without slippage or falling of the cup, thus that grasp is defined as stable [Feix et al., 2009]. In Section 5.8.2, a third experiment is described: the gripper applied a stable grasp on an object freely positioned in space. All these trials and experiments are described in the next sections.

5.8.1 Variable Cross-section Shape Grasping

The aim of this experiment is to show that the compliant and continuum physical structure of the gripper adapts to the shape of the object without previous knowledge of it: variable cross-section shape grasping. For this reason, three objects with different cross sections are grasped using the same motor command (both cables being pulled with a 34.3N force). If the same motor command causes all objects to be successfully grasped, this is a strong indication that the gripper's passive features (compliance and shape) are responsible for the adaptivity to the object. Grasping

success, in this experiment, is measured by the number of touch sensors on the object which have been contacted. The total number of sensors fitted on the lateral surface of the object is four. Since two diametrically opposite points of contact with an object are the minimum number of contacts required to successfully grasp an object, if two diametrically opposite sensors are reporting contact the grasp is deemed successful. If three sensors are reporting contact, the grasp is recognised as adaptive and if all four sensors' outputs are contacted the grasp is recognised as very adaptive. Contact with a sensor is marked by a change in the force measurement recorded by the sensor itself. Specifically, when the sensor measurement is above 0N, it is considered that the object has been contacted.

Experimental setup

The arrangement of the experimental setup is shown in Fig. 5.27. The gripper holder is fixed on a board and the gripper's motor input of 34.3N is applied in order to grasp the objects. This force is chosen because preliminary experiments showed that it ensured that the object is fully encircled and grasped firmly. The objects are fixed in the same point on the table surface, to ensure all the grasps are executed in a repeatable and consistent manner.

The lateral surfaces of the three objects are fitted with sensors, their position is illustrated in Figure 5.27. Since the chosen objects have curved surfaces, the tactile sensor Contact 500 (Pressure Profile Systems, Inc) is chosen to be fitted on them due to its small size and high flexibility. A NI-DAQ (National Instrument) board interfaced with a PC is used to obtain the sensors' measurements. LabView SignalExpress software[®] is used to analyse the output data received over the NI-DAQ board. Every sensor has been calibrated individually using a set of calibration weights. Incremental weights are placed on each sensor surface and sensor output (in Volts) vs Force (in Newtons) curves have been produced. These the tactile sensors possess a 200:1 sensitivity and a non-repeatability smaller than 2%. The sensors are fitted to the object's lateral surface since the grasping action in the HS gripper is always parallel to the ground, it is a lateral grasp. If these sensors are not contacted, their output is zero. If their output increases, this means that there has been a contact between the gripper and the object. In this experiments the main concern is on the presence or absence of contact, not the magnitude of the contact force.

Results

The gripper's passive ability to comply with objects' shape is tested for each object. Each experiment is repeated five times in order to ensure its repeatability and every time the same number of sensors have been touched for every object⁴. The change

⁴experiments conducted in cooperation with Yue Zheng

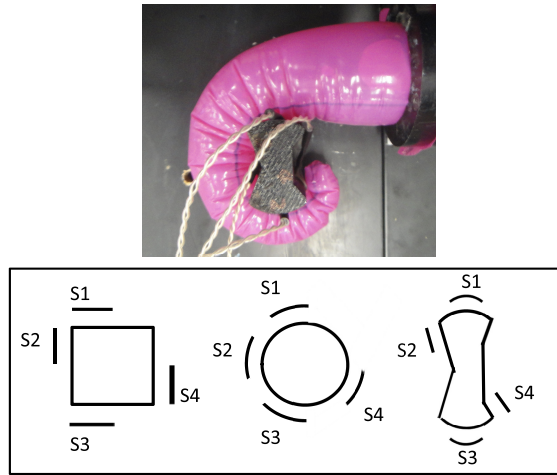


Figure 5.27: Photo: the continuous gripper as it is grasping the irregular object. Schematics: Position of the sensors on the tested objects, S stands for sensor: S1 represents the first sensor, S2 the second sensor and so on. The orientation of the object in the schematics is the same as the orientation of the object in the picture. From the left: square, round and irregular object. Figure from [Giannaccini et al., 2014], used with permission of Springer.

in force displayed by the sensors fixed on the object indicates whether it is touched by the gripper or not.

As seen in Figure 5.28, in most cases, the sensor gives a positive output (or change in output value) and this shows the presence of contact force. Table 5.1, Table 5.2 and Table 5.3 show how many times the four sensors are contacted in each object for the five trials.

Table 5.1: Number of Contacted Sensors for Square Object

Trial number	Sensor 1	Sensor 2	Sensor 3	Sensor 4
1	contacted	contacted	contacted	contacted
2	contacted	contacted	contacted	contacted
3	contacted	contacted	contacted	contacted
4	contacted	contacted	contacted	contacted
5	contacted	contacted	contacted	contacted

Table 5.2: Number of Contacted Sensors for Round Object

Trial number	Sensor 1	Sensor 2	Sensor 3	Sensor 4
1	contacted	contacted	contacted	contacted
2	contacted	contacted	contacted	contacted
3	contacted	contacted	contacted	contacted
4	contacted	contacted	contacted	contacted
5	contacted	contacted	contacted	contacted

For the first and second object, all sensors show a change in output value and thus have been contacted and for the third object, the irregular cross section one,

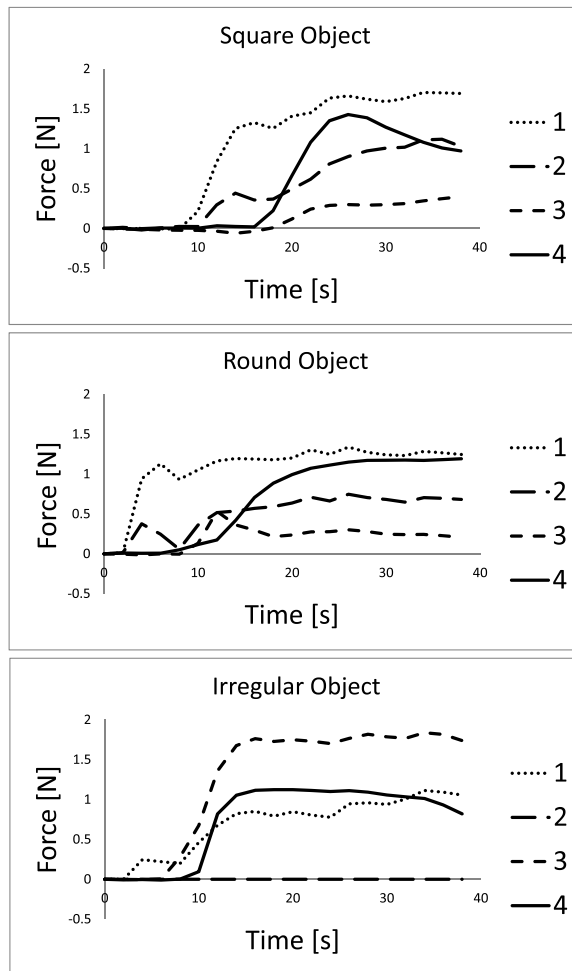


Figure 5.28: Force readings of the four sensors on the square, round and irregular object. These graphs show the results of three of the fifteen trials performed in this experiments. The important information is the presence of contact, not the value of contact force the HS gripper exerts on the object. The object is fully grasped during the first 15sec but the data has been recorded further to investigate whether the force on each contact point changed during a prolonged grasp. Figure from [Giannaccini et al., 2014], used with permission of Springer.

Table 5.3: Number of Contacted Sensors for Irregular Object

Trial number	Sensor 1	Sensor 2	Sensor 3	Sensor 4
1	contacted	not contacted	contacted	contacted
2	contacted	not contacted	contacted	contacted
3	contacted	not contacted	contacted	contacted
4	contacted	not contacted	contacted	contacted
5	contacted	not contacted	contacted	contacted

three out of four sensors display a change in output value (contact force). As it can be observed in the tables, there results are very consistent.

Thus, it is evident from these results that the gripper is able to easily mould to the round and square cross-shaped objects. In trials with the irregularly cross-shaped object, Sensor 2 is not contacted because of the HS gripper's bending trajectory and the object's intrinsic complex cross-shape geometry, which includes concave

sections. However, since three out of four sensors have been touched, the grasp is still successful and adaptive.

5.8.2 Experiments in the Application Domain

To focus on a specific application domain, the grasping of an everyday object such as a cup is chosen as a task, because it is a very common action in everyday life and it is necessary to perform the robot waiter scenario required by the INTRO project. Also, it is important to show that the gripper initial compliance is not a hindrance in grasping without a table to rest upon. The two following experiments have been conducted with the continuous gripper.

Grasping and holding a compliant plastic cup

The following experiment focuses on the ability of the gripper not only to grasp but also to hold a compliant plastic cup. The cup, shown in Figure 5.29, is placed on a removable slate, Figure 5.30.



Figure 5.29: Maximum and minimum diameter of a standard plastic cup

Subsequently, the gripper cables are driven with the maximum applicable force (34.3N), in order to keep consistency with the experiments in Section 5.8.1. Once the partially filled cup, which weighs 0.065kg, is grasped, as illustrated in Figure 5.30, the slate underneath the plastic cup is removed. It is observed that the cup remains in place and does not tilt. This demonstrates both the stability of the grasp and the purely horizontal grasping motion applied to the object. In the specific example of the compliant plastic cup, this last characteristic is vital since it ensures that a liquid contained in the cup would not spill. Furthermore, the compliant cup is only slightly locally deformed by the grasp due to the large contact area provided by the gripper. This characteristic facilitates sensible handing-over of fragile objects.

Grasping without resting on table

The following experiment aims to prove that the grasping and holding tasks can also be performed in free space. Thus, the gripper support is held at the edge of the

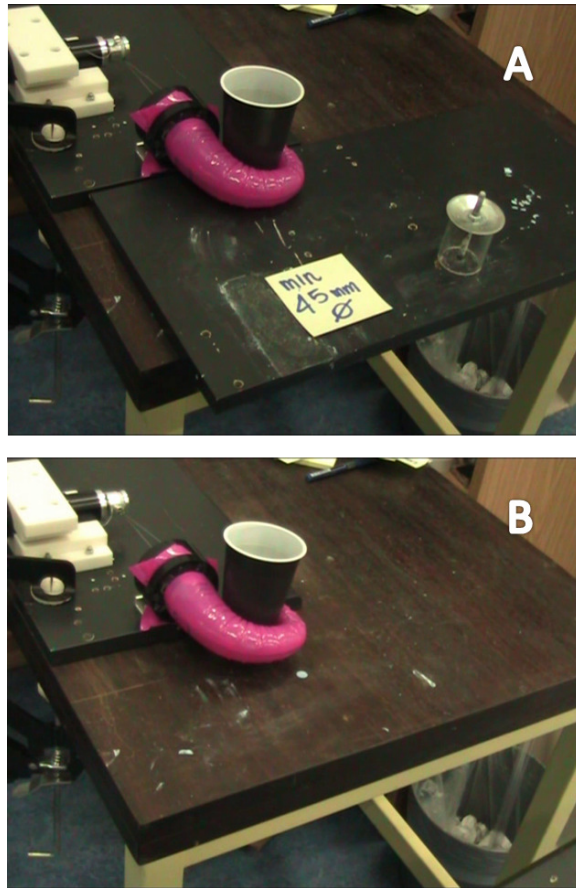


Figure 5.30: A: the compliant plastic cup is grasped B: the gripper is able to keep its position without needing the extra support. Figure from [Giannaccini et al., 2014], used with permission of Springer.

table and the gripper is hanging in mid-air, shown in Figure 5.31. Previously, the experiments are conducted with both gripper and object resting on a surface.

An object is held close to the gripper by a person, as shown in Figure 5.31. The robotic system is activated and the gripper starts curling and levelling itself on the horizontal plane. The object is successfully grasped, then released by the person but held in place by the gripper.

5.9 Discussion

The described experiments have demonstrated the versatility of the proposed gripper to achieve a stable grasping action under uncertain conditions.

The overall results of the planar behaviour experiments indicate that the continuous gripper features a greater workspace than the discrete gripper. For this reason, the continuous gripper is chosen as the better performing of the two variants. The confirmation of the similarity between the bending movement in hydrostatic skeletons and in the HS gripper, compared in Section 5.4, can be found in the graphs of the gripper's planar trajectory in Figure 5.20 and Figure 5.21.

Similarly, the mechanism that causes stiffening in hydrostatic skeletons is success-



Figure 5.31: Grasping raspering without resting on table. A: the object is held by the human B: the gripper has successfully grasped the object. Figure from [Giannaccini et al., 2014], used with permission of Springer.

fully reproduced in the gripper design, as demonstrated by the increase in stiffness shown in Figure 5.24 and Figure 5.25. Variable compliance is present in both gripper variants. It changes linearly in the discrete gripper while in the continuous gripper the change in the stiffness is described by a third order equation. This is due to the difference in cable structure which yields a different curling behaviour and water displacement. In order to explain this phenomenon, it is important to notice that the variable compliance measuring setup is placed in the base section of both grippers. Thus it measures more accurately the stiffness of that section. In the discrete gripper, the middle and tip sections curl up for small forces on the cables. The same sections do not show much movement above a 5N pulling force. Thus, water is displaced towards the base section for low pulling force on the cables, as can be deduced by the data in Figure 5.21. This behaviour is consistent with a more steep theoretical curve between pulling force on the cables and stiffness compared with the same curve for the continuous gripper. This is because, in the continuous gripper, all sections bend simultaneously. Hence, water is not as strongly pushed to the base section for forces on the cables up to 8.6N. This makes this part of the theoretical curve between pulling force on the cables and stiffness less steep than in the discrete gripper. For higher pulling forces on the cables, the theoretical curve between pulling force on the cables and stiffness in the continuous gripper becomes similar to an exponential curve. This sudden increase in stiffness is due to water being pushed in the base section by the curling of the middle and tip sections, which happens for forces on the cables higher than 12.13N, as it can be seen in Figure 5.20.

In addition to the effects on stiffness given by different bending behaviour in the two gripper variants, there is an effect common to both variants. In both grippers the forming of the creases makes V_{pot} closely match V_{curr} so that water can no longer shift around in the polyethylene shell. This makes the pressure against the shell walls increase together with structural stiffness. Hence, the stiffness of both gripper variants increases, for higher pulling forces on the cables.

The results of the experiments on compliance to the object cross section demonstrate that more points of contact are achieved when compared, for example, to the conventional rigid clamp gripper in [Schunk, 2013], where the pressure points are normally limited to two areas. In the case where an individually digit actuated multi-fingered gripper (e.g. an anthropomorphic hand) is used to perform a lateral grasp on roughly cylindrical objects with very different cross-sections, each digit of each finger would need to be individually controlled in order to obtain similar results. Hence, the absence of rigid or semi-rigid structures ensures that, in imitating a lateral grasp (or wrap) primitive, the design described in this chapter can adapt to different shapes passively, greatly simplifying control and the mechanical design.

However, some limitations are present in this design. The three main limitations are: i) the presence of only one ‘digit’ entails that some objects cannot be grasped;

ii) the gripper's physical structure is not resistant to wear and further development should be carried out to turn this prototype into a commercial product; iii) having cables on only one side of the gripper, meaning that it can only bend in one direction. This last point is solved by the design of the STIFF-FLOP manipulator by including a higher number of cables making it able to change configuration and avoid obstacles [Maghooa et al., 2015].

On the other hand, the HS gripper's compliance is advantageous in avoiding crushing the object, since it is very likely that it would create a larger contact area. Furthermore, due to its initially very compliant structure the HS gripper is more adaptable to the object's cross section shape compared to traditional grippers. In addition, only simple grasp control is required, thus little computational effort is necessary. In order to grasp an object, the HS gripper must be placed on the right of the object, since the gripper only has cables on one side. The gripper also needs to be placed so that the object is in the workspace identified by the curves in Figure 5.20.

5.10 Summary

In this chapter the working mechanism and design behind the HS gripper have been explained. Two versions of the grasping device have been produced and their behaviour in planar trajectories has been documented. It is quite interesting that such a small change in the gripper structure (continuous silicone tubes arrangement against discrete silicone tubes arrangement) can produce a noticeable difference in workspace range and behaviour in general. This is similar to the embodied intelligence paradigm which is described in Chapter 2 and inspired this work: shape and behaviour are strongly linked. A further aim of this chapter is to sustain the claim that compliance varies passively once the gripper cables are pulled. For this reason, experiments have been carried out to test the stiffness of the device in different phases of the grasping motion. Results show that stiffness does increase as cables are pulled. While these experiments focussed on the characterisation of the device, further experiments are aimed at testing its ability to adapt to different cross-shaped objects passively and with simple control. This has been shown by grasping different objects using in every trial the same input to the motor. Moreover, experiments have been successfully carried out to show the HS gripper's ability to hold an object in a stable manner and to grasp an object in free space. In addition, an empirical spiral equation model of the device bending behaviour has been provided to characterise forward kinematics. The sum of this experimental and modelling work is able to deliver a description of the HS gripper, of its limitations and positive qualities.

Chapter 6

Conclusions and Future Work

The main aim of this thesis is to design and produce a robot arm with inherently safe features and an adaptive gripper. It is shown in this thesis' work that the design of these devices can be greatly enhanced by the exploitation of variable compliance. The first device is a hybrid decoupling feature (HDF) aimed at reducing the impact of unexpected collisions against the arm and the second is a soft gripper inspired by hydrostatic skeletons, the HS gripper. The main contribution of this thesis' work is the design, building, testing and characterisation of these two devices.

6.1 Conclusions

One of the most common ways to reduce the potential harm caused by manipulators is to decrease the severity of impacts, during which the robot arm could transfer high quantities of energy to its environment. The HDF reduces the impact energy by decoupling the mass of its link and end-effector from the rest of the mass of the robot arm. The decoupling is a result of the change from a rigid to a compliant behaviour, hence variable compliance is key for the working mechanism. The main contribution the HDF design brings to the robot safety field is the ability to act on the passively achieved decoupling by varying the magnitude of the collision torque that triggers the decoupling. This is achieved by changing the orientation of the connecting link, one of its key components. The result of the implementation of HDF is described in the next paragraphs.

The methodological approach followed in the implementation of the HDF consist of three phases. Firstly, a mathematical model of the HDF design was implemented to test its functioning, secondly the HDF was built and finally it was tested. The relationship between the orientation of the connecting link and the threshold torque is best described by an exponential curve in the mathematical model while it is best fit by a second order equation in the experimental data. The mismatch is highest for high values of connecting link displacement. However, both curves reflect that threshold torque magnitude increases with increasing connecting link displacement.

This is the behaviour the HDF was built to achieve. This data shows that it is possible to set the threshold torque of the HDF to make the INTRO-BRL arm usable in different scenarios. Furthermore, the adjustment of the threshold torque can be set off-line, so that once the arm begins functioning its behaviour still retains all the passive characteristics listed above. The flexibility shown by the ability to change the torque threshold is the HDF's main advantage over the passive structures already in the literature. The HDF combines the flexibility of active mechanisms with the inherent safety of passive ones.

The testing of the HDF's passive mechanism revealed that the decoupling of the motor from the link is triggered only if the collision force exceeds a certain fixed limit. Any external force below such a threshold value will not impact on the arm's stiffness and accuracy. Because of the possibility to set the threshold torque in the HDF, it can be used at a setting that ensures that collision forces below the threshold of human pain should not compromise the functionality of the arm.

In addition, there are other arguments that can be used in claiming that the overall INTRO-BRL arm structure is intrinsically safe. For example: the inertia of the link, gripper and part of the decoupling joint that decouples together with the link is only 3.5kg, which is an important factor for safety in constrained impacts. Furthermore, motors and gearbox systems that do not enable high velocities to be reached are utilised, which is also an important factor for inherent safety. Additionally, the stiffness of the spring inserted in the HDF is as low as 1.74N/mm, thus the maximum stored elastic potential energy for a compression of 20mm, which is almost a maximum compression, is 0.348 joules. In order to give a practical example of such value, 0.348 joules are equivalent to the potential energy of 355 grams held 10cm above the ground. This magnitude of stored potential energy is unlikely to pose a threat for the user but it is enough to return the decoupling joint to the initial position once the collision contact is over. Minimising the stored elastic potential energy due to the spring is important since it has been pointed out that a considerable amount of energy can be stored in the spring components of variable compliance structures, which can create high link velocities, and thus be unsafe.

Variable compliance has also been utilised in this thesis' work in the grasping domain. The HS gripper, a variable compliance, novel gripper with simple, inexpensive structure can effectively grasp and hold cylindrical objects of different cross-sectional shapes without previous knowledge of their shape and with a simple open loop motor control. This is achieved thanks to its extremely compliant structure which allows it to passively conform to these objects. Unlike many continuum robots that are made of multiple compliant sections joined by rigid plates, the HS gripper is fully continuous, without any disruptions or rigid elements. This characteristic, inspired by hydrostatic skeletons, ensures adaptability to grasped objects. It has been further demonstrated that the gripper's compliance varies, ensuring both a compliant grasp

and a stable hold. This ability implies that the HS gripper is not only a novel and interesting concept but that variable compliance could be a key factor in adaptable grasping of unknown objects. In general, structural passive characteristics usually display a limited behaviour. However, the change in material properties brought about by the interaction between the water and the shell in the HS gripper remedies this shortcoming by passively coupling the appropriate degree of stiffness to each phase of the grasping task.

The absence of rigid structures, present in the HS gripper's design, has been pointed out in the description of similarly soft end-effectors as a safety factor. In general, soft structures are looked upon as inherently safer than rigid ones, but it could be argued that the forces in the gripper itself are not big enough to cause any harm. However, soft manipulators and grippers with their comparatively large contact areas, might be useful in order to prevent small force clamping injuries. They are not life-threatening but would be best avoided for comfortable interaction for the human user.

6.2 Future Work

Outside the scope of this thesis' work but possible future work on the HDF mechanism should involve its downsizing. This would further reduce the mass of the robotic arm. Furthermore, the downsizing would be important since a system like the HDF would have maximum effect if placed close to the end-effector. This is because many collisions take place at the end-effector and in that position a HDF-similar system would be able to decouple most of the robot arm's mass from the part involved in the collision.

In the experiments described in this thesis the HDF is adjusted off-line. However, the HDF's structure would also allow online adjustment of the threshold torque and since the adjustment time is short relative to the robot velocity, this would impact minimally on the intrinsic safety of the HDF. In order to determine when to switch from a threshold torque to the other, a set of sensors surrounding the INTRO-BRL arm would be necessary. These sensors would give the whole INTRO-BRL arm-HDF system the awareness to distinguish between situations in which a low threshold torque is required rather than a high threshold torque.

The HDF showed the ability to change its threshold torque while keeping the ability to passively decouple the system in case of collision. However, with the present design of the HDF, this only works in one dimension. It would be desirable to modify the HDF structure so that it works in two or three dimensions. The importance of such modification is reinforced by the high values obtained for the INTRO-BRL arm's potential energy in Chapter 3. These high values entail that if the arm were to drop vertically, it could possibly cause harm on a user. In this case,

a HDF which decouples in case of high collision forces along the vertical direction could help improve the safety of the system. Additionally, designing a completely passive safety mechanism also entails drawbacks. One of the main issues of the HDF is that it is triggered by different forces depending on the point of application of the external force. This issue is dealt with by keeping the threshold torque low so that the risk of harm is decreased. A further improvement to the overall safety of the INTRO-BRL arm would be to cover the arm's link with a cone shaped compliant shell. The shell would partially absorb the collision force. If more compliant material were used at the base than at the tip, this would reduce the impact of forces acting at the base. Less compliant material at the end-effector would prove useful to avoid impairing interaction with grasped objects.

Future work on the HS gripper could comprise the use of a composite material for the shell, which would provide better resistance to wear than polyethylene. The use of sensors to detect contact with the object should also be considered, to further improve the ability of the gripper to interact with the environment. Furthermore, to ensure that every direction of the passive compliance is exploited to aid the grasping action, the number of cables in the gripper should be increased to six. Thus, the gripper would be able to grasp in any orientation in space exploiting fully its continuum and omnidirectional compliance. A further direction of research could be the identification of the gripper's trajectories during object grasping when the gripper is not resting on a table.

Additionally, since the HS gripper's ability to vary its compliance and to adaptively grasp different cross-section objects has been shown in the experiments, it would be possible to replicate its design in order to grasp a wider range of objects. The HS gripper only addresses the grasping of certain forms (a height of at least 50mm is necessary), even if these forms can display a great variability in their shape. In its present design, it cannot grasp a flat object like a plate. In order to achieve this, it would be necessary to replicate the design of this device and assemble them in a gripper with multiple 'digits'. This new structure would be able to trap objects between digits and thus grasping a wider selection of objects compared to the current version of the HS gripper.

6.3 Contribution to the Robotics Field

In summary, the aim of this thesis' work, exploiting the concept of variable compliance to design and produce a robot arm with inherently safe features and a gripper which can adaptively mould its shape to objects has been achieved within the constraints of the experimental scenario under consideration. Variable compliance has been used in a mechanically rigid structure for safety purposes, while it has been utilised in a soft structure to fulfil a grasping task. In both cases, variable

compliance has been proved crucial in reaching the end-goal. Also in the research statement, the principles of embodied intelligence and bioinspiration are named as viable sources of inspiration for this thesis' work. Bioinspiration has proven to be of utmost importance in identifying the working mechanism of the underactuated HS gripper. Additionally, embodied intelligence has been relevant for the development of both the HDF and the HS gripper. The very structure of the HDF is the element which ensures a passive response to external collisions. By decoupling the rest of the INTRO-BRL arm inertia from the link and end-effector, the negative effect of collisions potentially harmful to the human user can be lessened. Similarly, the materials and morphology of the HS gripper are relevant in ensuring its variable compliance capabilities. For example, the effective incompressibility of degassed water ensures the desired fast transition between the initial compliant phase to the final rigid one.

In brief, both the HDF and the HS gripper have been designed to bring about safe and effective performance of the INTRO-BRL robot arm. Both systems have been built and experiments have been conducted on their performance, showing that the devices achieve their goals and pave the way for future implementations of variable compliance safety and grasping devices. These implementations would be very useful in the field of domestic assistive robotics, since they would help allow a safe and effective interaction of the robot arm with the human user. However, the possible applications of the systems shown are much wider and variable compliance, both in its mechanically rigid and soft declination, has shown to be a major component of a successful robot arm system for physical human-robot interaction.

Bibliography

- [Amend et al., 2012] Amend, J. R., Brown, E. M., Rodenberg, N., Jaeger, H. M., and Lipson, H. (2012). A positive pressure universal gripper based on the jamming of granular material. *Robotics, IEEE Transactions on*, 28(2):341–350.
- [Aoki et al., 2002] Aoki, T., Ohno, H., and Hirose, S. (2002). Design of slim slime robot ii (ssr-ii) with bridle bellows. In *Intelligent Robots and Systems, 2002. IEEE/RSJ International Conference on*, volume 1, pages 835–840. IEEE.
- [Avdeev et al., 2011] Avdeev, A., Eremenko, T., Festy, P., Gaymu, J., Bouteillec, N. L., and Springer, S. (2011). Populations and demographic trends of european countries, 1980-2010. *Population (english edition)*, 66(1):9–129.
- [Bicchi et al., 2008] Bicchi, A., Bavaro, M., Boccadamo, G., De Carli, D., Filippini, R., Grioli, G., Piccigallo, M., Rosi, A., Schiavi, R., Sen, S., et al. (2008). Physical human-robot interaction: Dependability, safety, and performance. In *Advanced Motion Control, 2008. AMC'08. 10th IEEE International Workshop on*, pages 9–14. IEEE.
- [Bicchi and Kumar, 2000] Bicchi, A. and Kumar, V. (2000). Robotic grasping and contact: A review. In *ICRA*, pages 348–353. Citeseer.
- [Bischoff et al., 2010] Bischoff, R., Kurth, J., Schreiber, G., Koeppe, R., Albuschäffer, A., Beyer, A., Eiberger, O., Haddadin, S., Stemmer, A., Grunwald, G., et al. (2010). The kuka-dlr lightweight robot arm-a new reference platform for robotics research and manufacturing. In *Robotics (ISR), 2010 41st international symposium on and 2010 6th German conference on robotics (ROBOTIK)*, pages 1–8. VDE.
- [Broekens et al., 2009] Broekens, J., Heerink, M., and Rosendal, H. (2009). Assistive social robots in elderly care: a review. *Gerontechnology*, 8(2):94–103.
- [Brown et al., 2010] Brown, E., Rodenberg, N., Amend, J., Mozeika, A., Steltz, E., Zakin, M. R., Lipson, H., and Jaeger, H. M. (2010). Universal robotic gripper based on the jamming of granular material. *Proceedings of the National Academy of Sciences*, 107(44):18809–18814.

- [Calisti et al., 2010] Calisti, M., Arienti, A., Giannaccini, M., Follador, M., Giorelli, M., Cianchetti, M., Mazzolai, B., Laschi, C., and Dario, P. (2010). Study and fabrication of bioinspired octopus arm mockups tested on a multipurpose platform. In *Biomedical Robotics and Biomechatronics (BioRob), 2010 3rd IEEE RAS and EMBS International Conference on*, pages 461–466. IEEE.
- [Camarillo et al., 2009] Camarillo, D. B., Carlson, C. R., and Salisbury, J. K. (2009). Configuration tracking for continuum manipulators with coupled tendon drive. *Robotics, IEEE Transactions on*, 25(4):798–808.
- [Camarillo et al., 2008] Camarillo, D. B., Milne, C. F., Carlson, C. R., Zinn, M. R., and Salisbury, J. K. (2008). Mechanics modeling of tendon-driven continuum manipulators. *Robotics, IEEE Transactions on*, 24(6):1262–1273.
- [Cheng et al., 2012] Cheng, N. G., Lobovsky, M. B., Keating, S. J., Setapen, A. M., Gero, K. I., Hosoi, A. E., and Iagnemma, K. D. (2012). Design and analysis of a robust, low-cost, highly articulated manipulator enabled by jamming of granular media. In *Robotics and Automation (ICRA), 2012 IEEE International Conference on*, pages 4328–4333. IEEE.
- [Chirikjian and Burdick, 1995] Chirikjian, G. S. and Burdick, J. W. (1995). Kinetically optimal hyper-redundant manipulator configurations. *Robotics and Automation, IEEE Transactions on*, 11(6):794–806.
- [Daerden and Lefeber, 2002] Daerden, F. and Lefeber, D. (2002). Pneumatic artificial muscles: actuators for robotics and automation. *European journal of mechanical and environmental engineering*, 47(1):11–21.
- [De Santis and Siciliano, 2008] De Santis, A. and Siciliano, B. (2008). Safety issues for human–robot cooperation in manufacturing systems. *Tools and Perspectives in Virtual Manufacturing*.
- [Deimel and Brock, 2013] Deimel, R. and Brock, O. (2013). A compliant hand based on a novel pneumatic actuator. In *Robotics and Automation (ICRA), 2013 IEEE International Conference on*, pages 2047–2053. IEEE.
- [Dogramadzi et al., 2014] Dogramadzi, S., Giannaccini, M. E., Harper, C., Sobhani, M., Woodman, R., and Choung, J. (2014). Environmental hazard analysis—a variant of preliminary hazard analysis for autonomous mobile robots. *Journal of Intelligent & Robotic Systems*, pages 1–45.
- [Dollar and Howe, 2010] Dollar, A. M. and Howe, R. D. (2010). The highly adaptive sdm hand: Design and performance evaluation. *The international journal of robotics research*, 29(5):585–597.

- [Eiberger et al., 2010] Eiberger, O., Haddadin, S., Weis, M., Albu-Schäffer, A., and Hirzinger, G. (2010). On joint design with intrinsic variable compliance: derivation of the dlr qa-joint. In *ICRA*, pages 1687–1694.
- [Engineeringtoolbox, 2013] Engineeringtoolbox (2013). engineeringtoolbox. <http://www.engineeringtoolbox.com/bulk-modulus-elasticity-d585.html>. [Online; accessed 10-Dicember-2013].
- [Eppner et al., 2012] Eppner, C., Bartels, G., and Brock, O. (2012). A compliance-centric view of grasping. Technical report, Technical Report.
- [Feix et al., 2009] Feix, T., Pawlik, R., Schriedmayer, H.-B., Romero, J., and Kragic, D. (2009). A comprehensive grasp taxonomy. In *Robotics, Science and Systems: Workshop on Understanding the Human Hand for Advancing Robotic Manipulation*, pages 2–3.
- [Festo, 2013a] Festo (2013a). festo. <http://www.festo.com/net/SupportPortal/Files/42050/BroschFCBHA30ENlo.pdf>. [Online; accessed 12-June-2013].
- [Festo, 2013b] Festo (2013b). festo. <http://www.festo.com/rep/encorp/assets/pdf/BHAen.phf>. [Online; accessed 26-February-2013].
- [Gatti, 2014] Gatti, P. L. (2014). *Applied Structural and Mechanical Vibrations: Theory and Methods*. CRC Press.
- [Giannaccini et al., 2012] Giannaccini, M., Zheng, Y., Dogramadzi, S., and Pipe, T. (2012). Towards a variable compliance hydrostatic skeleton inspired gripper. In *Biomedical Robotics and Biomechatronics (BioRob), 2012 4th IEEE RAS & EMBS International Conference on*, pages 246–251. IEEE.
- [Giannaccini et al., 2014] Giannaccini, M. E., Georgilas, I., Horsfield, I., Peiris, B., Lenz, A., Pipe, A. G., and Dogramadzi, S. (2014). A variable compliance, soft gripper. *Autonomous Robots*, 36(1-2):93–107.
- [Grebenstein et al., 2011] Grebenstein, M., Albu-Schffer, A., Bahls, T., Chalon, M., Eiberger, O., Friedl, W., Gruber, R., Haddadin, S., Hagn, U., Haslinger, R., et al. (2011). The dlr hand arm system. In *Robotics and Automation (ICRA), 2011 IEEE International Conference on*, pages 3175–3182. IEEE.
- [Haddadin, 2014] Haddadin, S. (2014). Considerations for new robot standards. In *Towards Safe Robots*, pages 317–336. Springer.
- [Haddadin et al., 2008] Haddadin, S., Albu-Schaffer, A., De Luca, A., and Hirzinger, G. (2008). Collision detection and reaction: A contribution to safe physical human-robot interaction. In *Intelligent Robots and Systems, 2008. IROS 2008. IEEE/RSJ International Conference on*, pages 3356–3363. IEEE.

- [Haddadin et al., 2010] Haddadin, S., Albu-Schaffer, A., Eiberger, O., and Hirzinger, G. (2010). New insights concerning intrinsic joint elasticity for safety. In *Intelligent Robots and Systems (IROS), 2010 IEEE/RSJ International Conference on*, pages 2181–2187. IEEE.
- [Haddadin et al., 2009] Haddadin, S., Albu-Schäffer, A., and Hirzinger, G. (2009). Requirements for safe robots: Measurements, analysis and new insights. *The International Journal of Robotics Research*, 28(11-12):1507–1527.
- [Ham et al., 2009] Ham, R. v., Sugar, T. G., Vanderborght, B., Hollander, K. W., and Lefeber, D. (2009). Compliant actuator designs. *Robotics & Automation Magazine, IEEE*, 16(3):81–94.
- [Hirata et al., 2000] Hirata, K. et al. (2000). Development of experimental fish robot. In *Sixth International Symposium on Marine Engineering*, pages 235–240.
- [Hirose and Umetani, 1978] Hirose, S. and Umetani, Y. (1978). The development of soft gripper for the versatile robot hand. *Mechanism and machine theory*, 13(3):351–359.
- [Hirzinger et al., 2001] Hirzinger, G., Albu-Schaffer, A., Hahnle, M., Schaefer, I., and Sporer, N. (2001). On a new generation of torque controlled light-weight robots. In *Robotics and Automation, 2001. Proceedings 2001 ICRA. IEEE International Conference on*, volume 4, pages 3356–3363. IEEE.
- [Hogan, 1984] Hogan, N. (1984). Impedance control: An approach to manipulation. In *American Control Conference, 1984*, pages 304–313. IEEE.
- [Icosym-nt, 2013] Icosym-nt (2013). icosym-nt. <http://icosym-nt.cvut.cz/odl/partners/fuh/coursemain/coursemain.html>. [Online; accessed 20-September-2013].
- [idspackaging.com, 2014] idspackaging.com (2014). Corona Treatment. http://www.idspackaging.com/common/paper/Paper_262/Corona%20treatment.pdf. [Online; accessed 18-May-2012].
- [Ikuta et al., 2003] Ikuta, K., Ishii, H., and Nokata, M. (2003). Safety evaluation method of design and control for human-care robots. *The International Journal of Robotics Research*, 22(5):281–297.
- [Ilievski et al., 2011] Ilievski, F., Mazzeo, A. D., Shepherd, R. F., Chen, X., and Whitesides, G. M. (2011). Soft robotics for chemists. *Angewandte Chemie*, 123(8):1930–1935.
- [ISO13482, 2014] ISO13482 (2014). Robots and robotic devices – Safety requirements for personal care robots.

- [Jien et al., 2009] Jien, S., Hirai, S., Ogawa, Y., Ito, M., and Honda, K. (2009). Pressure control valve for McKibben artificial muscle actuators with miniaturized unconstrained pneumatic on/off valves. In *Advanced Intelligent Mechatronics, 2009. AIM 2009. IEEE/ASME International Conference on*, pages 1383–1388. IEEE.
- [Jones and Walker, 2006a] Jones, B. A. and Walker, I. D. (2006a). Kinematics for multisection continuum robots. *Robotics, IEEE Transactions on*, 22(1):43–55.
- [Jones and Walker, 2006b] Jones, B. A. and Walker, I. D. (2006b). Practical kinematics for real-time implementation of continuum robots. *Robotics, IEEE Transactions on*, 22(6):1087–1099.
- [Kelly, 2007] Kelly, D. A. (2007). Penises as variable-volume hydrostatic skeletons. *Annals of the New York Academy of Sciences*, 1101(1):453–463.
- [Kier, 2012] Kier, W. M. (2012). The diversity of hydrostatic skeletons. *The Journal of experimental biology*, 215(8):1247–1257.
- [Kier and Smith, 1985] Kier, W. M. and Smith, K. K. (1985). Tongues, tentacles and trunks: the biomechanics of movement in muscular-hydrostats. *Zoological Journal of the Linnean Society*, 83(4):307–324.
- [KinovaRobotics, 2013] KinovaRobotics (2013). kinovarobotics. <http://kinovarobotics.com/products/jaco-research-edition/>. [Online; accessed 30-June-2013].
- [Kumar, 2015] Kumar, V. (2015). Background Twists in Kinematics and Wrenches in Statics. <ftp://ftp.cis.upenn.edu/pub/kumar/workshops/screwtheory/Background.ppt>. [Online; accessed 16-October-2015].
- [Lane et al., 1999] Lane, D. M., Davies, J. B. C., Robinson, G., O’Brien, D. J., Sneddon, J., Seaton, E., and Elfstrom, A. (1999). The amadeus dextrous sub-sea hand: design, modeling, and sensor processing. *Oceanic Engineering, IEEE Journal of*, 24(1):96–111.
- [Laschi et al., 2012] Laschi, C., Cianchetti, M., Mazzolai, B., Margheri, L., Follador, M., and Dario, P. (2012). Soft robot arm inspired by the octopus. *Advanced Robotics*, 26(7):709–727.
- [Lens et al., 2010] Lens, T., Kunz, J., Stryk, O. v., Trommer, C., and Karguth, A. (2010). Biorob-arm: A quickly deployable and intrinsically safe, light-weight robot arm for service robotics applications. In *Robotics (ISR), 2010 41st International Symposium on and 2010 6th German Conference on Robotics (ROBOTIK)*, pages 1–6. VDE.

- [Lens et al., 2011] Lens, T., Radkhah, K., and Von Stryk, O. (2011). Simulation of dynamics and realistic contact forces for manipulators and legged robots with high joint elasticity. In *Advanced Robotics (ICAR), 2011 15th International Conference on*, pages 34–41. IEEE.
- [Ma et al., 2013] Ma, R. R., Odhner, L. U., and Dollar, A. M. (2013). A modular, open-source 3d printed underactuated hand. In *Robotics and Automation (ICRA), 2013 IEEE International Conference on*, pages 2737–2743. IEEE.
- [Maghooa et al., 2015] Maghooa, F., Stilli, A., Noh, Y., Althoefer, K., and Wurde-
mann, H. A. (2015). Tendon and pressure actuation for a bio-inspired manipulator based on an antagonistic principle. In *Robotics and Automation (ICRA), 2015 IEEE International Conference on*, pages 2556–2561. IEEE.
- [Maheu et al., 2011] Maheu, V., Frappier, J., Archambault, P. S., and Routhier, F. (2011). Evaluation of the jaco robotic arm: Clinico-economic study for powered wheelchair users with upper-extremity disabilities. In *Rehabilitation Robotics (ICORR), 2011 IEEE International Conference on*, pages 1–5. IEEE.
- [Marghitu, 2001] Marghitu, D. B. (2001). *Mechanical engineer’s handbook*. academic press.
- [McMahan et al., 2006] McMahan, W., Chitrakaran, V., Csencsits, M., Dawson, D., Walker, I. D., Jones, B. A., Pritts, M., Dienno, D., Grissom, M., and Rahn, C. D. (2006). Field trials and testing of the octarm continuum manipulator. In *Robotics and Automation, 2006. ICRA 2006. Proceedings 2006 IEEE International Conference on*, pages 2336–2341. IEEE.
- [Meijer et al., 2003] Meijer, K., Bar-Cohen, Y., and Full, R. (2003). Biological inspiration for musclelike actuators of robots. *Biologically Inspired Intelligent Robots*, 122:25.
- [Melia et al., 2014] Melia, M., Schmidt, M., Geissler, B., König, J., Krahn, U., Ottersbach, H. J., Letzel, S., and Muttray, A. (2014). Measuring mechanical pain: The refinement and standardization of pressure pain threshold measurements. *Behavior research methods*, pages 1–12.
- [Menciassi et al., 2006] Menciassi, A., Accoto, D., Gorini, S., and Dario, P. (2006). Development of a biomimetic miniature robotic crawler. *Autonomous Robots*, 21(2):155–163.
- [Neppalli et al., 2009] Neppalli, S., Csencsits, M. A., Jones, B. A., and Walker, I. D. (2009). Closed-form inverse kinematics for continuum manipulators. *Advanced Robotics*, 23(15):2077–2091.

- [Neppalli and Jones, 2007] Neppalli, S. and Jones, B. A. (2007). Design, construction, and analysis of a continuum robot. In *Intelligent Robots and Systems, 2007. IROS 2007. IEEE/RSJ International Conference on*, pages 1503–1507. IEEE.
- [Nurzaman et al., 2013] Nurzaman, S. G., Iida, F., Laschi, C., Ishiguro, A., and Wood, R. (2013). Soft robotics.
- [OxfordDictionary, 2014] OxfordDictionary (2014). compliance. <http://www.oxforddictionaries.com/definition/english/compliance>. [Online; accessed 11-February-2014].
- [Özcan et al., 2004] Özcan, A., Tulum, Z., Pınar, L., and Başkurt, F. (2004). Comparison of pressure pain threshold, grip strength, dexterity and touch pressure of dominant and non-dominant hands within and between right-and left-handed subjects. *Journal of Korean medical science*, 19(6):874–878.
- [Park et al., 2007] Park, J.-J., Kim, B.-S., Song, J.-B., and Kim, H.-S. (2007). Safe link mechanism based on passive compliance for safe human-robot collision. In *Robotics and Automation, 2007 IEEE International Conference on*, pages 1152–1157. IEEE.
- [Park et al., 2009] Park, J.-J., Kim, H.-S., and Song, J.-B. (2009). Safe robot arm with safe joint mechanism using nonlinear spring system for collision safety. In *Robotics and Automation, 2009. ICRA'09. IEEE International Conference on*, pages 3371–3376. IEEE.
- [Park et al., 2008] Park, J.-J., Lee, Y.-J., Song, J.-B., and Kim, H.-S. (2008). Safe joint mechanism based on nonlinear stiffness for safe human-robot collision. In *Robotics and Automation, 2008. ICRA 2008. IEEE International Conference on*, pages 2177–2182. IEEE.
- [Pfeifer et al., 2007] Pfeifer, R., Lungarella, M., and Iida, F. (2007). Self-organization, embodiment, and biologically inspired robotics. *science*, 318(5853):1088–1093.
- [Pratt and Williamson, 1995] Pratt, G. A. and Williamson, M. M. (1995). Series elastic actuators. In *Intelligent Robots and Systems 95. 'Human Robot Interaction and Cooperative Robots', Proceedings. 1995 IEEE/RSJ International Conference on*, volume 1, pages 399–406. IEEE.
- [Raibert and Craig, 1981] Raibert, M. H. and Craig, J. J. (1981). Hybrid position/-force control of manipulators. *Journal of Dynamic Systems, Measurement, and Control*, 103(2):126–133.
- [Robotics, 2008] Robotics, O. (2008). Snake-arm robots access the inaccessible. *Nuclear Technology International*, 1:92–94.

- [Sardellitti et al., 2012] Sardellitti, I., Medrano-Cerda, G., Tsagarakis, N. G., Jafari, A., and Caldwell, D. G. (2012). A position and stiffness control strategy for variable stiffness actuators. In *Robotics and Automation (ICRA), 2012 IEEE International Conference on*, pages 2785–2791. IEEE.
- [Schunk, 2013] Schunk (2013). schunk. <http://www.gb.schunk.com>. [Online; accessed 30-January-2013].
- [Sciavicco and Siciliano, 2000] Sciavicco, L. and Siciliano, B. (2000). *Modelling and control of robot manipulators*. Springer.
- [ShadowRobotCompany, 2013] ShadowRobotCompany (2013). shadow. <http://www.shadowrobot.com/hand/motorhand>. [Online; accessed 26-February-2013].
- [Siciliano and Khatib, 2008] Siciliano, B. and Khatib, O. (2008). *Springer handbook of robotics*. Springer.
- [Spong et al., 2006] Spong, M. W., Hutchinson, S., and Vidyasagar, M. (2006). *Robot modeling and control*, volume 3. Wiley New York.
- [Standford, 2014] Standford (2014). impedance. <https://ccrma.stanford.edu/~jos/pasp/Impedance.html>. [Online; accessed 11-February-2014].
- [Stilli et al., 2014] Stilli, A., Wurdemann, H., and Althoefer, K. (2014). Shrinkable, stiffness-controllable soft manipulator based on a bio-inspired antagonistic actuation principle. In *Intelligent Robots and Systems (IROS 2014), 2014 IEEE/RSJ International Conference on*, pages 2476–2481. IEEE.
- [Taylor et al., 2007] Taylor, J. R., Hebrank, J., and Kier, W. M. (2007). Mechanical properties of the rigid and hydrostatic skeletons of molting blue crabs, callinectes sapidus rathbun. *Journal of Experimental Biology*, 210(24):4272–4278.
- [Taylor and Kier, 2003] Taylor, J. R. and Kier, W. M. (2003). Switching skeletons: hydrostatic support in molting crabs. *Science*, 301(5630):209–210.
- [Tonazzini et al., 2012] Tonazzini, A., Popova, L., Mattioli, F., and Mazzolai, B. (2012). Analysis and characterization of a robotic probe inspired by the plant root apex. In *Biomedical Robotics and Biomechatronics (BioRob), 2012 4th IEEE RAS & EMBS International Conference on*, pages 1134–1139. IEEE.
- [Totten, 1999] Totten, G. E. (1999). *Handbook of hydraulic fluid technology*, volume 125. CRC Press.
- [Trimmer et al., 2006] Trimmer, B. A., Takesian, A. E., Sweet, B. M., Rogers, C. B., Hake, D. C., and Rogers, D. J. (2006). Caterpillar locomotion: a new model for soft-bodied climbing and burrowing robots. In *7th International Symposium on*

Technology and the Mine Problem, volume 1, pages 1–10. Mine Warfare Association Monterey, CA.

- [Trivedi et al., 2008] Trivedi, D., Rahn, C. D., Kier, W. M., and Walker, I. D. (2008). Soft robotics: Biological inspiration, state of the art, and future research. *Applied Bionics and Biomechanics*, 5(3):99–117.
- [Vaidyanathan et al., 2000] Vaidyanathan, R., Chiel, H. J., and Quinn, R. D. (2000). A hydrostatic robot for marine applications. *Robotics and Autonomous Systems*, 30(1):103–113.
- [Vanderborght et al., 2013] Vanderborght, B., Albu-Schäffer, A., Bicchi, A., Burdet, E., Caldwell, D. G., Carloni, R., Catalano, M., Eiberger, O., Friedl, W., Ganesh, G., et al. (2013). Variable impedance actuators: A review. *Robotics and Autonomous Systems*, 61(12):1601–1614.
- [Villani and De Schutter, 2008] Villani, L. and De Schutter, J. (2008). Force control. *Springer Handbook of Robotics*, pages 161–185.
- [Webster and Jones, 2010] Webster, R. J. and Jones, B. A. (2010). Design and kinematic modeling of constant curvature continuum robots: A review. *The International Journal of Robotics Research*.
- [Webster et al., 2009] Webster, R. J., Romano, J. M., and Cowan, N. J. (2009). Mechanics of precurved-tube continuum robots. *Robotics, IEEE Transactions on*, 25(1):67–78.
- [Xu and Simaan, 2008] Xu, K. and Simaan, N. (2008). An investigation of the intrinsic force sensing capabilities of continuum robots. *Robotics, IEEE Transactions on*, 24(3):576–587.
- [Zinn et al., 2002] Zinn, M., Khatib, O., Roth, B., and Salisbury, J. K. (2002). Towards a human-centered intrinsically safe robotic manipulator. In *IARPIEEE/RAS joint workshop on technical challenges for dependable robots in human environments, Toulouse, France*.
- [Zinn et al., 2004] Zinn, M., Roth, B., Khatib, O., and Salisbury, J. K. (2004). A new actuation approach for human friendly robot design. *The international journal of robotics research*, 23(4-5):379–398.

Appendices

Appendix A

Appendix of Chapter 3

This appendix is relative to the code used for the analysis developed in Chapter 3.

A.1 Matlab Code for the INTRO-BRL arm

Code for the calculation of potential and kinetic energy of the INTRO-BRL arm:

```
%calculation of Kinematic and Potential Energy from Kinematic
parameters
%in this case, differently from the kinematics and e e velocities .m
files
%the parametres a1 and a2 have been substituted with l2 and l3 which
are
%the distances from the joints to the links' centres of mass. l1 is a
%constant due to the specific configuration of BIA; l2 is

%clear; clc; close;

syms t l2 l3 a3 m0 m1 m2 m3 g a2

d1 = sym('d1(t)');
%q2 = sym('q2(t)');
q2 = pi/4; %sym('q2(t)');
l2 = 62.5;
q3 = sym('q3(t)');
c3 = cos(q3);
s3 = sin(q3);

% transformation matrix from RF1 to RF0
R1 = [[1 0 0 0]; [0 1 0 0]; [0 0 1 d1]; [0 0 0 1]];
% transformation matrix from RF2 to RF1
R2 = [[cos(q2) sin(q2) 0 (l2*cos(q2))]; [sin(q2) cos(q2) 0 (l2*sin(q2)
)]; [0 0 1 0]; [0 0 0 1]];
```

```

% transformation matrix from RF2 to RF1 with a2
R2a = [[ cos(q2)  sin(q2)  0  (a2*cos(q2))]; [ sin(q2)  cos(q2)  0  (a2*sin(q2)
    )]]; [0  0  1  0]; [0  0  0  1]];
% transformation matrix from RF3 to RF2
R3 = [[c3  s3  0  (l3*c3)]; [s3  c3  0  (l3*s3)]; [0  0  1  0]; [0  0  0  1]];

% transformation matrix from RF2 to RF0
T1 = R1*R2;
% transformation matrix from RF2 to RF0 with a2
T1a = R1*R2a;
% transformation matrix from RF3 to RF0
T2 = T1a*R3;

%Creating the geometric Jacobian
%Position of the origin of RF0
O0 = [0  0  0];
%Position of the origin of RF1
O1 = R1(1:3,4);
%Position of the origin of RF2
O2 = T1(1:3,4);
%Position of the origin of RF3
O3 = T2(1:3,4);
%Jo for a prismatic joint
A = [0; 0; 0];
%Jq for a prismatic joint or Jo for a revolute one
B = [0; 0; 1];
%origin difference for second column J1
D0 = O2 - O1;
%origin difference for second column J2
D1 = O3 - O1;
%origin difference for third column J2
D2 = O3 - O2;
%Cross product for second column J1
CR0 = cross(B,D0);
%Cross product for second column J2
CR1 = cross(B,D1);
%Cross product for third column J2
CR2 = cross(B,D2);

%Geometric jacobian of Link 0
J0p = [0  0  1; 0  0  0; 0  0  0]';
J0o = [0  0  0; 0  0  0; 0  0  0]';
%Geometric jacobian of Link 1
J1p = [B CR0 A];
J1o = [0  0  0; 0  0  1; 0  0  0]';
%Geometric jacobian of Link 2
J2p = [B CR1 CR2];
J2o = [0  0  0; 0  0  1; 0  0  1]';

```

```

%Velocities in the Joint space
dq = [diff(d1,t); diff(q2,t); diff(q3,t)];

%Velocities at the end effector in the Cartesian space
%This gives a vector with Xvel, Yvel, Zvel
C = J2p*dq;

%Kinetic Energy calculation: the link length must be divided by 2 since
the
%centre of mass is the point being considered, also the inertia tensor
must
%also be considered at the centre of mass

%Kin Energy Link 0
K0 = (1/2)*transpose(dq)*m0*transpose(J0p)*J0p*dq;
%Kin Energy Link 1
K1 = (1/2)*transpose(dq)*m1*transpose(J1p)*J1p*dq;
%Kin Energy of Link 2, since omegas are aligned with the z axes of each
joint coordinate frame,
%the rotational kinetic energy reduces to I*omega^2, where I is is the
%moment of inertia about an axis through the centre of mass of the link
and
%parallel to the z axis
K2 = (1/2)*transpose(dq)*m2*transpose(J2p)*J2p*dq + transpose(dq)*
transpose(J2o)*((m2*(a3^2))/12)*J2o*dq;

K = expand(K0 + K1 + K2 );

m0 = 0.3; %mass of the moving plate in vertical column: in kg
m1 = 0.98; %mass of non rotating link: in kg
m2 = 1.87; %mass of rotating link: in kg
m3 = 0.34; %mass of holder , gripper and payload: in kg
g = 9.8;
a2 = 0.125; %full lenght of non rotating link... in m
l3 = 0.0625;
a3 = 0.660; %arm length..should be in m
v1 = 0:0.001:0.13; %m/sec velocity of prismatic joint 0:0.001:0.13;
%v2 = 0; %m/sec velocity of the fixed proximal link
v3 = 0:0.0184:2.41; % rps*2*pi = rad/sec 0:0.0184:2.41;

K0 = (m0*v1.^2)/2;
K1 = (m1*v1.^2)/2;
K2 = (1/2)*m2*v1.^2 + (1/2)*m2*l3^2.*v3.^2 + (1/12)*a3*m2.*v3.^2;
K3 = (1/2)*m3*v1.^2 + 1/2*a3*m3*v3.^2;

% Total of Kinetic Energy
K = K0 + K1 + K2 + K3;

```

```

figure
plot(v3,K)
xlabel('velocity (rad/sec)', 'FontSize',12)
ylabel('KinEn (Joules)', 'FontSize',12)

d = 0:0.001:0.500; %mm of arm height

% Potential energy: given by the gravitational force that acts on links
% 0, 1, 2 and gripper and payload m3 at the relative centres of
% gravity
P = (m0+m1+m2+m3)*g*d;

figure
plot (d,P)
xlabel('height (m)', 'FontSize',12)
ylabel('PotEn (Joules)', 'FontSize',12)

```

Appendix B

Appendix of Chapter 4

This appendix is relative to the force and torque analysis of the background material, Section B.1, additional information about the HDF mathematical model, Section B.2 and further analysis on the Design-testing experiments presented in Chapter 4, Section B.4.

B.1 Background work on Hybrid Decoupling Feature

By utilising the free body diagram method on the connecting link, of length l_2 , shown in Figure B.1, it is possible to analyse the forces and torques acting on the mechanical body. The friction forces due to the sliding of the connecting link against the frame are marked in Figure B.1 as F_{frv} and F_{frh} . Utilising Coulomb's law these forces are written as the product of the friction coefficient and the normal force. Since this is an analysis of the static equilibrium, it was chosen to use the static friction coefficient. After the balance of the forces along the x axis and the y axis is considered, the torques around point A are taken into account.

Forces along the x axis:

$$-\vec{F}_H + \vec{F}'_S \sin \epsilon - \mu_s \vec{F}'_s \cos \epsilon = 0 \quad (\text{B.1})$$

Forces along the y axis:

$$-\vec{F}_S + \vec{F}'_s \cos \epsilon - \mu_s \vec{F}_H = 0 \quad (\text{B.2})$$

where $\mu_s \vec{F}_H$ and $\mu_s \vec{F}'_s \cos \epsilon$ are friction forces directed against the direction of

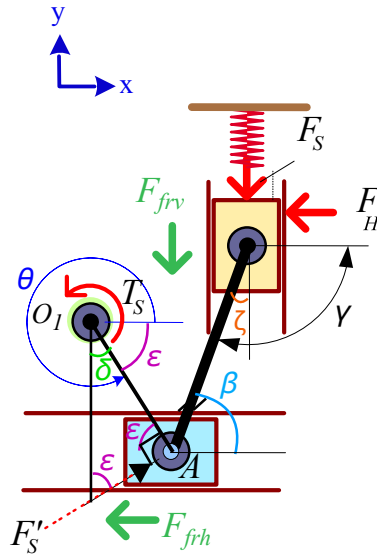


Figure B.1: Diagram for the connecting link. The friction forces are in green.

movement. Torques around point A are:

$$-\vec{F}_S l_2 \cos \beta - \vec{F}_H l_2 \sin \beta - \mu_s \vec{F}_H l_2 \cos \beta = 0 \quad (\text{B.3})$$

By substituting the value obtained for F_H in Eqn. B.1 inside Eqn. B.3 it is possible to obtain:

$$-\vec{F}_S l_2 \cos \beta = -\vec{F}_S (\sin \epsilon - \mu_s \cos \epsilon) l_2 (\sin \beta - \mu_s \cos \beta) \quad (\text{B.4})$$

$$\vec{F}_S = \frac{\vec{F}_S \cos \beta}{(\sin \epsilon - \mu_s \cos \epsilon)(\sin \beta - \mu_s \cos \beta)} \quad (\text{B.5})$$

As it can be observed in Figure B.1, $\epsilon = 2\pi - \theta$. Then the following trigonometric identities are utilised to substitute ϵ with the angle θ , which can be directly related to the mechanism as seen in Figure 4.2.

$$\sin(2\pi - \theta) = -\sin \theta \quad (\text{B.6})$$

$$\cos(2\pi - \theta) = \cos \theta \quad (\text{B.7})$$

In order to relate the free body diagram equations to the angle γ , which is called transmission angle, a similar method is followed. By observing Figure B.1 it is clear

that $\gamma = \zeta + \frac{\pi}{2}$ and that $\beta + \zeta = \frac{\pi}{2}$. By substituting the first expression into the second, it results that:

$$\beta = \pi - \gamma \quad (\text{B.8})$$

Taking into consideration the trigonometric identity $\sin(\pi - \gamma) = \sin\gamma$, $\cos(\pi - \gamma) = -\cos\gamma$ and uniting it with the previous observations then it is possible to rewrite Eqn. B.5 as:

$$\vec{F}_s = \frac{-\vec{F}_s \cos\gamma}{(-\sin\theta - \mu_s \cos\theta)(\sin\gamma + \mu_s \cos\gamma)} \quad (\text{B.9})$$

Equation B.9 relates the balance between the torque created by the spring force and the structural reaction to it before any external force is applied. Substituting this result in the expression for the spring torque: $\vec{T}_s = \vec{F}_s d$ and knowing that \vec{F}_s can be substituted by the product between the spring stiffness, k , and the spring pre-compression, s_0 , the mathematical expression for \vec{T}_s becomes:

$$\vec{T}_s = \frac{dks \cdot \cos\gamma}{(-\sin\theta - \mu_s \cos\theta)(\sin\gamma + \mu_s \cos\gamma)} \quad (\text{B.10})$$

In case an external force impacts the input link, an external torque is created. Due to the existence of the spring force caused by the spring compression, the output slider does not move until the external torque, \vec{T}_{ext} , exceeds a threshold value. The external torque required to initiate the movement of the output slider is defined as the threshold torque. Once the external torque exceeds this threshold, the spring is quickly compressed. The threshold torque is defined relative to the initial configuration of the mechanism, which is its configuration in normal operational time. This arrangement is shown in Figure B.2 and the threshold torque can be described as:

$$T_{th} = \frac{d_0 k * s_0 \cdot \cos\gamma_0}{(-\sin\theta_0 - \mu_s \cos\theta_0)(\sin\gamma_0 + \mu_s \cos\gamma_0)} \quad (\text{B.11})$$

Equation B.11 describes the physical principle on which the working mechanism of the SJM, shown in Figure B.2, is based on.

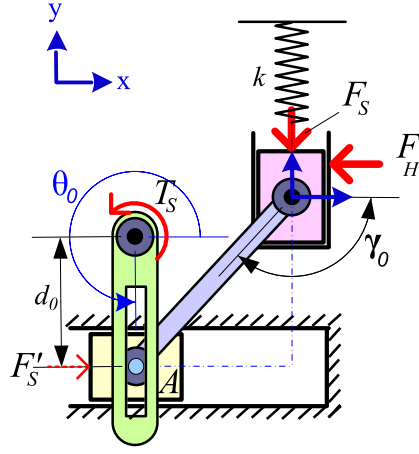


Figure B.2: The non linear spring system, composed by a double-slider mechanism with a spring, in its initial configuration [Park et al., 2008]

B.2 Intermediate Results of HDF Mathematical Model

Due to the length of the mathematical model of the HDF structure, the intermediate results, which link the position and orientation of the adjustment arm to the position and orientation of the guiding slot, are given in this appendix.

In the intermediate results, three mathematical relationships are drawn. Firstly, the required position of the adjustment arm along the bottom slot is calculated in order to get a certain guiding slot orientation. Secondly, the position of the connecting link along the spring guide is obtained as function of the position of the T-shaped element. Thirdly, the position of the connecting link along the spring guide is obtained as function of the position of the guiding slot. These mathematical relationships are useful towards the end goal of defining the relationship between the movement of the linear actuator and the threshold torque. The following mathematical relationships are obtained by considering the HDF in a static configuration. They all consider a sum of force vectors in the HDF. Since the configuration of the HDF before it is triggered is considered, the HDF is static and the sum of these vectors is zero. The overall structure of the HDF is reported in a drawing which shows the vector sum for each of the three cases.

Relationship between the adjustment arm's position and the guiding slot's position

The adjustment arm is linked with the guiding slot at the point B_2 .

The sum of vectors shown in Figure B.4 and Figure B.3 is equal to:

$$\vec{0} = \overrightarrow{O_1O_2} + \overrightarrow{O_2B_2} + \overrightarrow{B_2M_4} + \overrightarrow{M_4O_4} + \overrightarrow{O_4O_1} \quad (\text{B.12})$$

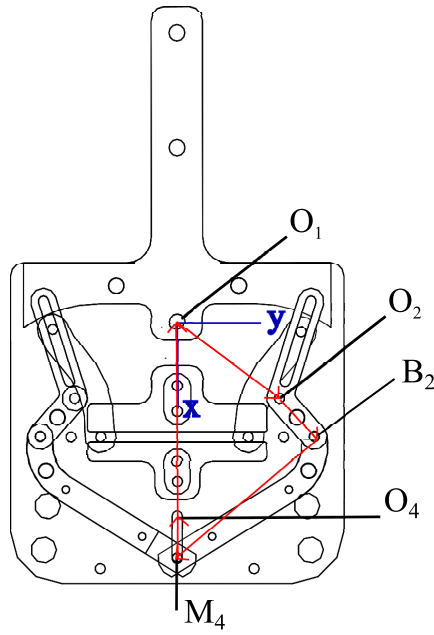


Figure B.3: Sum of vectors

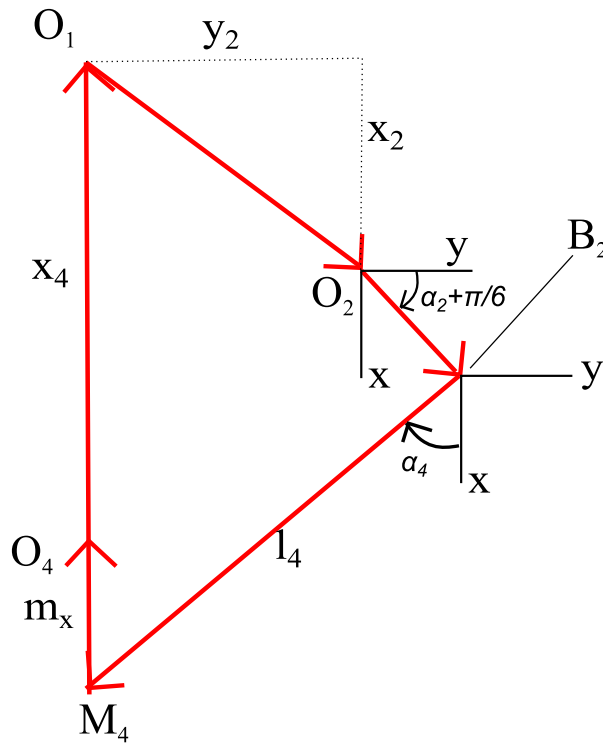


Figure B.4: Sum of vectors

$$\begin{pmatrix} x_2 \\ y_2 \end{pmatrix} + l_{22} \cdot \begin{pmatrix} \sin(\alpha_2 + \pi/6) \\ \cos(\alpha_2 + \pi/6) \end{pmatrix} + l_4 \cdot \begin{pmatrix} \cos \alpha_4 \\ -\sin \alpha_4 \end{pmatrix} - m_x \begin{pmatrix} 1 \\ 0 \end{pmatrix} - \begin{pmatrix} x_4 \\ 0 \end{pmatrix} = 0 \quad (\text{B.13})$$

where (x_2, y_2) is the position of the point O_2 relative to the origin in O_1 of the global coordinate system. Similarly, $(x_4, 0)$ is the position of the point O_4 relatively

to the global coordinate system's origin: O_1 . Looking at the balance of force on the x and y axis:

$$\begin{cases} x_2 + l_{22} \cdot \sin(\alpha_2 + \pi/6) + l_4 \cdot \cos \alpha_4 - m_x - x_4 = 0 \\ y_2 + l_{22} \cdot \cos(\alpha_2 + \pi/6) - l_4 \cdot \sin \alpha_4 = 0 \end{cases} \quad (\text{B.14})$$

From the equilibrium of forces along the y axis is possible to obtain:

$$\alpha_4 = \arcsin\left(\frac{y_2 + l_{22} \cdot \cos(\alpha_2 + \pi/6)}{l_4}\right) \quad (\text{B.15})$$

By substituting Eqn. B.15 in the equilibrium of forces along the x axis, it follows that:

$$m_x = x_2 - x_4 + l_{22} \cdot \sin(\alpha_2 + \pi/6) + l_4 \cdot \cos\left(\arcsin\left(\frac{y_2 + l_{22} \cdot \cos(\alpha_2 + \pi/6)}{l_4}\right)\right) \quad (\text{B.16})$$

By utilising trigonometric identities Eqn. B.16 becomes:

$$m_x = x_2 - x_4 + l_{22} \cdot \sin(\alpha_2 + \pi/6) + l_4 \cdot \sqrt{1 - \left(\frac{y_2 + l_{22} \cdot \cos(\alpha_2 + \pi/6)}{l_4}\right)^2} \quad (\text{B.17})$$

Thus, it is possible to obtain the value of the angle α_2 depending on the movement of the linear actuator: m_x . This equation is very useful to achieve the end goal of a link between the linear actuator movement and the threshold torque.

Contact between the guiding slot and the T-shaped element

The following vector precisely defines the distance between two centres of rotation in HDF: $\overrightarrow{O_1O_2} = \begin{pmatrix} x_2 \\ y_2 \end{pmatrix}$. The points M_1 and M_2 are considered to be the same given the small difference in the real system. Another approximation made in this model is relevant to this sum of vectors. It is the assumption that the curvature of the sides of the T-shaped element is approximated to a straight line. This assumption leads to the vector $\overrightarrow{O_1M_1}$ having the same orientation as the y axis of the global coordinate system, in case the angle α_1 is zero. The angle α_1 is zero in case the HDF has not been triggered. In case it is triggered, then the T-shaped element rotates around O_1 and α_1 is no longer zero. In Figure B.6, the more general case is shown. This is the case where HDF has been triggered by a force oriented as the y axis of the global coordinate system and α_1 is not zero.

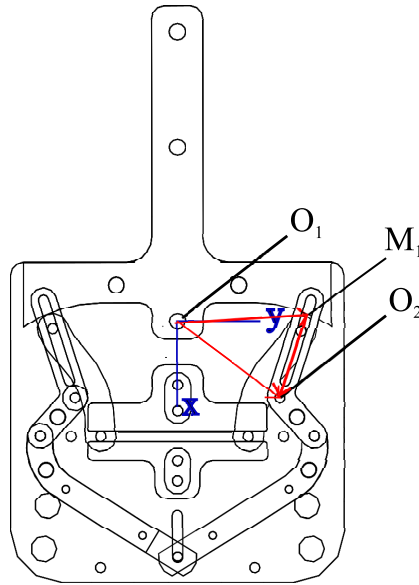


Figure B.5: Sum of vectors

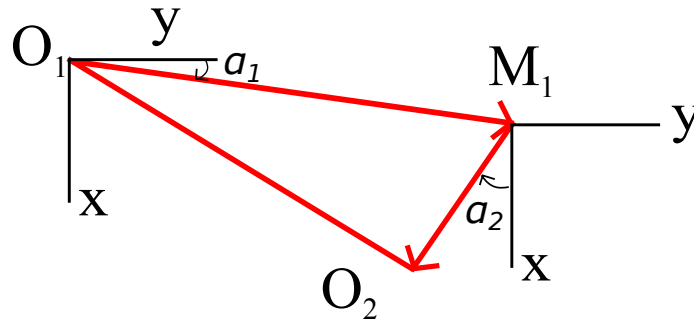


Figure B.6: Vectors and angles

The sum of vectors shown in Figure B.6 is equal to:

$$\overrightarrow{O_1O_2} = \overrightarrow{O_1M_1} + \overrightarrow{M_1O_2} \quad (\text{B.18})$$

this vector sum can also be written as:

$$\begin{pmatrix} x_2 \\ y_2 \end{pmatrix} = p_1 \cdot l_1 \cdot \begin{pmatrix} \sin \alpha_1 \\ \cos \alpha_1 \end{pmatrix} + p_2 \cdot l_{21} \cdot \begin{pmatrix} \cos \alpha_2 \\ -\sin \alpha_2 \end{pmatrix} \quad (\text{B.19})$$

Looking at the balance of force on the x and y axis:

$$\begin{cases} x_2 = p_1 \cdot l_1 \cdot \sin \alpha_1 + p_2 \cdot l_{21} \cdot \cos \alpha_2 \\ y_2 = p_1 \cdot l_1 \cdot \cos \alpha_1 - p_2 \cdot l_{21} \cdot \sin \alpha_2 \end{cases} \quad (\text{B.20})$$

From the balance of forces along the y axis it follows:

$$p_1 = \frac{y_2 + p_2 \cdot l_{21} \cdot \sin \alpha_2}{l_1 \cdot \cos \alpha_1} \quad (\text{B.21})$$

Substituting Eqn. B.21 in the balance of forces along the x axis, it is obtained:

$$x_2 = \frac{y_2 + p_2 \cdot l_{21} \cdot \sin \alpha_2}{l_1 \cdot \cos \alpha_1} \cdot l_1 \cdot \sin \alpha_1 + p_2 \cdot l_{21} \cdot \cos \alpha_2 \quad (\text{B.22})$$

By rearranging Eqn. B.22, the equation becomes:

$$x_2 \cdot \cos \alpha_1 - y_2 \cdot \sin \alpha_1 = p_2 \cdot l_{21} \cdot (\cos \alpha_2 \cdot \cos \alpha_1 + \sin \alpha_2 \cdot \sin \alpha_1) \quad (\text{B.23})$$

Solving for p_2 :

$$p_2 = \frac{x_2 \cdot \cos \alpha_1 - y_2 \cdot \sin \alpha_1}{l_{21} \cdot \cos(\alpha_2 - \alpha_1)} \quad (\text{B.24})$$

Substituting Eqn. B.24 in Eqn. B.21, it is obtained:

$$p_1 = \frac{y_2 + \frac{(x_2 \cdot \cos \alpha_1 - y_2 \cdot \sin \alpha_1) \cdot \sin \alpha_2}{\cos(\alpha_2 - \alpha_1)}}{l_1 \cdot \cos \alpha_1} \quad (\text{B.25})$$

Finally, the contact between the guiding slot and the T-shaped element is given by :

$$\overrightarrow{O_2 M_1} = -\frac{x_2 \cdot \cos \alpha_1 - y_2 \cdot \sin \alpha_1}{l_{21} \cdot \cos(\alpha_2 - \alpha_1)} \cdot l_{21} \cdot \begin{pmatrix} \cos \alpha_2 \\ -\sin \alpha_2 \end{pmatrix} \quad (\text{B.26})$$

the vector $\overrightarrow{O_2 M_1}$ is negative due to its position and orientation relatively to the global coordinate system. It also makes sense it is negative since it has opposite direction compared to the $\overrightarrow{M_1 O_2}$, which is positive.

Position of the connecting link along the spring guide

The last sum of vectors aims at finding a connection between the values of the angle α_2 and the angle α_3 .

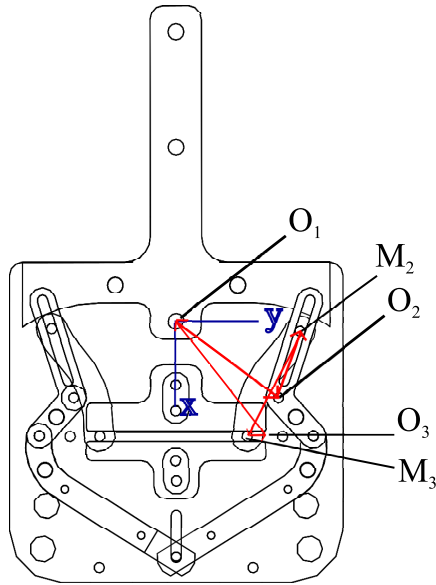


Figure B.7: Sum of vectors. In this drawing a small distance is shown between the points M_3 and O_3 , so that the difference between the two can be appreciated, but in reality these two points are assumed as being the same in case the HDF has not been triggered, which means that the T-shaped element has not rotated around O_1 and α_1 is zero

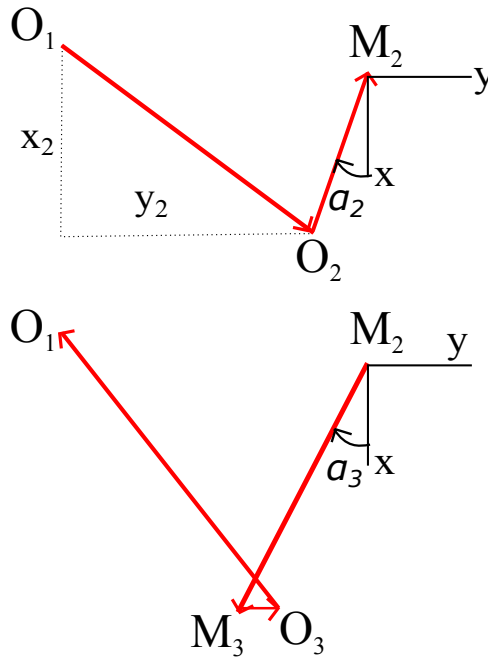


Figure B.8: Sum of vectors. In this drawing the vectorial sum is divided in two parts, for clarity

The sum of vectors shown in Figure B.7 and Figure B.8 is equal to:

$$\vec{0} = \overrightarrow{O_1O_2} + \overrightarrow{O_2M_2} + \overrightarrow{M_2M_3} + \overrightarrow{M_3O_3} + \overrightarrow{O_3O_1} \quad (\text{B.27})$$

this vector sum can also be written as:

$$\begin{pmatrix} x_2 \\ y_2 \end{pmatrix} - p_2 \cdot l_{21} \cdot \begin{pmatrix} \cos \alpha_2 \\ -\sin \alpha_2 \end{pmatrix} + l_3 \cdot \begin{pmatrix} \cos \alpha_3 \\ -\sin \alpha_3 \end{pmatrix} + \begin{pmatrix} 0 \\ m_y \end{pmatrix} - \begin{pmatrix} x_3 \\ y_3 \end{pmatrix} = \vec{0} \quad (\text{B.28})$$

Looking at the balance of force on the x and y axis:

$$\begin{cases} x_2 - x_3 - p_2 \cdot l_{21} \cdot \cos \alpha_2 + l_3 \cdot \cos \alpha_3 & = 0 \\ y_2 + p_2 \cdot l_{21} \cdot \sin \alpha_2 - l_3 \cdot \sin \alpha_3 + m_y - y_3 & = 0 \end{cases} \quad (\text{B.29})$$

From the balance of forces along the y axis it follows:

$$-m_y = y_2 - y_3 - l_3 \cdot \sin \alpha_3 + p_2 \cdot l_{21} \cdot \sin \alpha_2 \quad (\text{B.30})$$

Under the assumption that $m_y = 0$ (that is to say, the T-shaped element is in its initial position), it follows that $\alpha_1 = 0$. These new values are substituted in Eqn. B.30 and the following relation is obtained:

$$0 = y_2 - y_3 + p_2 \cdot l_{21} \cdot \sin \alpha_2 - l_3 \cdot \sin \alpha_3 \quad (\text{B.31})$$

The expression for p_2 explicit in Eqn. B.24 is substituted in Eqn. B.31.

$$l_3 \cdot \sin \alpha_3 = y_2 - y_3 + \frac{x_2 \cdot \cos \alpha_1 - y_2 \cdot \sin \alpha_1}{\cos(\alpha_2 - \alpha_1)} \cdot \sin \alpha_2 \quad (\text{B.32})$$

Keeping in mind that it is assumed there no external force acting on the HDF, $\alpha_1 = 0$ and the overall result is Eqn. B.33:

$$l_3 \cdot \sin \alpha_3 = y_2 - y_3 + \frac{x_2 \cdot \sin \alpha_2}{\cos \alpha_2} \quad (\text{B.33})$$

By rearranging the equation it is found:

$$\alpha_3 = \arcsin \left(\frac{y_2 - y_3 + x_2 \cdot \tan \alpha_2}{l_3} \right) \quad (\text{B.34})$$

As it can be observed, the angle α_3 is dependent on the angle α_2 . This implies that the orientation of the connecting link, given by α_3 , is varied by changing the orientation of the guiding slot, given by α_2 . The results obtained in this section are

necessary in order to derive the mathematical expression for the threshold torque.

B.3 Calculations on the Wrenches Study of the HDF

Following the wrench study on the connecting link in Section 4.5.2, the calculations below show the step-by-step derivation of the threshold torque needed to trigger the HDF's mechanism.

In Coulomb's law, friction forces are expressed as the product of the static friction coefficient and the force normal to the friction force. In M_2 all the contacts are steel against steel and the static friction coefficient for those is μ_{ss} . Hence, $\overrightarrow{X_{fr2 \rightarrow 3}} \cdot \cos \alpha_3$ becomes $\mu_{ss} \cdot \overrightarrow{Y_{2 \rightarrow 3}} \cdot \cos \alpha_2$ and $\overrightarrow{X_{fr2 \rightarrow 3}} \cdot \sin \alpha_3$ can be written as $\mu_{ss} \cdot \overrightarrow{Y_{2 \rightarrow 3}} \cdot \sin \alpha_2$. In M_3 the contacts are between steel and PTFE and the static coefficient for those is μ_{sp} , hence $\overrightarrow{Y_{fr0 \rightarrow 3}}$ becomes $\mu_{sp} \cdot \overrightarrow{X_{0 \rightarrow 3}}$. The third equation provides a relationship between the external force applied to the T-shaped element and the effort the spring has to provide in order to keep a static equilibrium. This equation gives the following relationship:

$$\overrightarrow{X_{0 \rightarrow 3}} = \overrightarrow{F_{s \rightarrow 3}} \cdot \frac{\cos \alpha_3}{\sin \alpha_3 - \mu_{sp} \cdot \cos \alpha_3} \quad (\text{B.35})$$

From the rearrangement of the second equation in the system 4.18, it is found:

$$\overrightarrow{Y_{2 \rightarrow 3}} = \frac{-\overrightarrow{F_{s \rightarrow 3}} - \mu_{sp} \cdot \overrightarrow{X_{0 \rightarrow 3}}}{\mu_{ss} \cdot \sin \alpha_2 - \cos \alpha_2} \quad (\text{B.36})$$

If Eqn. B.36 is substituted in the first equation of the system 4.18, it is as follows:

$$\overrightarrow{X_{1 \rightarrow 3}} = \frac{-\overrightarrow{F_{s \rightarrow 3}} - \mu_{sp} \cdot \overrightarrow{X_{0 \rightarrow 3}}}{\mu_{ss} \cdot \sin \alpha_2 - \cos \alpha_2} (\sin \alpha_2 + \mu_{ss} \cdot \cos \alpha_2) + \overrightarrow{X_{0 \rightarrow 3}} \quad (\text{B.37})$$

if Eqn. B.35 is substituted in this equation and after rearranging and solving for $\overrightarrow{X_{1 \rightarrow 3}}$ it is obtained:

$$\overrightarrow{X_{1 \rightarrow 3}} = \overrightarrow{F_{s \rightarrow 3}} \cdot \left(\frac{\cos \alpha_3 \cdot (\cos \alpha_2 - \mu_{ss} \cdot \sin \alpha_2) + \sin \alpha_3 \cdot (\sin \alpha_2 + \mu_{ss} \cdot \cos \alpha_2)}{(\sin \alpha_3 - \mu_{sp} \cdot \cos \alpha_3)(\cos \alpha_2 - \mu_{ss} \cdot \sin \alpha_2)} \right) \quad (\text{B.38})$$

Recalling Eqn.B.39:

$$\vec{T}_R = p_1 \cdot l_1 \cdot \vec{X}_{3 \rightarrow 1} \cdot \cos \alpha_3 \quad (\text{B.39})$$

and substituting Eqn. B.38 in it, it is obtained:

$$\vec{T}_R = -p_1 \cdot l_1 \cdot \vec{F}_{s \rightarrow 3} \cdot \left(\frac{\cos \alpha_3 \cdot (\cos \alpha_2 - \mu_{ss} \cdot \sin \alpha_2) + \sin \alpha_3 \cdot (\sin \alpha_2 + \mu_{ss} \cdot \cos \alpha_2)}{(\sin \alpha_3 - \mu_{sp} \cdot \cos \alpha_3)(\cos \alpha_2 - \mu_{ss} \cdot \sin \alpha_2)} \right) \cos \alpha_3 \quad (\text{B.40})$$

This is the resistance torque: the one an external torque needs to overcome in order to trigger the HDF and is also called threshold torque, T_{th} . The threshold torque is the torque that meets the principle of static equilibrium. If the external torque is less than this threshold torque, the connecting link is stuck in the initial position, thanks to the force applied by the spring. If the applied external torque is equal or higher than the threshold torque, the HDF is triggered.

It is assumed that the spring has a stiffness k and a pre-compression s_0 , which comprise the spring force:

$$\vec{F}_{s \rightarrow 3} = k \cdot s_0 \quad (\text{B.41})$$

if $\alpha_1 = 0$, which represents the initial, untriggered state of the HDF, is substituted in Eqn. B.25, the result is:

$$p_1 \cdot l_1 = y_2 + x_2 \cdot \tan \alpha_2 \quad (\text{B.42})$$

where y_2 and x_2 are the distances along the y and x general coordinate system axes between the point O_1 and O_2 . If those two expressions are replaced in Eqn. B.40, the following is obtained:

$$\vec{T}_{th} = -(y_2 + x_2 \cdot \tan \alpha_2) \cdot k \cdot s_0 \cdot \left(\frac{\cos \alpha_3 \cdot (\cos \alpha_2 - \mu_{ss} \cdot \sin \alpha_2) + \sin \alpha_3 \cdot (\sin \alpha_2 + \mu_{ss} \cdot \cos \alpha_2)}{(\sin \alpha_3 - \mu_{sp} \cdot \cos \alpha_3)(\cos \alpha_2 - \mu_{ss} \cdot \sin \alpha_2)} \right) \cos \alpha_3 \quad (\text{B.43})$$

Eqn B.43 bears a marked resemblance to Eqn. B.11, in case angle θ is equal to $\pi/2$. The spring force is expressed as stiffness multiplied by pre compression in both cases, the distance d_0 in Eqn. B.11 is similar to $p_1 \cdot l_1$ and the expression for the torque in Eqn. B.11 is dependent on γ and θ as Eqn. B.43 is dependent on α_2 and α_3 . Other terms are instead pertinent to the HDF mechanism only.

If the mathematical expressions in Eqn. B.44, which is shown again here for clarity:

$$\alpha_3 = \arcsin\left(\frac{y_2 - y_3 + x_2 \cdot \tan \alpha_2}{l_3}\right) \quad (\text{B.44})$$

is substituted in B.43, the final expression is found:

$$\begin{aligned} \overrightarrow{T_{th}} = & -(y_2 + x_2 \cdot \tan \alpha_2) \cdot k \cdot s_0 \cdot \\ & \frac{\cos\left(\arcsin\left(\frac{y_2 - y_3 + x_2 \cdot \tan \alpha_2}{l_3}\right)\right) \cdot (\cos \alpha_2 - \mu_{ss} \cdot \sin \alpha_2) + \sin\left(\arcsin\left(\frac{y_2 - y_3 + x_2 \cdot \tan \alpha_2}{l_3}\right)\right) \cdot (\sin \alpha_2 + \mu_{ss} \cdot \cos \alpha_2)}{(\sin\left(\arcsin\left(\frac{y_2 - y_3 + x_2 \cdot \tan \alpha_2}{l_3}\right)\right) - \mu_{sp} \cdot \cos\left(\arcsin\left(\frac{y_2 - y_3 + x_2 \cdot \tan \alpha_2}{l_3}\right)\right))(\cos \alpha_2 - \mu_{ss} \cdot \sin \alpha_2)} \\ & \cdot \cos\left(\arcsin\left(\frac{y_2 - y_3 + x_2 \cdot \tan \alpha_2}{l_3}\right)\right) \end{aligned} \quad (\text{B.45})$$

B.4 Design-testing Experiments Results: Statistical Analysis

The following pages contain the curve fit equations and statistical analysis for the data relative to the design-testing experiments.

The first set of data is relative to the threshold torque experiment where the HDF has a 0.78N/mm spring and Eqn. B.46 is relative to the curve fit in Figure 4.28.

$$\overrightarrow{TT}_{R0.78}(T) = a_{1,2}\overrightarrow{T}_{1,2}^2 + a_{1,1}\overrightarrow{T}_{1,1} + a_{1,0} \quad (\text{B.46})$$

where \overrightarrow{TT} is the threshold torque required to activate the decoupling, \overrightarrow{T} are the torques applied on the INTRO-BRL arm link and $a_{x,y}$ are the constants: $a_{1,2} = 0.081 \frac{1}{Nm}$, $a_{1,1} = -0.598$, $a_{1,0} = 2.582 Nm$. The standard deviation of the data set is available in Table B.1.

The second set of experiments has been conducted with a 1.34 N/mm stiffness spring. The experimental curve which describes the relationship between the threshold torque necessary to decouple the HDF and the position of the adjustment arms in their slot can be described in the following second order equation:

$$\overrightarrow{TT}_{R1.34}(T) = a_{3,2}\overrightarrow{T}_{3,2}^2 + a_{3,1}\overrightarrow{T}_{3,1} + a_{3,0} \quad (\text{B.47})$$

where \overrightarrow{TT} is the threshold torque required to activate the decoupling, \overrightarrow{T} are the torques applied on the INTRO-BRL arm link and $a_{x,y}$ are the constants: $a_{3,2} = 0.102 \frac{1}{Nm}$, $a_{3,1} = -0.614$, $a_{3,0} = 3.864$. The R^2 for the fitting of the threshold torque in the right side of HDF is 0.946. The standard deviation of the data set is

Table B.1: HDF Threshold Torque Values Statistical Analysis (Right, 0.78 N/mm spring)

Parameter	Value [Nm]	95% low limit	95% high limit	Standard Deviation
$\overrightarrow{TT}_{0mm}$	0.69	0.343	1.036	0.395
$\overrightarrow{TT}_{1mm}$	0.681	0.412	0.951	0.308
$\overrightarrow{TT}_{2mm}$	0.58	0.318	0.842	0.3
$\overrightarrow{TT}_{3mm}$	0.607	0.167	1.047	0.502
$\overrightarrow{TT}_{4mm}$	0.702	0.318	1.085	0.437
$\overrightarrow{TT}_{5mm}$	0.727	0.476	0.978	0.286
$\overrightarrow{TT}_{6mm}$	0.852	0.749	0.955	0.118
$\overrightarrow{TT}_{7mm}$	0.891	0.584	1.198	0.35
$\overrightarrow{TT}_{8mm}$	0.937	0.438	1.435	0.569
$\overrightarrow{TT}_{9mm}$	1.158	1.002	1.314	0.177
$\overrightarrow{TT}_{10mm}$	1.366	0.907	1.824	0.523
$\overrightarrow{TT}_{11mm}$	1.849	1.37	2.33	0.548
$\overrightarrow{TT}_{12mm}$	2.272	1.113	3.431	1.322
$\overrightarrow{TT}_{13mm}$	2.887	1.01	4.765	2.142
$\overrightarrow{TT}_{14mm}$	3.853	0.855	6.85	3.42

available in Table B.2.

Table B.2: HDF Threshold Torque Values Statistical Analysis (Right, 1.34 N/mm spring)

Parameter	Value [Nm]	95% low limit	95% high limit	Standard Deviation
$\overrightarrow{TT}_{0mm}$	0.969	0.475	1.462	0.563
$\overrightarrow{TT}_{1mm}$	1.001	0.652	1.349	0.398
$\overrightarrow{TT}_{2mm}$	1.14	0.753	1.546	0.452
$\overrightarrow{TT}_{3mm}$	1.241	0.775	1.706	0.531
$\overrightarrow{TT}_{4mm}$	1.378	0.81	1.946	0.648
$\overrightarrow{TT}_{5mm}$	1.47	1.105	1.833	0.414
$\overrightarrow{TT}_{6mm}$	1.498	1.151	1.845	0.395
$\overrightarrow{TT}_{7mm}$	1.687	1.361	2.014	0.373
$\overrightarrow{TT}_{8mm}$	1.792	1.16	2.424	0.721
$\overrightarrow{TT}_{9mm}$	2.052	1.812	2.292	0.273
$\overrightarrow{TT}_{10mm}$	2.351	1.824	2.878	0.601
$\overrightarrow{TT}_{11mm}$	3.094	1.787	4.401	1.491
$\overrightarrow{TT}_{12mm}$	3.182	1.051	5.312	2.43
$\overrightarrow{TT}_{13mm}$	4.72	2.448	6.992	2.59
$\overrightarrow{TT}_{14mm}$	5.87	2.782	8.957	3.52

The third set of experiments has been conducted with a 1.74 N/mm stiffness spring. The experimental curve which describes the relationship between the threshold torque necessary to decouple the HDF and the position of the adjustment arms in their slot in the right side of HDF can be described in the following second order equation:

$$\overrightarrow{TT}_{R1.74}(T) = a_{5,2}\overrightarrow{T}_{5,2}^2 + a_{5,1}\overrightarrow{T}_{5,1} + a_{5,0} \quad (\text{B.48})$$

where \overrightarrow{TT} is the threshold torque required to activate the decoupling, \overrightarrow{T} are the torques applied on the INTRO-BRL arm link and $a_{x,y}$ are the constants: $a_{5,2} = 0.136 \frac{1}{Nm}$, $a_{5,1} = -0.785$, $a_{5,0} = 4.438 Nm$. The R^2 for the fitting of the threshold torque in the right side of HDF is 0.963. The standard deviation of the data set is available in Table B.3.

Table B.3: HDF Threshold Torque Values Statistical Analysis (Right, 1.74 N/mm spring)

Parameter	Value [Nm]	95% low limit	95% high limit	Standard Deviation
$\overrightarrow{TT}_{0mm}$	1.131	0.88	1.382	0.286
$\overrightarrow{TT}_{1mm}$	1.201	0.878	1.524	0.368
$\overrightarrow{TT}_{2mm}$	1.165	0.677	1.653	0.557
$\overrightarrow{TT}_{3mm}$	1.324	0.94	1.707	0.44
$\overrightarrow{TT}_{4mm}$	1.674	1.321	2.026	0.402
$\overrightarrow{TT}_{5mm}$	1.651	1.027	2.274	0.711
$\overrightarrow{TT}_{6mm}$	1.968	1.184	2.751	0.894
$\overrightarrow{TT}_{7mm}$	2.046	1.771	2.32	0.313
$\overrightarrow{TT}_{8mm}$	2.242	1.444	3.039	0.91
$\overrightarrow{TT}_{9mm}$	2.676	1.984	3.368	0.789
$\overrightarrow{TT}_{10mm}$	3.209	1.615	4.803	1.819
$\overrightarrow{TT}_{11mm}$	3.467	1.85	5.085	1.954
$\overrightarrow{TT}_{12mm}$	4.784	3.072	6.497	1.954
$\overrightarrow{TT}_{13mm}$	6.195	3.816	8.574	2.714
$\overrightarrow{TT}_{14mm}$	7.585	4.438	10.733	3.591

In the following pages the curve fitting equations relative to the left side of the HDF during the design testing experiments are reported together with the statistical analysis. For the 0.78N/mm spring stiffness the equation is:

$$\overrightarrow{TT}_{L0.78}(T) = a_{2,2}\overrightarrow{T}_{2,2}^2 + a_{2,1}\overrightarrow{T}_{2,1} + a_{2,0} \quad (\text{B.49})$$

where \overrightarrow{TT} is the threshold torque required to activate the decoupling, \overrightarrow{T} are

the torques applied on the INTRO-BRL arm link and $a_{x,y}$ are the constants: $a_{2,2} = 0.086 \frac{1}{Nm}$, $a_{2,1} = -0.637$, $a_{2,0} = 2.566 Nm$. The R^2 for the fitting of the threshold torque in the left side of HDF is 0.933, which show a good fit with the data. The standard deviation of the data set is available in Table B.4.

Table B.4: HDF Threshold Torque Values Statistical Analysis (Left, 0.78 N/mm spring)

Parameter	Value [Nm]	95% low limit	95% high limit	Standard Deviation
$\overrightarrow{TT}_{0mm}$	0.588	0.359	0.818	0.262
$\overrightarrow{TT}_{1mm}$	0.61	0.517	0.699	0.104
$\overrightarrow{TT}_{2mm}$	0.673	0.391	0.954	0.321
$\overrightarrow{TT}_{3mm}$	0.614	0.185	1.042	0.489
$\overrightarrow{TT}_{4mm}$	0.711	0.278	1.145	0.494
$\overrightarrow{TT}_{5mm}$	0.693	0.482	0.904	0.241
$\overrightarrow{TT}_{6mm}$	0.81	0.628	0.992	0.207
$\overrightarrow{TT}_{7mm}$	0.862	0.235	1.49	0.716
$\overrightarrow{TT}_{8mm}$	1.101	0.485	1.716	0.702
$\overrightarrow{TT}_{9mm}$	1.188	0.173	2.204	1.158
$\overrightarrow{TT}_{10mm}$	1.357	0.661	2.054	0.795
$\overrightarrow{TT}_{11mm}$	1.653	0.416	2.89	1.411
$\overrightarrow{TT}_{12mm}$	2.208	0.211	4.205	2.278
$\overrightarrow{TT}_{13mm}$	2.885	1.516	4.255	1.562
$\overrightarrow{TT}_{14mm}$	4.243	2.096	6.39	2.45

As can be seen from Eqn. B.46 and Eqn. B.49, the relationship between the two variables is not linear. The threshold torque value is very stable for displacements in the slots up to 7 mm and then it increases rapidly for larger displacements. This behaviour is the same for both sides of HDF.

The experimental curve which describes the relationship between the threshold torque necessary to decouple the HDF and the position of the adjustment arms in their slot when the spring stiffness is 1.34N/mm can be described in the following second order equation:

$$\overrightarrow{TT}_{L1.34}(T) = a_{4,2}\overrightarrow{T}_{4,2}^2 + a_{4,1}\overrightarrow{T}_{4,1} + a_{4,0} \quad (\text{B.50})$$

where \overrightarrow{TT} is the threshold torque required to activate the decoupling, \overrightarrow{T} are the torques applied on the INTRO-BRL arm link and $a_{x,y}$ are the constants: $a_{4,2} = 0.094 \frac{1}{Nm}$, $a_{4,1} = -0.438$, $a_{4,0} = 3.551 Nm$. The R^2 for the fitting of the threshold torque in the left side of HDF is 0.946, which show a good fit with the data. The standard deviation of the data set is available in Table B.5.

Table B.5: HDF Threshold Torque Values Statistical Analysis (Left, 1.34 N/mm spring)

Parameter	Value [Nm]	95% low limit	95% high limit	Standard Deviation
$\overrightarrow{TT}_{0mm}$	0.888	0.669	1.107	0.25
$\overrightarrow{TT}_{1mm}$	0.964	0.751	1.176	0.241
$\overrightarrow{TT}_{2mm}$	1.107	0.829	1.386	0.318
$\overrightarrow{TT}_{3mm}$	1.302	0.263	2.34	1.185
$\overrightarrow{TT}_{4mm}$	1.385	0.478	2.291	1.034
$\overrightarrow{TT}_{5mm}$	1.545	0.856	2.234	0.786
$\overrightarrow{TT}_{6mm}$	1.748	0.694	2.802	1.202
$\overrightarrow{TT}_{7mm}$	1.883	1.244	2.523	0.73
$\overrightarrow{TT}_{8mm}$	1.999	0.88	3.12	1.277
$\overrightarrow{TT}_{9mm}$	2.377	1.744	3.01	0.721
$\overrightarrow{TT}_{10mm}$	2.585	1.491	3.679	1.248
$\overrightarrow{TT}_{11mm}$	3.173	2.575	3.771	0.682
$\overrightarrow{TT}_{12mm}$	3.504	2.05	4.959	1.66
$\overrightarrow{TT}_{13mm}$	4.573	2.574	6.571	2.28
$\overrightarrow{TT}_{14mm}$	6.279	4.36	8.197	2.19

The results for the left side of HDF with a stiffness spring of 1.74N/mm are shown in Figure 4.29. The experimental curve that describes the relationship between the threshold torque necessary to decouple the HDF and the position of the adjustment arms in their slot can be described in the following second order equation:

$$\overrightarrow{TT}_{L1.74}(T) = a_{6,2}\overrightarrow{T}_{6,2}^2 + a_{6,1}\overrightarrow{T}_{6,1} + a_{6,0} \quad (\text{B.51})$$

where \overrightarrow{TT} is the threshold torque required to activate the decoupling, \overrightarrow{T} are the torques applied on the INTRO-BRL arm link and $a_{x,y}$ are the constants: $a_{6,2} = 0.073 \frac{1}{Nm}$, $a_{6,1} = -0.025$, $a_{6,0} = 4.236 Nm$. The R^2 for the fitting of the threshold torque in the left side of HDF is 0.99, which show a very good fit with the data. The standard deviation of the data set is available in Table B.6.

B.5 Matlab Code for Threshold torque determination

```
clear; clc; close;
%mx = 0.0143; %0.0067; %0.013; %:0.002:0; %m it is 0.0166 if a2 is
0.3142
```

Table B.6: HDF Threshold Torque Values Statistical Analysis (Left, 1.74 N/mm spring)

Parameter	Value [Nm]	95% low limit	95% high limit	Standard Deviation
$\overrightarrow{TT}_{0mm}$	1.369	0.719	2.02	0.742
$\overrightarrow{TT}_{1mm}$	1.335	0.578	2.092	0.864
$\overrightarrow{TT}_{2mm}$	1.592	0.617	2.568	1.113
$\overrightarrow{TT}_{3mm}$	1.76	0.676	2.843	1.236
$\overrightarrow{TT}_{4mm}$	1.939	1.231	2.647	0.808
$\overrightarrow{TT}_{5mm}$	2.155	0.98	3.331	1.341
$\overrightarrow{TT}_{6mm}$	2.543	1.858	3.227	0.781
$\overrightarrow{TT}_{7mm}$	2.554	1.503	3.605	1.2
$\overrightarrow{TT}_{8mm}$	2.914	1.044	4.784	2.133
$\overrightarrow{TT}_{9mm}$	3.276	2.534	4.018	0.846
$\overrightarrow{TT}_{10mm}$	3.799	2.34	5.257	1.664
$\overrightarrow{TT}_{11mm}$	4.37	2.244	6.496	2.425
$\overrightarrow{TT}_{12mm}$	4.588	3.282	5.894	1.5
$\overrightarrow{TT}_{13mm}$	5.743	3.64	7.845	2.4
$\overrightarrow{TT}_{14mm}$	6.439	5.157	7.721	1.453

```

m = [0.0143 0.0123 0.0103 0.0083 0.0063 0.0033];
m1 = [0.0163 0.0153 0.0143 0.0133 0.0123 0.0113 0.0103 0.0093 0.0083
      0.0073 0.0063 0.0053 0.0043 0.0033 0.0023];
m2 = 0.0163:0.0002:0.0023;
m3 = 0.0143:0.0002:0.0023;
dis = [2 4 6 8 10 13];
dis1 = [0 1 2 3 4 5 6 7 8 9 10 11 12 13 14];
dis2 = 0:0.1972:14;
muss = 0.08; %0.78;
musp = 0.04;
%syms mx; %it is 0.0166 if a2 is 0.3142
x2 = 0.03; %m
x4 = 0.07586; %m
l22 = 0.02; %m
b = pi/6;
l4 = 0.0715; %m
y2 = 0.04; %m
syms a2;
%a2 = 0.3142; %equiv to 18degrees
k = 1340; %N/m
k1 = 1740;
s0 = 0.006; %m
%y2 = 0.04;
%x2 = 0.03;
y3 = 0.035;

```

```

l3 = 0.046; %a1%
%a2 = 0.314159265;
%a3 = 0.436332313;

for i = 1:71 %15 %6
    mx = m2(i);
    rad(i) = solve(x2^2 + x4 + l22*sin(a2 + b) + l4*sqrt(1 + ((y2 + l22*cos
        (a2 + b))/l4)^2) == mx, a2)
end

for i = 1:71 %15 %6
    a2 = rad(i);
    % a2*2

    TTcomp(i) = (y2 + x2*tan(a2))*k1*s0*cos(asin((y2 - y3+x2*tan(a2))/l3))
        *((cos(asin((y2 - y3+x2*tan(a2))/l3)))*(cos(a2) - (muss*sin(a2)))) + (
        sin(asin((y2 - y3+x2*tan(a2))/l3)))*(sin(a2) + (muss*cos(a2))))/((
        sin(asin((y2 - y3+x2*tan(a2))/l3)) - (musp*cos(asin((y2 - y3+x2*tan(a2)
        )/l3))))*(cos(a2) - muss*sin(a2)))

end

%deg = (rad*180)/pi;
p = polyfit(dis2,rad,1)
%h = polyfit(dis2,TTcomp,2)
%f = polyval(p,dis2);
%table = [dis2 rad f rad f]

%ft=fittype('exp1');
%cf=fit(dis2,TTcomp,ft)

figure
plot(dis2,rad,'*')
xlabel('Displacement [mm]', 'FontSize',12)
ylabel('Angle \alpha_{2} [radians]', 'FontSize',12)
figure
plot(dis2,TTcomp)
xlabel('Displacement [mm]', 'FontSize',12)
ylabel('Threshold Torque [Nm]', 'FontSize',12)

```

B.6 Characterisation Experiments Results: Statistical Analysis

In the Characterisation Experiments in Chapter 4, the experimental curve which describes the relationship between the threshold torque necessary to decouple the

Table B.7: HDF Critical Force Values Statistical Analysis, Right side (Load Cell)

Parameter	Value [Nm]	Standard Deviation
$\overrightarrow{TT}_{1mm}$	0.6	0.07
$\overrightarrow{TT}_{2mm}$	0.92	0.09
$\overrightarrow{TT}_{3mm}$	1.02	0.07
$\overrightarrow{TT}_{4mm}$	1.08	0.29
$\overrightarrow{TT}_{5mm}$	1.22	0.09
$\overrightarrow{TT}_{6mm}$	1.33	0.12
$\overrightarrow{TT}_{7mm}$	1.55	0.08
$\overrightarrow{TT}_{8mm}$	1.75	0.09
$\overrightarrow{TT}_{9mm}$	1.98	0.19
$\overrightarrow{TT}_{10mm}$	2.19	0.11
$\overrightarrow{TT}_{11mm}$	2.39	0.18
$\overrightarrow{TT}_{12mm}$	2.76	0.32

HDF and the position of the adjustment arms in their slot in case the HDF has not been lubricated, can be described in the following equation:

$$\overrightarrow{TT}_R(F) = a_{7,2}\overrightarrow{T}_{7,2}^2 + a_{7,1}\overrightarrow{T}_{7,1} + a_{7,0} \quad (\text{B.52})$$

where \overrightarrow{TT} is the threshold torque required to activate the decoupling action, \overrightarrow{T} is the torque applied on the INTRO-BRL arm link. For the right side, $a_{x,y}$ are the constants: $a_{7,2} = 0.008 \frac{1}{Nm}$, $a_{7,1} = 0.076$, $a_{7,0} = 0.64 Nm$. The second order polynomial used to fit the experimental curve is a good fit for the whole data set. This is confirmed by the fact that the R^2 for the fitting of the HDF threshold torque in Figure 4.32 is 0.992. For the left side, $a_{x,y}$ are the constants: $a_{8,2} = 0.012 \frac{1}{Nm}$, $a_{8,1} = 0.017$, $a_{8,0} = 0.647 Nm$. The second order polynomial used to fit the experimental curve is a good fit for the whole data set, its R^2 error is 0.975. These two polynomial curves are being calculated because they can be used directly to give a description of the HDF behaviour and thus can be utilised directly in its control. The standard deviation of the data set is available in Table B.7 and in Table B.8. The standard deviation in the measurements is much lower than in the experiments in Section B.4. This shows that the characterisation experiments are able to provide a much more reliable description of the HDF behaviour than the previous experiments. However, it is interesting to notice that the standard deviation values still reach the 0.53 and 0.49 in the left side of the HDF.

The experimental curve which describes the relationship between the threshold torque and the position of the adjustment arms in their slot in case the HDF is

Table B.8: HDF Critical Force Values Statistical Analysis, Left side (Load Cell)

Parameter	Value [Nm]	Standard Deviation
$\overrightarrow{TT}_{1mm}$	0.6	0.36
$\overrightarrow{TT}_{2mm}$	0.83	0.12
$\overrightarrow{TT}_{3mm}$	0.88	0.12
$\overrightarrow{TT}_{4mm}$	0.93	0.08
$\overrightarrow{TT}_{5mm}$	1	0.49
$\overrightarrow{TT}_{6mm}$	1.12	0.53
$\overrightarrow{TT}_{7mm}$	1.44	0.16
$\overrightarrow{TT}_{8mm}$	1.53	0.1
$\overrightarrow{TT}_{9mm}$	1.78	0.37
$\overrightarrow{TT}_{10mm}$	1.99	0.23
$\overrightarrow{TT}_{11mm}$	2.03	0.22
$\overrightarrow{TT}_{12mm}$	2.69	0.2

lubricated can be described as:

$$\overrightarrow{TT}_R(F) = a_{9,2}\overrightarrow{T}_{9,2}^2 - a_{9,1}\overrightarrow{T}_{9,1} + a_{9,0} \quad (\text{B.53})$$

where \overrightarrow{TT} is the threshold torque required to activate the decoupling action, \overrightarrow{T} is the torque applied on the INTRO-BRL arm link. For the right side, $a_{x,y}$ are the constants: $a_{9,2} = 0.013 \frac{1}{Nm}$, $a_{9,1} = 0.019$, $a_{9,0} = 0.962 Nm$. The second order polynomial used to fit the experimental curve is a good fit for the whole data set. This is confirmed by the fact that the R^2 for the fitting of the HDF threshold torque in Figure 4.33 is 0.967. The standard deviation of the data set is available in Table B.9. For the left side, $a_{x,y}$ are the constants: $a_{10,2} = 0.015 \frac{1}{Nm}$, $a_{10,1} = 0.019$, $a_{10,0} = 0.819 Nm$. The second order polynomial used to fit the experimental curve is a good fit, its R^2 for the fitting of the HDF threshold torque in Figure 4.33 is 0.99. The standard deviation of the data set is available in Table B.9 and in Table B.10.

As can be seen in Figure 4.33, Table B.9 and Table B.10, the standard deviation is still lower than in the experiments in Section B.4 and it does not reach the peaks it reached without lubricant. The average standard deviation for the left side of HDF without the lubricant is 0.25 and with the lubricant is 0.15. Hence, the best way to reduce the standard deviation and thus ensure repeatable results is to lubricate the structure.

Table B.9: HDF Critical Force Values Statistical Analysis, Right side (Load Cell)

Parameter	Value [Nm]	Standard Deviation
$\overrightarrow{TT}_{1mm}$	0.99	0.09
$\overrightarrow{TT}_{2mm}$	0.92	0.104
$\overrightarrow{TT}_{3mm}$	0.92	0.12
$\overrightarrow{TT}_{4mm}$	1.08	0.09
$\overrightarrow{TT}_{5mm}$	1.31	0.08
$\overrightarrow{TT}_{6mm}$	1.3	0.15
$\overrightarrow{TT}_{7mm}$	1.62	0.1
$\overrightarrow{TT}_{8mm}$	1.54	0.22
$\overrightarrow{TT}_{9mm}$	1.72	0.094
$\overrightarrow{TT}_{10mm}$	1.87	0.29
$\overrightarrow{TT}_{11mm}$	2.35	0.27
$\overrightarrow{TT}_{12mm}$	2.62	0.11

Table B.10: HDF Critical Force Values Statistical Analysis, Left side (Load Cell)

Parameter	Value [Nm]	Standard Deviation
$\overrightarrow{TT}_{1mm}$	0.84	0.16
$\overrightarrow{TT}_{2mm}$	0.83	0.13
$\overrightarrow{TT}_{3mm}$	0.88	0.07
$\overrightarrow{TT}_{4mm}$	0.9	0.14
$\overrightarrow{TT}_{5mm}$	1.11	0.09
$\overrightarrow{TT}_{6mm}$	1.25	0.26
$\overrightarrow{TT}_{7mm}$	1.51	0.24
$\overrightarrow{TT}_{8mm}$	1.55	0.15
$\overrightarrow{TT}_{9mm}$	1.91	0.32
$\overrightarrow{TT}_{10mm}$	1.97	0.08
$\overrightarrow{TT}_{11mm}$	2.34	0.06
$\overrightarrow{TT}_{12mm}$	2.76	0.09

Appendix C

Appendix of Chapter 5

C.1 Variable Compliance Experiments Results: Statistical Analysis

The statistical details regarding the stiffness values for the variable compliance experiments of Section 5.6.2 is reported here. In the statistical analysis data from both the continuous and discrete gripper are reported; respectively in Table C.1 and in Table C.2.

Table C.1: Continuous Gripper Stiffness Values Statistical Analysis

Parameter	Value	95% low limit	95% high limit	Standard Deviation
S_{0N}	1.009	0.846	1.173	0.144
$S_{8.6N}$	1.095	1.031	1.160	0.056
$S_{15.6N}$	1.262	1.143	1.381	0.105
$S_{22.6N}$	2.104	1.674	2.533	0.380

Table C.2: Discrete Gripper Stiffness Values Statistical Analysis

Parameter	Value	95% low limit	95% high limit	Standard Deviation
S_{0N}	0.705	0.646	0.764	0.052
$S_{8.6N}$	1.056	1.002	1.111	0.048
$S_{15.6N}$	1.476	1.363	1.589	0.099
$S_{22.6N}$	1.635	1.517	1.752	0.104

Once the values for this experiment are obtained, a polynomial fit is used for the data. The data for the continuous gripper is fitted in a second order polynomial (Eq. C.1) and the data for the discrete gripper is fitted in a first order polynomial (Eq. C.2). In equations (Eq. C.1) and (Eq. C.2) F is in Newtons and k is in

Newtons/millimetres.

$$\vec{k}_c(\vec{F}) = a_{1,2}\vec{F}_{1,2}^2 + a_{1,1}\vec{F}_{1,1} + a_{1,0} \quad (\text{C.1})$$

$$\vec{k}_d(\vec{F}) = a_{2,1}\vec{F}_{2,1} + a_{2,0} \quad (\text{C.2})$$

where \vec{k} is the system stiffness, \vec{F} is the force applied on the cables and $a_{x,y}$ are the constants: $a_{1,2} = 0.0036 \frac{1}{Nmm}$, $a_{1,1} = -0.0343 \frac{1}{mm}$, $a_{1,0} = 1.0346 \frac{N}{mm}$, $a_{2,1} = 0.043 \frac{1}{mm}$, $a_{2,0} = 0.7142 \frac{N}{mm}$.

In order to avoid overfitting, a second order polynomial has been chosen as the fit for the data relative to the continuous gripper. As can be observed in Figure 5.24, this causes the fit to the experimental curve to assume higher values for zero pulling forces than for pulling forces of 5N. However, in general, the experimental curve is fitted well by the second order polynomial, also shown by the fact that the R^2 for the fitting of the experimental curve is 0.973. The R^2 for the fitting of the fitting of the discrete gripper stiffness is 0.978, which also indicates a good fit.

These equations not only characterise the grasping system and show its ability to obtain structural stiffness but could also be utilised by a higher-level control system. They provide the system designers with an important indication of the mapping between applied pulling force (\vec{F}_p) and change in compliance.

C.2 Matlab Code for the HS gripper

Code for the calculation of forward kinematics of the HS gripper:

```
%% Print all the trials in individual figures
for k=1:6

    figure

    for i=1:15
        % Print centre line
        eval(['plot(Trial0 ' num2str(k) '(i,1:2:18), Trial0 ' num2str(k)
              '(i,2:2:18)) '])
        hold on

        % Print external line
        eval(['plot(Trial0 ' num2str(k) '(i,19:2:36), Trial0 ' num2str(k)
              '(i,20:2:36), ' char(39) 'k' char(39) ' ' ')])
    end
end
```

```

    % Print internal line
    eval(['plot(Trial0 ' num2str(k) '(i,37:2:54),Trial0 ' num2str(k)
          '(i,38:2:54),' char(39) 'g' char(39) ')'])
end

    title(['Trial Number: ' num2str(k)])

end

clear i k

%% STEP 1 Split the data of Trialxx for the curve fitting tool
clear all
load RawData.mat

% Trial01_Sc=ones(2,1);
% Trial02_Sc=ones(2,1);
% Trial03_Sc=ones(2,1);
% Trial04_Sc=ones(2,1);
% Trial05_Sc=ones(2,1);
% Trial06_Sc=ones(2,1);

endelement = 2; % 0: Include, 1:Not Include the last element (0,0)

for trialnum=1:6
    for i=1:15

        % Create the Centre Line Matrices
        %plot(Trial01(i,1:2:18),Trial01(i,2:2:18))
        eval(['auxDataX = Trial0 ' num2str(trialnum) '(i,1:2:18)*Trial0 '
              num2str(trialnum) '_Sc(1);']);
        %eval(['auxDataX = Trial0 ' num2str(trialnum) '(i,1:2:18);']);
        eval(['auxDataY = Trial0 ' num2str(trialnum) '(i,2:2:18)*Trial0 '
              num2str(trialnum) '_Sc(2);']);
        %auxDataX = Trial01(i,1:2:18);
        %auxDataY = Trial01(i,2:2:18);

        % Translate the points to the origin for the spiral fitting
        auxDataX = auxDataX - auxDataX(end,1);
        auxDataY = auxDataY - auxDataY(end,1);

        % Calculate the polar coordinates
        r = sqrt(auxDataX.^2+auxDataY.^2);
        phi = atan2(auxDataY, auxDataX);

        % Assign Matrices

```

```

eval(['Trial0 ' num2str(trialnum) '_C_' num2str((i 1)*10) '_X='
      auxDataX(1:end ' num2str(endelement) ');'])
eval(['Trial0 ' num2str(trialnum) '_C_' num2str((i 1)*10) '_Y='
      auxDataY(1:end ' num2str(endelement) ');'])
eval(['Trial0 ' num2str(trialnum) '_C_' num2str((i 1)*10) '_r=r'
      (1:end ' num2str(endelement) ');'])
eval(['Trial0 ' num2str(trialnum) '_C_' num2str((i 1)*10) '_phi='
      phi(1:end ' num2str(endelement) ');'])

%           Create the External Line Matrices
%plot(Trial01(i,19:2:36),Trial01(i,20:2:36),'k')
eval(['auxDataX = Trial0 ' num2str(trialnum) '(i,19:2:36)*Trial0'
      ' num2str(trialnum) '_Sc(1);']);
%eval(['auxDataX = Trial0 ' num2str(trialnum) '(i,19:2:36);']);
eval(['auxDataY = Trial0 ' num2str(trialnum) '(i,20:2:36)*Trial0'
      ' num2str(trialnum) '_Sc(2);']);
%eval(['auxDataY = Trial0 ' num2str(trialnum) '(i,20:2:36);']);

%auxDataX = Trial01(i,19:2:36);
%auxDataY = Trial01(i,20:2:36);

auxDataX = auxDataX auxDataX(end 1);
auxDataY = auxDataY auxDataY(end 1);

r = sqrt(auxDataX.^2+auxDataY.^2);
phi = atan2(auxDataY, auxDataX);

eval(['Trial0 ' num2str(trialnum) '_E_' num2str((i 1)*10) '_X='
      auxDataX(1:end ' num2str(endelement) ');'])
eval(['Trial0 ' num2str(trialnum) '_E_' num2str((i 1)*10) '_Y='
      auxDataY(1:end ' num2str(endelement) ');'])
eval(['Trial0 ' num2str(trialnum) '_E_' num2str((i 1)*10) '_r=r'
      (1:end ' num2str(endelement) ');'])
eval(['Trial0 ' num2str(trialnum) '_E_' num2str((i 1)*10) '_phi='
      phi(1:end ' num2str(endelement) ');'])

%           Create the Internal Line Matrices
%plot(Trial01(i,37:2:54),Trial01(i,38:2:54),'g')
eval(['auxDataX = Trial0 ' num2str(trialnum) '(i,37:2:54)*Trial0'
      ' num2str(trialnum) '_Sc(1);']);
%eval(['auxDataX = Trial0 ' num2str(trialnum) '(i,37:2:54);']);
eval(['auxDataY = Trial0 ' num2str(trialnum) '(i,38:2:54)*Trial0'
      ' num2str(trialnum) '_Sc(2);']);
%eval(['auxDataY = Trial0 ' num2str(trialnum) '(i,38:2:54);']);
%auxDataX = Trial01(i,37:2:54);
%auxDataY = Trial01(i,38:2:54);

auxDataX = auxDataX auxDataX(end 1);

```

```

auxDataY = auxDataY auxDataY(end 1);

r = sqrt(auxDataX.^2+auxDataY.^2);
phi = atan2(auxDataY, auxDataX);

eval(['Trial0 ' num2str(trialnum) '_I_ ' num2str((i 1)*10) '_X=
      auxDataX(1:end ' num2str(endelement) ');'])
eval(['Trial0 ' num2str(trialnum) '_I_ ' num2str((i 1)*10) '_Y=
      auxDataY(1:end ' num2str(endelement) ');'])
eval(['Trial0 ' num2str(trialnum) '_I_ ' num2str((i 1)*10) '_r=r
      (1:end ' num2str(endelement) ');'])
eval(['Trial0 ' num2str(trialnum) '_I_ ' num2str((i 1)*10) '_phi=
      phi(1:end ' num2str(endelement) ');'])

      end
end

clear auxD* i phi r trialnum endelement

%% STEP 2 Do the fitting for the data to the spiral equation

par_phivsr_a = zeros(6,15);
par_phivsr_b = zeros(6,15);
par_phivsr_R2 = zeros(6,15);
par_phivsr_sse = zeros(6,15);
for trialnum=1:6
    for i=0:10:140
        clear cf_
        eval(['r = Trial0 ' num2str(trialnum) '_I_ ' num2str(i) '_r;'])
        r = r min(r);
        eval(['tmp = Trial0 ' num2str(trialnum) '_I_ ' num2str(i) '_phi
              ;'])
        phi = tmp min(tmp)+0.001;
        clear tmp

        st_phivsr_ = [24.556632041750123818 0.073301546389193089626 ];
        ft_phivsr_ = fitype('power1');
        % Fit this model using new data
        [cf_phivsr_ ,gof] = fit(phi(:),r(:),ft_phivsr_);%,'Startpoint',
            st_phivsr_);

        par_phivsr_a(trialnum,i/10+1) = cf_phivsr_.a;
        par_phivsr_b(trialnum,i/10+1) = cf_phivsr_.b;

        par_phivsr_R2(trialnum,i/10+1) = gof.rsquare;
        par_phivsr_sse(trialnum,i/10+1) = gof.sse;
    end
end
clear gof *_phivsr_ trialnum

```

```

%% STEP 3 Do the fitting for the power parameters with the
displacement

displ=0:10:140;
displ(1)=0.1;

par_avsdisp_a = zeros(6,1);
par_avsdisp_b = zeros(6,1);
par_avsdisp_R2 = zeros(6,1);
par_avsdisp_sse = zeros(6,1);

par_bvsdisp_a = zeros(6,1);
par_bvsdisp_b = zeros(6,1);
par_bvsdisp_c = zeros(6,1);
par_bvsdisp_R2 = zeros(6,1);
par_bvsdisp_sse = zeros(6,1);

for trialnum=1:6
    a=par_phivsr_a(trialnum,:);
    b=par_phivsr_b(trialnum,:);

    % This is the custom exclude rule
    ex_([1 2]) = 1;

    % Fit the model for Parameter a
    st_avsdisp_ = [3102.9433760075726241 0.041530680943691819507 ];
    ft_avsdisp_ = fitype('exp1');
    [cf_avsdisp_,gof] = fit(displ',a',ft_avsdisp_', 'Exclude', ex_);%, '
        Startpoint', st_avsdisp_);

    par_avsdisp_a(trialnum)=cf_avsdisp_.a;
    par_avsdisp_b(trialnum)=cf_avsdisp_.b;
    par_avsdisp_R2(trialnum)=gof.rsquare;
    par_avsdisp_sse(trialnum)=gof.sse;
    clear gof

    % Fit the model for Parameter b
    st_bvsdisp_ = [0.39579097962058779059 0.37045117059057081077
        0.12250797592940740333 ];
    ft_bvsdisp_ = fitype('power2');
    [cf_bvsdisp_,gof] = fit(displ',b',ft_bvsdisp_', 'Exclude', ex_);%, '
        Startpoint', st_bvsdisp_);

    par_bvsdisp_a(trialnum)=cf_bvsdisp_.a;
    par_bvsdisp_b(trialnum)=cf_bvsdisp_.b;
    par_bvsdisp_c(trialnum)=cf_bvsdisp_.c;
    par_bvsdisp_R2(trialnum)=gof.rsquare;
    par_bvsdisp_sse(trialnum)=gof.sse;

```

```

        clear gof
    end

%% plot stuff
figure

for trialnum=1:6
    subplot(2,3,trialnum);plot(displ,par_phivsr_a(trialnum,:))
end

%%
for trialnum=1:6
    for i=140:10:0
        eval(['tmp = Trial0 ' num2str(trialnum) '_I_ ' num2str(i) '_X;'])
        tmpX(i/10+1,:)=tmp;
        eval(['tmp = Trial0 ' num2str(trialnum) '_I_ ' num2str(i) '_Y;'])
        tmpY(i/10+1,:)=tmp;
    end
    subplot(2,3,trialnum);plot(displ,tmpX(:,trialnum));hold on;clear
        tmp

        subplot(2,3,trialnum);plot(displ,tmpY(:,trialnum),'r');clear tmp
    end

%% PLT Plot the end effector coordinates in relation to the
    displacement

    displ=0:10:140;
    for trialnum=1:6
        for i=140:10:0
            eval(['tmp = Trial0 ' num2str(trialnum) '_I_ ' num2str(i) '_X(end
                );'])
            tmpX(i/10+1,trialnum)=tmp;
            eval(['tmp = Trial0 ' num2str(trialnum) '_I_ ' num2str(i) '_Y(end
                );'])
            tmpY(i/10+1,trialnum)=tmp;

            tmpr(i/10+1,trialnum) = sqrt(tmpX(i/10+1,trialnum)^2+tmpY(i
                /10+1,trialnum)^2);
            tmpphi(i/10+1,trialnum) = atan2(tmpY(i/10+1,trialnum),tmpX(i
                /10+1,trialnum)^2);
        end
        subplot(2,3,trialnum);plot(displ,tmpX(:,trialnum));hold on;clear
            tmp
        subplot(2,3,trialnum);plot(displ,tmpY(:,trialnum),'r');clear tmp
        axis([0 140 70 70]);axis square on
    end

%% STEP 2b Calculate end effector coordinates in polar

```

```

displ=0:10:140;
for trialnum=1:6
    for i=140:10:0
        eval(['tmp = Trial0 ' num2str(trialnum) '_I_ ' num2str(i) '_X(end
            );'])
        tmpX(i/10+1,trialnum)=tmp;
        eval(['tmp = Trial0 ' num2str(trialnum) '_I_ ' num2str(i) '_Y(end
            );'])
        tmpY(i/10+1,trialnum)=tmp;

        tmpr(i/10+1,trialnum) = sqrt(tmpX(i/10+1,trialnum)^2+tmpY(i
            /10+1,trialnum)^2);
        tmpphi(i/10+1,trialnum) = atan2pos(tmpY(i/10+1,trialnum),tmpX(i
            /10+1,trialnum));
    end

    % Move it a bit for the fitting tool
    tmpphi(1,trialnum)=0.001;

    % Translate to the origin (for the spiral model)
    tmpr(:,trialnum) = tmpr(:,trialnum) - min(tmpr(:,trialnum));

    %subplot(2,3,trialnum);plot(tmpX(:,trialnum),tmpY(:,trialnum));hold
        on;clear tmp
    %figure
    %subplot(2,3,trialnum);plot(tmpphi(:,trialnum),tmpr(:,trialnum));
    %axis([0 140 70 70]);axis square on
end

%% STEP 3b1 Fit the end effector polar coordinates to spiral function

for trialnum=1:6
    r = tmpr(:,trialnum);
    phi = tmpphi(:,trialnum);

    st_ = [9.251530139372093231 0.63351448193155901478 ];
    ft_ = fittype('power1');

    % Fit this model using new data
    [cf_pol,gof] = fit(phi,r,ft_,'Startpoint',st_);

    par_ee_pol_a(trialnum)=cf_pol.a;
    par_ee_pol_b(trialnum)=cf_pol.b;
    par_ee_pol_R2(trialnum) = gof.rsquare;
end

```

```

%% STEP 3b2   Fit the end effector cartesian coordinates to sin
              function

for trialnum=1:6
    X = mean(tmpX')';
    %X = tmpX(:,trialnum);
    Y = tmpY(:,trialnum);

    ft_ = fittype('sin2');

    % Fit this model using new data
    st_ = [32.436043158870639047 0.0448798950512827588
           1.2432843803429167728 6.6293909236383008476
           0.0897597901025655176 0.17434896263689417251 ];
    [cf_cart ,gof] = fit (displ ',X,ft_', 'Startpoint ',st_);

    par_ee_cart_X_a1 (trialnum)=cf_cart.a1;
    par_ee_cart_X_a2 (trialnum)=cf_cart.a2;
    par_ee_cart_X_b1 (trialnum)=cf_cart.b1;
    par_ee_cart_X_b2 (trialnum)=cf_cart.b2;
    par_ee_cart_X_c1 (trialnum)=cf_cart.c1;
    par_ee_cart_X_c2 (trialnum)=cf_cart.c2;
    par_ee_cart_X_R2 (trialnum) = gof.rsquare;

    [cf_cart ,gof] = fit (displ ',Y,ft_);

    par_ee_cart_Y_a1 (trialnum)=cf_cart.a1;
    par_ee_cart_Y_a2 (trialnum)=cf_cart.a2;
    par_ee_cart_Y_b1 (trialnum)=cf_cart.b1;
    par_ee_cart_Y_b2 (trialnum)=cf_cart.b2;
    par_ee_cart_Y_c1 (trialnum)=cf_cart.c1;
    par_ee_cart_Y_c2 (trialnum)=cf_cart.c2;
    par_ee_cart_Y_R2 (trialnum) = gof.rsquare;
end

%% STEP 3b3   Fit the end effector cartesian coordinates to sin/cos
              function

for trialnum=1:6
    %X = mean(tmpX')';
    X = tmpX(:,trialnum);
    Y = tmpY(:,trialnum);

    % you need to flip the equations
    X = flipud(X);
    Y = flipud(Y);

    % And also control the variable they are fitting against

```

```

t=linspace(0,1.5*pi,15);

fo_X = fitoptions('method','NonlinearLeastSquares','Lower',[10 0.5
    20],'Upper',[20 1.5 20]);
st_ = [12 1.1 10];
set(fo_X,'Startpoint',st_);
ft_X = fitype('a*x.*sin(b*x)+c',...
    'dependent',{ 'y' }, 'independent',{ 'x' },...
    'coefficients',{ 'a', 'b', 'c' });

% Fit this model using X data
[cf_cart,gof] = fit(t',X,ft_X,fo_X);

disp('=====' )
disp(cf_cart)
par_ee_cart_X_a(trialnum)=cf_cart.a;
par_ee_cart_X_b(trialnum)=cf_cart.b;
par_ee_cart_X_c(trialnum)=cf_cart.c;
par_ee_cart_X_R2(trialnum) = gof.rsquare;

fo_Y = fitoptions('method','NonlinearLeastSquares','Lower',[10 0.5
    20],'Upper',[20 1.5 20]);
st_ = [15 1 5];
set(fo_Y,'Startpoint',st_);
ft_Y = fitype('a*x.*cos(b*x)+c',...
    'dependent',{ 'y' }, 'independent',{ 'x' },...
    'coefficients',{ 'a', 'b', 'c' });

% Fit this model using new data
[cf_cart,gof] = fit(t',Y,ft_Y,fo_Y);

disp(cf_cart)
par_ee_cart_Y_a(trialnum)=cf_cart.a;
par_ee_cart_Y_b(trialnum)=cf_cart.b;
par_ee_cart_Y_c(trialnum)=cf_cart.c;
par_ee_cart_Y_R2(trialnum) = gof.rsquare;
end

%% PLT 2 Plot X,Y of Internal end effector using errorbars WITH SIN/
COS
clf
X_mean = zeros(15,1);
X_max = zeros(15,1);
X_min = zeros(15,1);
Y_mean = zeros(15,1);
Y_max = zeros(15,1);
Y_min = zeros(15,1);

```

```

%displ_ft=linspace(0,1.5*pi,15)';

%displ_ft=0.034*displ;

% **** Flipping for the sake of displacement
displ_ft=0.034*(140*displ); % This is more correct cause displacement
    goes from 0 to 140

X_mean = ft_X(mean(par_ee_cart_X-a),mean(par_ee_cart_X-b),mean(
    par_ee_cart_X-c),displ_ft);
Y_mean = ft_Y(mean(par_ee_cart_Y-a),mean(par_ee_cart_Y-b),mean(
    par_ee_cart_Y-c),displ_ft);

% Flip the tmpX/tmpY data
tmpX=flipud(tmpX);
tmpY=flipud(tmpY);

for i=1:15
%     %X_mean(i)=mean(tmpX(i,:));
%     X_min(i)=X_mean(i)    min(tmpX(i,:));
%     X_max(i)=X_mean(i)    max(tmpX(i,:));
%
%     %Y_mean(i)=mean(tmpY(i,:));
%     Y_min(i)=Y_mean(i)    min(tmpY(i,:));
%     Y_max(i)=Y_mean(i)    max(tmpY(i,:));

% **** Flipping for the sake of displacement
%X_mean(i)=mean(tmpX(i,:));
X_min(i)=X_mean(i)    min(tmpX(16 i,:));
X_max(i)=X_mean(i)    max(tmpX(16 i,:));

%Y_mean(i)=mean(tmpY(i,:));
Y_min(i)=Y_mean(i)    min(tmpY(16 i,:));
Y_max(i)=Y_mean(i)    max(tmpY(16 i,:));
end

% Plot the mean values of the coordinates
%plot(displ,mean(tmpX'),'x');hold on;
%plot(displ,mean(tmpY'),'rx');

% **** Flipping for the sake of displacement
plot(displ,flipr(mean(tmpX')),'x');hold on;
plot(displ,flipr(mean(tmpY')),'rx');

% Plot the fit and the deviation bars
errorbar(displ,X_mean,X_min,X_max,' ');
errorbar(displ,Y_mean,Y_min,Y_max,'r ');
% This is auxiliary to make the legend correct

```

```

plot(0,X_mean(1));plot(0,Y_mean(1),'r')
title('End effector Coordinates vs. Wire Displacement','FontSize',16)
xlabel('Displacement (mm) ','FontSize',16)
ylabel('Coordinate (mm) ','FontSize',16)
legend('X Coordinate Measurements Mean','Y Coordinate Measurements Mean
','X Fit','Y Fit','X Measurement Limits','Y Measurement Limits');
axis([ 20 160 80 100])
axis square on
%%text( 10, 60, 'Fitting equation:  $x = a*\sin(b*dis)+c$  and  $y = a*\cos(b*dis
)+c$  ','FontSize',10.3,'Interpreter','latex')

%% PLT Plot X,Y of Internal end effector using errorbars
clf
X_mean = zeros(15,1);
X_max = zeros(15,1);
X_min = zeros(15,1);
Y_mean = zeros(15,1);
Y_max = zeros(15,1);
Y_min = zeros(15,1);

displ_ft=linspace(0,140,15)';
%X_mean = ft_(median(par_ee_cart_X_a1),median(par_ee_cart_X_b1),median(
par_ee_cart_X_c1),median(par_ee_cart_X_a2),median(par_ee_cart_X_b2)
,median(par_ee_cart_X_c2),displ_ft);
%Y_mean = ft_(median(par_ee_cart_Y_a1),median(par_ee_cart_Y_b1),median(
par_ee_cart_Y_c1),median(par_ee_cart_Y_a2),median(par_ee_cart_Y_b2)
,median(par_ee_cart_Y_c2),displ_ft);

X_mean = ft_(mean(par_ee_cart_X_a1),mean(par_ee_cart_X_b1),mean(
par_ee_cart_X_c1),mean(par_ee_cart_X_a2),mean(par_ee_cart_X_b2),
mean(par_ee_cart_X_c2),displ_ft);
Y_mean = ft_(mean(par_ee_cart_Y_a1),mean(par_ee_cart_Y_b1),mean(
par_ee_cart_Y_c1),mean(par_ee_cart_Y_a2),mean(par_ee_cart_Y_b2),
mean(par_ee_cart_Y_c2),displ_ft);

for i=1:15
%X_mean(i)=mean(tmpX(i,:));
X_min(i)=X_mean(i) min(tmpX(i,:));
X_max(i)=X_mean(i) max(tmpX(i,:));

%Y_mean(i)=mean(tmpY(i,:));
Y_min(i)=Y_mean(i) min(tmpY(i,:));
Y_max(i)=Y_mean(i) max(tmpY(i,:));
end

% Plot the mean values of the coordinates
plot(displ,mean(tmpX'),'x');hold on;
plot(displ,mean(tmpY'),'rx');
% Plot the fit and the deviation bars

```

```

errorbar(displ,X_mean,X_min,X_max,'r')
errorbar(displ,Y_mean,Y_min,Y_max,'r')
% This is auxiliary to make the legend correct
plot(0,X_mean(1));plot(0,Y_mean(1),'r')
title('End effector Coordinates vs. Wire Displacement')
xlabel('Displacement (mm)')
ylabel('Coordinate (mm)')
legend('X Coordinate Mean','Y Coordinate Mean','X Fit','Y Fit','X
Measurement Limits','Y Measurement Limits');
axis([ 20 160 80 100])
axis square on
text(10,60,'Fitting equation: a1*sin(b1*x+c1) + a2*sin(b2*x+c2)',
FontSize,10.3,'Interpreter','latex')

%% Sample code

phi = 0:0.1:4;

a = 1;

r = a*phi.^10;

polar(phi,r,'m')

x = r.*cos(phi);
y = r.*sin(phi);

plot(x,y)

r2 = sqrt(x.^2+y.^2);

phi2 = atan2pos(y,x);

polar(phi2,r2,'m')

%% Batch plotting stuff 01
% Compare between the different trials
hold off
plot(Trial01_E_100_phi,Trial01_E_100_r)
hold on
plot(Trial02_E_100_phi,Trial02_E_100_r,'r')
plot(Trial03_E_100_phi,Trial03_E_100_r,'g')
plot(Trial04_E_100_phi,Trial04_E_100_r,'k')
plot(Trial05_E_100_phi,Trial05_E_100_r,'m')
plot(Trial06_E_100_phi,Trial06_E_100_r,'c')
% btw this one looks great in terms of repeatability

%% Batch plotting stuff 02 THIS IS GOOD

```

```

% See the relationship between phi and r for the different
    displacements
clf
trialnum=3;
for i=0:10:140
    subplot(4,4,i/10+1)
    eval(['plot(Trial0 ' num2str(trialnum) '_C_' num2str(i) '_phi',Trial0
        ' num2str(trialnum) '_C_' num2str(i) '_r)'])
    hold on
    eval(['plot(Trial0 ' num2str(trialnum) '_E_' num2str(i) '_phi',Trial0
        ' num2str(trialnum) '_E_' num2str(i) '_r,' char(39) 'r' char
        (39) ')'])
    eval(['plot(Trial0 ' num2str(trialnum) '_I_' num2str(i) '_phi',Trial0
        ' num2str(trialnum) '_I_' num2str(i) '_r,' char(39) 'g' char
        (39) ')'])
    title(['Displacement ' num2str(i)])
    %axis ([ 3 3 0 200])
    %pause(0.5)
end

% Putting a legend
subplot(4,4,16);plot(0.5,0.5,'r');hold on;plot(0.5,0.5);plot(0.5,0.5,'g
')
h=legend('External Line','Centre Line','Internal Line','Location','West
');
set(h,'FontSize',18)
clear h

% Putting Labels
subplot(4,4,9)
%text(2,300,'phi','FontSize',24)
subplot(4,4,15)
%text(2.5,40,'r','FontSize',24)

% Putting a Title
%subplot(4,4,3)
%text(3,800,['phi vs. r relation in Trial ' num2str(trialnum)],'
FontSize',28)

%% Measure the distance of each curve
trialnum=4;

for k=0:10:140
    eval(['X = Trial0 ' num2str(trialnum) '_E_' num2str(k) '_X;'])
    eval(['Y = Trial0 ' num2str(trialnum) '_E_' num2str(k) '_Y;'])
    dis=0;
    for i =2:7
        dX = X(i) - X(i-1);
        dY = Y(i) - Y(i-1);
    end
end

```

```

        dis = dis+sqrt(dX^2+dY^2);
    end
    disTrial3_E(k/10+1)=dis;
end

%% And print them
plot(disTrial3_C)
hold on
plot(disTrial3_E,'g')
plot(disTrial3_I,'k')

%%

h1 = figure;
%h2 = figure;
%h3 = figure;

for i=1:15
    %set(0,'CurrentFigure',h1)
    %title('Center Line')

    %plot(Trial01(i,1:2:18),Trial01(i,2:2:18))
    eval(['plot(Trial0 ', num2str(k) ' (i,1:2:18),Trial0 ', num2str(k)
        '(i,2:2:18)) '])
    hold on
    %set(0,'CurrentFigure',h2)
    %title('External Line')

    %plot(Trial01(i,19:2:36),Trial01(i,20:2:36),'k')
    eval(['plot(Trial0 ', num2str(k) ' (i,19:2:36),Trial0 ', num2str(k)
        '(i,20:2:36), ' char(39) 'k' char(39) ' ')])
    hold on
    %set(0,'CurrentFigure',h3)
    %title('Internal Line')

    %plot(Trial01(i,37:2:54),Trial01(i,38:2:54),'g')
    eval(['plot(Trial0 ', num2str(k) ' (i,37:2:54),Trial0 ', num2str(k)
        '(i,38:2:54), ' char(39) 'g' char(39) ' ')])
    hold on
end

```

C.3 Forward Kinematics Analysis

In order to establish a kinematic model for the HS gripper, it is observed that its tip follows a spiral trajectory. Based on this, a number of experiments are

conducted in order to evaluate this assumption and establish a connection between the displacement of the actuating string and the location of the tip, and hence find the forward kinematics of the gripper. The results of the analysis are reported in Section 5.7, while the following paragraphs describe the step by step process. In order to establish a kinematic model of the HS gripper it is observed that its tip follows a spiral trajectory.

The general equation, in polar coordinates, for spirals is given as:

$$r = a \cdot \theta^{\frac{1}{n}} \quad (\text{C.3})$$

where, a and n are parameters defining the size and winding of the spiral respectively. The simplest form of spiral is the Archimedes' spiral with parameter $n = 1$, thus, a linear relationship between θ and r .

Polar coordinates can be expressed in Cartesian ones simply via the equations:

$$x = r \cdot \cos(\theta) \quad (\text{C.4a})$$

$$y = r \cdot \sin(\theta) \quad (\text{C.4b})$$

and by combining (C.3) and (C.4) a connection between x , y and θ can be derived.

$$x = a \cdot \theta \cdot \cos(\theta) \quad (\text{C.5a})$$

$$y = a \cdot \theta \cdot \sin(\theta) \quad (\text{C.5b})$$

To evaluate Eq. C.5 a set of experiments (six in number) are conducted. In these experiments the displacement of the cables d is increased by specific steps (i.e. 10mm) and recorded, using a vision tracking system, the x and y coordinates of the end-effector. Then, using the curve fitting toolbox in Matlab[®], the slightly varied Eq. C.5 is fitted to the data. Specifically the varied equations are:

$$x = a_x \cdot \theta \cdot \sin(b_x \cdot \theta + \pi/2) + c_x \quad (\text{C.6a})$$

$$y = a_y \cdot \theta \cdot \sin(b_y \cdot \theta) + c_y \quad (\text{C.6b})$$

The fitting process provided the parameters that would allow establishment of the forward kinematic model of the gripper. Also, polar coordinate angle θ must be related to the actuation parameter, the displacement d of the cables. By observa-

Table C.3: Parameters Fitting Statistical Analysis

Parameter	Value [mm]	95% low limit	95% high limit	Standard Deviation
a_x	12.775	11.787	13.757	0.548
b_x	1.075	1.040	1.109	0.026
c_x	6.490	4.008	9.972	0.988
a_y	13.070	10.171	15.976	1.119
b_y	1.045	1.006	1.084	0.014
c_y	4.514	-0.749	9.837	1.242

tion, the spiral-like shape of the gripper has 1.5 turns when fully closed, while the maximum displacement of the cables is 140mm.

It must be noted that a spiral described by Eq. C.3 is considered starting in the ‘tip’, while here it is presented from the base of the gripper which is the spiral point at $\theta = 1.5 \cdot \pi$. Hence, in order to align the observed data and the model equation, the relation between θ and displacement d , in mm, is given as a decrease of the displacement:

$$\theta = \frac{1.5 \cdot \pi}{140} \cdot (140 - d) \Rightarrow \theta = 0.034 \cdot (140 - d) \quad (\text{C.7})$$

The statistical details regarding the definition of the parameters can be seen in Table C.3.

Finally, the forward kinematics equations for the tip are reported in C.8a and C.8b. These equations provide the mapping between the displacement of the cables d and the tip’s position on the horizontal plane.

$$x = a_x \cdot 0.034 \cdot d \cdot \sin(b_x \cdot 0.034 \cdot d + \pi/2) + c_x \quad (\text{C.8a})$$

$$y = a_y \cdot 0.034 \cdot d \cdot \sin(b_y \cdot 0.034 \cdot d) + c_y \quad (\text{C.8b})$$

where a_x is 12.775mm, b_x is 1.075mm, c_x is 6.49mm, a_y is 13.07mm, b_y is 1.045mm, c_y is 4.514mm.